DE WAAL D

A SPECTROSCOPIC STUDY OF THE SOLID STATE CHEMISTRY OF SOME VANADIUM COMPOUNDS

PhD UP 1991

A SPECTROSCOPIC STUDY OF THE SOLID STATE CHEMISTRY OF SOME VANADIUM COMPOUNDS

by

Danita de Waal

submitted in partial fulfilment of the
requirements for the degree

PHILOSOPHIAE DOCTOR

in the

Faculty of Science

University of Pretoria

May 1991

C O N T E N T S

ACKNOWLEDGEMENTS

First I wish to thank Prof. A.M. Heyns for the opportunity to do this work and to present it at various occasions. Also for the chance to do some of the work at the University of Regensburg, Germany. I am also grateful to him for leading and motivating me throughout the study.

I want to thank Prof. K.-J. Range for his contribution to the paper on the Raman kinetic study, the joint work on ammonium hexavanadate and the privilege to do some work with him and his group in Regensburg.

Then I wish to thank Mr Adri Watkins, for the assistance with initial work using the cryostat, and Mrs Linda Prinsloo for recording UV/VIS spectra of the lanthanides and high temperature Raman spectra of KVO_3. Also, Mrs Anita van Deventer for the preparation of some of the samples for the high temperature reaction in Chapter V.

The financial support by the following institutions is greatfully acknowledged: University of Pretoria, FRD and CEFIM.

My sincere thanks to Mrs Elsa Baransky for typing this work.

This work has led to the following publications:

1. D. de Waal, A.M. Heyns and K.-J. Range, A Raman spectroscopic determination of the decomposition kinetics of ammonium metavanadate, Mat. Res. Bull. 25, 43-50 (1990).

2. K.-J. Range, C. Eglmeier, A.M. Heyns and D. de Waal, Ammonium hexavanadate: Preparation, Crystal structure, Infrared spectra and high pressure reactions, Z. Naturforsch, 456, 31-38 (1990).

3. D. de Waal, A.M. Heyns, K.-J. Range and C. Eglmeier, Infrared spectra of the ammonium ion in ammonium metavanadate, Spectrochim. Acta 46A (11), 1639-1648 (1990).

4. D. de Waal, A.M. Heyns, K.-J. Range and C. Eglmeier, Infrared spectra of the ammonium ion in ammonium hexavanadate, Spectrochim. Acta 46A (11), 1649-1657 (1990).

The following papers have been accepted for publication in Materials Research Bulletin:

1. D. de Waal, A.M. Heyns and K.-J. Range, An investigation of the high temperature reaction of the alkali metal metavanadates, MVO_3 (M = Na, K), with the lanthanide oxides, Ln_2O_3 (Ln = Nd, Er).

2. D. de Waal, Vibrational spectra of the two phases of $NaVO_3$ and the solid solution $Na(V_{0.66}P_{0.34})O_3$.

3. D. de Waal and A.M. Heyns, Vibrational spectra of $NaVO_3$, KVO_3 and the solid solutions $(Na_{0.88}K_{0.12})VO_3$ and $(Na_{0.5}K_{0.5})VO_3$.

A paper on the emission spectra of $ErVO_4$ and $EuVO_4$ is currently being prepared for publication.

SUMMARY

In this study the solid state chemistry of some metavanadate compounds has been further explored. Firstly the decomposition of NH_4VO_3 was re-investigated and in particular the first reaction step and the reaction product of this decomposition were studied in detail. The structure of $(NH_4)_2V_6O_{16}$ was determined as monoclinic, space group $P2_1/m$. Vibrational spectra of the $V_6O_{16}^{2-}$ anion were analyzed by means of group theoretical analysis of the normal vibrations.

Raman spectroscopy was used to follow the kinetics of the abovementioned decomposition step. This method directly monitors the amount of reactant present. The decomposition mechanism was determined and the activation energy of the reaction was calculated.

Although the crystal structures of NH_4VO_3 and $(NH_4)_2V_6O_{16}$ are known, little is known about the nature of hydrogen bonds in these compounds. Since the Raman active N-H bonds in NH_4VO_3 are of very low intensity, making it very difficult to study isotopically dilute ions, the low temperature infrared spectra of the N-D stretching modes of isotopically dilute NH_3D^+ ions in both NH_4VO_3 and $(NH_4)_2V_6O_{16}$ are reported here. These results indicate that both normal and bifurcated hydrogen bonds occur in NH_4VO_3 and $(NH_4)_2V_6O_{16}$.

In the alkali metal metavanadates no evidence of the dielectric phase transition in KVO_3 could be found by means of Raman spectroscopy and X-ray powder diffraction. The phase transition in $NaVO_3$ involving changes in the crystal structure was investigated by means of far-infrared spectroscopy. Infrared and Raman spectra of the solid solutions $Na(V_{0.66}P_{0.34})O_3$, $(Na_{0.88}K_{0.12})VO_3$ and $(Na_{0.5}K_{0.5})VO_3$ are reported in comparison with those of the end member phases. Translation modes of the cations could accordingly be identified unambiguously. However, the product obtained from the high temperature reaction of an alkali metal metavanadate and a lanthanide oxide is not a solid solution. Infrared and Raman spectroscopy, X-ray powder diffraction and scanning electron microscopy with EDX-analysis revealed that the lanthanide orthovanadate is formed with the alkali metal oxide as a probable second product. Emission and/or absorption spectra of $LnVO_4$. (Ln = Er, Eu, Nd) are reported together with a vibrational analysis and infrared and Raman spectra of the VO_4^{3-}-ion in the zircon phase.

OPSOMMING

Gedurende hierdie studie is aandag gegee aan verskeie aspekte van die vastetoestand chemie van sommige metavanadate. Eerstens is die eerste ontbindingstap van NH_4VO_3 weer ondersoek en die produk van hierdie ontbinding is verder bestudeer. Die struktuur van $(NH_4)_2V_6O_{16}$ is bepaal as monoklinies, ruimtegroep $P2_1/m$. Vibrasiespektra van die $V_6O_{16}^{2-}$ anioon is ondersoek d.m.v. groep teoretiese analise van die normaal vibrasies.

Die kinetika van die bogenoemde ontbinding is bepaal d.m.v. Raman spektroskopie. Die ontbindingsmeganisme is bepaal en die aktiveringsenergie van die reaksie kon bereken word.

Hoewel die kristalstruktuur van NH_4VO_3 en $(NH_4)_2V_6O_{16}$ bekend is, is daar min inligting beskikbaar oor die aard van waterstofbindings in hierdie verbindings. Raman aktiewe N-H vibrasies het 'n lae intensiteit wat 'n studie van isotoop verdunde NH_3D^+ ione bemoeilik, en daarom is lae temperatuur infrarooi spektra van die ione gebruik. Resultate dui op die teenwoordigheid van beide normale en tweeledige waterstofbindings in NH_4VO_3 en $(NH_4)_2V_6O_{16}$.

By die alkali-metaal metavanadate kon die diëlektriese fase-oorgang in KVO_3 nie met Raman spektroskopie of X-straalpoeier diffraksie waargeneem word nie. Die fase oorgang in $NaVO_3$ (kristalstruktuurverandering) is ondersoek d.m.v. ver-infrarooi spektroskopie. Infrarooi en Ramanspektra van die vaste oplossings $Na(V_{0.66}P_{0.34})O_3$, $(Na_{0.88}K_{0.12})VO_3$ en $(Na_{0.5}K_{0.5})VO_3$ word vergelyk met die van die eindfases. Translasiemodes van die katione kan geïdentifiseer word. Die produk van die hoë temperatuur reaksie van MVO_3(M = Na, K) met Ln_2O_3 (Ln = Nd, Er) is egter nie 'n vaste oplossing nie. Infrarooi en Raman spekstroskopie, X-straal poeier diffraksie en skanderingselektronmikroskopie met EDX-analise het bewys dat $LnVO_4$ vorm met M_2O as tweede produk. Emissie en/of absorpsie spektra $LnVO_4$ (Ln = Er, Eu, Nd) word gerapporteer. 'n Vibrasie analise van die VO_4^{3-}-ioon in $LnVO_4$ word gekorreleer met infrarooi en Raman spektra van die 'zircon' fase.

ABBREVIATIONS

1. Description of vibrational modes

ν - stretch	ν_L - libration
δ - deformation	ν_T - translation
ρ_w - wag	w - weak
ρ_r - rock	m - medium
ρ_t - twist	s - strong
as (subscript) - asymmetric	v - very
s (subscript) - symmetric	b - broad
sp - sharp	sh - shoulder

2. Infrared and Raman activity

(IR) Infrared active
(R) Raman active
(IR/R) Infrared and Raman active
(0) Infrared and Raman inactive

3. General

(z) - zircon phase
(s) - scheelite phase
RT - room temperature

CHAPTER I

GENERAL INTRODUCTION

Various spectroscopic methods were used in this study of some aspects of the solid state chemistry of a number of vanadium compounds.

Following a re-examination of several published methods for the preparation of ammonium hexavanadate, single crystals of $(NH_4)_2V_6O_{16}$ were grown by a reaction of V_2O_5 with NH_4Cl in hot aqueous solution [II.2.1]. These are monoclinic, space group $P2_1/m$ with a = 7.858(2), b = 8.412(2), c = 4.995(1)Å, β = 96.43(2)^o and Z = 1 [II.2.2] The structure comprises layers built of V_2O_8 double square pyramids and distorted VO_6 octahedra. The vibrational spectra of the $V_6O_{16}^{2-}$-anion in $(NH_4)_2V_6O_{16}$ were analyzed by means of a group-theoretical analysis of the normal vibrations, followed by an assignment of the vibrational wavenumbers [II.3].

Raman spectroscopy could then be used to follow the kinetics of the thermal decomposition of solid ammonium metavanadate, NH_4VO_3, to ammonium hexavanadate, $(NH_4)_2V_6O_{16}$ [II.4]. This method avoids the disadvantages of mass-loss determinations because it directly monitors the amount of reactant present. Time-dependent isothermal measurements of the intensity of the $\nu(VO_2)_s$ band (927 cm^{-1}) were made between 423 and 443 K, and the reaction was deceleratory throughout. By applying the ln-ln method, derived from a

generalized Avrami-Erofe'ev equation, to the experimental data, a value of n = 0.9 was found, a situation similar to first-order kinetics. The activation energy of the decomposition process could be calculated from the measurements at various temperatures [II.4].

A method [III.2] whereby the symmetry of the ammonium ion in a crystal may be determined from the number and relative intensities of N–D stretching and bending fundamentals of isotopically dilute NH_3D^+ ions was used to investigate the nature of hydrogen bonding in both NH_4VO_3 [III.3] and $(NH_4)_2V_6O_{16}$ [III.4]. The N–D stretching modes of isotopically dilute NH_3D^+ ions in NH_4VO_3 are in agreement with splitting into C_s,C_s and $C_1(2)$ components under C_s site symmetry for the NH_4^+ ion. The three bands observed represent the three bonding distances in the crystal and the position, shape and low temperature behaviour of each band confirmed the existence of two types of hydrogen bonding in NH_4VO_3. The low temperature infrared modes of NH_4^+ and ND_4^+ in NH_4VO_3 and ND_4VO_3, respectively, could be assigned under space group Pbcm. Temperature dependence of these modes also reflected the presence of both normal and bifurcated hydrogen bonds in NH_4VO_3. The infrared bands of the NH_4^+ and ND_4^+ groups in $(NH_4)_2V_6O_{16}$ and its deuterated analogue could be assigned with a fair amount of certainty at 90 K under the space group $P2_1/m$ (C_{2h}^2). The N–D stretching modes of isotopically dilute NH_3D^+ ions in the crystal were also in agreement with C_s site symmetry for the ammonium ion. The frequencies, shapes and temperature dependence of these modes suggest that both normal and hydrogen bonds are formed. The latter closely resembles corresponding bonds in NH_4VO_3, but the normal hydrogen bonds are not as strong as corresponding ones in NH_4VO_3. This could be expected as NH_4^+ ions are dynamic in character in $(NH_4)_2V_6O_{16}$ and remain so down to temperatures of 90 K.

The spectroscopic properties of the alkali metal metavanadates, $NaVO_3$ and KVO_3, as well as solid solutions thereof, were then investigated [IV]. The phase transition in KVO_3 involving changes in the dielectric properties was studied by means of Raman spectroscopy and X-ray powder diffraction. A temperature dependence study of the Raman active modes did not reflect the reported changes in the dielectric properties of the compound around 593 K. Infrared and Raman spectra of the two solid solutions $(Na_{0.88}K_{0.12})VO_3$ and $(Na_{0.5}K_{0.5})VO_3$ were compared to those of KVO_3 and α-$NaVO_3$, and translation modes of the cations could accordingly be identified unambiguously. The frequency dependence of the various vibrational, rotational and translational modes of the $(VO_3^-)_n$-chain on composition was reported and compared to the high pressure behaviour of some vibrations in NH_4VO_3. The phase transition in $NaVO_3$ involving changes in the crystal structure was investigated by means of far-infrared spectroscopy which provided a clear distinction between α- and β-$NaVO_3$. Infrared and Raman spectra of the phosphorus substituted compound $Na(V_{0.66}P_{0.34})O_3$ will be presented in comparison with those of α-$NaVO_3$ in [IV.5.3.1].

The changes occurring in the dielectric constant of an alkali metal metavanadate after it had been treated at high temperatures with a small percentage of a lanthanide oxide were previously ascribed to solid solution formation. The products obtained from the high temperatures with a small percentage of a lanthanide oxide were previously ascribed to solid solution formation. The products obtained from the high temperature reaction of an alkali metal metavanadate, $NaVO_3$ or KVO_3, with a lanthanide oxide, Er_2O_3 or

Nd_2O_3, were analyzed by means of infrared and Raman spectroscopy, X-ray powder diffraction and scanning electron microscopy with energy dispersive X-ray analysis [V]. This revealed that a small amount of the lanthanide orthovanadate is formed in the metavanadate mass. The reaction that takes place could be described by the following reaction equation: $2\ MVO_3 + Ln_2O_3 \xrightarrow{\Delta} 2\ LnVO_4 + M_2O$. With stoichiometric amounts of the reagents under vacuum conditions full conversion occurred to the lanthanide orthovanadate, $LnVO_4$. Raman spectra of these $LnVO_4$[Ln = Er, Eu] compounds had unusually strong transitions in the order of ten times the intensity of vibrational modes. This could be attributed to emission transitions in the various lanthanide ions. Room temperature absorption and emission spectra of $ErVO_4$ and $EuVO_4$ are shown in [VII] together with a vibrational analysis as well as infrared and Raman spectra of the VO_4^{3-}-ion in $LnVO_4$[Ln = Er, Eu] with the zircon structure.

CHAPTER II

THE DECOMPOSITION OF AMMONIUM METAVANADATE, NH_4VO_3, TO AMMONIUM HEXAVANADATE, $(NH_4)_2V_6O_{16}$

II.1 INTRODUCTION

The thermal decomposition of ammonium metavanadate, NH_4VO_3, according to the overall reaction

$$2\ NH_4VO_3 \longrightarrow V_2O_5 + H_2O + 2\ NH_3 \qquad \text{II.1}$$

is an important step in the production of vanadium pentoxide V_2O_5 [1]. Previous work [2-17] on the decomposition reaction include a vibrational spectroscopic study of NH_4VO_3 at elevated temperatures and pressures by Heyns et. al. [10], isothermal decomposition studies of NH_4VO_3 and $(NH_4)_2V_6O_{16}$ by Brown et. al. [12-14] and the thermal decomposition of NH_4VO_3 in open and closed systems by Range et. al. [11].

In spite of the very simple form of reaction II.1, the mechanism of the decomposition reaction seems to be much more complicated, as was discussed by Range et. al. [11]. It has been shown that ammonium hexavanadate, $(NH_4)_2V_6O_{16}$, is indeed the most important, and perhaps only, intermediate

when NH_4VO_3 is heated in air in an open system (the "non-reduction" case, reaction II.2).

$$6\ NH_4VO_3 \longrightarrow (NH_4)_2V_6O_{16} + 4\ NH_3 + 2\ H_2O \qquad \text{II.2}$$

On the other hand, under equilibrium conditions, i.e. when the NH_3 is kept in the system, a redox reaction takes place which yields $(NH_4)_2V_6O_{16}(OH)_2$ as the first intermediate, reaction II.3.

$$6\ NH_4VO_3 \longrightarrow (NH_4)_2V_6O_{12}\ (OH)_2 + 2\ NH_3 + 4\ H_2O + N_2 \qquad \text{III.3}$$

This compound in turn can be further decomposed to give VO_2 (in absence of air) or V_2O_5 (in the presence of air) [11].

Very little structural details were available in the literature for the intermediate $(NH_4)_2V_6O_{16}$ which is produced in very large amounts by technical processes used for the recovery of vanadium from vanadium-bearing titano magnetite ores [1]. The best method for the preparation of single crystals of the compound were presently investigated and the crystal structure could then be determined by X-ray methods [18].

It has been shown [19, 20] that a Raman spectroscopy can be a useful tool in the study of solid-state reaction kinetics. After a vibrational analysis and an interpretation of the infrared and Raman spectra of $V_6O_{16}^{2-}$ Raman spectroscopy could be used to follow the kinetics of the decomposition of solid ammonium metavanadate to ammonium hexavanadate.

II.2 THE CRYSTAL STRUCTURE OF $(NH_4)_2V_6O_{16}$

II.2.1 Preparation of the samples

Four methods for the preparation of $(NH_4)_2V_6O_{16}$ were re-examined in order to obtain crystals of a sufficient size and quality to determine the crystal structure and to get samples as pure as possible for further thermal decomposition studies. All the products were characterized by chemical analysis for V, H and N with information on the crystalline phases present from X-ray Guinier patterns. Where some of the products proved amorphous to X-rays, the mid-infrared spectra were used to identify the compounds which formed. The results of some representative experiments are shown in Table II.1.

Method A: The thermal decomposition of NH_4VO_3 (as described by Ephraim and Beck [21], according to the equation:

$$6\ NH_4VO_3 \xrightarrow{478\ K} (NH_4)_2V_6O_{16} + 2\ H_2O + 4\ NH_3$$

This very simple reaction is difficult to control as further loss of water and ammonia from the $(NH_4)_2V_6O_{16}$ eventually yields V_2O_5. The product after 30 hours has a red-brown colour and the V/N ratio of 4.04 shows that some V_2O_5 had already been formed. After 9 days lines of $(NH_4)_2V_6O_{16}$ became visible on the Guinier pattern and after 3 weeks only V_2O_5 could be identified.

Table II.1 Properties of the samples which were obtained with the different methods proposed for the synthesis of $(NH_4)_2V_6O_{16}$ [18]

Method	A Ephraim and Beck [21]	B Kelmers [22]	C Levanto [23]	D Théobald [24]
Colour :	red-brown	red	orange	orange-yellow
Chemical analysis[a]:				
%V	49.65	48.25	50.50	50.69
%N	3.38	1.96	4.46	4.46
%H	1.42	1.47	1.44	1.38
V/N	4.04	6.77	3.12	3.13
X-ray analysis :	amorphous[b] $(NH_4)_2V_6O_{16}$[c] V_2O_5[d]	amorphous	$(NH_4)_2V_6O_{16}$	$(NH_4)_2V_6O_{16}$
Mid-infra-red spectra:	$(NH_4)_2V_6O_{16}$[b] $(NH_4)_2V_6O_{16} + V_2O_5$[c] V_2O_5[d]	unknown compound(s) with a trace of $(NH_4)_2V_6O_{16}$	$(NH_4)_2V_6O_{16}$	$(NH_4)_2V_6O_{16}$

[a] Calculated for $(NH_4)_2V_6O_{16}$: V = 51.14%, N = 4.69%, H = 1.35%

[b] Heated at 478 K for 30 hours,

[c] 9 days

[d] 3 weeks

All samples invariably contained small amounts of water.

This method is thus not very suitable for the preparation of pure $(NH_4)_2V_6O_{16}$ as an admixture of V_2O_5 is almost unavoidable and the products are not very crystalline. In addition there is the possibility of side reactions resulting from the reduction of vanadium(V) by ammonia [11].

Method B: The acidification of a hot aqueous solution of NH_4VO_3 (Kelmers [22], according to the equation:

$$6\ NH_4VO_3 + 4\ H^+ \longrightarrow (NH_4)_2V_6O_{16} + 4\ NH_4^+ + 2\ H_2O$$

The NH_4VO_3 was dissolved in water and heated to 358 K in a three neck flask equipped for stirring and reflux. H_2SO_4(c) was added to the light yellow solution until it had a dark red colour. The slurry was allowed to reflux at 358 K for 19 hours. The precipitate was filtered off, washed with H_2O and dried to remove occluded water.

This method gave the worst results. A red amorphous powder with V/N = 6.77 was obtained. The mid-IR spectra showed the presence of very little $(NH_4)_2V_6O_{16}$ while the main product(s) could not be identified from these spectra. Although it might be possible to optimize the reaction conditions in order to increase the yield of $(NH_4)_2V_6O_{16}$ time limitations, and the fact that methods C and D gave much better results, persuaded us not to proceed further on this way.

Method C: The precipitation of $(NH_4)_2V_6O_{16}$ from an acidified aqueous solution of $NaVO_3$ with $(NH_4)_2SO_4$ (Levanto [23]), according to the equation:

$$6\ NaVO_3 + 3(NH_4)_2SO_4 + 4\ H^+ \longrightarrow (NH_4)_2V_6O_{16} + 3\ Na_2SO_4 + 4\ NH_4^+ + 2\ H_2O$$

From this method almost pure $(NH_4)_2V_6O_{16}$ could be obtained. The V/N ratio for the orange-coloured sample was 3.12, and Guinier patterns showed $(NH_4)_2V_6O_{16}$ as the only crystalline phase present. In the IR spectrum the bands characteristic of $(NH_4)_2V_6O_{16}$ were sharp and well resolved. The sample obtained by this method was used further for the high pressure experiments. The only disadvantage of the method is its failure to produce larger crystals.

Method D: The reaction of V_2O_5 with NH_4Cl in aqueous solution (Théobald et. al. [24]) according to the equation:

$$3\ V_2O_5 + 2\ NH_4Cl + H_2O \longrightarrow (NH_4)_2V_6O_{16} + 2\ HCl$$

This method was originally developed for the preparation of the mixed-valence compound $(NH_4)_2V_3O_8$ by the reaction of V_2O_5 with NH_4Cl, using metallic tin as reducing agent. Some ammonium hexavanadate was found to be a by-product of the reaction. It was then found that by intentionally omitting tin from the reaction $(NH_4)_2V_6O_{16}$ is formed as the only solid product. Thus pure $(NH_4)_2V_6O_{16}$ was prepared by adding V_2O_5 to a saturated solution of NH_4Cl and allowing the mixture to reflux between 363 ad 373 K for approximately 3 hours, yielding a bright yellow product.

The purity of these samples compared well with those obtained using method C. Table II.1 shows the data for the product after 10 days of heating. Longer heating times in a closed, highly evacuated flask resulted in the formation of coarsely crystallized platelets. Most of the crystals were heavily intergrown. A small individuum could be isolated for crystal structure analysis after inspection of the crystals by X-ray film techniques [18].

II.2.2 Crystal structure

The crystal structure of $(NH_4)_2V_6O_{16}$ is shown in Figure II.1. The single crystals of ammonium hexavanadate were found to be monoclinic and belong to space group $P2_1/m$ with a = 7.858(2), b = 8.412(2), c = 4.995(1)Å, $\beta = 96.43(2)^o$, and Z = 1 [18]. The N, and two O atoms occupy 2(e) positions with symmetry C_s and V(2) and three O atoms are on 2(f) positions with C_1

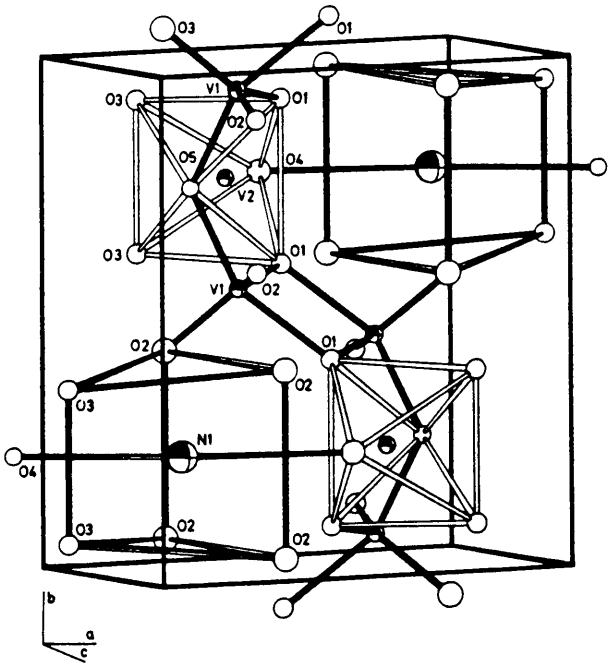

Figure II.1 The crystal structure of $(NH_4)_2V_6O_{16}$

symmetry [25]. The structure resembles that of $K_2V_6O_{16}$ [26] and comprises two kinds of crystallographically independent vanadium atoms. V(1) is surrounded by five oxygens forming a square pyramid with one very short V–O distance (1.595Å). A sixth oxygen (O(4)) is much further apart (V(1)-O(4) = 2.919Å) and completes a heavily distorted octahedron (Figure II.2). The mean V(1)-O distance is 1.828Å, or including O(4) in the coordination sphere, 2.010Å. Two square pyramids are sharing an edge, thus forming V_2O_8 groups with the apices of the pyramids alternatively pointing up and down (Figure II.3). The O–O distance in the shared edge (2.340Å) is the shortest

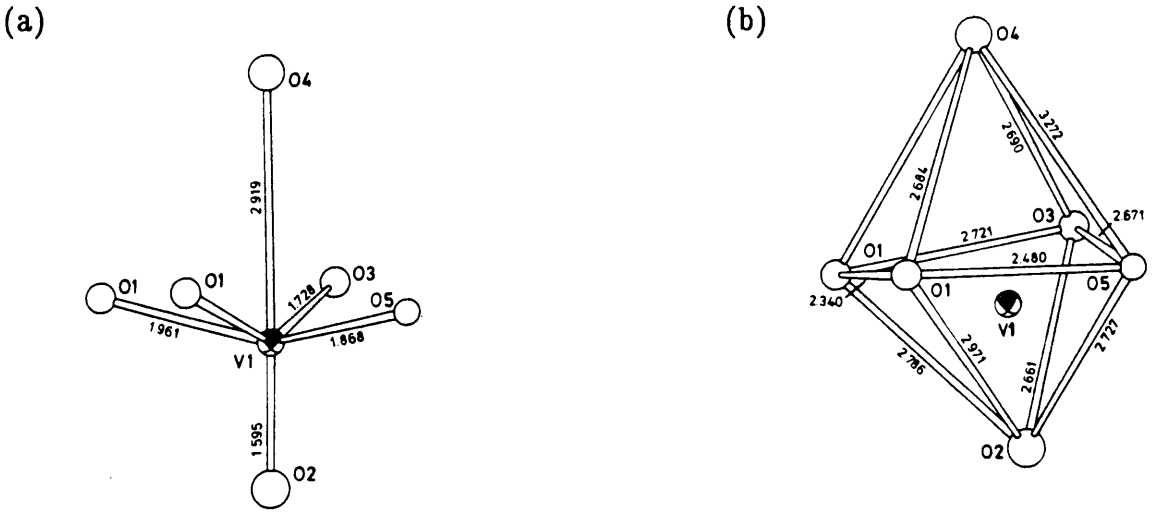

Figure II.2 The oxygen polyhedron around V(1)
(a) V—O distances, (b) O—O distances

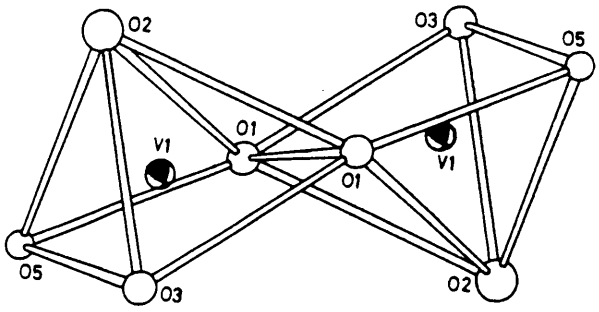

Figure II.3 V_2O_8 groups formed by two square pyramids

one found in the structure of $(NH_4)_2V_6O_{16}$. The V_2O_8 double pyramids are connected via corner-sharing with each other, resulting in zig-zag-chains along [010] (Figure II.1). The octahedron of oxygens around V(2) (Figure II.4) is much less distorted than that around V(1). A very short V–O distance(1.589Å) can be found here as well. The mean V(2)–O distance is 1.916Å. The $V(2)O_6$ octahedron connect adjacent $V(1)_2O_8$ zig-zag-chains, thus forming sheets extending in the b,c-plane.

Figure II.4 The oxygen polyhedron around V(2)
(a) V—O distances, (b) O—O distances

The coordination polyhedron around nitrogen is not so well characterized as those around V(1) and V(2). It can perhaps be best described as a bicapped trigonal prism (Figure II.5). From the N–O distance (Table II.2), however, a 10-fold or even 12-fold coordination could be discussed as well [18].

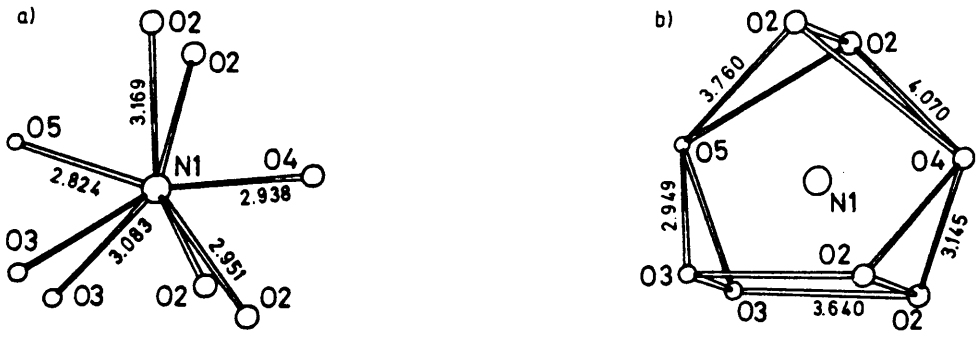

Figure II.5 The coordination around N
(a) N—O distances, (b) O—O distances

Table II.2 Selected interatomic distances [Å] in $(NH_4)_2V_6O_{16}$ [18]

V(1)-O(2)	1.595(4)		O(3)-V(1)	1.728(3)	
-O(3)	1.728(3)		-V(2)	1.974(3)	
-O(5)	1.868(2)		-O(3)	2.545(5)	
-O(1)	1.961(3)		O(4)-V(2)	1.589(5)	
-O(1)	1.988(3)		-O(1)	2.684(6)	2x
-O(4)	2.919(4)		-O(3)	2.690(5)	2x
-V(2)	3.106(1)		-V(1)	2.919(4)	2x
V(2)-O(4)	1.599(5)		-N(1)	2.938(8)	
-O(1)	1.836(3)	2x	O(5)-V(1)	1.868(2)	2x
-O(3)	1.974(3)	2x	-V(2)	2.287(5)	
-O(5)	2.287(5)		-O(1)	2.480(5)	2x
-V(1)	3.106(1)		-O(3)	2.671(6)	2x
O(1)-V(1)	1.836(3)		-O(2)	2.727(3)	2x
-V(1)	1.961(3)		-N(1)	2.824(8)	
-V(1)	1.988(3)		N(1)-O(5)	2.824(8)	
-O(1)	2.340(5)		-O(4)	2.938(8)	
O(2)-V(1)	1.595(4)		-O(2)	2.951(7)	2x
-O(3)	2.661(5)		-O(3)	3.083(6)	2x
-O(5)	2.727(3)		-O(2)	3.169(7)	2x
-O(1)	2.786(5)		-O(3)	3.380(5)	2x
-N(1)	2.951(7)		-O(2)	3.642(6)	2x

II.2.3 High pressure reactions

The products which are obtained after the high-pressure treatment of $(NH_4)_2V_6O_{16}$ at 10-40 kbar, 673-1173 K, and subsequent quenching to ambient conditions are illustrated in Figure II.6. Four well-defined regions are found, depending on the reaction conditions applied.

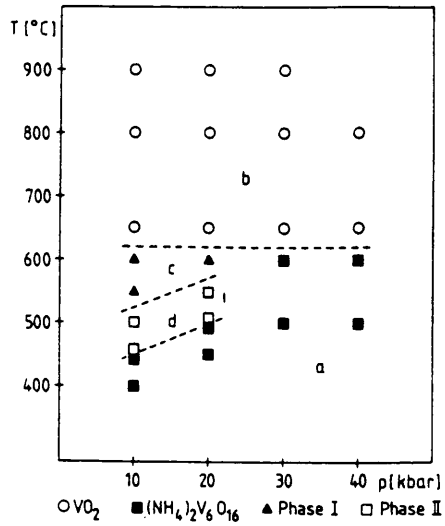

Figure II.6 Decomposition products of $(NH_4)_2V_6O_{16}$ recovered after high-pressure reaction at the p,T-conditions indicated

$(NH_4)_2V_6O_{16}$ is stable up to 723 K at 10 kbar and up to 873 K at 40 kbar (region a, Figure II.6). At high temperatures (region b) VO_2 is obtained at all pressures. It is interesting to note that, whereas $(NH_4)_2V_6O_{16}$ transforms directly to VO_2 at 30 kbar, some intermediates have been found at lower pressures. The stoichiometrics of the intermediates found in regions c and d are still unknown.

Compared to the diversity of different pathways for the closed system thermal decomposition of NH_4VO_3 (Figure 5 in ref. [11]), the reaction of $(NH_4)_2V_6O_{16}$ appear to follow a rather simple scheme. This is certainly due to the fact that the NH_4^+/V ratio of 1:3 in $(NH_4)_2V_6O_{16}$ limits the number of electrons which can can be transferred to a vanadium atom to one. This in turn means that the reduction process must terminate at V(IV) in contrast to NH_4VO_3 (NH_4^+/V ratio of 1:1). If V(IV) has been reached no additional NH_4^+ ions are left to form NH_4^+ containing V(IV) compounds. The situation is therefore completely different from that found for NH_4VO_3 (e.g. the formation of $(NH_4)_2V_6O_{12}(OH)_2$ [11]), but only for stoichiometrical reasons [18].

II.3 THE $V_6O_{16}^{2-}$ ION

II.3.1 Vibrational analysis and spectra

The number of vibrations expected in the $(NH_4)_2V_6O_{16}$ crystal can be predicted by using the correlation method as described by Fateley [27]. These are the 20 $A_g(R)$ + 16 $B_g(R)$ + 15 $A_u(IR)$ + 1 $B_u(IR)$ modes. In addition to these there are the A_u + 2 B_u acoustic vibrations . This is the result when the ammonium ion is treated as a monoatomic cation, similar to K^+ or Cs^+. As the positions of the hydrogen atoms in $(NH_4)_2V_6O_{16}$ could not be determined by X-ray methods, predictions for vibrations of the ammonium ion in the hexavanadate crystal can be made by correlation of the tetrahedral

symmetry of the free ion with the site group C_s and the factor group C_{2h}. Further analysis, using isotopical dilution methods will be discussed in [III.4].

The vibrational spectra of $V_6O_{16}^{2-}$ have been reported by Kristallov et. al. [28] and the vibrational spectra of all the alkali metal and ammonium hexavanadates are practically identical, indicating not only that these compounds are isostructural but also that the bond lengths and angles in the vanadium-oxygen sub-lattice are similar. The vanadium (1)- and (2)-oxygen polyhedra are highly distorted because of their connection through vertices and edges and V–O bond lengths differ considerably. Thus the vibrational spectrum due to the stretches of the anionic sub-lattice can be regarded in a first approximation as corresponding not to the stretches of the polyhedra but to the vibrations of individual V–O bonds [25]. The expected wavenumbers of the vibrations have been estimated by Kristallov et. al. [28], using an equation obtained in the harmonic oscillator approximation and previously used effectively for the alkaline earth metal vanadates [28]:

$$\nu = \frac{36.67}{R-0.1264} \qquad \text{eq. (II.1)}$$

where ν is the wavenumber in cm^{-1} and R the bond length in nm.

The wavenumbers of the V–O–V bridges with respect to the plane of symmetry were estimated using the dependence of the quantity $(\nu_{as} - \nu_s)/(\nu_{as} + \nu_s)$ on

the angle of the bridge [18] and the average value of wavenumbers $\nu_o = (\nu_{as} + \nu_s)/2$, determined from equation (II.1). The vibrations of a double bridge,

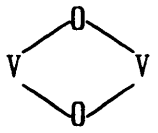

were determined from the approximate equations for a four membered planar symmetrical ring [29].

$$(\nu_s^2 - \nu_{as}^2)/(\nu_s^2 + \nu_{as}^2) = \cos \alpha \text{ and } (\nu_s^2 + \nu_{as}^2)/2 = \nu_o^2$$

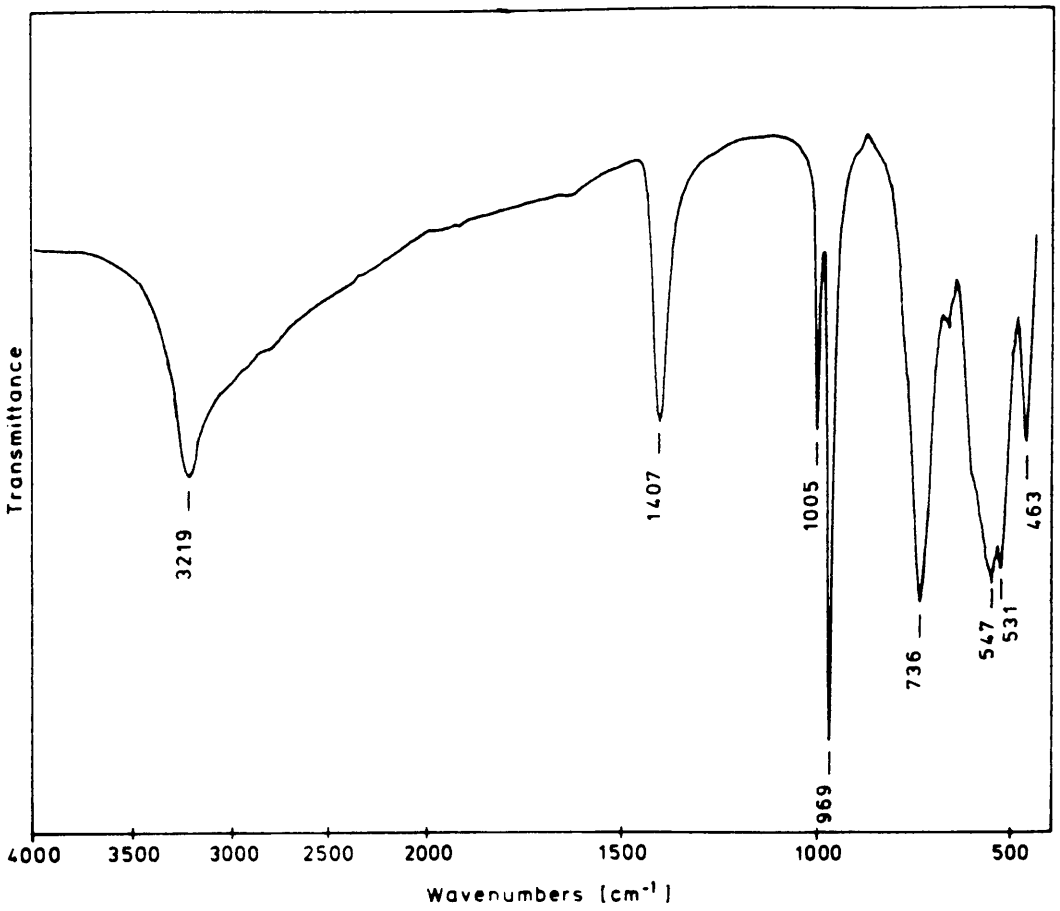

Figures II.7 The mid-infrared spectrum of the orange-yellow decomposition product of NH_4VO_3 [11] identified as $(NH_4)_2V_6O_{16}$

Table II.3 Comparison of the wavenumbers (in cm^{-1}) of the infrared and Raman spectra of $V_6O_{16}^{2-}$ in ammonium hexavanadate

This work			Kristallov [28]			Assignment
ν_{calc}	IR	R	IR	R	ν_{calc}	
1128	1005	996	1010	985	1179	
		978		970		
			972			
1108	969	966		955	1019	
790		808	775	810	785	
	736		738			
641		675	675	665	692	ν(V–O)
607					614	
			600	630	593	
	547	558		550	548	
526	531	521	530	510	538	
		492		490		
	457/463		464	445	452	
	409	427	410	425		δ(V–O–V)
358		374		360	360	ν(V–O)
	326	315		310		
	300	302		300		$R^{C_3}(NH_4^+)$
				285		
	259	260		250		
	239	244		230		
		221		210	215	
		187		185		
		154		155		
		111		220		$T(NH_4^+)$

The infrared and Raman spectra of $(NH_4)_2V_6O_{16}$ are shown in Figures II.7-II.9. Wavenumbers are compared to the values obtained by Kristallov et. al. [28] in Table II.3. Calculations using the same model for V—O stretching vibrations generally gave better results, probably as a result of the more accurate values of V—O bond lengths in Table II.2.

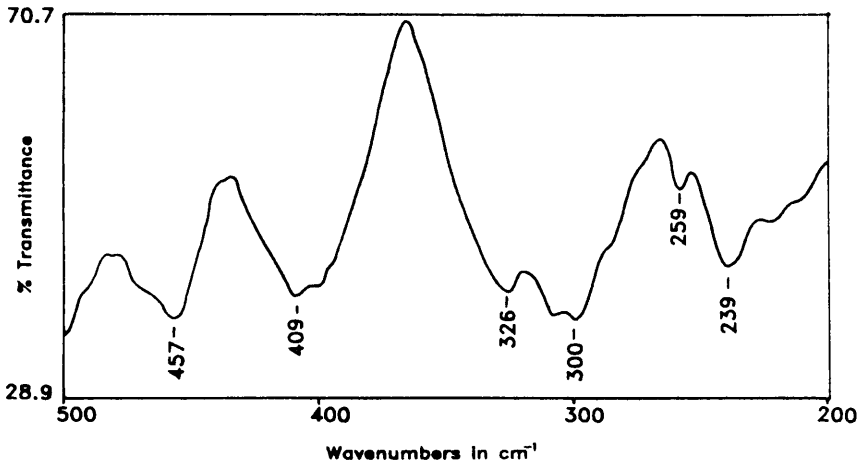

Figure II.8 Far-infrared spectrum of $(NH_4)_2V_6O_{16}$

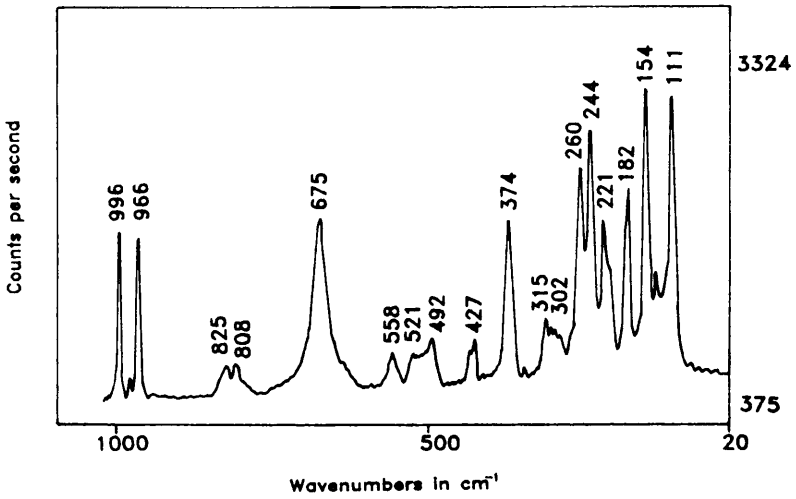

Figure II.9 Raman spectrum of $(NH_4)_2V_6O_{16}$

II.4 A RAMAN SPECTROSCOPIC DETERMINATION OF THE REACTION KINETICS OF THE DECOMPOSITION OF NH_4VO_3 TO $(NH_4)_2V_6O_{16}$

II.4.1 Advantages of the method

In most of the studies of the thermal decomposition of NH_4VO_3 [30-33] dynamic thermal analysis has been used. A noticeable exception to this is the detailed study of Brown et. al. [12-14], which was carried out under isothermal conditions. The latter authors used time-dependent measurements of mass losses during the decomposition to determine the mechanism of the reaction.

Obviously the mass losses associated with the thermal decomposition of NH_4VO_3 in the "non-reduction" and "reduction" cases are different. Because some ammonia can always be trapped in the sample or absorbed as a reactive layer on the surface during the decomposition process, a participation of the redox reaction in the whole process is almost unavoidable. Therefore, monitoring only the mass losses during the decomposition will merely give "mass-loss kinetics" which can agree with the true decomposition kinetics but will not necessarily do so. The fact that most of the intermediate decomposition products of NH_4VO_3 appear with a darkbrown or even black colour illustrates that problem very clearly.

Similar objections can be raised against the deduction of intermediate compounds and the "determination" of their composition from mass losses and nitrogen determination only, assuming a 2:1 ratio of deliberated NH_3 and H_2O and not cross-checking the results by analyses for H and V.

It has been shown elsewhere that Raman spectroscopy can be a useful tool in the study of solid-state reaction kinetics [19, 20]. Because it directly monitors the amount of reactant present during the decomposition it avoids the problems mentioned above.

II.4.2 Experimental

A high-temperature cell, described in [Appendix D(2)], was used to heat the samples of analytical grade NH_4VO_3. A He–Ne laser was used to excite the spectra for Raman measurement. Powdered NH_4VO_3 samples (ca. 0.1 x 0.1 x 0.3 mm) were contained in open glass tubes with a diameter of 3 mm.

The temperature dependence of the Raman spectra of NH_4VO_3 has been reported elsewhere [10]. From this data, the $\nu(VO_2)$ band at 927 cm^{-1} seemed most suitable for kinetic measurements because it has the highest relative intensity and its wavenumber is nearly independent of temperature. The intensity of the band was recorded between 925 and 930 cm^{-1} with intervals of 45 seconds at 423, 428, 438 and 443 K. The temperatures quoted are correct within 5 K. The reaction proceeded very slowly below 423 K and the NH_4VO_3 turned brown or even black at temperatures above 443 K. Thus temperatures outside the range from 423 to 443 K are unsuitable for kinetic measurements using Raman spectroscopy.

II.4.3 Results and discussion

As was shown elsewhere [11], ammonium hexavanadate, $(NH_4)_2V_6O_{16}$, is the most important, and perhaps only, intermediate product obtained by slow heating of NH_4VO_3 in air ("non-reduction" case). In the present study again no signs of other intermediates could be found. The Raman spectra of pure NH_4VO_3 and $(NH_4)_2V_6O_{16}$ are shown in Figure II.10. It is clearly evident that the NH_4VO_3 band at 927 cm^{-1} ($\nu(VO_2)_s$) is well separated from the $(NH_4)_2V_6O_{16}$ band close to this wavenumber at 964 cm^{-1} (ν(V–O)) and it can therefore be assumed that the intensity of the 927 cm^{-1} band in NH_4VO_3 will accurately reflect the amount of NH_4VO_3 present during decomposition.

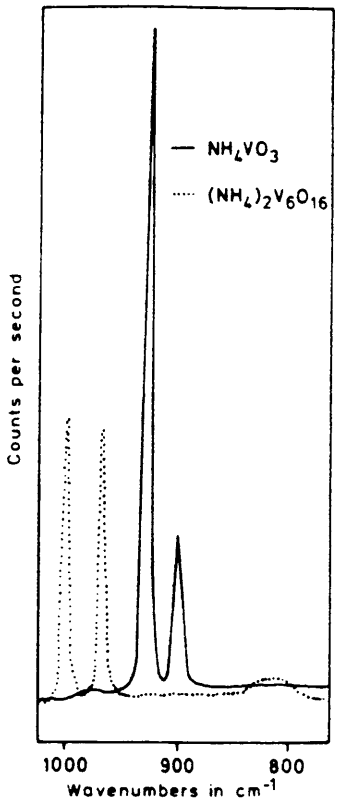

Figure II.10 The Raman spectra of NH_4VO_3 and $(NH_4)_2V_6O_{16}$ in the frequency range 800 - 1000 cm^{-1}

The evaluation of the experimental data must take into account possible errors during the measurements. Three main sources of errors have to be considered, viz.

(i) statistical errors, mainly due to counting statistics,

(ii) insufficient constancy of temperature during a given run and inaccuracy of absolute temperature at this run, and

(iii) uncertainty with respect to t_0, the time at which the reaction actually starts.

Errors due to (i) have been corrected by a smoothing procedure which used a simple three-point method. The smoothing, of course, does not effect the general shape of the χ_r vs. time curves but improves the fitting considerably. The smoothed isothermal kinetic results obtained are shown in Figure II.11.

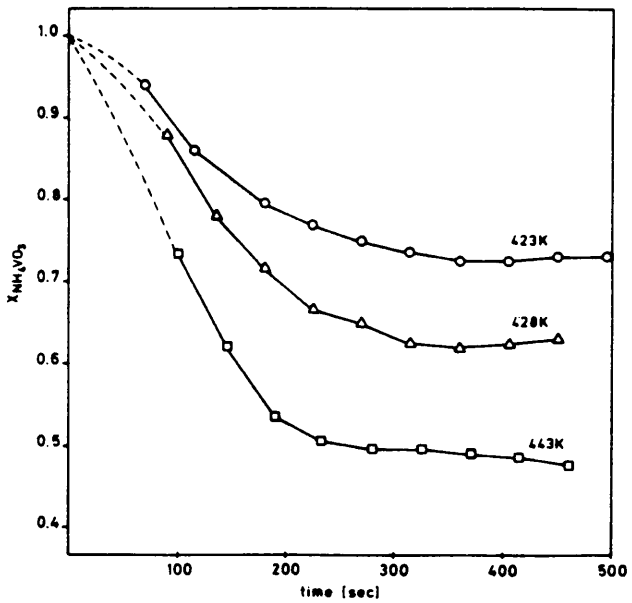

Figure II.11 Graphical representation of the fraction of unreacted NH_4VO_3 ($\chi_{NH_4VO_3}$) against time during decomposition at three different temperatures

It has been stated above that the temperatures quoted are believed to be correct within 5 K. The constancy of the temperature during a given run, however, is much better. Thus, errors due to (ii) should have no marked effect on the kinetics of a given run, but could influence more seriously the calculated energies of activation, especially due to the rather limited range of temperatures, which could be used in the present study.

Undoubtedly, the uncertainty with respect to t_0 is the most important error which has to be considered in the analyses of any solid state kinetics. Such uncertainties can arise either for experimental reasons, e.g. the time needed to heat the sample to a given temperature, or from induction periods inherent in the kinetic process.

It has been pointed out [34] and will be shown again in due course that a wrong choice of t_0 can even lead to completely wrong rate laws. This effect is, of course, not so important for processes with rather long reaction times, because in this case t_0 is small compared to the actual reaction times t.

For reactions which proceed fast, as in the present case, an experimental correction for t_0 is almost impossible. Therefore, we used an analytical method to determine approximate values of t_0. As can be seen from Figure II.11, the reactions are decelaratory throughout, even from the very first measured points on. Thus, a kinetic analysis using the "ln-ln method" seemed to be justified. From the generalized Avrami-Erofe'ev equation [35-38]

$$1 - (\chi_p) = \exp(-kt^n) \qquad \text{eq. II.2}$$

one can easily derive

$$\ln[\ln(\frac{1}{\chi_r})] = n.\ln t + \ln k \qquad \text{eq. II.3}$$

where χ_r and χ_p are the fractions of reactant and product(s), respectively, t is the time and k the rate constant. Plots of $\ln[\ln(\frac{1}{\chi_r})]$ vs. lnt should provide straight lines of various fixed slopes n for every different kinetic expression. Values of n for a number of different rate equations which have found application in kinetic studies of solid state reactions been tabulated [39-41] and are shown in Table II.4.

Table II.4 Values of n for some rate equations. The slope in each case was determined theoretically from data in [40]. Note that $1-\chi_p = \chi_r$.

Rate equation		Slope
Three-dimensional diffusion:	$[1-(1-\chi_p)^{\frac{1}{3}}]^2 = kt$	0.53
Ginstling-Brounshtein:	$[1-(2\chi_p/3)]-(1-\chi_p)^{\frac{2}{3}} = kt$	0.55
Two-dimensional diffusion:	$(1-\chi_p)\ln(1-\chi_p) + \chi_p = kt$	0.55
One-dimensional diffusion:	$\chi_p^2 = kt$	0.58
1st order	$1-\chi_p = \exp(-kt)$	1.00
Mampel intermediate law		
Contracting volume	$1-(1-\chi_p)^{\frac{1}{3}} = kt$	1.04
Contracting area	$1-(1-\chi_p)^{\frac{1}{2}} = kt$	1.08
Zero-order		1.18
Avrami-Erofe'ev	$(1-\chi_p)^{\frac{1}{2}} = kt$	2.00
	$(1-\chi_p)^{\frac{1}{3}} = kt$	3.00
	$(1-\chi_p)^{\frac{1}{4}} = kt$	4.00

When eq. II.3 is applied to the experimental data of Figure II.11, not corrected for t_o, the problem inherent becomes immediately evident (Figure II.12). Not even three points are on a straight line. For the initial points n adopts values of around 1.5, and as these values decrease, more points are included in a linear regression analysis. Because all points are situated beyond the position of the maximum decomposition rate, it is more or less arbitrary to decide how many points should be included. Figure II.13 shows the effect of various t_o corrections on the $\ln[\ln(\frac{1}{\chi_r})]$ vs. lnt plots. Starting with $t_o = 0$ (Figure II.12a), increasing t_o values tend to decrease the initial slope continuously with a steady improvement of the straight-line approximation (Figure II.12b,c). At the other extreme, a very high (and rather unrealistic) value for t_o changes the initial curvature of the plot (Figure II.12d) pointing out definitely an overcorrection. We therefore determined for each isothermal set of χ_r data the value of t_o which gives the best straight-line fit of the first three points by an iteration procedure. The t_o values so obtained were of the order of 30 seconds, resulting in slopes n of about 0.9 for all isothermal data sets. The value of 0.9 for n is closest to n = 1, i.e., the Avrami equation eq. II.2 represents a situation close to first order kinetics.

Figure II.13 shows the obedience of the experimental data to the equation

$$\ln \chi_r = -k(t - t_o) \qquad \text{eq. II.4}$$

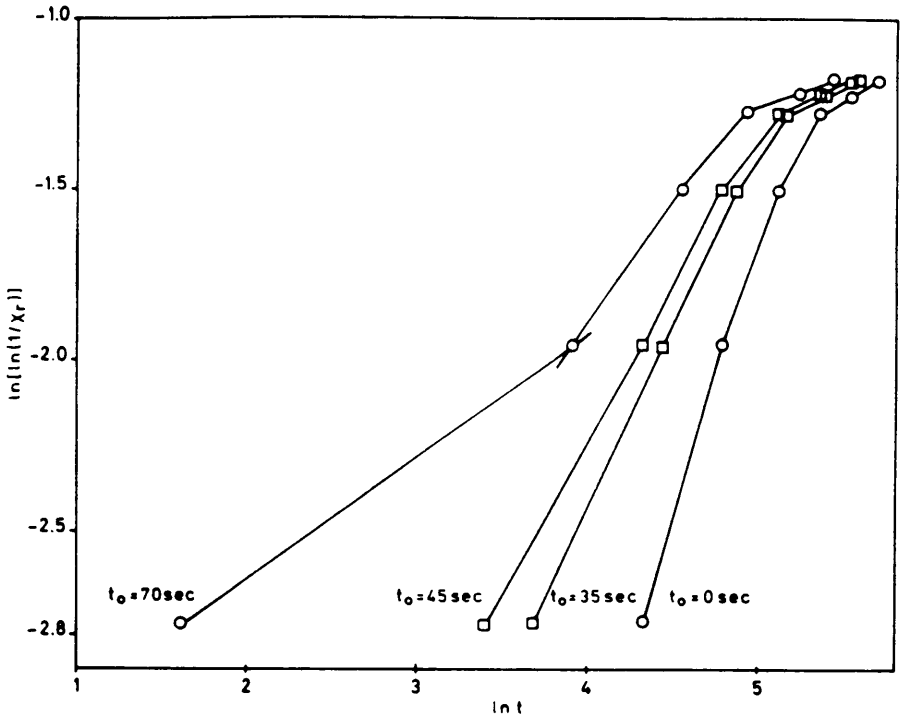

Figure II.12 The effect of various t_0 corrections on the ln-ln analysis of kinetic data at 423 K

(a) no correction ($t_0 = 0$) (b) t_0 = 35 sec.

(c) t_0 = 45 sec. (d) t_0 = 70 sec.

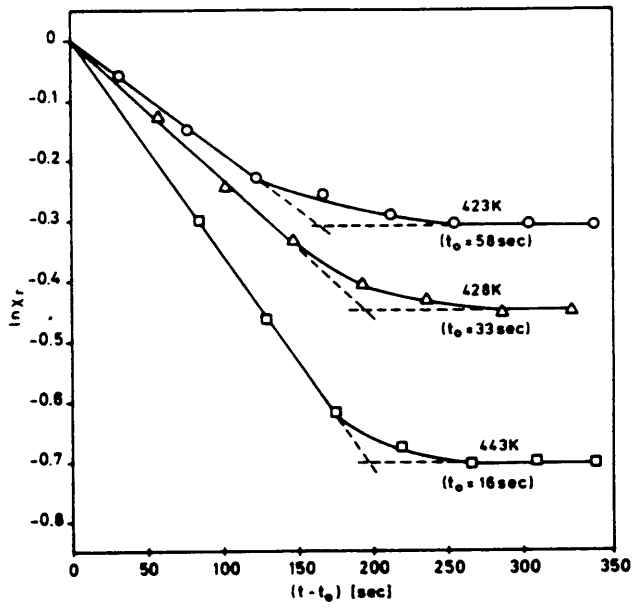

Figure II.13 The obedience of the experimental data of the equation

$$\ln \chi_r = -k(t - t_0)$$

The derived rate constants k and values for t_o at different temperatures are: $1.90 \times 10^{-3}\ s^{-1}$, t_o = 58s (423 K); $2.31 \times 10^{-3}\ s^{-1}$, t_o = 33s (428 K); $3.58 \times 10^{-3}\ s^{-1}$, t_o = 16s (443 K). From these data an activation energy of E_A = 48.6 $kJ.mole^{-1}$ can be calculated assuming that the Arrhenius equation can be applied over the entire temperature range. This value compares rather well with the values of E_A = 49-56 $kJ.mole^{-1}$, found for the thermal decomposition of powdered $(NH_4)_2CrO_4$ [19] and is considerably lower than the value of E_A = 106 $kJ.mole^{-1}$, obtained by Brown et. al. [13]. The difference can perhaps be explained by particle size effects. In the case of $(NH_4)_2CrO_4$ the activation energies for the thermal decomposition of micro-crystals and powdered samples differ by as much as a factor of nearly 2 [19].

II.4.4 Conclusions

The potential of Raman spectroscopy as a useful tool in the study of solid state reactions has been demonstrated. In addition to kinetic measurements, Raman spectroscopy provides direct evidence of structural changes during the course of the reaction.

It must be pointed out very clearly, however, that the analysis of even rather accurate data for solid state kinetics usually does not allow for the differentiation between reaction mechanisms, having expected n values which are close together (e.g. the contracting volume equation, n = 1.04 and the contracting area equation, n = 1.08). A deviation from idealized representations is expected in real systems as this is an indication of a

strained and distorted reaction interface which develops because the volume of the solid reactant is almost always significantly different from the volume of the product which is formed. In addition very often identical values of n can be expected for different reaction mechanisms.

Therefore, structural evidence has to be included in the discussion as well. The value of n = 1, valid for the thermal decomposition of NH_4VO_3 , can be derived from either a diffusionless transformation with nucleation at the start plus continuing nucleation of grain boundaries or a diffusion-controlled reaction with the growth of isolated plates or needles of finite size [41-43]. Considering the chain structure of NH_4VO_3 and $(NH_4)_2V_6O_{16}$ [17, 18] we feel the latter mechanism to be an adequate description of the thermal decomposition of ammonium metavanadate.

CHAPTER III

ISOTOPICAL DILUTION OF THE AMMONIUM ION IN NH_4VO_3 AND $(NH_4)_2V_6O_{16}$

III.1 INTRODUCTION

The vibrational isotope effect was first observed in the rotation-vibrational spectrum of HCl in 1920 [44] and showed the $^{35}Cl/^{37}Cl$ isotopic splitting. Shortly after the discovery of heavy hydrogen by Urey et.al. [45] in 1932 the infrared spectrum of $D^{35}Cl$ present in HCl was reported, showing the first measurement of the H/D isotope shift [46]. Today isotopical substitution finds various applications in vibrational spectroscopy. A few of these are the simple identification of bands, using it as a probe for the assignment of bands to irreducible representations, for a rough estimation of anharmonicities, the correction of frequencies due to Fermi resonance, the structure determination of unstable species isolated in a matrix at low temperatures and force constant refinements [46]. A method has been described by Oxton et.al [47] whereby the symmetry of the ammonium ion in a crystal may be determined from the number and relative intensities of the N-D stretching and bending fundamentals of isotopically dilute NH_3D^+ ions. These modes give rise to sharp bands in the infrared spectrum at liquid nitrogen temperature. This method described in [III.2] will be employed in [III.3] and [III.4] to determine the nature of the symmetry and hydrogen bonding of the ammonium ion in both NH_4VO_3 and $(NH_4)_2V_6O_{16}$.

III.2 SYMMETRY DETERMINATION OF THE AMMONIUM ION IN A CRYSTAL FROM LOW TEMPERATURE INFRARED SPECTRA OF THE NH_3D^+ SPECIES

The symmetry of a site occupied by an ammonium ion in a crystal can in principle be any one of the 32 crystallographic point group symmetries. This can usually, but not always, be deduced from the result of a crystal structure determination. When such a determination is not available or the site symmetry is ambiguous or incorrect additional information on the ammonium ion can be obtained from an infrared spectrum.

The spectroscopic characteristics of an NH_4^+ ion at a site of symmetry S depend on the effective symmetry, E of the ion at that site. This effective symmetry is determined by the maximum subgroup common to T_d and S, that is by the intersection:

$$Td \cap S = E$$

The intersections of T_d with the 32 crystallographic point groups are subgroups of T_d and E can at most indicate the site symmetry within the homomorphisms $S \longrightarrow E$ as shown in Table III.1. Another limitation is the spectroscopic distinguishability of the subgroups of T_d for NH_4^+ - from the number of infrared-active fundamentals only those sets of S can be identified that correspond to one of the following sets of subgroups of T_d: (T_d,T); (C_{3v},C_3); D_{2d}; C_{2v}; $(S_4, D_2, C_s, C_2, C_1)$. The determination of the number of modes for NH_4^+ and ND_4^+ is, however, complicated due to Fermi resonance, the possibility of the existence of non-equivalent ammonium ions and factor group splitting as well as site group splitting.

Table III.1 Effective symmetries of the NH_4^+ (E) and NH_3D^+(E') ions at crystal sites with symmetries S [47]

S[a]	E	E'[b]
Oh, Td	Td	$C_{3v}(4)$
O, Th, T	T	$C_3(4)$
$D_{6h}(2)$, D_{3h}, $C_{6v}(2)$, D_{3d}, C_{3v}	C_{3v}	C_{3v}, $C_s(3)$
D_6, C_{6h}, C_{3h}, C_6, D_3, S_6, C_3	C_3	C_3, $C_1(3)$
$D_{4h}(2)$, D_{2d}	D_{2d}	$C_s(4)$
C_{4h}, S_4	S_4	$C_1(4)$
$C_{4v}(2)$, $D_{2h}(3)$, $^cC_{2v}$	C_{2v}	$C_s(2)$, $C_s(2)$
$D_4(2)$, D_{2h}, $^cD_2$	D_2	$C_1(4)$
C_{2h}, ^cC_s	C_s	C_s, C_s, $C_1(2)$
C_4, C_{2h}, $^cC_2$	C_2	$C_1(2)$, $C_1(2)$
C_i, C_1	C_1	C_1, C_1, C_1, C_1

[a] The number of nonequivalent choices of symmetry operations of E from the symmetry operations of S is indicated in parentheses.

[b] The number of equivalent orientations of the NH_3D^+ ion of given symmetry E' relative to the parent NH_4^+ ion of symmetry E is indicated in parentheses.

[c] This S symmetry yields two different E symmetries dependency on the choice of the symmetry operation from this point group.

A method which avoids these complications is offered by the use of the isotopically dilute NH_3D^+ ion. The infrared spectra of this ion show [48] that the modes which are of principal interest are not subject to Fermi resonance and occur in frequency regions which are usually clear of other absorptions. At low temperatures the bands become sharp and reflect the symmetry of the ammonium ion more clearly. With low percentages of D the NH_3D^+ ions are distributed at random through the crystal and can be described as "isotopically isolated", so that the NH_3D^+ ion acts as a true probe of the symmetry and orientation of the ammonium ion in the structure. In principle the same could be said for the NHD_3^+ ion in a ND_4^+ matrix, but in practice the requirement of almost complete deuteration is less easily satisfied.

The replacement by D of one of the H atoms in NH_4^+ in a crystal site will give rise to four equally probable orientations whose equivalence will depend on E. The effective symmetry (or symmetries) E' of the NH_3D^+ ion(s) is given by the intersection

$$C_{3v} \cap E = E'$$

of the maximum point group of the NH_3D^+ ion with E or a subgroup of that intersection, i.e. C_{3v}, C_3, C_s or C_1. From the correlation table of C_{3v}, N–D stretching and bending modes for the various symmetries will take the form:

Site	ν_1	ν_4
C_{3v}	A_1	E
C_3	A	E
C_s	A'	A' + A"
C_1	A	A + A

The number and relative intensities of the bands expected from ν_1 and ν_4 correspond to the symmetries of the four possible orientations of the NH_3D^+ ion and are shown in the column E' in Table III.1. The number in parentheses refer to the number of equivalent orientations. In predicting the expected ratios it is assumed that, within each compound, each component of a vibrational mode contributes unit intensity.

The presence of sets of non-equivalent ammonium ions will not necessarily be detected by this method as two non-equivalent sets of C_{2v} symmetry and equal abundance could not be distinguished from one set of equivalent C_1 sites [47].

III.3 INFRARED SPECTRA OF THE AMMONIUM ION IN NH_4VO_3

III.3.1 Introduction

Infrared and Raman spectroscopy have been used in the past to investigate the properties of the ammonium ion in ammonium metavanadate [10, 48 and 49]. In the room temperature infrared spectrum of NH_4VO_3 , however, the assignment of individual components like ν_1 and ν_3 in the broad N–H stretching region is virtually impossible [10]. Low temperature spectra of isotopically dilute NH_3D^+ ions are particularly useful in this respect as its vibrations are not complicated by vibrational coupling and Fermi resonance between the various possible vibrational levels, e.g. ν_1, ν_3, $2\nu_4$, $2\nu_3$ and $\nu_2 + \nu_4$, as may be the case for NH_4^+ and ND_4^+. The procedure of using isolated NH_3D^+ ions as a probe to investigate the NH_4^+ environment

in the crystal is performed by incorporating a low percentage of deuterium into the crystal so that factor group effects are negligible [50, (III.2)]. The frequency of the sharp N–D stretching fundamental $\nu_1(NH_3D^+)$ is also far removed from the spectral region where NH_4^+ ions absorb thus enabling the unambiguous assignment [48] of this band. This technique made it possible to investigate the properties of the ammonium ion in various crystal structures [51, 62], and was employed here to study the ammonium ion in solid NH_4VO_3. The results showed no evidence of a low temperature transition in NH_4VO_3 and spectra recorded over the entire temperature range studied can be interpreted in terms of the room temperature crystal structure.

NH_4VO_3 belongs to space group Pbcm (D_{2h}^{11}) with Z = 4 [63]. The N, V, O(1), O(2), H(1), H(2) atoms all occupy sites 4(d) with site symmetry C_s, O(3) atoms 4(c) sites with symmetry C_2 and H(3) atoms 8(e) sites with C_1 symmetry. The structure of the metavanadates, including hydrogen bonds in NH_4VO_3 is shown in Figure III.1.

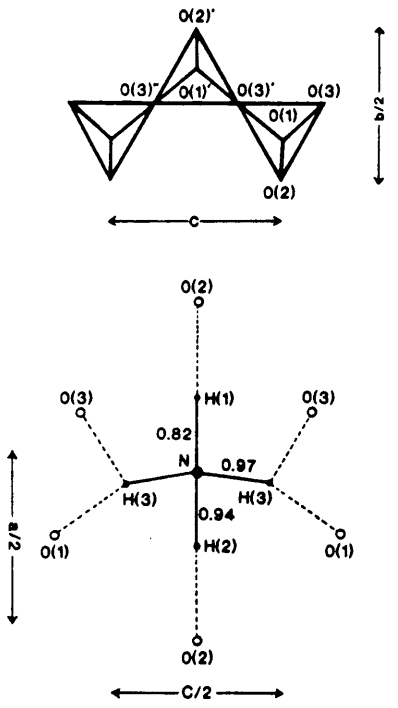

Figure III.1 Recommended atomic nomenclature for metavanadates and the hydrogen bonding arrangement in NH_4VO_3

III.3.2 Experimental

III.3.2.1 Preparation of NH_4VO_3

(1) From NH_4VO_3 [64]

One drop of a 25% NH_3 solution was added to 10 ml of H_2O to obtain a basic solution which was heated and removed from the hot plate before 0.5 g NH_4VO_3 was dissolved in the solution. All remaining solid was filtered off and 0.05 g NH_4Cl was added to the filtrate. The mixture was cooled to 273 K and kept at this temperature for one hour. Ammonium metavanadate was filtered off, washed with cold water and allowed to dry overnight in a desiccator.

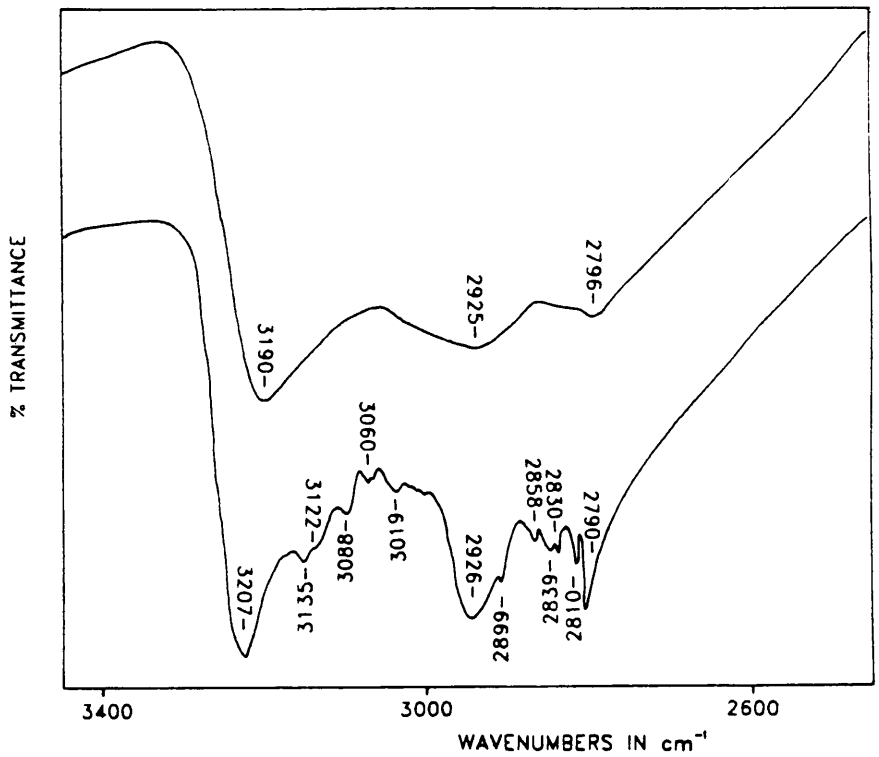

Figure III.2 The N–H stretching region in NH_4VO_3 at room temperature (top) and 80 K (bottom)

(2) From V_2O_5 [19]

6.5 g V_2O_5 was stirred in H_2O for 10 minutes. 10 ml of a 25% NH_4OH solution was added to the mixture and stirred until it had reached room temperature (about half an hour). The remaining brown solid was filtered off and the filtrate allowed to evaporate slowly at room temperature. White ammonium metavanadate was filtered off after one day and washed with H_2O.

III.3.2.2 Preparation of deuterated samples

Two different methods were used to prepare deuterated NH_4VO_3:

(1) NH_4VO_3 containing between 1 and 75% D

The method described in III.3.2.(1) was used to obtain these samples, by substituting H_2O with appropriate stoichiometric mixtures of H_2O and D_2O and using ND_4Cl as a substitute for NH_4Cl.

(2) ND_4VO_3

V_2O_5 was reacted with ND_3 in D_2O under inert conditions to obtain ND_3VO_3 (method in III.3.2.1(2)). Some D–H exchange occurred when the solid product was exposed to air.

III.3.2.3 Infrared spectra

Mid-infrared spectra of all samples were recorded both at room temperature and 80 K on the Bomen Michelson-100 FT-IR spectrometer with a resolution of

4 cm^{-1}. All samples were in the form of KBr pellets, and to ensure that frequency shifts due to ion exchange between the sample and KBr do not occur the 1% D sample was also recorded in the form of a CsCl pellet with identical results to those obtained in KBr. For the temperature dependence study samples were recorded at various temperatures between 80 and 291 K on a Bruker IFS 113 V spectrometer with a resolution of 1 cm^{-1}. For low temperature recordings a continuous flow cryostat [Appendix D(2)] was used to keep samples at different temperatures between room temperature and 80 K.

III.3.3 Vibrational analysis of the ammonium ion and its deuterated analogues

Correlation of the fundamental modes of the ammonium ion with those of its deuterated analogues are shown in Table III.2 with the site and factor group correlation of NH_4^+ in NH_4VO_3 and ND_4^+ in ND_4VO_3 in Table III.3.

Table III.2 Correlation of fundamental modes of the isotopically substituted ammonium ions [48]

'Free ion' symmetry:	NH_4^+ T_d	NH_3D^+ C_{3v}	$NH_2D_2^+$ C_{2v}	NHD_3^+ C_{3v}	ND_4^+ T_d
Mode					
ν_1	A_1	A_1	A_1	A_1	A_1
ν_2	E	E	$A_1 + A_2$	E	E
ν_3	F_2	$A_1 + E$	$A_1 + B_1 + B_2$	$A_1 + E$	F_2
ν_4	F_2	$A_1 + E$	$A_1 + B_1 + B_2$	$A_1 + E$	F_2

Table III.3 Site and factor group correlation for NH_4^+ in NH_4VO_3 and ND_4^+ in ND_4VO_3

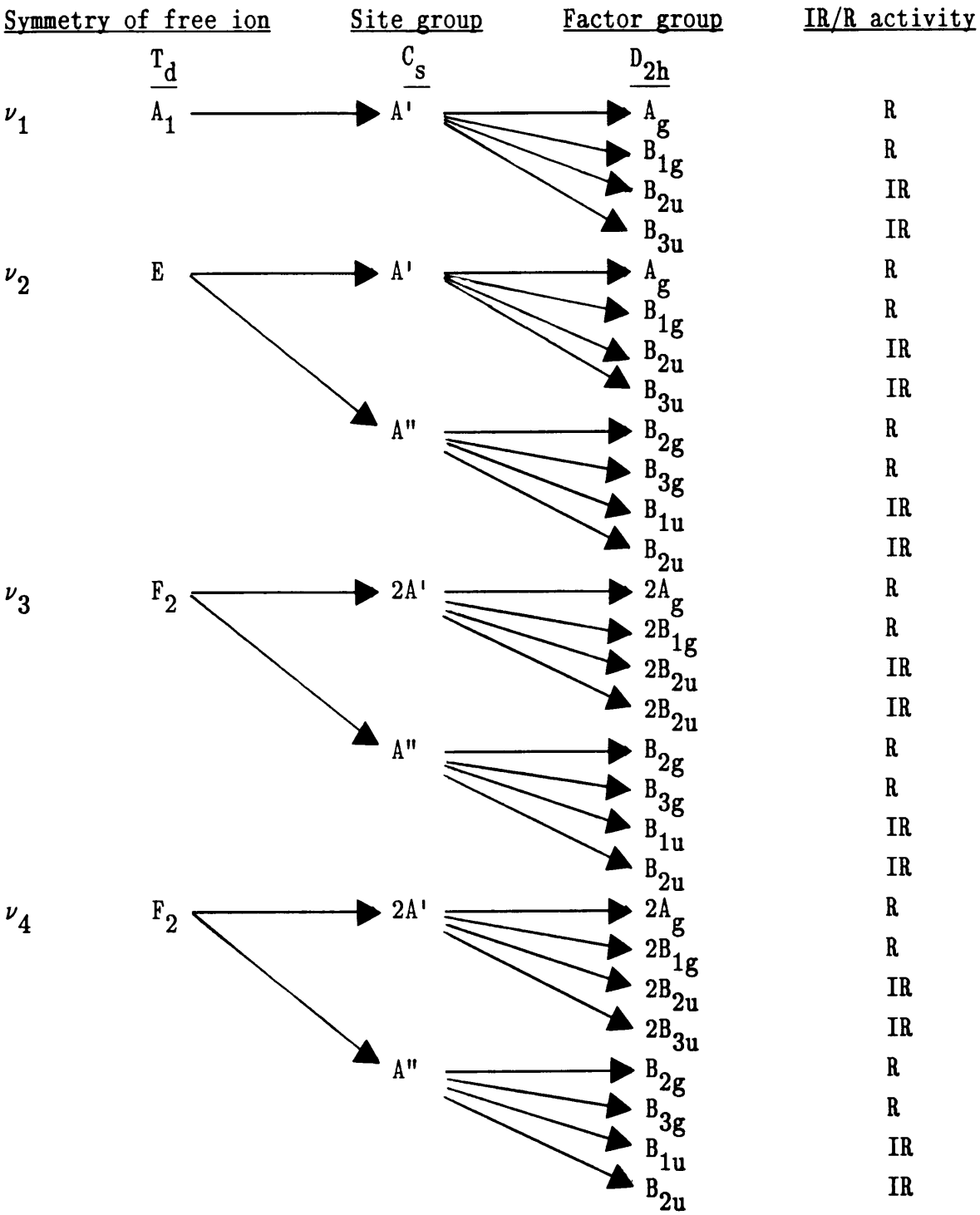

The fundamental vibrational modes of the NH_4^+ tetrahedron are $\nu_1(A_1)$ the totally symmetric stretching mode, $\nu_2(E)$ the doubly degenerate bending mode, ν_3 (F_2) the triply degenerate asymmetrical stretching mode and $\nu_3(F_2)$ the triply degenerate triply degenerate bending mode. Under the site group of C_s all the modes of NH_4^+ become both infrared and Raman active. $\nu_1(A_1)$ is predicted to remain a single mode (A) while $\nu_2(E)$ should split into two bands (A' and A") with each of $\nu_3(F_2)$ and $\nu_4(F_2)$ splitting into three bands (2A' + A"). Factor group splittings will cause A' type modes to split into $A_g(R)$, $B_{1g}(R)$, $B_{2u}(IR)$, $B_{3u}(IR)$ and A" type modes into $B_{2g}(R)$, $B_{3g}(R)$, $B_{1u}(IR)$, $B_{2u}(IR)$. It can be expected, however, that only site group splittings will possibly be resolved in the vibrational spectra.

The correlation of NH_3D^+ and NHD_3^+ modes with the number of modes expected under the effective symmetry of these ions in solid NH_4VO_3 is shown in Table III.4. With an effective symmetry of C_s for NH_4^+ in NH_4VO_3 the ν_1(N–D) stretching mode of NH_3D^+ should split into C_s,C_s and $C_1(2)$ components, depending on whether the N–D bond coincides with the σ-plane of the crystal (C_s symmetry) or C_s symmetry with the N–D bond pointing in the opposite direction but still in the σ-plane of the crystal, or having two equivalent positions of C_1 symmetry. This is, of course, in agreement with the three bond distances [63] of N–H(1) = 0.82Å, N–H(2) = 0.94Å and N–H(3) = 0.97Å (2 bonds). The bending mode ν_4 splits into ν_{4a} (A_1) and $\nu_{4bc}(E)$ for 'free' NH_3D^+ groups and the latter into six components under C_s symmetry.

Table III.4 Correlation of NH_3D^+/NHD_3^+ modes with the site symmetry of the ammonium ion and the effective NH_3D^+/NHD_3^+ symmetry

	'Free ion' symmetry	Site symmetry	Effective NH_3D^+/NHD_3^+ symmetry		
	C_{3v}	C_s	2 C_s		$C_1(2)$
ν_1	A_1	A'	2A'	+	A
ν_4	E	A'	2A'	+	A
		A"	2A"	+	A

III.3.4 Vibrational spectra

III.3.4.1 Pure NH_4VO_3

It has been reported [10] that an unambiguous assignment of ammonium bands between 2500 and 3500 cm^{-1} in the room temperature vibrational spectra of NH_4VO_3 proves to be difficult if not impossible because of complications resulting from vibrational coupling and Fermi resonance in this region. This also seems to hold true for spectra of NH_4VO_3 recorded at low temperatures down to 80 K. Broad bands in the room temperature spectrum split into several bands at 80 K as is shown in Figure III.2. Full assignment of the low temperature spectrum of NH_4VO_3 is included in Tables III.5 and III.6. Comparison and assignment of the modes at room temperature and 80 K is shown in Table B.1 (Appendix B).

Table III.5 Assignment of low temperature infrared active modes of NH_4VO_3 and variously deuterated samples between 3450 and 2000 cm^{-1}

Assignment	Wavenumbers in cm^{-1}						
	100% NH_4VO_3	1% D	5% D	30% D	50% D	75% D	90% D
$\nu_3(NH_4^+)$, $\nu_3(NHD_3^+)$	3207s	3215s	3209s	3211vs	3208s	3202m	3201w
$\nu_3(NH_3D^+)$	-	-	-	-	-	-	3179sh
$\nu_3(NH_4^+)$	3135s	3142sh	3140sh	3134sh	-	-	-
$\nu_3(NH_4^+)$, $\nu_3(NHD_3^+)$	3122s	-	-	-	3124m	3123w	3122w
$\nu_2 + \nu_4(NH_4^+)$	3088sh	3088sh	3086sh	-	-	-	-
$\nu_2 + \nu_4(NH_4^+)$	3060m	3060m	3061sh	-	-	-	-
$\nu_1 + \nu_5(NH_4^+)$	3019m	3025m	3020sh	3027sh	-	2984sh	3009sh
$\nu_1(NH_2D_2^+)$	-	-	-	-	2946m	-	-
$\nu_1(NH_4^+)$, $\nu_3(NH_3D^+)$	2926s	2927m	2928s	2934s	-	2935m	2934w
$\nu_3(NH_2D_2^+)$	-	-	-	-	2919m	-	-
ν_1, $2\nu_4(NH_4^+)$	2899sh	-	-	-	-	-	-
$2\nu_4(NH_4^+)$	2858m	2857m	-	-	-	-	2866w/ 2861w
$\nu_1(NH_2D_2^+)$	2839w	-	2836s	2835m	2834w	2833m	2838sh
$2\nu_4(NH_4^+)$	2830sh	-	-	-	-	-	-
$2\nu_4(NH_4^+)$	2810m	-	2810s	2812m	-	-	-
$2\nu_4(NH_4^+)$	2790s	2793s	2795s	2798s	2798w	-	2781w
$2\nu_4(NHD_3^+)$	-	-	-	2729vw	2728w	2725m	2728vw
$2\nu_{4b}(NH_2D_2^+)$	-	-	-	2669vw	2669w	-	2669vw
$\nu_2 + \nu_4(NHD_3^+)$	-	-	-	2478vvw	-	2472vw	-

Table III.5 (cont.)

Assignment	Wavenumbers in cm^{-1}						
	100% NH_4VO_3	1% D	5% D	30% D	50% D	75% D	90% D
$\nu_3(ND_4^+)$	-	-	-	2409vw	2409sh	2404sh	2407vs
$\nu_3(ND_4^+)$	-	-	-	2386w	2389m	2385m	2384vs
$\nu_1(NH_3D^+)$	-	2370w	2371w	2370m	2377m	2377m	-
$\nu_3(NHD_3^+)$	-	-	-	-	-	2369s	-
$\nu_1(NH_3D^+)$	-	2348w	2345vw	2352w	2354w	-	2354sh
$\nu_1(NH_2D_2^+)$	-	-	-	-	2337w	-	-
$2\nu_2(ND_4^+)$	-	-	-	-	-	2316sh	2309w
$\nu_2 + \nu_4(ND_4^+)$	-	2273ws	-	-	-	2272sh	2271sh
$\nu_3(NHD_3^+)$	-	-	-	-	-	-	2219sh
$2\nu_4(ND_4^+)$	-	-	2248vw	2249w	2254sh	2250w	-
$\nu_1(NH_3D^+)$	-	2196m	2199m	2202m	2190m	-	-
$\nu_1(ND_4^+)$	-	-	2185sh	2184m	2167sh	2186s	2192s
$2\nu_4(ND_4^+)$	-	-	-	2134vw	2134m	2127s	2125s
$2\nu_4(ND_4^+)$	-	-	-	-	2115w	2110m	2110s
$\nu_2 + \nu_6(NH_4^+)$	2000bw	2012bw	2001bw	-	-	-	-
$\nu_2 + \nu_6(NH_4^+)$	1944bw	-	-	-	-	-	-

Table III.6 Assignment of low temperature infrared active modes of NH_4VO_3 and variously deuterated samples between 2000 and 1000 cm^{-1}

Assignment	Wavenumbers in cm^{-1}						
	100% NH_4VO_3	1% D	5% D	30% D	50% D	75% D	90% D
$\nu_4 + \nu_6(NH_4^+)$	1759b	-	-	-	-	-	-
$\nu_4 + \nu_6(NH_4^+)$	1770b	1776m	1776w	1778vw	1781w	1788w	-
$\nu_4 + \nu_6(NH_4^+)$	1737b	-	-	-	-	-	-
$\nu_2(NH_4^+)$	1663sp	1664m	1650w	1655vw	-	-	-
$\nu_2(NH_3D^+)$	-	1611w	1611w	1608vw	1608vw	1610w	1646vw
$\nu_{2a}NH_2D_2^+)$	-	-	-	1564vw	1563w	1559m	1558m
$\nu_2 + \nu_6(ND_4^+)$	-	-	-	1445sh	-	1455w	1456m
$\nu_4(NH_4^+)$	1422vs	1422vs	1433sh	1432sh	-	1435sh	-
$\nu_4(NH_4^+)$	1414vs	1411vs	1420vs	1419vs	1414m	1415m	1417m
$\nu_4(NH_4^+)$	1406sh	-	1410vs	1411vs	1403sh	1400w	1410m
$\nu_2(NHD_3^+)$	-	-	-	-	1385sh	1384sh	1396m
$\nu_4 + \nu_6(ND_4^+)$	-	-	1344w	1344w	1344w	1344m	1344m
$\nu_{4b}(NH_2D_2^+)$	-	-	1325w	1325w	1325w	1325m	1325m
$\nu_4(NH_3D^+)$	-	1276m	1276m	1276m	1278w	1277m	1272w
$\nu_4(NH_3D^+)$	-	1267m	1267m	1268m	1268w	1269m	1268w
$\nu_4(NH_3D^+)$	-	1257m	1257m	1258m	1260w	1260m	1257w
$\nu_4(NH_3D^+)$	-	1250m	1250m	1250m	1252sh	1251m	-
$\nu_2(ND_4^+)$	-	-	1194vw	1192vw	1190w	1190m	1192w
$\nu_{4c}(NH_2D_2^+)$	-	-	1187vw	1188w	1189sh	-	-
$\nu_2(ND_4^+)$	-	1144w	1182vw	1182w	1182w	1183m	1184m
$\nu_4(ND_4^+)$	-	1127vw	1124w	1124w	1123m	1123m	1126m
$\nu_{4bc}(NHD_3^+)$, $\nu_{4a}(NHD_3^+)$	-	-	-	1091w	1080w	1089m	-
$\nu_4(ND_4^+)$	-	1050vvw	1078vvw	1078vvw	1077w	1078m	1078vs

Three broad bands and some possible shoulders in the N-H stretching region of the room temperature spectrum split into nine bands and four shoulders of strong to medium intensity at low temperatures. Although high intensity bands can usually be associated with fundamental vibrations rather than overtones and combination bands it is possible that coupling in this region might be responsible for changes in intensity. The ν_1 fundamental was expected to remain single under site group C_s and to split into two infrared and two Raman active bands under D_{2h} symmetry and a single band at 2925 cm^{-1} in the room temperature spectrum was assigned to this mode. This band occurs at 2926 cm^{-1} in the low temperature spectrum and a second band appearing as a shoulder at 2899 cm^{-1} could possibly be assigned to the second band expected for ν_1 under factor group splitting. This band could, however, also be assigned to one of the components of $2\nu_4$ in addition to five other bands at 2790, 2810, 2830, 2839 and 2858 cm^{-1}. The bending fundamental ν_4 is expected to split into three bands (2A' + A") under C_s site symmetry and into six infrared and six Raman active modes under unit cell symmetry, as has already been shown. Three components were in fact reported for ν_4 in the room temperature Raman spectrum at 1416, 1438 and 1462 cm^{-1} [10]. One high intensity band is observed in the room temperature infrared spectrum at

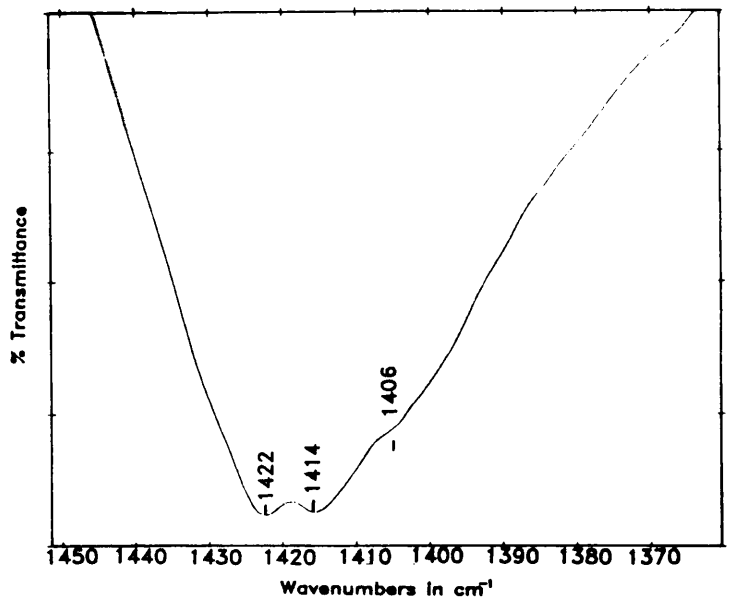

Figure III.3 Infrared spectrum of NH_4VO_3 at 80 K (N-H bending mode)

1417 cm^{-1} that splits into at least three bands at 1406, 1414 and 1422 cm^{-1} at 80 K and probably represent the site group components under C_s. This is shown in Figure III.3. The band is broad and asymmetrical on the low frequency side, and could possibly reveal further splitting at liquid helium temperatures.

It can be assumed that the highest frequency vibration in Figure III.2 corresponds to a stretching mode involving the longest N–H bond, N–H (3) [10]. This mode occurs at 3190 cm^{-1} in the room temperature infrared spectrum (Figure III.2) and is assigned to ν_3. As in the Raman spectrum [10] splitting of this fundamental cannot be resolved at room temperature but the three bands occurring at the highest frequencies in the low temperature spectrum, viz. the ones at 3207, 3135 and 3122 cm^{-1} are tentatively assigned to the three modes expected for ν_3 under C_s symmetry.

Other bands in the 2500 to 3500 cm^{-1} region of the low temperature spectrum can be assigned to combination modes such as $\nu_1 + \nu_5$ at 3019 cm^{-1} (according to the position of ν_5 in ammonium halides) and $\nu_2 + \nu_4$ at 3088 and 3060 cm^{-1} (Table III.5).

Although the ν_2 bending mode is expected split into two bands under C_s symmetry it is observed as a single band in both the room and low temperature spectra at 1659 and 1663 cm^{-1}, respectively. Combination modes involving the librational mode ν_6, $\nu_i + \nu_6$ (i = 2,4), are identified at 1737, 1770 ($\nu_4 + \nu_6$) and 1944, 2004 cm^{-1} ($\nu_2 + \nu_6$) at low temperature. [Figure B.1 (Appendix B)]. These bands are easily identified, even at room temperature where they appear as single bands at 1737 and 2000 cm^{-1}. These frequencies indicate that the hydrogen bonds in NH_4VO_3 are most probably not fluxional as has also been observed in another study by Heyns et.al. [10]. The ν_6 mode is calculated to occur between 330 and 380 cm^{-1} (Table III.7) at 362 cm^{-1} in the far-infrared spectrum of ammonium metavanadate [65].

Table III.7 Calculation of ν_6 from $\nu_i + \nu_6$ (i = 2,4)

	Wavenumbers in cm^{-1}			Wavenumbers in cm^{-1}	
$\nu_2 + \nu_6$	2000	$\nu_4 + \nu_6$	1795	1795	1737
ν_2	1659	ν_4	1422	1414	1406
ν_6	341	ν_6	373	356	331

III.3.4.2 Deuterated samples of ammonium metavanadate

The low temperature spectra of the various deuterated samples of NH_4VO_3 are shown in Figures III.4 and III.5. A full assignment of these spectra appears in Tables III.5 and III.6.

(1) 1% Deuterated NH_4VO_3

Assignments of the mid-infrared spectra of one percent deuterated ammonium metavanadate at both room temperature and 80 K, are shown in Appendix B (Table B.2).

Isotopically dilute NH_3D^+ gives three sharp bands in the N-D stretching region at 2370, 2348, 2196 cm^{-1}. These can be considered as representing at least two types of hydrogen bond interactions in solid NH_4VO_3. The two weaker bands at 2370 and 2348 cm^{-1} are likely to represent the bifurcated hydrogen bonds that is N-H-O(1) and N-H-O(3) in Figure III.1, while the lower frequency component at 2196 cm^{-1} is likely to represent very strong normal hydrogen bonding as might be expected to be present in the almost straight line N-H-O(2) band in Figure III.1. The difference in strength between the two types of hydrogen bonds must be considerable as the

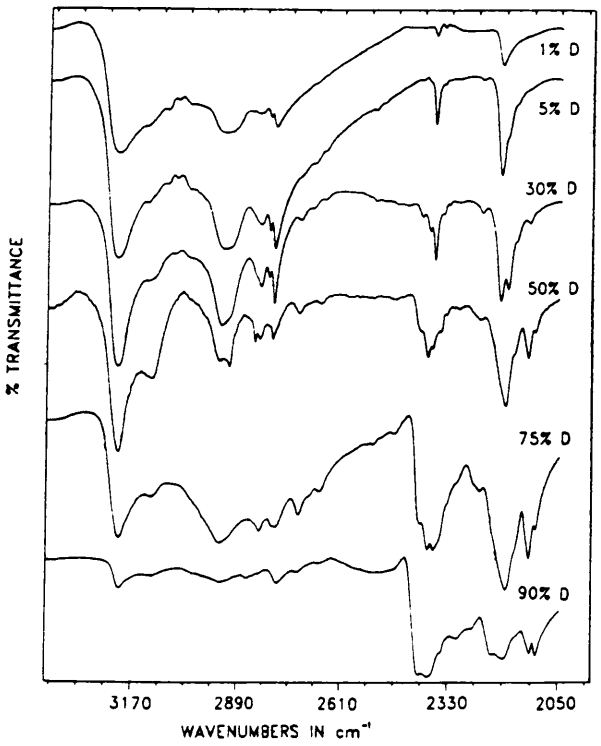

Figures III.4 Low temperature infrared spectra of various percentage deuterated samples of NH_4VO_3 between 3380 and 1980 cm^{-1}

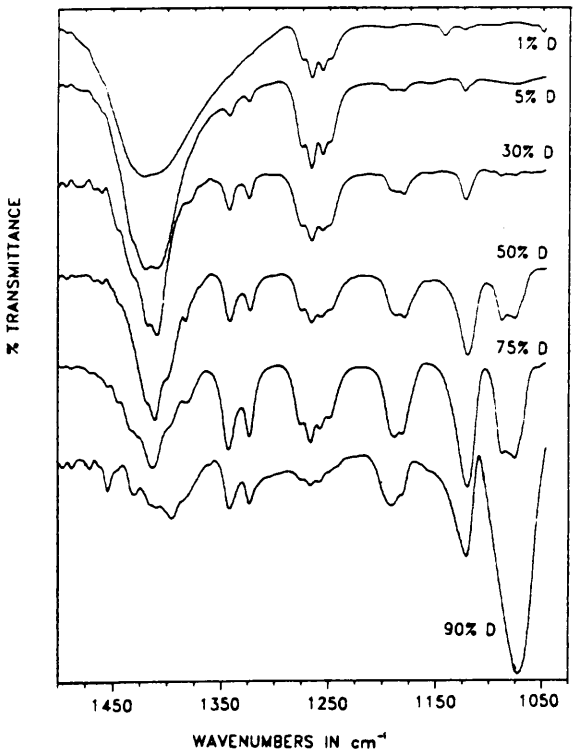

Figures III.5 Low temperature infrared spectra of various percentage deuterated samples of NH_4VO_3 between 1500 and 1025 cm^{-1}

wavenumbers of the bands that represent these are separated by more than 150 cm^{-1} and the lower frequency band has a high relative intensity that can also be an indication of hydrogen bond strength. The bending mode, $\nu_{4bc}(NH_3D^+)$, was expected to split into six components under C_s but occurs as a single band at room temperature at 1257 cm^{-1}. This band at 80 K, splits into four components at 1276, 1267, 1257 and 1250 cm^{-1}.

The mode at 1615 and 1611 cm^{-1} in the room and low temperature spectra, respectively, is assigned to the ν_2 fundamental of NH_3D^+. Very weak bands of the fully deuterated species ND_4^+ are also present in this spectrum with a single ν_2 fundamental at 1144 cm^{-1} in both the room and low temperature spectra and ν_4 at 1047 cm^{-1} (room temperature), 1127 and 1050 cm^{-1} (80 K).

(2) <u>5% Deuterated NH_4VO_3</u>

Assignments of the mid-infrared spectra of the ammonium band region of approximately 5% deuterated NH_4VO_3 measured at both room temperature and 80 K are shown in Appendix B (Table B.3).

Although the room temperature spectrum is very similar to the one obtained for 1% deuterated NH_4VO_3 several new bands can be observed in the low temperature spectrum. Two of the $\nu_1(NH_3D^+)$ bands at 2371 and 2199 cm^{-1} are higher in intensity than in the 1% deuterated sample as would be expected, and two shoulders are now visible towards lower wavenumbers on the 2199 cm^{-1} band at 2185 and 2166 cm^{-1}. These can be assigned to the ν_1 and $2\nu_4$ modes of ND_4^+, respectively. A very weak band at 2248 cm^{-1} can also be assigned to the latter mode of the two bands appearing as shoulders at 1344 and 1325 cm^{-1}

the first can be attributed to the combination mode $\nu_4 + \nu_6$ of ND_4^+ while the other is assigned to ν_{4b} of $NH_2D_2^+$. Four of the five low intensity bands between 1050 and 1200 cm^{-1} seem to originate from ND_4^+. Two bands are observed for each of the ν_2 and ν_4 fundamentals at 1194, 1182 and 1124, 1079 cm^{-1}, respectively.

It is interesting to note the change in relative intensities of $\nu_2(NH_4^+)$ at 1650 cm^{-1} and $\nu_2(NH_3D^+)$ at 1611 cm^{-1}. In the infrared spectrum of the 1% deuterated sample (Figure B.2) the NH_4^+ mode had a slightly higher intensity than that of $\nu_2(NH_3D^+)$ but the reverse is true of the 5% deuterated NH_4VO_3 spectrum.

(3) 30% Deuterated NH_4VO_3

Assignments of the mid-infrared spectra of 30% deuterated NH_4VO_3 at both room temperature and 80 K are shown in Table B.4 (Appendix B).

At 30% deuteration the band that was present at 3088 cm^{-1} in the spectrum of pure NH_4VO_3 has disappeared. This supports the assignment of this band to the combination mode $\nu_2 + \nu_4$ (NH_4^+). The highest relative intensity for the bands assigned to NH_3D^+ vibrations is found in this spectrum as would be expected from the statistical distribution of the $NH_{4-x}D_x^+$ species. In the 2100-2400 cm^{-1} region new bands appear that can be assigned to ND_4^+ modes. Two bands of medium intensity at 2202 and 2184 cm^{-1} are tentatively assigned to ν_1 as two infrared active bands are expected for this fundamental under factor group splitting. Weak bands at 2409 and 2386 cm^{-1} are similarly

assigned to the ν_3 fundamental while the overtones $2\nu_4$ are present at 2134 and 2249 cm^{-1}. Towards lower wavenumbers N–D bands have higher intensities than before. A new shoulder at 1445 cm^{-1} is assigned to the $\nu_2 + \nu_6$ combination mode of ND_4^+ as ν_6 has been observed at 267 cm^{-1} [65]. A new weak band at 1091 cm^{-1} is attributed to a bending mode in the NHD_3^+ species.

(4) 50% Deuterated NH_4VO_3

Assignments in the mid-infrared spectra of 50% deuterated NH_4VO_3 at room temperature and 80 K are shown in Table B.5 (Appendix B).

With less NH_4^+ ions in the lattice at 50% deuteration, two N–H stretching modes of the $NH_2D_2^+$ species become visible at 2946 and 2919 cm^{-1}. In the N–D stretching region $NH_2D_2^+$ is represented by a new band at 2337 cm^{-1}. There is a change in the relative intensity of $\nu_3(ND_4^+)$ and $\nu_1(NH_3D^+)$ at 2389 and 2377 cm^{-1} with the former increasing relative to the latter from 30 to 50% D.

(5) 75% Deuterated NH_4VO_3

Assignments in the mid-infrared spectra of 75% deuterated NH_4VO_3 are shown in Table B.6 (Appendix B).

In the spectrum of 75% deuterated NH_4VO_3, all N–D modes of ND_4^+ are of higher intensity than the remaining N–H bands. N–D stretching vibrations in the 2000-2400 cm^{-1} region are taking a similar shape to that of N–H vibrations between 2500 and 3400 cm^{-1} in pure NH_4VO_3. Two new combination modes for ND_4^+, $2\nu_2$ and $\nu_2 + \nu_4$, appear as shoulders at 2316 and 2272 cm^{-1}.

(6) 90% Deuterated NH_4VO_3

Assignments in the mid-infrared spectra of 90% deuterated NH_4VO_3 are shown in Table B.7 (Appendix B).

The 2000-2500 cm^{-1} region in the spectrum of 90% D NH_4VO_3 (Figure III.5) can now be related to the 2500-3500 cm^{-1} region in the undeuterated compound. In both, three broad bands occur in the room temperature spectrum which split into several bands and shoulders at low temperature. Unambiguous assignment of the various modes remains impossible as various fundamentals, combination modes and overtones are expected in this region (e.g. ν_1, ν_3, $\nu_2 + \nu_4$, $2\nu_2$ and $2\nu_4$), but the bands at 2407 and 2384 cm^{-1} are tentatively assigned to ν_3 and the single mode at 2192 cm^{-1} to ν_1 of ND_4^+. The shoulder at 2354 cm^{-1} which was assigned to $\nu_1(NH_3D^+)$ possibly overlaps with the third mode expected for $\nu_3(ND_4^+)$. The combination band $\nu_2 + \nu_4$ is observed at 2271 cm^{-1}. Two bands at 2125 and 2110 cm^{-1} are attributed to $2\nu_4$ with $2\nu_2$ at 2309 cm^{-1} as two sharp bands at lower wavenumbers (Figure III.5) 1078 and 1126 cm^{-1}, have been assigned to ν_4 and a band and a shoulder at 1192 and 1184 cm^{-1} to ν_2. The two combination modes $\nu_2 + \nu_6$ and $\nu_4 + \nu_6$ are observed at 1456 and 1344 cm^{-1}.

III.3.4.3 Comparison between spectra of deuterated samples of NH_4VO_3

(1) N-H stretching vibrations

The region 2500 to 3600 cm^{-1} in Figure III.4 is broad and seems to contain multiple bands as in the case of pure NH_4VO_3 discussed in [III.3.4.1] of the three bands tentatively asigned to the ν_3 fundamental of NH_4^+ under site symmetry C_s [III.3.4.1] the one occurring at the highest wavenumber is

present between 3208 and 3215 cm^{-1} in all deuterated samples up to 50%. At higher deuteration this is shifted towards lower wavenumbers and appears at 3201 cm^{-1} in the sample of highest D content and is assigned to $\nu_3(NHD_3^+)$. (Table III.5). The $\nu_1(NH_4^+)$ vibration at 2926 cm^{-1} in the sample of zero deuterium content can only be observed up to 5% deuteration after which it is too close to the very intense band at 2934 cm^{-1} to be observed. The latter can be attributed to a N–H stretch in NH_3D^+ because it reaches highest relative intensity at 30% D content. In the 50% deuterated sample N–H stretching vibrations of of $NH_2D_2^+$ reaches maximum intensity at wavenumbers 2946, 2919 and 2834 cm^{-1} (Table III.5).

(2) <u>N-D stretching vibrations</u>

Isotopically dilute NH_3D^+ ions give three sharp bands in the region of 2370, 2348 and 2196 cm^{-1} in low percentage deuterated samples. At intermediate D contents several more bands appear in the 1000 to 2500 cm^{-1} region as is shown in Figure III.4. The bands assigned to $\nu_1(NH_3D^+)$ reaches maximum intensity in the 30% deuterated sample as would be expected from the statistical distribution of the $NH_{4-x}D_x^+$ species.

At high D contents the predominant species is ND_4^+ resulting in two modes at 2407 and 2384 cm^{-1} being assigned to $\nu_3(ND_4^+)$. Several bands in this region may be assigned to overtone and combination modes of this species such as $2\nu_4$, $2\nu_2$ and $\nu_3 + \nu_4$. The N–D stretching modes of $NH_2D_2^+$ and NHD_3^+ are assigned to bands reaching maximum intensity at 50 and 75% D content. These occur at 2337 and 2369 cm^{-1} , respectively.

(3) Bending vibrations

Bending modes for all the species occur between 1050 and 1500 cm^{-1} in Figure III.5. All three modes expected for $\nu_4(NH_4^+)$ under site symmetry C_s appear in the low temperature spectrum at 1422, 1414 and 1406 cm^{-1} but only one of the two modes similarly predicted for $\nu_2(NH_4^+)$ is observed at 1663 cm^{-1} (Table III.6). Two bands can be assigned to each of the ν_2(1192 and 1184 cm^{-1}) and ν_4 (1126 and 1078 cm^{-1}) modes of ND_4^+ as these bands reach maximum intensity in the sample with highest D content.

Four of the six modes predicted for $\nu_4(NH_3D^+)$ are observed between 1250 and 1276 cm^{-1}. Further splitting of these bands would possibly be observed if the sample is cooled down to liquid helium temperature. The ν_4 modes of the other remaining species occur at 1325, 1188 ($NH_2D_2^+$) and 1089 cm^{-1} (NHD_3^+) [Table III.6].

The ν_2 modes in the 1500 to 1700 cm^{-1} region is shown in Figure III.6. In the spectrum of the sample with 1% D content ν_2 is observed at 1663 (NH_4^+) and 1611 cm^{-1} (NH_3D^+). Relative intensities of these bands are reversed in

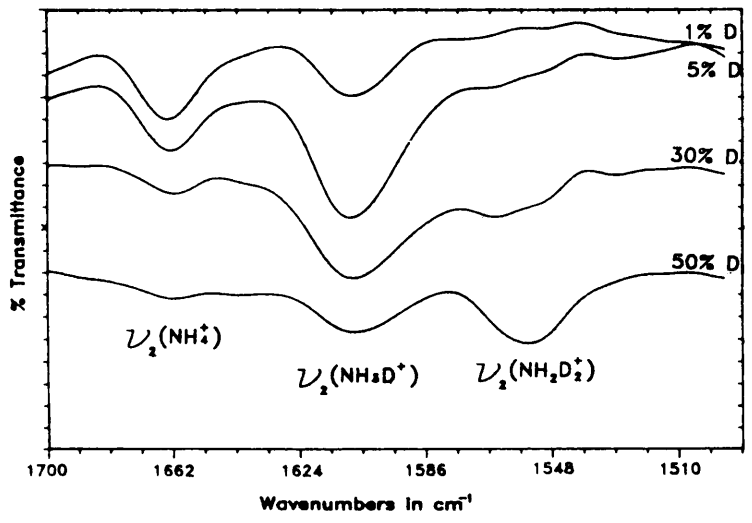

Figure III.6 Low temperature infrared spectra of variously deuterated NH_4VO_3 samples showing ν_2 modes of different isotopic species

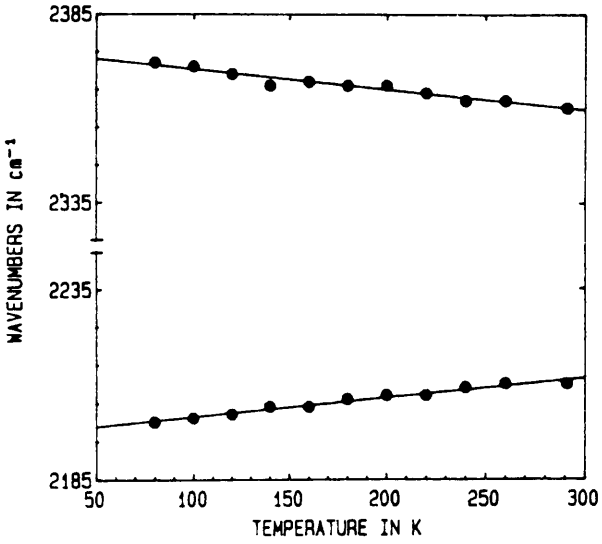

Figures III.7 Temperature dependence of two of the N–D stretching modes of isotopically dilute NH_3D^+ in NH_4VO_3

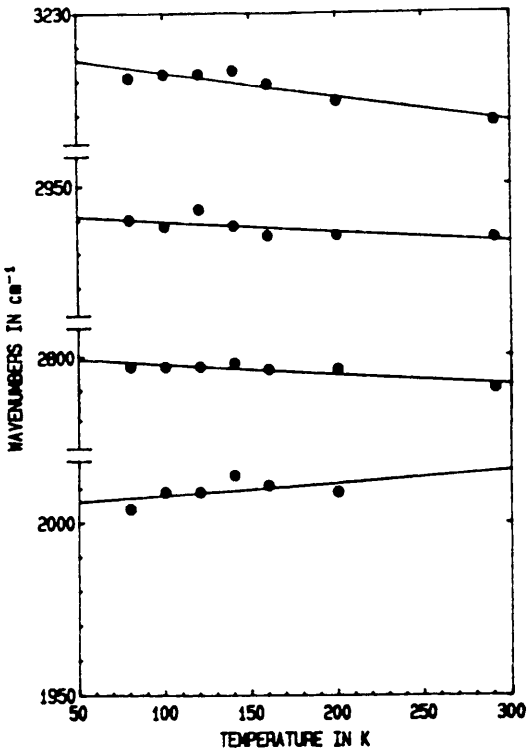

Figure III.8 The temperature dependence of some NH_4^+ modes in NH_4VO_3: ν_3, ν_1, $2\nu_4$ and $\nu_2 + \nu_6$

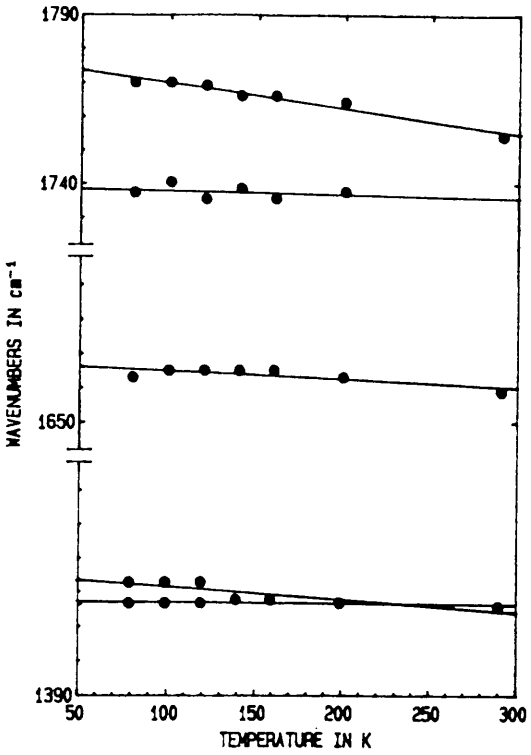

Figure III.9 The temperature dependence of some NH_4^+ modes in NH_4VO_3: $\nu_4 + \nu_6$ (two modes), ν_2 and ν_4 (2 modes)

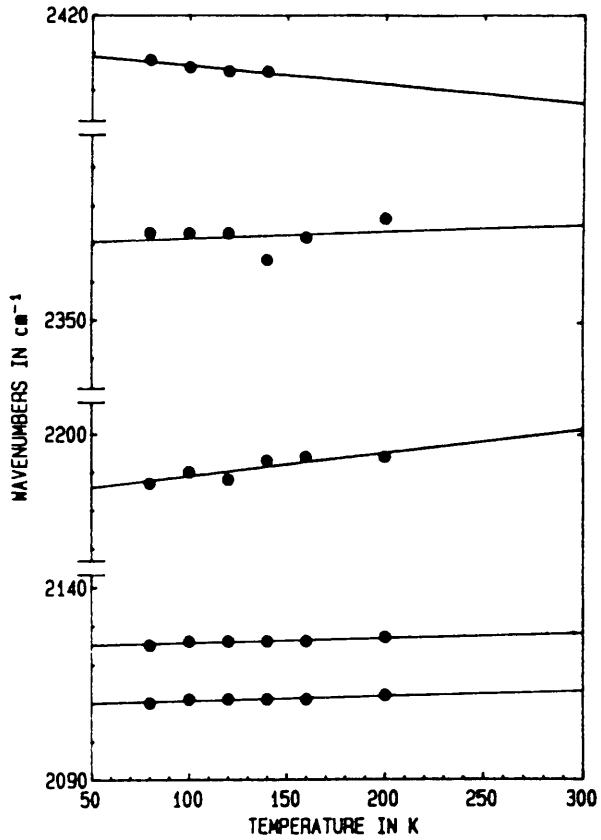

Figure III.10 The temperature dependence of some ND_4^+ modes in ND_4VO_3: ν_3(2 modes), ν_1 and $2\nu_4$ (2 modes)

Table III.7 Temperature dependence of some infrared active modes in NH_4VO_3 and its deuterated analogues between 80 K and room temperature

Mode	$d\nu/dT$ in $cm^{-1}\ K^{-1}$			
	100% NH_4VO_3	1% D	30% D	90% D
$\nu_3(NH_4^+)$	-0.07	-0.07	-0.07	-0.08
$\nu_1(NH_4^+)$	-0.03	+0.002	+0.002	+0.01
$2\nu_4(NH_4^+)$	-0.03	-0.01	-0.01	-0.03
$\nu_2 + \nu_6(NH_4^+)$	-0.04	+0.06		
$\nu_4 + \nu_6(NH_4^+)$	-0.08			
$\nu_4 + \nu_6(NH_4^+)$	-0.01			
$\nu_2(NH_4^+)$	-0.02			
$\nu_4(NH_4^+)$	-0.04			
$\nu_4(NH_4^+)$	-0.005			
$\nu_1(NH_3D^+)$		-0.05	-0.09	
$\nu_1(NH_3D^+)$		+0.05	+0.04	
$\nu_3(ND_4^+)$				-0.05
$\nu_3(ND_4^+)$				+0.02
$\nu_1(ND_4^+)$			+0.09	+0.06
$2\nu_4(ND_4^+)$				+0.01
$2\nu_4(ND_4^+)$				+0.004
$\nu_2(ND_4^+)$				-0.04
$\nu_4(ND_4^+)$				-0.004
$\nu_4(ND_4^+)$				-0.01

5% D. This effect is increased at 30% D and a new band at 1564 cm^{-1} can be attributed to ν_2 ($NH_2D_2^+$) as it reaches maximum relative intensity at 50% D content. The ν_2 (NHD_3^+) mode occurs as a shoulder at 1384 cm^{-1} (Table III.6, 75% D).

III.3.4.4 TEMPERATURE DEPENDENCE OF SOME AMMONIUM MODES IN NH_4VO_3

The behaviour of some infrared active NH_4^+, ND_4^+ and NH_3D^+ modes between 80 K and room temperature is shown in Figures III.7-III.10 with $d\nu/dT$ values in Table III.7. Details of the wavenumbers are shown in Table B.8 (Appendix B). The dependence of some N–H and N–D bands on high temperatures (room temperature to 473 K) was already reported [10]. At low temperatures further information on the nature of hydrogen bonding in the crystal can be obtained as more bands are observed, especially in those of isotopically dilute NH_3D^+ that are of very low intensity at room temperature.

Temperature dependence of NH_3D^+ modes in NH_4VO_3 is shown in Figure III.7. At 80 K these modes occur at 2370, 2348 and 2196 cm^{-1} in 1% deuterated NH_4VO_3. It was difficult to follow the very weak band at 2348 cm^{-1} above 80 K but the other two modes remain visible up to room temperature. Of these two the N–D stretch at 2370 cm^{-1} probably represents the N–H(3) bond which forms a bifurcated hydrogen bond as it moves towards lower frequencies with an increase in temperature at a rate of -0.05 cm^{-1} K^{-1}. Temperature change has the opposite effect on the mode at 2196 cm^{-1} that probably represents N–H(1) with the normal, almost straight line hydrogen bonding. This band moves upwards at a rate of 0.05 cm^{-1} K^{-1}. Similar results were obtained for these modes in the 5% deuterated sample (Table III.7).

Results obtained for the NH_4^+ and ND_4^+ species show similar behaviour to that obtained for NHD_3^+. It was assumed that the highest frequency vibration in the spectrum corresponds to a stretching mode involving N–H(3) in NH_4^+ while the one assigned to ν_1 (NH_4^+) can be associated with either N–H(1) or N–H(2) in the almost straight line hydrogen bond [10]. The highest frequency mode at 3207 cm^{-1} in pure NH_4VO_3 shows a decrease in wavenumbers with increasing temperature (Figure III.8). Similar results for this mode were obtained in the samples with various percentages of deuterium. This shows that the hydrogen atom H(3) becomes increasingly more associated with a particular oxygen atom with a concomitant increase in hydrogen band strength.

The mode associated with N–H(1) and N–H(2) shows a downward frequency shift in pure NH_4VO_3 but changes in the opposite direction in all deuterated samples, showing that strong coupling probably exists between the ν_1 and $2\nu_4$ modes in the N–H frequency range in pure NH_4VO_3.

The stretching modes in ND_4^+ which represent the three different bond lengths are most likely the bands assigned to $\nu_3(ND_4^+)$ [N–D(3), N–D(2)] and ν_1 (ND_4^+) [N–D(1)]. Of these three the highest wavenumber band shifts downwards at a rate of -0.05 cm^{-1} K^{-1} upon an increase in temperature while the other two that represent the almost straight line hydrogen bonds shift upwards at respective rates of 0.02 and 0.06 cm^{-1} K^{-1} (Figure III.10, Table III.7). This, together with results obtained for the temperature dependence of NH_4^+ and NH_3D^+ modes, is in agreement with the reported results for Raman mode behaviour [10] between room temperature and 473 K, showing that both normal and bifurcated hydrogen bonds are present in NH_4VO_3 with the weak bifurcated bond increasing in strength at higher temperatures while the normal bonds decrease in strength at ambient conditions. This is also reflected in the bending vibrations where two components of $\nu_4(NH_4^+)$ at 1422 and 1416 cm^{-1}

become a single band above 120 K [(Figure III.9)] The former band shows a decrease in frequency of -0.04 cm^{-1} K^{-1} while little overall change occurs for the second between 80 K (1416 cm^{-1}) and room temperature (1415 cm^{-1}).

III.4 INFRARED SPECTRA OF THE AMMONIUM ION IN $(NH_4)_2V_6O_{16}$

III.4.1 Introduction

The space group of $(NH_4)_2V_6O_{16}$ has been reported as $P2_1/m$ with NH_4^+, V(1), O(1) and O(2) occupying 2(e) positions with C_s symmetry and the V(2), O(3) and O(4) atoms in 4(f) positions with C_1 symmetry [66, 67]. In the structure analysis of the compound [18, [II.2]] the coordination of oxygen atoms surrounding the vanadium and nitrogen atoms was determined (Figures II.2, 4, 5) [II.2] but the position of hydrogen atoms remained unresolved.

The NH_4^+-ion in $(NH_4)_2V_6O_{16}$ is surrounded by several oxygen atoms belonging to the hexavanadate groups, as can be seen in Figures (II.5) [II.2]. The eight closest oxygen atoms surround the ammonium ion at distances ranging between 2.824 and 3.169Å [18]. This can be compared with the N–O distances in NH_4VO_3 which vary between 2.85 and 3.40Å [63]. It can be expected that the ammonium in $(NH_4)_2V_6O_{16}$, with a coordination number of eight, will be highly dynamic [18].

Infrared and Raman spectra of ammonium hexavanadate have been reported at room temperature [25] but only up to 1080 cm^{-1}, involving mainly V–O vibrations. Another room temperature spectrum up to 4000 cm^{-1} [11] revealed that N–H bands were not in agreement with the number predicted under $P2_1/m$.

Low temperature spectra of the compound could reveal further splitting of bands and provide more information on the ammonium ion. Because coupling and Fermi resonance in the N-H stretching region could complicate the spectrum a low temperature infrared study of isotopical dilute NH_3D^+ ions in $(NH_4)_2V_6O_{16}$ was used to determine the nature of hydrogen bonds in the crystal. Bands of the different isotopical species were identified.

III.4.2 Experimental

III.4.2.1 Preparation of $(NH_4)_2V_6O_{16}$ and deuterated samples

$(NH_4)_2V_6O_{16}$ was prepared according to the method described in [II.2.1 D]. Deuterated samples were obtained by substituting H_2O with stoichiometric mixtures of H_2O and D_2O during preparation. No samples containing more than ~70% D could be prepared as the ammonium hexavanadate did not form when NH_4Cl was substituted with ND_4Cl.

III.4.2.2 Infrared spectra

As for NH_4VO_3 [III.3.2.3] the infrared spectra were recorded both at room temperature and 90 K on a Bomem Michelson-100 FTIR spectrometer with a resolution of 4 cm^{-1}. All samples were in the form of KBr pellets and to ensure that frequency shifts due to ion exchange did not occur the 5% deuterated sample was also recorded in the form of a CsCl pellet with identical results to that obtained with KBr. During the temperature dependence study, spectra were recorded at various temperatures between 80 and 291 K on a Bruker IFS 113V spectrometer with a resolution of 1 cm^{-1}.

During low temperature recordings a continuous flow cryostat [Appendix D (2)] was used with liquid nitrogen to keep samples at different temperatures between 80 K and room temperature. It is known that N–D stretching vibrations in other systems [48, 68] have half the integrated intensity of the N–H bands. This enabled the degree of deuteration in each sample to be estimated.

III.4.3 Vibrational analysis of the ammonium ion and deuterated analogues in $(NH_4)_2V_6O_{16}$

The correlation of fundamental modes of isotopically substituted ammonium ions were shown in Table III.2. Site and factor group correlation of NH_4^+ in undeuterated, and ND_4^+ in fully deuterated $(NH_4)_2V_6O_{16}$ appear in Table III.8.

Under site group C_s all the modes are both infrared and Raman active. $\nu_1(A_1)$ is predicted to remain single while $\nu_2(E)$ should split into two bands and both $\nu_3(F_2)$ and $\nu_4(F_2)$ into three bands each. Further factor group splitting should result in the same number of bands in the infrared and Raman spectra as half the modes under $P2_1/m$ are infrared active and the other half Raman active: A' splits into A_g (R) + B_u (IR) and A" into B_g (R) + A_u (IR).

The correlation of NH_3D^+ and NHD_3^+ modes in ammonium hexavanadate is the same as for NH_4VO_3 (Table III.4 [III.3.3]) with an effective site symmetry of C_s. This means that three components can be expected for the stretching mode $\nu_1(NH_3D^+)$ and six for the $\nu_{4bc}(NH_3D^+)$ bending mode.

Table III.8 Site and factor group correlation for NH_4^+ in $(NH_4)_2V_6O_{16}$ and ND_4^+ in $(ND_4)_2V_6O_{16}$

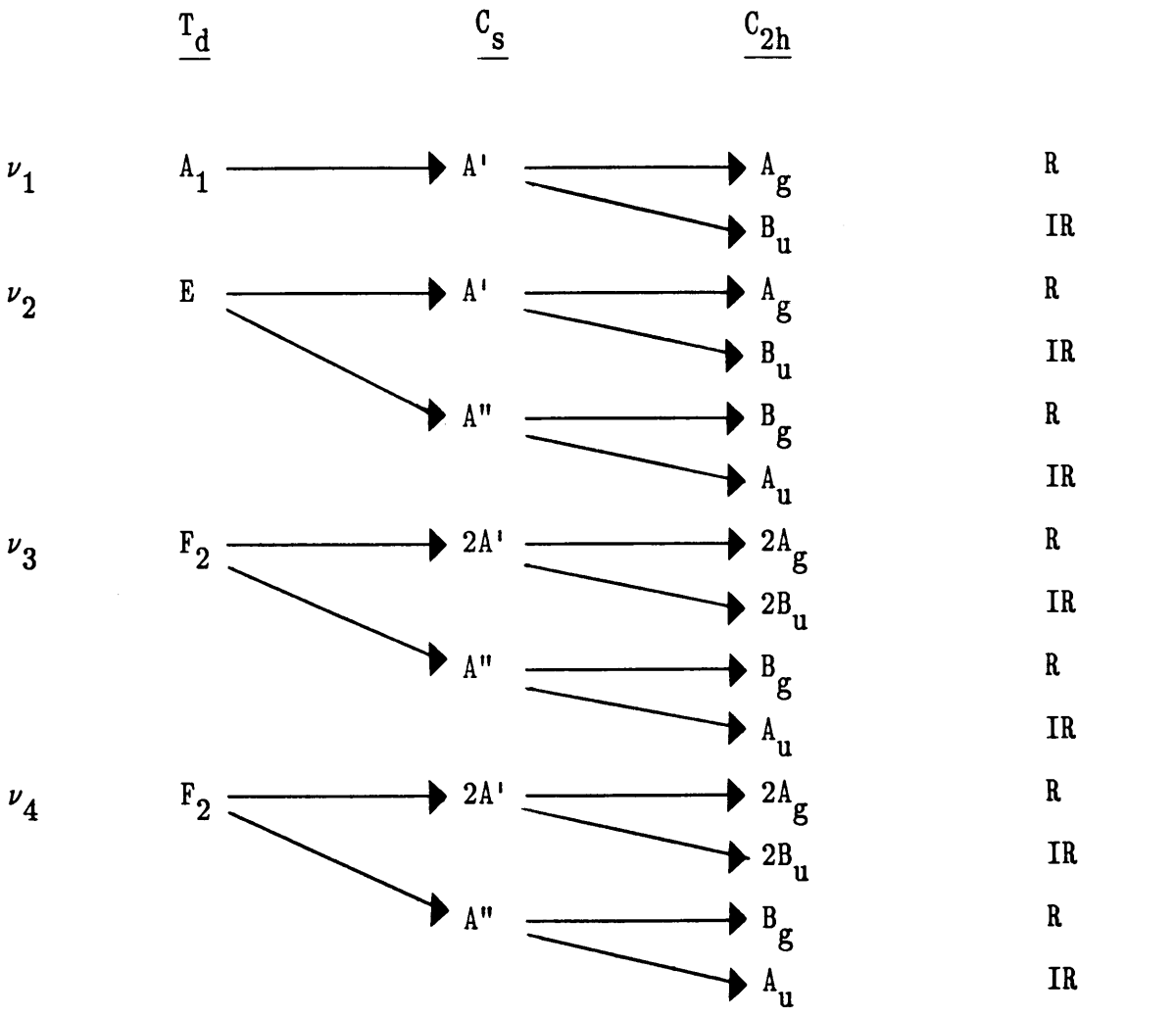

III.4.4 Infrared spectra

III.4.4.1 Pure $(NH_4)_2V_6O_{16}$

The N–H stretching region in the infrared spectra of $(NH_4)_2V_6O_{16}$ at room temperature and 90 K are shown in Figure III.11 with the low temperature spectra of pure and variously deuterated samples of the same compound in Figures III.12 and III.13. A full assignment of the spectra is given in Tables III.8 and III.9. It was previously reported [11] that only one of the two stretching modes (ν_1 and ν_3) is observed in the room temperature infrared spectrum of pure $(NH_4)_2V_6O_{16}$ and that even though the low C_s symmetry of ammonium in this compound should cause splitting of degenerate vibrations, single modes are present for both ν_3 and ν_4. These modes were observed at 3216 cm^{-1} (Figure III.11) and 1405 cm^{-1} at room temperature.

At low temperatures, a tentative assignment of the N–H modes can be made as follows: 3250(ν_3), 3194(ν_3) and 3177(ν_3), thereby accounting for all three infrared active components of ν_3. ν_1 can be assigned to the satellite at 3115 cm^{-1} which shows indications of being split. This is, of course, in contradiction to the selection rules. The absorption peak at 3041 cm^{-1} can be assigned to $\nu_2 + \nu_4$. ν_2 does not split into two components, even at 90 K where it appears at 1638 cm^{-1}, but ν_4 splits into three components at 1420, 1398 and 1385 cm^{-1} at low temperature (Figure III.13) with the $2\nu_4$ overtone at 2814 and 2766 cm^{-1} (Figures III.11 and III.12). Extremely weak features at 1974 and 1930 cm^{-1} probably represent the combination bands of $\nu_2 + \nu_6$,

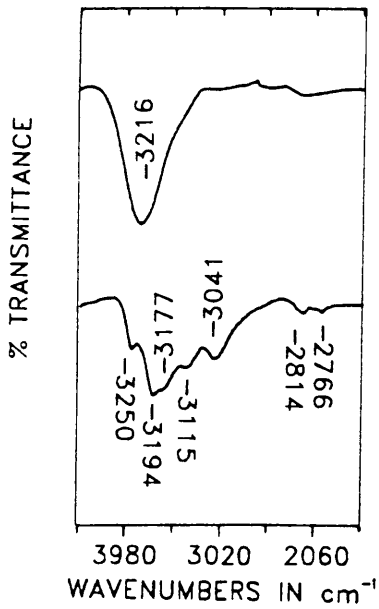

Figure III.11 The N–H stretching region in $(NH_4)_2V_6O_{16}$ at room temperature (top) and 90 K (bottom)

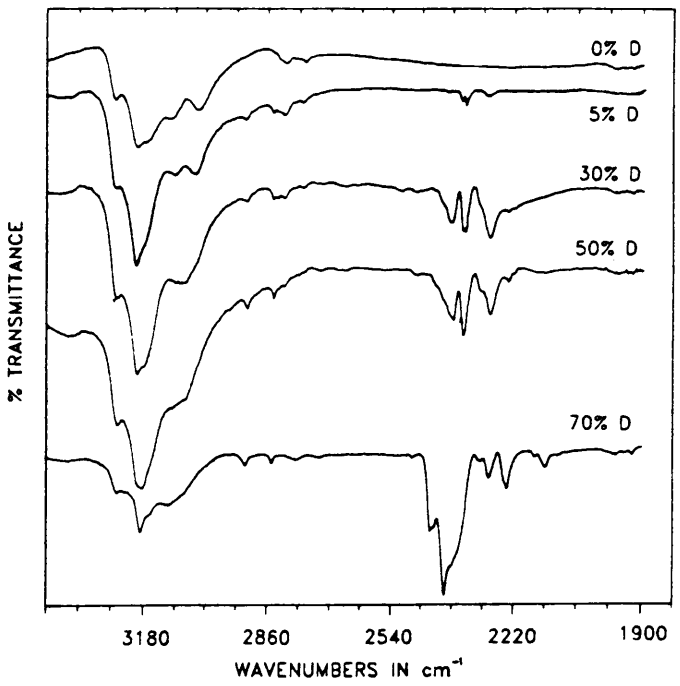

Figure III.12 Low temperature infrared spectra of $(NH_4)_2V_6O_{16}$ and various percentage deuterated samples between 3400 and 1900 cm^{-1}

Table III.8 Low temperature infrared modes of the deuterated species in $(NH_4)_2V_6O_{16}$ between 3500 and 2000 cm^{-1}

Assignment	Wavenumbers in cm^{-1}				
	100% $(NH_4)_2V_6O_{16}$	5% D	30% D	50% D	70% D
$\nu_3(NH_4^+)$, $\nu_3(NHD_3^+)$	3250m	3247m	3250m	3247m	3243m
$\nu_3(NH_4^+)$, $\nu_3(NHD_3^+)$	3194m	3197s	3198s	3188s	3185s
$\nu_3(NH_4^+)$, $\nu_3(NHD_3^+)$	3177sh	3177sh	3184sh	-	3140sh
$\nu_1(NH_4^+)$, $\nu_1(NHD_3^+)$	3115m	3103m	3103m	3120m.sh	3117m
$\nu_2 + \nu_4(NH_4^+)$	-	-	3090sh	-	-
$\nu_2 + \nu_4(NH_4^+)$	3041m	3050m	3079sh	3060m	3070sh
$\nu_3(NH_2D_2^+)$	-	2917w	2918vw	2915w	2916w
$2\nu_4(NH_4^+)$	2846w	2846w	2848w	2846w	2847w
$\nu_3(NH_3D^+)$	-	-	2836w	-	-
$2\nu_4(NH_4^+)$	2814w	2818w	2820w	2819vw	-
$2\nu_4(NH_4^+)$	2766w	2770vw	2774vw	-	2786w
$2\nu_2(NHD_3^+)$	-	2739vw	-	-	2727w
$2\nu_4(NH_3D^+)$	-	-	2479vw	2474vw	2482vw
$\nu_3(ND_4^+)$	-	-	-	-	2436s
$\nu_3(ND_4^+)$	-	-	-	2420	2427s
$\nu_3(NHD_3^+)$	-	-	-	2404sh	2404vs
$\nu_3(ND_4^+)$	-	-	-	2390sh	-
$\nu_1(ND_4^+)$	-	2388sh	2386w	2379w	2385vs.sh
$\nu_1(NH_3D^+)$	-	2356w.sp	2359w	2355w	-
$\nu_1(NH_3D^+)$	-	2345w.sp	2351w	2355w	-
$2\nu_4(NHD_3^+)$	-	-	-	2306sh	2306vw
$\nu_1(NH_3D^+)$	-	2287w	2287w	2284w	2283w
$2\nu_2(ND_4^+)$	-	-	2241vw	2237vw	2238w
$2\nu_4(ND_4^+)$	-	-	-	-	2165vw
$2\nu_4(ND_4^+)$	-	-	-	-	2139w

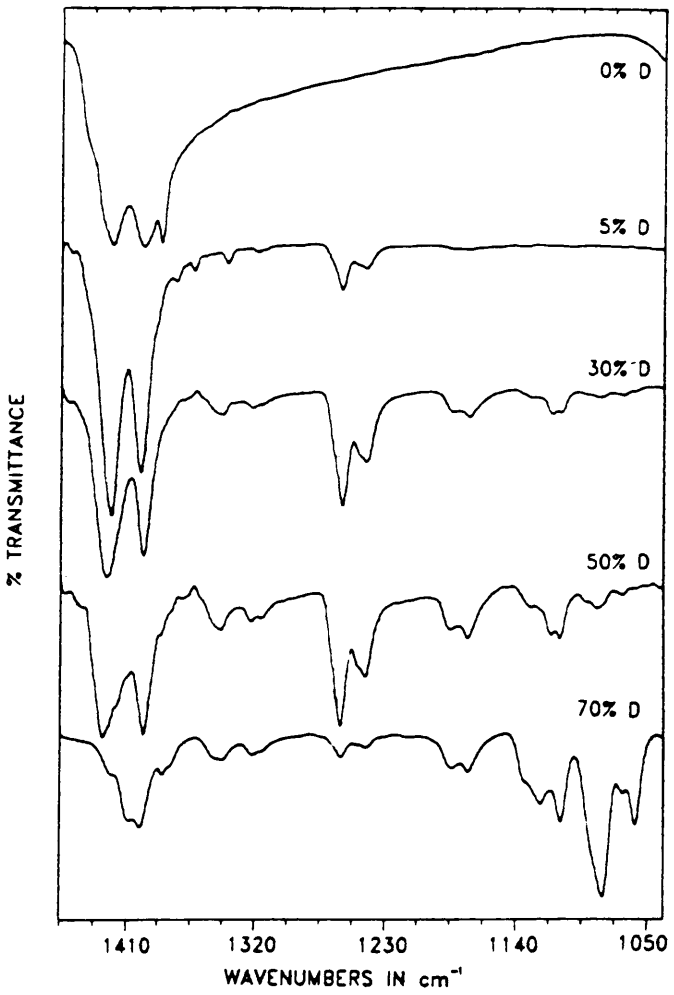

Figure III.13 Low temperature infrared spectra of $(NH_4)_2V_6O_{16}$ and various percentage deuterated samples between 1450 and 1050 cm^{-1}

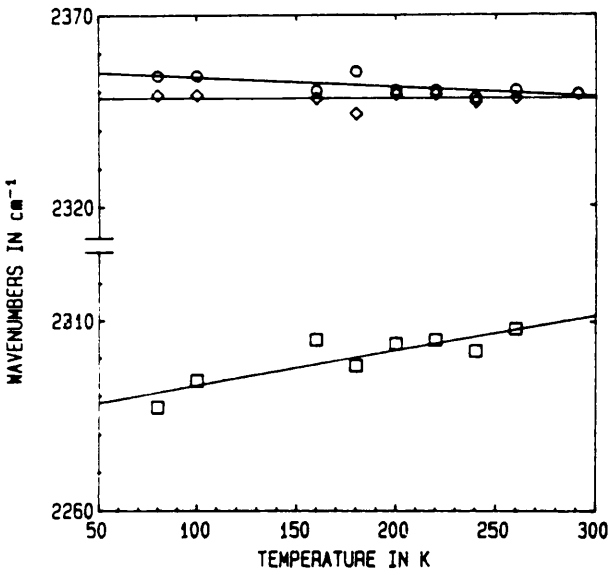

Figure III.14 Temperature dependence of the stretching modes of isotopically dilute NH_3D^+ in $(NH_4)_2V_6O_{16}$

however, there are no indications of the occurrence of $\nu_4 + \nu_6$ which should appear in the frequency range 1700 to 1750 cm^{-1}. These observations show that the NH_4^+ ions in $(NH_4)_2V_6O_{16}$ are more dynamical than the ones in NH_4VO_3 where the combination bands $\nu_i + \nu_6$ (i = 2,4) could easily be identified at ambient temperatures [10]. The values of ν_6, calculated to be equal to 336 and 292 cm^{-1} in $(NH_4)_2V_6O_{16}$ are considerably lower than the ones in NH_4VO_3 at ambient conditions. This shows that the NH_4^+ ions in $(NH_4)_2V_6O_{16}$ have more reorientational freedom than the ones in NH_4VO_3, even though the N–O distances in $(NH_4)_2V_6O_{16}$ are shorter on average than the ones in NH_4VO_3. Upon cooling the samples to 90 K no considerable sharpening of the combination band $\nu_2 + \nu_6$ took place, showing that the NH_4^+ ions remain dynamic even at very low temperatures. The fundamental stretching modes in particular, however, cannot be assigned unambiguously in $(NH_4)_2V_6O_{16}$ since, like in all the other NH_4^+ compounds, the frequency region where these bands occur, is also complicated by the occurrence of combinations and overtones such as $\nu_2 + \nu_4$ and $2\nu_4$ that have been observed here. For this reason the infrared spectrum of the isotopically dilute NH_3D^+ species was recorded since the N–D stretching frequency is not complicated by Fermi resonance between energy levels such as ν_3, ν_1, $2\nu_4$ and $\nu_2 + \nu_4$.

III.4.4.2 Deuterated samples of $(NH_4)_2V_6O_{16}$

The case of the influence of deuteration on an ammonium ion with C_s symmetry has already been discussed in detail for NH_4VO_3 [III.3.3]. Similar to this the ν_1 mode of the NH_3D^+ species in deuterated $(NH_4)_2V_6O_{16}$ should split into C_s, C_s and C_1(s) components.

Atmospheric CO_2 has absorption bands in the infrared between 2386 and 2317 cm^{-1} which is observed even after purging the instrument with dry nitrogen. This prevented the use of 0.5-1% deuterated $(NH_4)_2V_6O_{16}$ samples to study low intensity $\nu_1(NH_3D^+)$ bands in the same frequency region. At 5% deuteration NH_3D^+ modes are considerably stronger than those of CO_2 in the same region.

Assignments in the mid-infrared spectra of each deuterated sample of $(NH_4)_2V_6O_{16}$ at both room temperature and 80 K are shown in Tables C.1-5 (Appendix C).

(1) 5% Deuterated $(NH_4)_2V_6O_{16}$

In Figure III.12 the N–D stretching modes in 5% D $(NH_4)_2V_6O_{16}$ are represented by three components at 2356, 2345 and 2287 cm^{-1} at 90 K and can be compared to those in NH_4VO_3 as it also contains NH_4^+ ions of C_s symmetry. In the latter, NH_4^+ ions are bonded by normal, strong hydrogen bonds on the one hand and weaker bifurcated hydrogen bonds on the other hand [10]. The N–D stretching modes of isotopically dilute NH_3D^+ reflect these differences in hydrogen bonding, and the three predicted components are observed at 2196, 2348 and 2370 cm^{-1} [69, [III.3]]. The latter two frequencies correspond to the ones at 2345 and 2356 cm^{-1} in $(NH_4)_2V_6O_{16}$, suggesting the existence of bifurcated hydrogen bonds in this compound as well. The

hydrogen bond associated with the $\nu_1(NH_3D^+)$ band at 2287 cm^{-1} is normal and quite strong, even though less so than the bond corresponding to the 2196 cm^{-1} band in NH_4VO_3. Of the six modes predicted for $\nu_{4bc}(NH_3D^+)$, only two are observed at 1261 and 1245 cm^{-1} at low temperature.

The following $NH_2D_2^+$ modes are present as low-intensity bands in 5% deuterated $(NH_4)_2V_6O_{16}$: ν_3 at 2917 cm^{-1} (Figure III.12), ν_2 at 1559 cm^{-1} and 1319 cm^{-1} (Figure III.13). Weak bands at 1363 and 1176, 1160 cm^{-1} can be attributed to the ν_2 and ν_4 modes of NHD_3^+, with a band at 1339 cm^{-1} being assigned to $\nu_4 + \nu_6(ND_4^+)$ and a weak shoulder at 2388 cm^{-1} to ν_1 of the same species.

(2) <u>30% Deuterated $(NH_4)_2V_6O_{16}$</u>

At 30% deuteration even more bands become visible. A new shoulder at 3184 cm^{-1} is assigned to the N–H stretch, $\nu_3(NHD_3^+)$. A band at 2836 cm^{-1} reaches maximum intensity in this spectrum and is therefore assigned to $\nu_3(NHD_3^+)$ on grounds of statistical distribution of the $NH_{4-x}D_x^+$ species. All other bands assigned to NH_3D^+ also reach maximum relative intensity at 30% D, including a weak new band at 2479 cm^{-1} which is assigned to $2\nu_4(NH_3D^+)$. A shoulder at 1116 cm^{-1} can be attributed to $\nu_4(NH_2D_2^+)$.

(3) <u>50% Deuterated $(NH_4)_2V_6O_{16}$</u>

Some NH_4^+ vibrations can still be distinguished in the spectrum of 50% deuterated $(NH_4)_2V_6O_{16}$ but bands representing the $NH_2D_2^+$, NHD_3^+ and ND_4^+ species become more prominent. ND_4^+ modes in the N–D stretching region

start to overlap with those of NH_3D^+: $\nu_3(ND_4^+)$ occurs at 2404 cm^{-1} and $\nu_1(ND_4^+)$ at 2379 cm^{-1}. One shoulder in this region can be attributed to $\nu_3(NHD_3^+)$ while another at 2306 cm^{-1} coincides with $2\nu_4(NH_3D^+)$. In the bending region the ν_2 and ν_4 modes of $NH_2D_2^+$ at 1583 cm^{-1} and 1316, 1185, 1116 cm^{-1}, respectively, reach maximum intensity here as would be expected at 50% deuteration. Two new bands in this region, at 1131 and 1094 cm^{-1} can be assigned to the ν_4 bending mode of NHD_3^+. These bands reach maximum intensity at 70% deuterium content.

(4) 70% Deuterated $(NH_4)_2V_6O_{16}$

From the low temperature spectrum of 70% D ($(NH_4)_2V_6O_{16}$ it becomes clear that the number of observed fundamentals in $(NH_4)_2V_6O_{16}$ closely agrees with the theoretical predictions. Three bands in the N–D stretching region at 2436, 2427 and 2404 cm^{-1} can tentatively be assigned to ν_3, leaving a single mode at 2385 cm^{-1} to be attributed to ν_1. The three components predicted for ν_4 are observed at 1059, 1067 and 1083 cm^{-1}. In $(NH_4)_2V_6O_{16}$ only one of the two bands expected from ν_2 becomes visible as a weak band, but in $(ND_4)_2V_6O_{16}$ two modes of considerable intensity appear at 1124 and 1109 cm^{-1}, thus accounting for all the fundamentals predicted for ND_4^+ under $P2_1/m$. Overtones in the N–D stretching region are well separated from the fundamentals and occur at 2238 cm^{-1} ($2\nu_2$) and 2165, 2139 cm^{-1} ($2\nu_4$), respectively. As opposed to undeuterated $(NH_4)_2V_6O_{16}$ where only one of the two $\nu_i + \nu_6$ (i = 2,4) bands, viz. $\nu_2 + \nu_6$, was observed, both are present in $(NH_4)_2V_6O_{16}$ where $\nu_2 + \nu_6$ appear as a strong mode at 1409 cm^{-1} and $\nu_4 + \nu_6$ as a weak mode at 1345 cm^{-1}. Both these bands occur close to other modes at 70% deuteration, one in the middle of two strong $\nu_4(NH_4^+)$ components and the

other between $\nu_4(NH_4^+)$ and $\nu_4(NH_2D_2^+)$, which is probably responsible for the enhancement of these modes in $(NH_4)_2V_6O_{16}$. ν_6 is calculated at between 260 and 300 cm^{-1}. The new bands at 2727 and 2482 cm^{-1} can be assigned to $2\nu_2(NHD_3^+)$ and $2\nu_4(NH_3D^+)$. In the N-H stretching region three bands that occurred at 3250, 3194 and 3177 cm^{-1} in 100% $(NH_4)_2V_6O_{16}$ and were assigned to $\nu_3(NH_4^+)$ shifted to 3243, 3185 and 3140 cm^{-1}. These bands can now be attributed to the N-H stretch in NHD_3^+.

III.4.4.3 Comparison between spectra of deuterated samples

(1) N-H stretching vibrations

As in ammonium metavanadate the N-H stretching region consists of a broad band that split into multiple other bands at low temperature (Figure III.11). The three bands at the highest frequencies were tentatively assigned to $\nu_3(NH_4^+)$ (Table III.8). At the high deuteration percentage these broad bands became sharp and shifted to lower frequencies which represent N-H stretches in the NHD_3^+ species. ν_3 modes in $NH_2D_2^+$ can be identified at 2915 cm^{-1} where it reaches maximum relative intensity in the 50% deuterated $(NH_4)_2V_6O_{16}$ spectrum. The very weak band at 2836 cm^{-1} is only observed in the 30% D $(NH_4)_2V_6O_{16}$ sample and is thus attributed to the N-H stretch in NH_3D^+.

(2) N-D stretching vibrations

Isotopically dilute NH_3D^+ ions give rise to three sharp bands at 2356, 2345 and 2287 cm^{-1} in low percentage deuterated samples which is in agreement with the three components predicted for ν_1 (NH_3D^+) of an ammonium ion with C_s symmetry. These bands reach maximum intensity at 30% deuteration.

At intermediate D contents N–D stretching bands for NHD_3^+ appear in the 2000 to 2500 region at 2404 cm^{-1}, and at high D contents the ND_4^+ bands occur between 2380 and 2440 cm^{-1}.

(3) Bending vibrations

Comparison of bending vibrations of NH_4^+ and the variously deuterated species in ammonium hexavanadate between 1050 and 1500 cm^{-1} were shown in Figure III.13 and Table III.9.

All three components predicted for ν_4 under $P2_1/m$ are observed for NH_4^+ and ND_4^+ in 100% $(NH_4)_2V_6O_{16}$ and the highest deuterated sample respectively. In NH_4^+ one of the two expected band for ν_2 can be observed but both are assigned in ND_4^+. Two of the six bands predicted for $\nu_4(NH_3D^+)$ are observed at 1260 and 1245 cm^{-1}. Bending vibrations of NHD_3^+ are identified at 1379 (ν_2), 1184, 1173 and 1136 cm^{-1} (ν_4) and those of $NH_2D_2^+$ at 1583 (ν_2), 1324, 1316 and 1116 cm^{-1} (ν_4).

III.4.4.4 Temperature dependence of some ammonium modes in $(NH_4)_2V_6O_{16}$

The temperature dependence of the various infrared active ammonium bands, especially those of isotopically dilute NH_3D^+, can provide more information about the nature of hydrogen bonds in the $(NH_4)_2V_6O_{16}$ crystal $\frac{d\nu}{dT}$-values for the various modes are shown in Table III.10. The behaviour of $\nu_1(NH_3D^+)$ modes of $(NH_4)_2V_6O_{16}$ between 80 K and room temperature are shown in Figure III.14. The highest frequency mode at 2356 cm^{-1} shows a decrease in wavenumbers with the increase in temperature at a rate of -0.03 cm^{-1} K^{-1} [69]. A comparison between NH_3D^+ modes in the two compounds was shown

Table III.9 Low temperature infrared modes of the deuterated species in $(NH_4)_2V_6O_{16}$ between 2000 and 1000 cm^{-1}

Assignment	Wavenumbers in cm^{-1}				
	100% $(NH_4)_2V_6O_{16}$	5% D	30% D	50% D	70% D
$\nu_2 + \nu_6(NH_4^+)$	1974vw	-	1967vw.b	-	-
$\nu_2 + \nu_6(NH_4^+)$	1930vw	-	-	1950w.b	1923w.b
$\nu_2(NH_4^+)$	1638b.w	1653vw	-	-	-
$\nu_2(NH_2D_2^+)$	-	1559w	1588w	1583w	1558w
$\nu_4(NH_4^+)$	1420s	1421vs	1423s	1426m	1420sh
$\nu_2 + \nu_6(ND_4^+)$	-	-	-	1412sh	1409m
$\nu_4(NH_4^+)$	1398s	1399vs	1398s	1397m.sp	1402m
$\nu_4(NH_4^+)$	1385s	1375w	-	1386sh	1385w
$\nu_2(NHD_3^+)$	-	1363vw	-	1370vw	1379w
$\nu_4 + \nu_6(ND_4^+)$	-	1339vw	1345w	1346w	1345w
$\nu_2(NH_2D_2^+)$	-	1319vw	1322w	1324w	1323w
$\nu_2(NH_2D_2^+)$	-	-	-	1316w	1316vw.sh
$\nu_4(NH_3D^+)$	-	1261w	1260s	1260m	1260w
$\nu_4(NH_3D^+)$	-	1245w	1245m	1245w	1243w
$\nu_4(NHD_3^+)$	-	-	1183w	1185w	1184m
$\nu_4(NHD_3^+)$	-	1176vw	1173w	1174w	1173m
$\nu_4(NHD_3^+)$	-	~1160vw	-	1131sh	1136m
$\nu_2(ND_4^+)$	-	-	-	-	1124s
$\nu_4(NH_2D_2^+)$	-	-	1116w.sh	1116w	-
$\nu_4(ND_4^+)$	-	~1104vvw	1111w	1111w	1109s
$\nu_4(NHD_3^+)$	-	-	-	1094sh	-
$\nu_4(ND_4^+)$	-	-	1084vw	1085vw	1083vs
$\nu_4(ND_4^+)$	-	-	1068vw	1069vw	1067sh
$\nu_4(ND_4^+)$	-	-	-	-	1059s

Table III.10 Temperature dependence of some infrared active modes in $(NH_4)_2V_6O_{16}$ and its deuterated analogues between 80 K and room temperature

Mode	$d\nu/dT$ [cm^{-1} K^{-1}]			
	100% $(NH_4)_2V_6O_{16}$	5% D	30% D	90% D
$\nu_3(NH_4^+)$	-0.07			
$\nu_3(NH_4^+)$	+0.18		+0.22	
$\nu_1(NH_4^+)$	-0.01		-0.27	
$\nu_2 + \nu_4(NH_4^+)$	-0.01			
$2\nu_4(NH_4^+)$	-0.001			
$2\nu_4(NH_4^+)$	+0.02			
$\nu_2(NH_4^+)$				
$\nu_4(NH_4^+)$	-0.07		-0.16	
$\nu_4(NH_4^+)$	+0.04		+0.03	
$\nu_1(NH_3D^+)$		-0.03		
$\nu_1(NH_3D^+)$		-0.002		
$\nu_1(NH_3D^+)$		+0.09		
$\nu_3(ND_4^+)$				+0.09
$\nu_1(ND_4^+)$				-0.11
$\nu_2(ND_4^+)$				+0.04
$\nu_4(ND_4^+)$				-0.02

previously [69]. The $\nu_1(NH_3D^+)$ band in $(NH_4)_2V_6O_{16}$ at 2345 cm^{-1} shifts very slowly towards lower frequency ($d\nu/dT$ = -0,002 cm^{-1} K^{-1}) and therefore remains virtually unchanged between 80 K and room temperature. From these results it can be assumed that both these bands in $(NH_4)_2V_6O_{16}$ represent a N–H bond in which the hydrogen atom becomes more and more associated with a particular oxygen atom at higher temperatures with a concomitant increase in hydrogen bond strength, suggesting that the bands represent bifurcated hydrogen bonds, as the bands at 2370 and 2348 cm^{-1} [69] in NH_4VO_3 do.

The third $\nu_1(NH_3D^+)$ mode in $(NH_4)_2V_6O_{16}$ at 2287 cm^{-1} shows a blue shift upon an increase in temperature at a rate of 0.009 cm^{-1} K^{-1}. It can be assumed that this band represents a N–H bond associated with normal hydrogen bonding as its behaviour shows a decrease in strength of the bond at higher temperatures. However, when compared with the strong, normal and almost straight line hydrogen bonds in NH_4VO_3 represented in the spectrum by a band at a much lower frequency (2196 cm^{-1}) and of greater intensity than the one in $(NH_4)_2V_6O_{16}$ it becomes clear that the normal hydrogen bonds in $(NH_4)_2V_6O_{16}$ are not of the same strength as that in NH_4VO_3. This could be expected as it was already established that NH_4^+ ions in $(NH_4)_2V_6O_{16}$ have more reorientational freedom than the ones in NH_4VO_3.

The three bands in the N–H stretching region at 3250, 3194 and 3115 cm^{-1} can probably be associated with three different N–H bond lengths in $(NH_4)_2V_6O_{16}$. The highest frequency band that can be assumed to represent the longest N–H bond shows a decrease in wavenumber with increasing temperature at a rate of -0.07 cm^{-1} K^{-1} (Figure III.15). Similar behaviour is observed for the 3115 cm^{-1} band with $d\nu/dT$ = -0.01 cm^{-1} K^{-1}. The hydrogen bonds associated with these bands increase in strength at higher temperatures, showing the

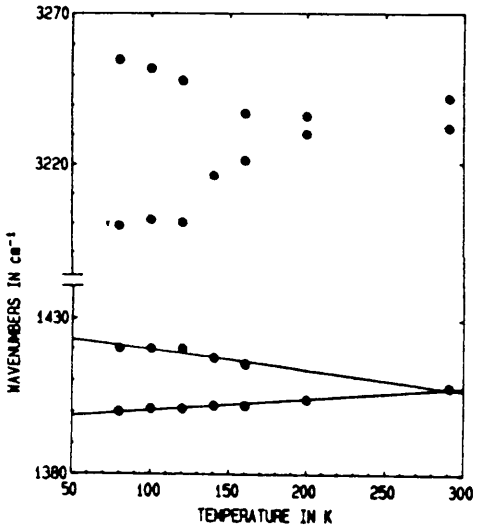

Figure III.15 The temperature dependence of some NH_4^+ modes in pure $(NH_4)_2V_6O_{16}$; two ν_3(top) and two ν_4 bands (bottom)

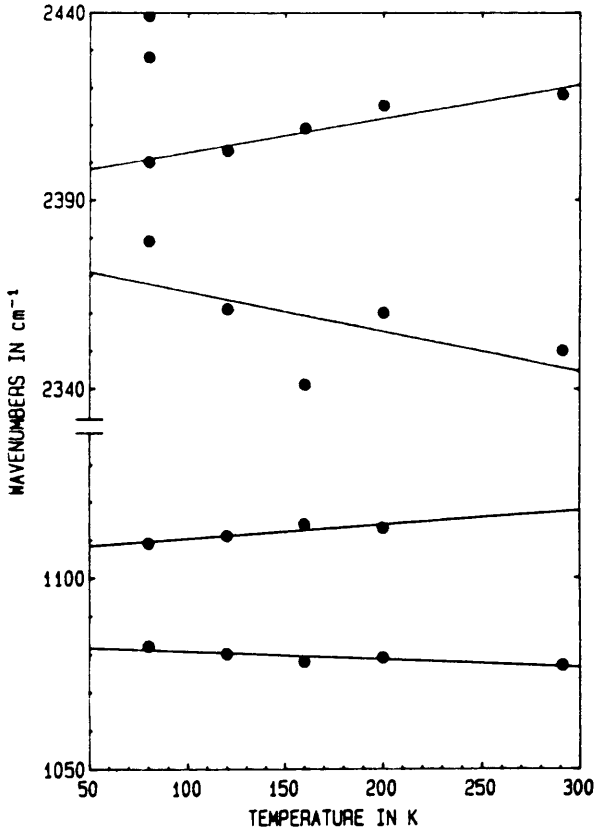

Figure III.16 The temperature dependence of some ND_4^+ modes in pure $(NH_4)_2V_6O_{16}$; ν_3, ν_1, ν_2 and ν_4

typical behaviour of bifurcated hydrogen bonding which was also observed in the two higher frequency $\nu_1(NH_3D^+)$ modes. The 3194 cm^{-1} band moves towards higher frequencies with increasing temperature which is the normal behaviour for a hydrogen bond. Similar behaviour for the different bonds is repeated for N–H and N–D stretching vibrations in 30% D $(NH_4)_2V_6O_{16}$ and the highest deuterated sample (Figure III.16), respectively. The two components of the bending vibration $\nu_4(NH_4^+)$ reflect the opposite behaviour of the two types of hydrogen bonding identified in $(NH_4)_2V_6O_{16}$ (Figure III.15) as the one shows a decrease in frequency at a rate of -0.07 cm^{-1} K^{-1} while the other moves towards higher frequency at 0.04 cm^{-1} K^{-1}. In $(NH_4)_2V_6O_{16}$ the ν_2 and ν_4 bending modes also move in opposite directions upon an increase in temperature [70].

III.5 $(NH_4)_6V_{10}O_{28}.6\ H_2O$

In the ammonium metavanadate series the compound prepared by Lacharte [71], and described as $(NH_4)_2V_4O_{11}.2\text{-}3\ H_2O$, was prepared for crystal structure determination purposes [72] and the recording of vibrational spectra for this work. It was found by chemical analyses, however, that the compound $(NH_4)_6V_{10}O_{28}.6\ H_2O$ (ammonium decavanadate hexahydrate) had formed as orange crystals from a saturated solution of NH_4VO_3 with 1 ml CH_3COOH and 100 ml EtOH. The crystal structure was determined as $P\bar{1}$ with the structure parameters a = 10.165, b = 10.297, c = 16.735, α = 83.46, β = 87.14 and $\gamma = 71.03^o$ (Z = 2) [72]. As was the case for $(NH_4)_2V_6O_{16}$ the hydrogen positions in the decavanadate could not be determined by X-ray methods. The determination of the nature of hydrogen bonding in $(NH_4)_6V_{10}O_{28}.6\ H_2O$ could prove an interesting study in the future. The structure of ammonium decavanadate hexahydrate is shown in Figure III.17.

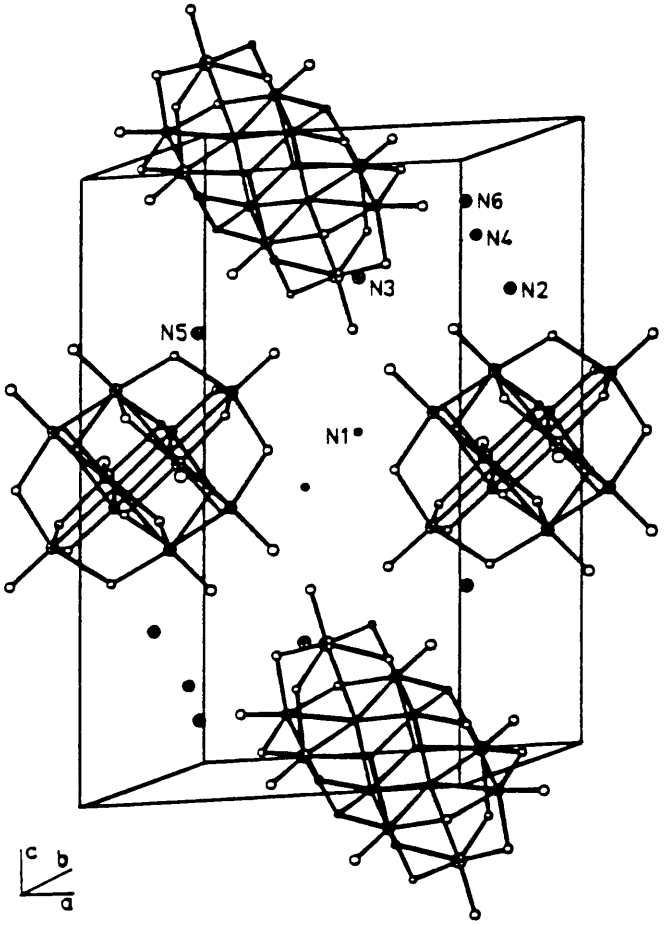

Figure III.17 Crystal structure of $(NH_4)_6V_{10}O_{28}\cdot 6H_2O$

CHAPTER IV

VIBRATIONAL SPECTRA OF $NaVO_3$, KVO_3 AND THE SOLID SOLUTIONS $(Na_{0.88}K_{0.12})VO_3$, $(Na_{0.5}K_{0.5})VO_3$ AND $Na(V_{0.66}P_{0.34})O_3$

IV.I SOLID SOLUTIONS

Solid solutions are very common in crystalline materials. A solid solution is basically a crystalline phase that can have variable composition. Its properties like conductivity can often be modified by changing the composition and this useful property can be used in designing new materials with specific properties. Simple solid solutions consist of two types, one being a substitutional solid solution in which an atom or ion is replaced by another of the same charge, and the other an interstitial solid solution in which the new atom or ion is introduced into a site previously unoccupied with no exchange of atoms or ions. A considerable variety of more complex solid solution mechanisms may be derived from these two basic types by having both substitutional and interstitial formation occurring together or by introducing ions of different charge to those in the host structure [73].

Certain requirements must be met for a substitutional solid solution to form. The first is that ions replacing each other must be of the same charge

and the second that they must be similar in size. It has been suggested [73] that a difference of no more than 15% in the radii of metal atoms that are replacing each other can be tolerated if a substantial range of solid solutions is to form. For solid solutions in non-metallic systems, however, the limiting difference in size appears to be larger, as Na^+ and K^+ often form solid solutions with each other even though the K^+ ion is ~40% larger than the Na^+ ion (Pauling crystal radii: Na^+-0.95; K^+-1.33). Even Li^+ and Na^+ replace each other over a limited range of compositions and Na^+ is ~60% larger than Li^+. The difference in size of Li^+ and K^+, however, appears to be too large for significant ranges of solid solution to form.

For a complete range of a solid solution to form it is essential that the two end member-phases be isostructural, but the fact that two phases are isostructural does not necessarily mean that they will form solid solutions with each other. Complete ranges of solid solution form in favourable cases, but it is far more common to have only limited ranges of solid solution. In the latter case the restriction that end-member phases be isostructural no longer holds.

In systems where the two ions that are replacing each other are of considerably different size the larger ion may usually be partially replaced by a smaller one, but it is more difficult to do the reverse by replacing the small ion by a larger one.

Many types of atom or ion may replace each other to form substitutional solid solutions. Silicates and germinates are often isostructural and form solid solutions with each other by Si^{4+}/Ge^{4+} replacement. The lanthanides

are also very good at forming solid solutions with each other because of their similarity in size. This easy solid solution formation was a cause of the great difficulty experienced by early chemists to separate the lanthanides. Anions may also replace each other in substitutional solid solutions, but this is not very common. A reason for this may be the fact that not many pairs of anions are similar in size and bonding requirements. Many alloys are substitutional solid solutions, e.g. in brass Cu and Zn atoms replace each other over a wide range of compositions.

Interstitial solid solutions form in many metals in which small atoms e.g. H, C, B, N can enter into empty interstitial sites in the host structure of the metal.

More complex solid solutions mechanisms are required when cation substitution takes place between two cations of different charge. There are four possibilities, summarized below [73].

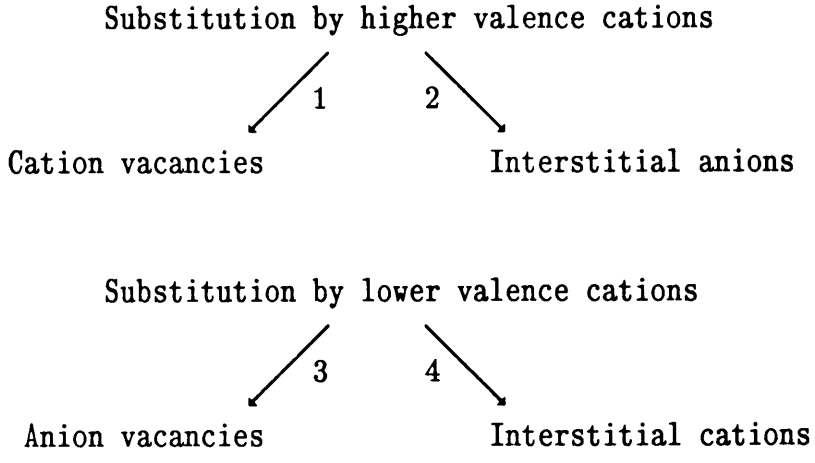

A similar scheme can be considered for anion substitution, but this does not occur frequently in solid solutions.

If the replaceable cation of the host structure has a lower charge than that of the replacing cation, additional charges are needed in order to preserve electroneutrality. Charge balance may be maintained by creating either cation vacancies or interstitial anions.

1. Cation vacancies

An example is that of NaCl which is able to dissolve a small amount of $CaCl_2$. The mechanism involves the replacement of two Na^+ ions by one Ca^{2+} ion - one Na^+ site remains vacant. The formula may then be written as $Na_{1-2x}Ca_xV_xCl$, where V represents a vacant cation site.

2. Interstitial anions

An example is that of CaF_2 which can dissolve small amounts of YF_3. The total number of cations remains constant and fluoride interstitials are created to give the solid solution formula: $(Ca_{1-2x}Y_x)F_{2+x}$.

If the replaceable cation of the host structure has a higher charge than that of the replacing cation, charge balance may be maintained by creating either anion vacancies or interstitial cations.

3. Anion vacancies

An example is that of cubic, lime-stabilized zirconia, $(Zr_{1-x}Ca_x)O_{2-x}$. The total number of cations remains constant and replacement of Zr^{4+} with Ca^{2+} requires the creation of oxide vacancies.

4. Interstitial cations

An example is that of stuffed quartz structures with the formula $Li_x(Si_{1-x}Al_x)O_2$. The structure of quartz may be modified in this way by partial replacement of $Si^{4+}(SiO_2)$ by Al^{3+} $(LiAlO_2)$. At the same time alkali metal cations enter normally empty interstitial holes in the quartz framework.

A variety of other complex solid solution mechanisms can occur of which one is double substitution where two substitutions take place simultaneously [73].

IV.2 SOME OF THE ALKALI METAL METAVANADATES AND THEIR SOLID SOLUTIONS

The alkali metal metavanadates and known solid solutions thereof are structurally related to the silicate pyroxenes. Metavanadates containing the small alkali metal cations Li^+ [74] and Na^+ [75], as well as solid solutions of Na^+ and K^+ [76], crystallize in a monoclinic or clinopyroxene structure while larger ones, e.g. K^+, Rb^+ and Cs^+ [77] form orthorhombic or orthopyroxene crystals. Space groups for the two respective structures are C2/c and Pbcm.

In the search for solid solutions of the (Na, K)(V, P)O_3 system Bergman et. al. [78] reported that no V, P substitution takes place while Ohashi [79] reported the existence of a few phases. Perraud [80] and Glazyrin [81] reported the formation of $(Na_{0.5}K_{0.5})$ VO_3 of a 25 mole % potassium substituted compound has also been suggested [80]. Idler et. al. [76] attempted to synthesize $Na(V_{0.67}P_{0.33})O_2$, $(Na_{0.75}K_{0.12})VO_3$ and $(Na_{0.5}K_{0.5})VO_3$ and found by means of X-ray analysis that crystals of the following three compounds were formed: $Na(V_{0.66}P_{0.34})O_3$, $(Na_{0.88}K_{0.12})VO_3$ and $(Na_{0.5}K_{0.5})VO_3$. Changes in the α-$NaVO_3$ structure upon substitution were then reported in terms of rotation and displacement of tetrahedral chains of VO_3^- groups.

The vibrational spectra of the above mentioned compounds are reported here in comparison with the pure alkali metal metavanadates α-$NaVO_3$ and KVO_3 to obtain full assignment of the bands. In addition results these are correlated with those obtained in a study of NH_4VO_3. A full assignment of the vibrational bands is made, the rotation and translation modes in the chains are identified and variations upon cation substitution are reported. The MVO_3(M = Li, Na, K) salts have been reported to undergo phase transitions upon heating showing variations in their dielectric properties [82, 83]. In the present study the phase transitions in $NaVO_3$ and KVO_3 are investigated by means of Raman and infrared spectroscopy, and these results are compared with those reported elesewhere [10] as well as with the results obtained on the variations of dielectric properties [82].

IV.3 THE TWO PHASES OF SODIUM METAVANADATE

IV.3.1 Preparation of α- and β-$NaVO_3$

Two phases of $NaVO_3$, viz α and β, have already been identified [84]. The β-phase can be obtained by wet preparation [85] according to the reaction $NH_4VO_3 + NaOH \xrightarrow{\Delta} NaVO_3 + H_2O + NH_3\uparrow$ while the α-product is formed at high temperatures, either by heating the β-compound to 543-673 K as the α-β transition is irreversible, or through the reaction $V_2O_5 + Na_2CO_3 \xrightarrow{900^oC} 2NaVO_3 + CO_2\uparrow$ in a platinum crucible [86].

X-ray analysis established β-$NaVO_3$ to belong either to the centric space group C2/c or the noncentric space group Cc [87], EPR-investigations of Mn^{2+} doped $NaVO_3$ and the fact that infrared bands and Raman shifts of the β-form almost coincide seem to indicate the non-centrosymmetric space group Cc (C^4, no. 9) [88]. α-$NaVO_3$ has a monoclinic pyroxene structure and belongs to space group C2/c (C^6_{2h}, No. 15) [89] with V and O atoms in 8f sites with C_i-symmetry and Na in 4e sites with C_2-symmetry.

IV.3.2 Vibrational analysis and spectra

The results of a vibrational analysis of the two phases are summarized in Tables IV.1 and IV.2.

Table IV.1 Vibrations of β-$NaVO_3$ (Spacegroup Cc)

	A'(IR, R)	A'(IR, R)
$(VO_3)^{n-}_n$ internal	8	8
$(VO_3)^{n-}_n$ translation	3	3
Na^+ translation	3	3
$(VO_3)^{n-}_n$ rotation	1	1
Total	15	15

Table IV.2 Vibrations of β-$NaVO_3$ (Spacegroup C2/c)

	A_g(IR, R)	B_g(IR, R)	A_u(IR)	B_u(IR)
$(VO_3)_n^{n-}$ internal	10	10	10	10
$(VO_3)_n^{n-}$ translation	1	2	1	2
Na^+ translation	1	2	1	2
$(VO_3)_n^{n-}$ rotation	1	0	1	0
Total	13	14	13	14

The infrared and Raman spectra of both phases have been compared by Seetharaman et. al. [89] but far-infrared spectra were not reported below 300 cm^{-1}. While the phase transition is characterized by subtle charges in the Raman spectra [89], infrared results in Figure IV.1 and IV.2 reflect definite changes in the crystal structures.

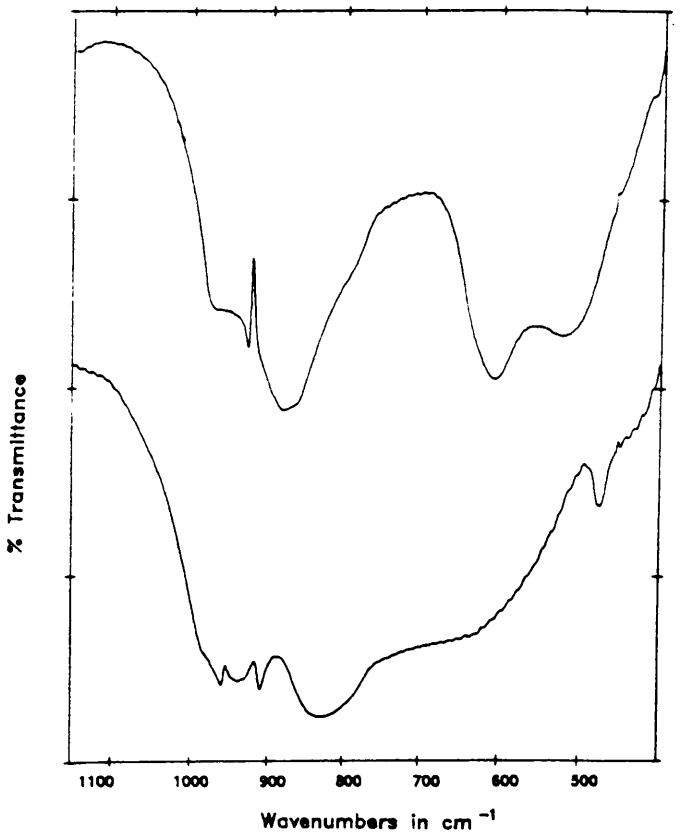

Figure IV.1 Mid infrared spectra of α (bottom) and β-$NaVO_3$ (top)

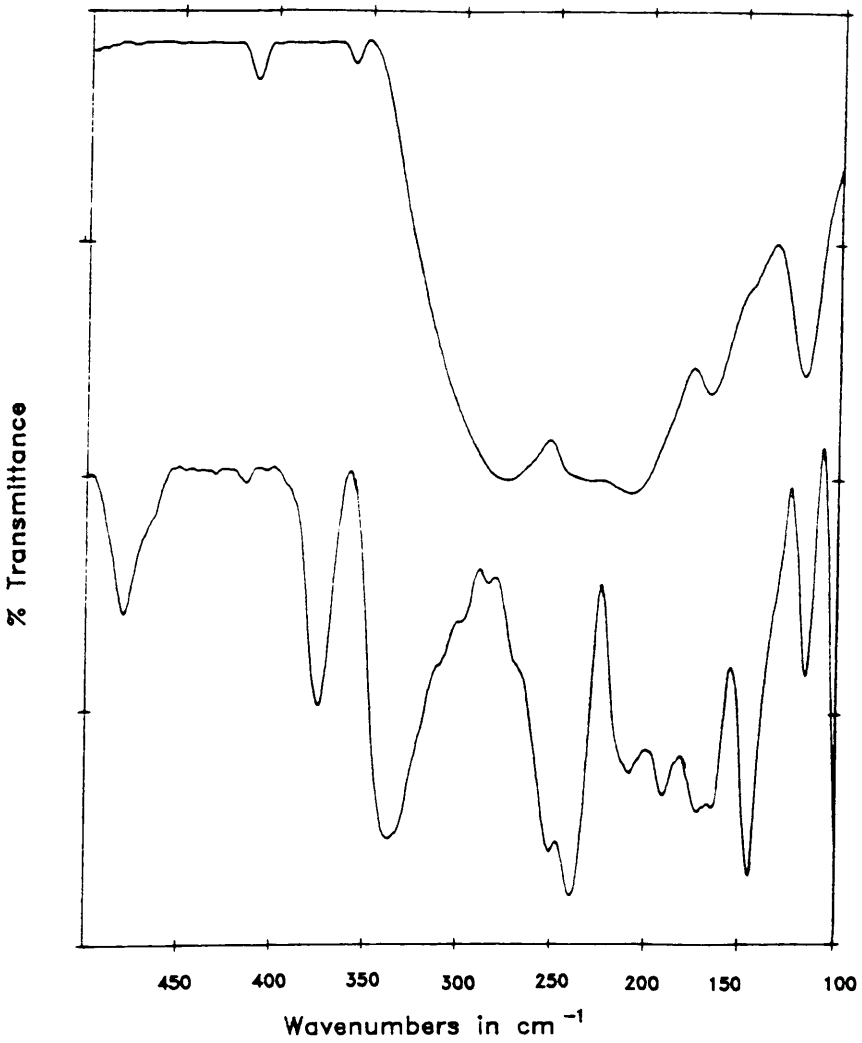

Figure IV.2 Far-infrared spectra of α-(bottom) and β-$NaVO_3$ (top)

A comparison of the two phases and assignment of infrared and Raman active modes are presented in Table IV.3. The far-infrared spectrum of β-$NaVO_3$ (Figure IV.2) is characterized by broad bands while those of the high temperature phase consists of better defined peaks. The symmetric VOV stretching vibration at 480 cm^{-1} in the α-phase appears at a considerably lower wavenumber, 412 cm^{-1}, in the β-phase. The increase in frequency difference between the symmetric and antisymmetric VOV stretching frequencies in the Raman spectra from α- and β-$NaVO_3$ gives a qualitative

Table IV.3 Comparison and assignent of vibrational modes in α- and β-$NaVO_3$

α-$NaVO_3$		β-$NaVO_3$		
Raman	IR	Raman	IR	Assigment
956 vs	961 s.sp	944 vs.	957 b	$\nu_s(VO_2)$*
941 w	941 s		930 sp	
919 s	911 s.sp	909 m.sp.	882 vs.	$\nu_{as}(VO_2)$*
907 vw	836 b	889 m		
636 m		732 m		$\nu_{as}(VOV)$*
547 w		557 w	607 vs	Combinations*
			526 b	
507 m	480 m	428 m	412 vw	$\nu_s(VOV)$*
378 w	374 m		360 w	$\delta(VO_2)$*
358 w	339 m			
343 w	333 s		277 vw	
315 vw		288 m		
254 m	263 s			$\nu_L(VO_3^-)$
243 m		256 m	229 b	$\delta(VOV)$*
219 m	239 m	200 m	210 sh	
	217 m			
	203 m			
	194 m			
177 w	175 m	160 w	168 s	
	147 m	147 sh		$\nu_T(Na^+)$
	135 m	134 m		
		124 vw	119 s.sp	$\nu_T(VO_3^-)$
102 v.vw	99 m			
87 w	85 m	80 vw		
69 vw	70 w			
60 w	65 w	50 w		

*Assignments by Seetharam et. al. [89]

indication of the change in the VOV bridge angle [89]. Absorption bands in the infrared spectra of both phases between 300 and 150 cm^{-1} are assigned to VOV bending modes. A VO_3^- chain librational mode in α-$NaVO_3$ is observed at 263 cm^{-1} with the translational modes at 99, 85, 70 and 65 cm^{-1} in the infrared and at 87 and 60 cm^{-1} in the Raman spectra.

IV.4 KVO_3

IV.4.1 Crystal structure

KVO_3 has the same orthorhombic pyroxene structure as NH_4VO_3 with space group Pbcm (D_{2h}^{11}, no. 57) [77]. The structure is also based on VO_4 tetrahedra forming a chain running parallel to the c-axis. These chains are held together by K^+ ions with six fold coordination to the oxygens, indicated by broken lines in Figures IV.3(a) and (b).

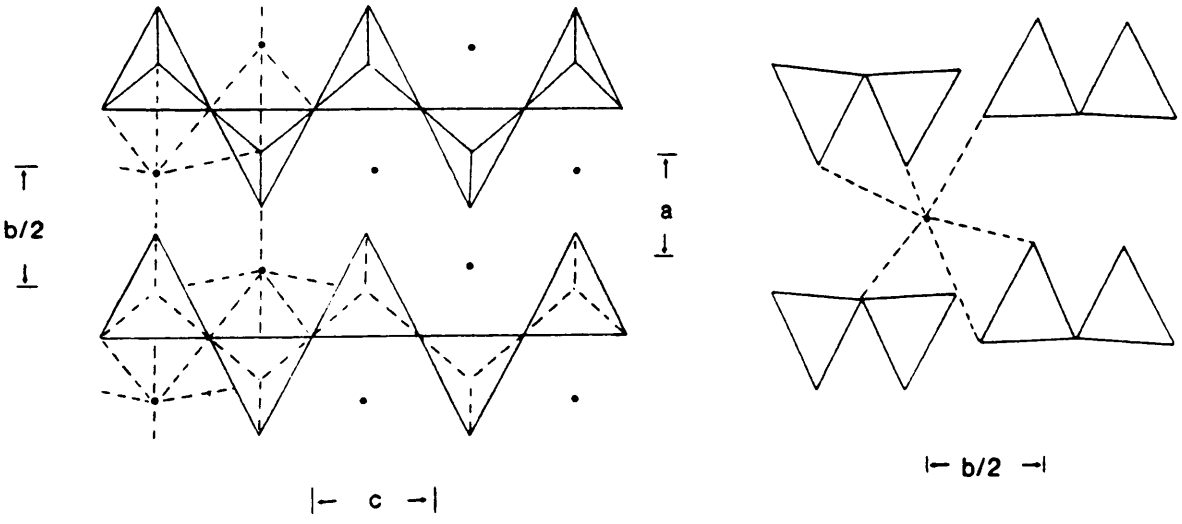

Figure IV.3 The structure of orthormbic KVO_3 (left) with the coordination of K projection along the c-axis. K-O bonds are indicated by broken lines, showing the six fold coordination of K (right)

IV.4.2 Vibrational analysis and spectra

Intramolecular vibrations of the VO_3^- chain as determined by the correlation method [90] and the result of coupling between chains under D_{2h} are shown in Table IV.4. Vibrations in the KVO_3 crystal (crystal structure D_{2h}^{11}) are analyzed in Table IV.5. Approximate forms of modes of a simplified planar $[V_2O_2]$-chain backbone as reported by Adams et. al. [91] are illustrated in Figure IV.4. Infrared and Raman spectra have been recorded at room temperature and 80 K [91, 92] and those at ambient conditions are shown in Figures IV.5 and IV.6 with comparison and assignment of modes in Table IV.6.

IV.4.3 The ferroelectric phase transition in KVO_3

Temperature dependence studies of Raman active modes and X-ray diffraction patterns of KVO_3 gave no clear indication of the occurrence of the reported phase transition [82] involving variations of its dielectric properties around 593 K (Figure IV.7), although there are indications of some minor frequency shifts occurring at the phase transition temperature.

IV.5 Solid solutions of the $(Na,K)(V,P)O_3$ system

IV.5.1 Preparation of the samples

The alkali metal metavanadates were prepared by heating V_2O_5 and the alkali metal carbonate at 1223 K for 5 hours in a platinum crucible. The whole range of solid solutions was obtained in this way with stoichiometric mixtures of K_2CO_3 and Na_2CO_3 used for the sodium-potassium substitution. The correct combination of $NaPO_3$ and $NaVO_3$ was heated together to 1173 K to obtain $Na(V_{0.66}P_{0.34})O_3$.

Table IV.4 VO_3^--chain vibrations [91]

Single chain		Coupling between chains
C_{2v}		D_{2h}
6 A_1	⟶	$6(A_g + B_{3u})$
3 A_2	⟶	$3(B_{1g} + B_{2u})$
4 B_1	⟶	$4(B_{2g} + B_{1u})$
7 B_2	⟶	$7(B_{2g} + A_u)$

Table IV.5 Vibrations of KVO_3

	A_g(R)	B_{1g}(IR,R)	B_{2g}(IR,R)	B_{3g}(IR,R)	A_u(-)	B_{1u}(IR)	B_{2u}(IR)	B_{3u}(IR)
$(VO_3)_n^{n-}$								
internal	6	7	4	3	3	4	7	6
$(T+T_A)$	1	0	1	1	0	1	1	1
R_z	0	1	0	1	0	0	0	0
$K^+(T+T_A)$	2	2	1	1	1	1	2	2
Total	9	10	6	5	5	6	10	9

Table IV.6 Assignment of vibrations in KVO_3

Raman	IR	Park et. al. [92]		Adams et. al. [91]
948 vw	965 s.sp	A_g	$\nu_s(VO)_2$	↑
936 vs	914 vs	A_g		ν(V = O) and
906 w	894 vs.sp	B_{2g}	$\nu_{as}(VO_2)$	ν(VOV)
	860 b	B_{2g}		↓
647 w	674 b	B_{2g}	ν_{as}(VOV)	↑
497 w	499 m	A_g	ν_s(VOV)	
	457 vw.sp	A_g		$\delta(VO_2)$
	433 vw	B_{1g}	δ(VOV)	↓
358 vw		B_{1g}		
	349 w	B_{1g}		↑
326 vw		B_{1g}		VO_2
	311 s	B_{1g}		ρ_r, ρ_t, ρ_w
242 w	254 vw	B_{3g}	$\nu_L(VO_3^-)$ chain	and
211 w		A_g	δ(VOV)	chain deformation
	170 s	A_g		↓
	161 s	A_g	$\nu_T(K^+)$	↕
	122 m	A_g/B_{1g}		↓
95 vw		A_g	$\nu_T(VO_3^-)$	Lattice modes
74 vw		B_{1g}/B_{2g}		↓

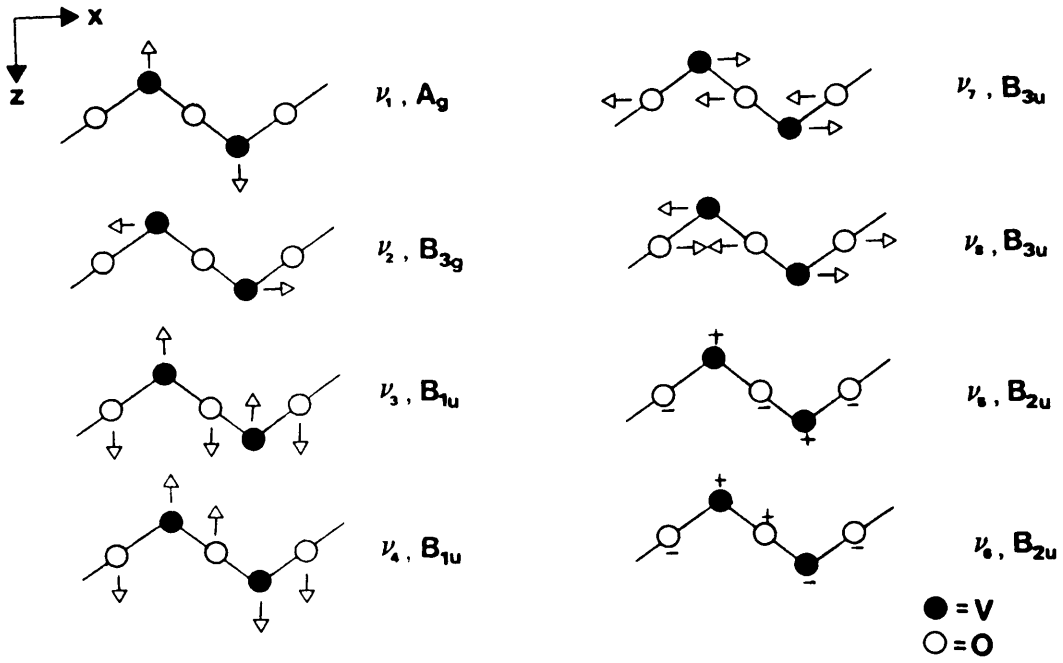

Figure IV.4 Approximate forms of the six in-plane and two out-of-plane modes of the simplified $D_{2h}[V_2O_2]$ chain backbone [91]

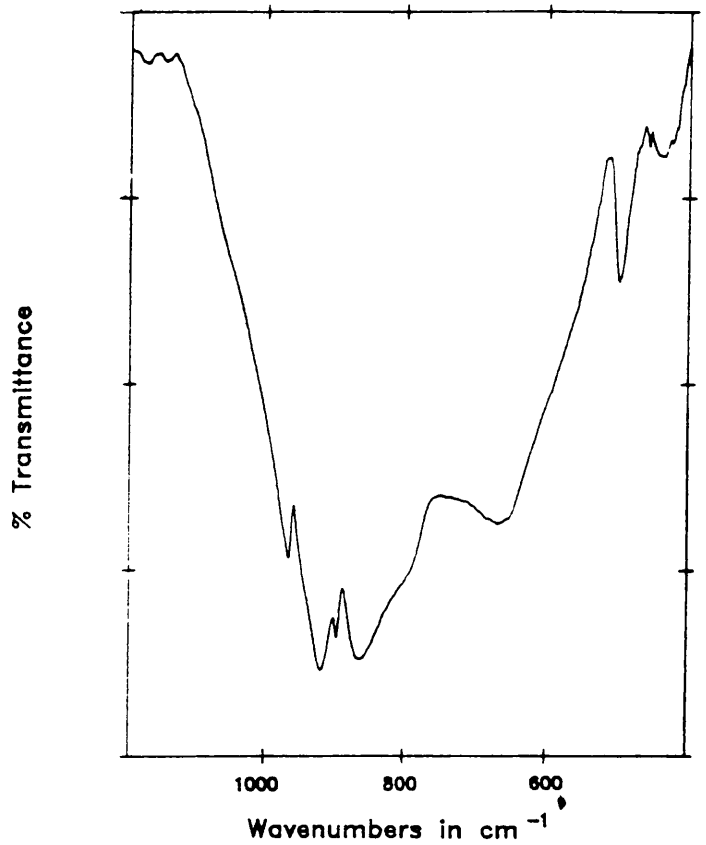

Figure IV.5 Mid-infrared spectrum of KVO_3 at room temperature

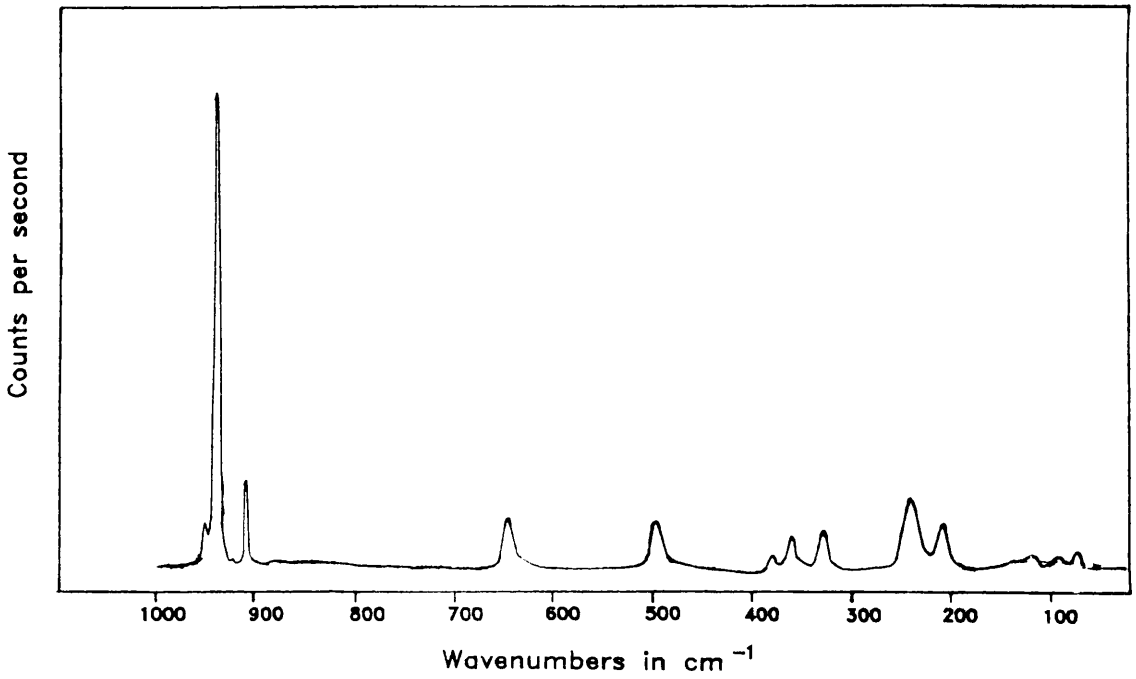

Figure IV.6 Raman spectrum of KVO_3 at ambient conditions

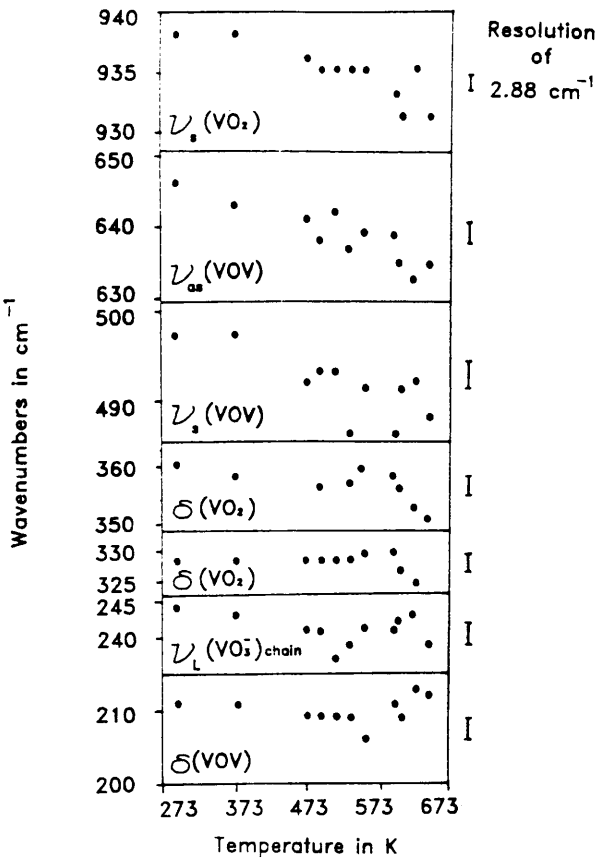

Figure IV.7 Temperature dependence of some Raman active KVO_3 modes

IV.5.2 **Crystal structures**

The structure of the solid solutions [76] are based on XO_4 (X = V, P) tetrahedra sharing two vertices to form a chain along the c-axis. Chains form parallel layers separated by one half of the a-axis providing two types of metal cation sites between them. M1 is the smaller, approximately octahedral site and M2 the larger, more irregular site. In α-$NaVO_3$ and $Na(V_{0.66}P_{0.34})O_3$ both sites are occupied by Na^+ while K^+ preferentially occupies the larger M2 sites in $(Na_{0.88}K_{0.12})VO_3$ with Na^+ in M1 and the rest of the M2 sites. These three compounds have the modified diopside structure (Figure IV.8A), $(Na_{0.5}K_{0.5})VO_3$, however, adopts the true diopside structure with Na^+ in M1 and K^+ in M2 sites (Figure IV.8B).

The M2 site in $(Na_{0.5}K_{0.5})VO_3$ can be considered to be eight fold coordinated as the <M2-O> distance over the six nearest neighbours has increased to 2.780Å while the M2-to-bridging-oxygen, O3(6) distance decreased to 2.946Å. This difference in coordination is illustrated in Figure IV.8A and B. The placing of a larger cation in M2 has the effect of an increase in the size of the site. This is indicated by an increase of the <M2-O> distance from 2.513Å in α-$NaVO_3$ to 2.780Å in $(Na_{0.5}K_{0.5})VO_3$ while there is only a slight increase in the <M1-O> distance in the same series (Table IV.7).

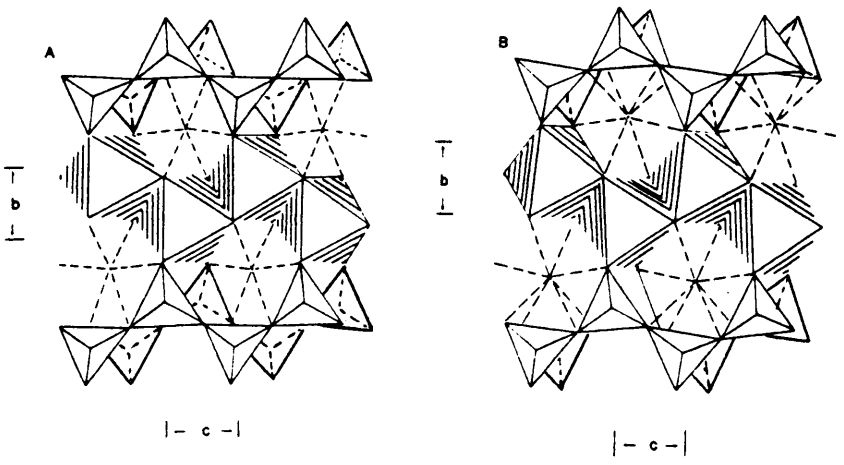

Figure IV.8 Structures of monoclinic pyroxenes: A: α-$NaVO_3$, $Na(V_{0.66}P_{0.34})O_3$ and $(Na_{0.88}K_{0.12})VO_3$, and B: $(Na_{0.5}K_{0.5})VO_3$ [76]

Table IV.7 Structural parameters in the alkali metal metavanadates [76]

	$Na(V_{0.66}P_{0.34})O_3$	α-$NaVO_3$	$(Na_{0.88}K_{0.12})VO_3$	$(Na_{0.5}K_{0.5})VO_3$	KVO_3	NH_4VO_3
Spacegroup	C2/c	C2/c	C2/c	C2/c	Pbcm	Pbcm
a (in Å)	10.421	10.552	10.553	10.553	5.176	4.909
b	9.475	9.468	9.580	9.997	10.794	11.780
c	5.715	5.879	5.850	5.804	5.680	5.830
Z	8	8	8	8	4	4
β (deg)	107.62	108.47	107.65	104.17	-	-
ϕ (deg)	6.6	5.5	8.1	12.0		
δ-ϵ (deg)	3.1	2.6	3.9	5.9		
Δ	1.324	1.435	1.238	0.625		
<M1 - O>	2.349	2.364	2.371	2.398	2.73	
<M2 - O>	2.507	2.513	2.572	2.780	3.5	
<X - O>	1.681	1.723	1.717	1.722		
Chain-config.	0	0	0	0	E	E

In NH_4VO_3 M1≡N and M2≡H

The VO_4 tetrahedron maintains a constant dimension across the series, and the $\langle V\text{-}O\rangle_{bridge}$ distance varies very little among the metavanadates, suggesting that $(VO_3)_\infty$ chains are even more rigid than $(SiO_3)_\infty$ chains. Two simultaneous movements of the rigid chain, namely rotation of tetrahedra and back-to-back displacement in the c-direction result from the expansion of the M2 site to accommodate a larger cation [76].

The following three configurations of chains in the pyroxenes have been defined [76, 77].

(1) Extended/E-chain

Chain angle O3-O3(4)-O3' = 180^o ϵ : The angle between the O1-O1(4) edge of

δ-ϵ = 0^o the octahedron M1 and unit vector u parallel to the c-axis.

δ : Angle between the O1-O3(4) edge at the tetrahedron and $\vec{u}$.

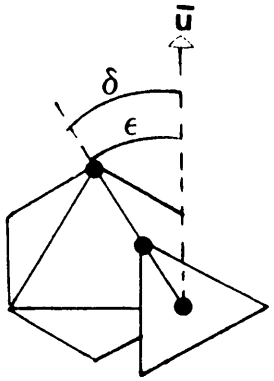

E

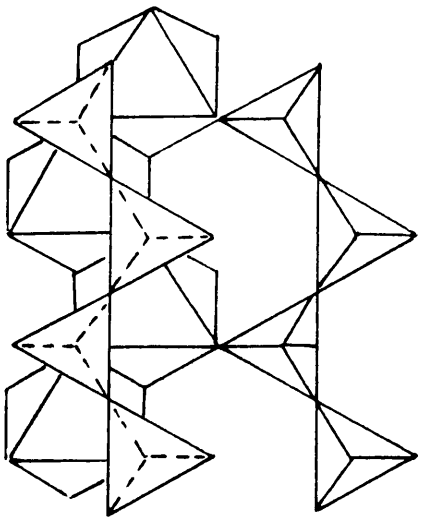

Each tetrahedron can be rotated about an axis normal to the layers and passing through O1 (apical O) which links the tetrahedron to two M1 octahedra. If the triangular face normal to the axis is oriented similarly to the nearest parallel faces of the two octahedra sharing this oxygen, the chain can be described as a:

(2) S-rotated chain $\delta - \epsilon = 30^{o}$ (ideal)

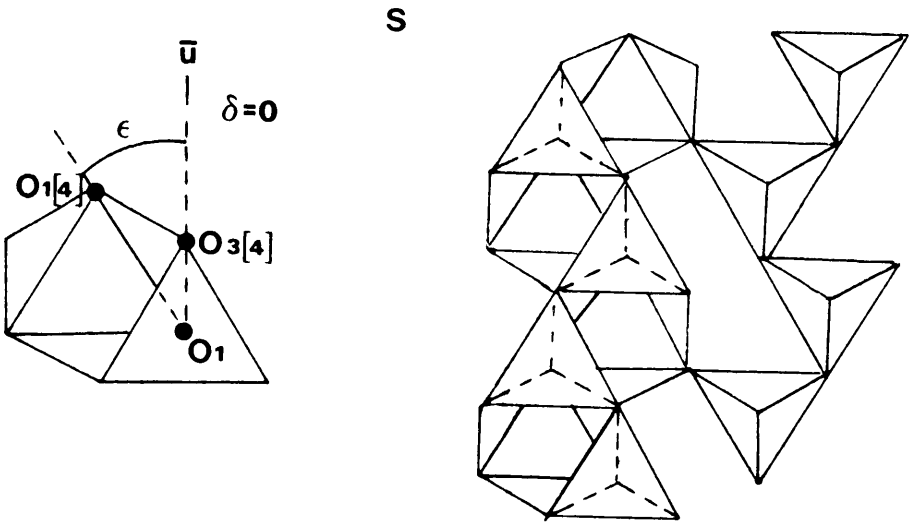

Rotation in the opposite direction results in oppositely oriented forces.

(3) O-rotated chain $\delta - \epsilon = -30^{o}$ (ideal)

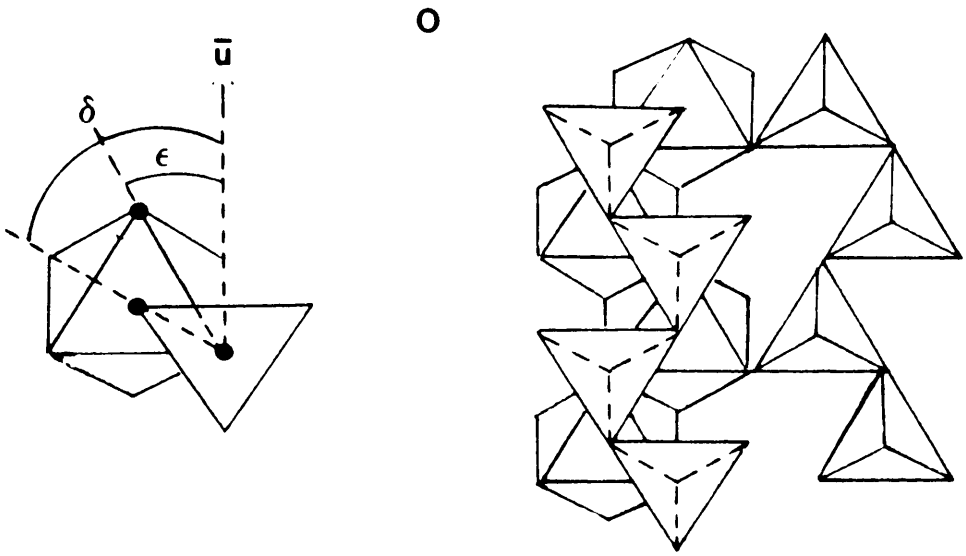

Real values of δ-ϵ lie between 30^{o} and -30^{o} and together with $\phi = [180^{o} - \langle O(3)\text{-}O_3(4)\text{-}O(3)]$ this measures the tetrahedral chain rotation.

The monoclinic pyroxenes have O-rotated chains and the orthorhombic pyroxenes E-rotated chains. Idler et. al. [76] correlated <M2-O> and (δ-ϵ) values, concluding that an increase in size of the M2 cation leads to an increased amount of O-rotation. This results in an increase in the b-axis and a decrease in the c-axis.

Rotation of the chain only would lead to a structural misfit, so that a concomitant "back-to-back" displacement of the chain becomes necessary [76]. Parameters measuring chain displacement are δ and β. Changes in these parameters suggest that a decreasing <X-O> has the same effect on the structure as an increasing <M2-O>.

IV.5.3 Infrared and Raman spectra

In addition to the vibrations expected for α-$NaVO_3$, $13A_g(IR) + 14B_g(IR, R) + 13A_u(IR) + 14B_u(IR)$ (Table IV.2), six translation modes, $A_2 + 2B_g + A_u + 2B_u$, are predicted for K^+ in $(Na_{0.55}K_{0.12})VO_3$ and $(Na_{0.5}K_{0.5})VO_3$ under space group C2/c. All six modes are active in the infrared and only three of these Raman active. It is not expected that crystal effects will result in the same number of modes for XO_3^- (X = V,P) in $Na(V_{0.66}P_{0.34})O_3$ as for VO_3^- chains in $NaVO_3$ as only one third of vanadium atoms are replaced with phosphorus atoms with no evidence of any ordering between V and P.

IV.5.3.1 $Na(V_{0.66}P_{0.34})O_3$

Raman, mid- and far-infrared spectra of α-$NaVO_3$, $Na(V_{0.66}P_{0.34})O_3$ and $NaPO_3$ are compared in Figures IV.9-IV.11. From these it is evident that phosphorus substitution had taken place, forming a new compound which is different from both α-$NaVO_3$ and $NaPO_3$.

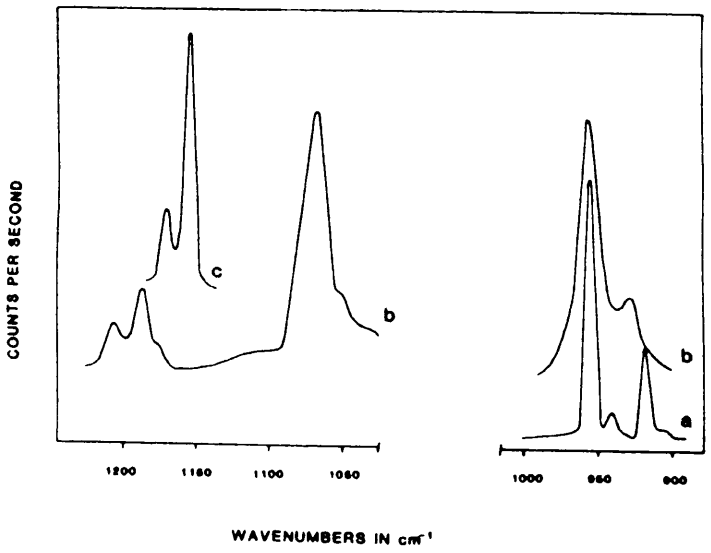

Figure IV.9 Raman spectra of $Na(V_{0.66}P_{0.34})O_3$ (b) compared to that of α-$NaVO_3$(a) and $NaPO_3$ (c) between 900 and 1200 cm^{-1}

Only two VO_2 terminal stretching vibrations are observed in the Raman spectrum of $Na(P_{0.66}V_{0.34})O_3$ at 956 and 929 cm^{-1} compared to four modes in $NaVO_3$ at 956, 941, 919 and 907 cm^{-1} (Figure IV.9). P–O stretching vibrations have shifted considerably from 1172 and 1156 cm^{-1} in $NaPO_3$ to 1196 ($\nu(PO_3^-)_{as}$) and 1078 cm^{-1} ($\nu(PO_3^-)_s$) in the solid solution. In the infrared these modes occur at 1209 and 1075 cm^{-1} (Figure IV.10). Vibrations attributed to bridging phosphorus-oxygen bonds appear as shoulders at 753 and 721 cm^{-1}. <X-O> bond lengths (X = V,P) are shortened from 1.723 to 1.681Å upon substitution of V with P [76] resulting in a 6 to 28 cm^{-1} red shift of infrared active terminal V-O stretching modes from $NaVO_3$ to $Na(V_{0.66}P_{0.34})O_3$.

The far-infrared (Figure IV.11) include four $\delta(PO_3)$ modes between 470 and 370 cm^{-1} in the phosphorus substituted sodium metavanadate which are comparable with their positions in $NaPO_3$ (Table IV.8)). One of each of the ν(VOV) and $\delta(VO_2)$ bands remain visible (at 480 and 374 cm^{-1} respectively) only as shoulders of $\delta(PO_3^-)$ bands. The librational mode of the VO_3^- chain at 263 cm^{-1} in $NaVO_3$ moves down to 254 cm^{-1} in $Na(V_{0.66}P_{0.34})O_3$.

Table IV.8 Comparison of vibrational modes of $NaVO_3$, $Na(V_{0.66}P_{0.34})O_3$ and $NaPO_3$

$NaVO_3$			$Na(V_{0.66}P_{0.34})O_3$		$NaPO_3$		
Assignment	IR	Raman	IR	Raman	IR	Raman	Assignment
			1209 s.sp	1196 w	1296	1172 m	$\nu_{as}(PO_3^-)$
			-	-	1162	1156 s	
			1075 s	1078 m	1100	-	$\nu_s(PO_3^-)$
			-	-	1059	-	
$\nu_s(VO_2)$	961 s.sp	956 vs	963 vs	956 b	984	-	
	941 s	941 w	929 vs	929 w.sh	-	-	
$\nu_{as}(VO_2)$	911 s.sp	919 s	883 vs	-	872		$\nu_{as}(OPO)$
	836 s.b.	907 vw	830 vs	-	-	-	
	-	-	753 sh	-	778	745 vw	$\nu_s(OPO)$
	-	-	721 sh	-	718	698 m	$\delta(PO_3^-)$
$\nu_{as}(VOV)$	-	636 m	615 m	657 vw.b	-	-	
Comb.	-	-	536 w	545 w	601	-	
	-	-	-	-	543	-	
	-	-	-	-	517	525 vw	
$\nu_s(VOV)$	480 sh	507 m	480 sh	511 w	-	-	
	445 vw	-	466 w	-	462	-	
	-	-	428 w	-	425	-	
$\delta(VO_2)$	374 w	378 w	390 w	-	386	387 w	
	333 m	358/343 w	337 w	350 w	338		
$\nu_L(VO_3^-)$	263 m	254 w	254 m	-			
$\delta(VOV)$	238 m	243 m	241 m	244 w			
	217 vw	219 m	217 vw.sh	-			
	194 b	-	194 w	-			
	175 w	-	170 m	-			
$\nu_T(Na^+)$	147 m	143 w	146 m	-			
	135 m	-	-	-			
$\nu_T(VO_3^-)$	99 m	-	99 w	-			
	85 m	87 w	88 w	90 vw			
	70 w	-	70 w	-			
	65 w	60 vw	56 w	62 vw			
			45 m				

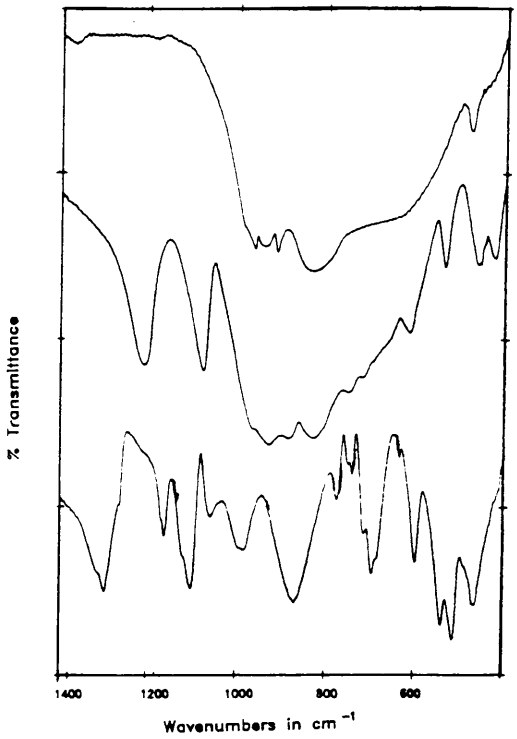

Figure IV.10 Mid-infrared spectra of α-$NaVO_3$ (top), $Na(V_{0.66}P_{0.34})O_3$ (middle) and $NaPO_3$ (bottom)

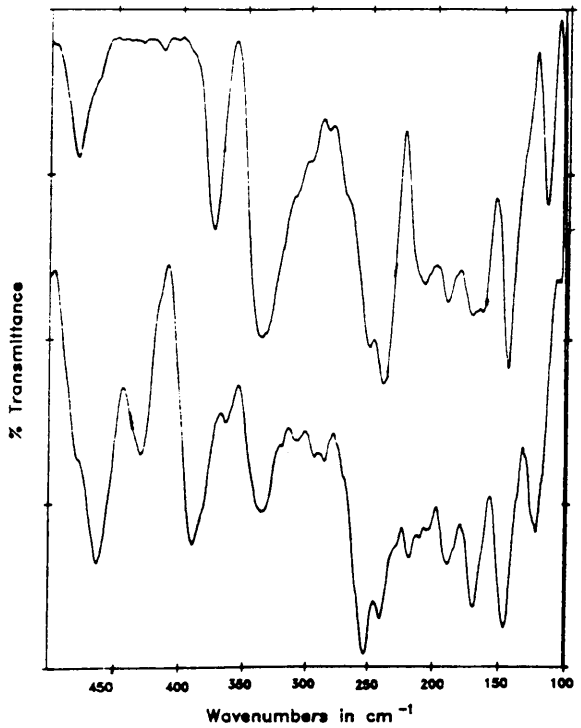

Figure IV.11 Far-infrared spectra of α-$NaVO_3$ (top) and $Na(V_{0.66}P_{0.34})O_3$

IV.5.3.2 $(Na_{0.88}K_{0.12})VO_3$ and $(Na_{0.5}K_{0.5})VO_3$

Raman spectra of α-$NaVO_3$ and $(Na_{0.5}K_{0.5})VO_3$ are compared in Figure IV.12. The spectra are in some respects very similar but closer scrutiny shows that significant frequency shifts occur. In the 800-1000 cm^{-1} region four bands representing symmetrical and asymmetrical terminal V-O stretching vibrations show a significant variation in relative intensities. The $\delta(VO_2)$ band of $NaVO_3$ at 378 cm^{-1} is not observed in the spectrum of $(Na_{0.5}K_{0.5})VO_3$ while δ(VOV) at 219 cm^{-1} ($NaVO_3$) becomes a weak band at 209 cm^{-1} in $(Na_{0.5}K_{0.5})VO_3$. Raman active translation modes of the metavanadate chain at 87 and 60 cm^{-1} in α-$NaVO_3$ move down to 84 and 45 cm^{-1} in the solid solution. The changes in frequency of VOV stretching modes with Na/K composition are shown in Figure IV.13 with $(Na_{0.5}K_{0.5})VO_3$ showing the VOV vibrations influenced by both the sodium and potassium cations (Table IV.9).

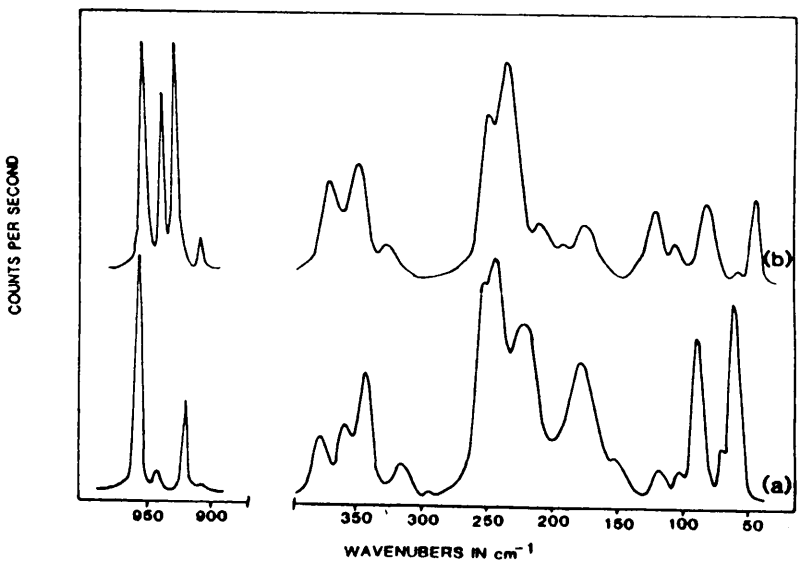

Figure IV.12 Raman spectra of (a) α-$NaVO_3$ and (b) $(Na_{0.5}K_{0.5})VO_3$

Infrared bands of terminal and bridging V-O bonds in the $(Na,K)(V, P)O_3$ system are shown in Figures IV.14 and IV.15 with assignments in Table IV.10. Mid-infrared spectra of the solid solutions resemble those of pure $NaVO_3$ while the spectra of the 505 K^+ substituted compound have more similarities with that of KVO_3. <V-O> bond lengths change slightly with composition but show no specific trend [76] (Table IV.7). This is also reflected by the changes in wavenumbers of V-O stretching modes, Figures IV.14 and IV.18.

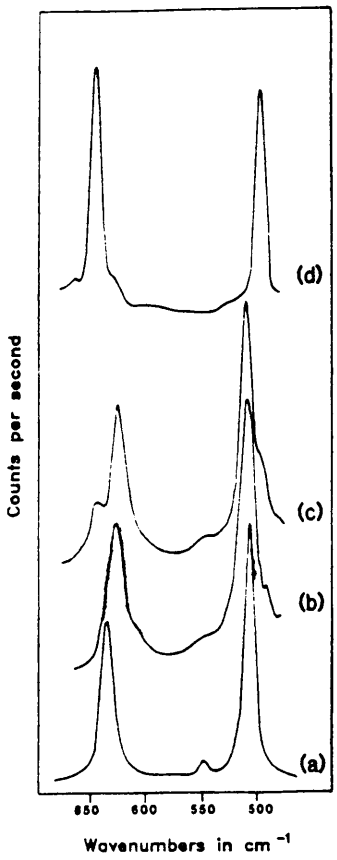

Figure IV.13 Comparison between VOV stretching vibrations in (a) α-$NaVO_3$, (b) $(Na_{0.88}K_{0.12})VO_3$, (c) $(Na_{0.5}K_{0.5})VO_3$ and (d) KVO_3

Table IV.9 Comparison of Raman active modes in the alkali metal metavanadates

α-$NaVO_3$	$(Na_{0.88}K_{0.12})VO_3$	$(Na_{0.5}K_{0.5})VO_3$	KVO_3	Assigment
956 vs	953 vs	953 vs	948 vw	$\nu_s(VO_2)$
941 s		938 m	936 vs	
919 s	926 s	928 s		$\nu_{as}(VO_2)$
907 vw		908 w	906 w	
636 m	627 m	647/626 m	647 w	$\nu_{as}(VOV)$
550 vw	547 w			Combination
507 m	510 m	511 m	497 w	$\nu_s(VOV)$
378 w	369 w	360 vw	358 vw	$\delta(VO_2)$
358 w	348 vw	348 vw	326 vw	
343 w				
254 m	252 w	251 w	242 w	$\nu_L(VO_3^-)$
243 m		237 w		$\delta(VOV)$
219 m		209 vw.w	211 w	
177 w				
	163 m	163 m-s	161 s	$\nu_T(K^+)$
	138 w	143 w	-	$\nu_T(Na^+)$
	119 s	119 m	122 m	$\nu_T(K^+)$
87 w	87 vw	84 vw	95 vw	$\nu_T(VO_3^-)$
60 w		45 vw		

Table IV.10 Comparison of infrared active modes in some alkali metal metavanadates

α-$NaVO_3$	$(Na_{0.88}K_{0.12})VO_3$	$(Na_{0.5}K_{0.5})VO_3$	KVO_3	Assigment
961 s.sp	958 s	963 sh	965 s.sp	$\nu_s(VO_2)$
941 s	940 s	922 vs.sp	916 vs	
911 s.sp	910 s.sp	910 vs		$\nu_{as}(VO_2)$
		894 sh	894 vs.sp	
836 s.b	831 vs.b	835 s.sh	800 b	
	688 b	661 m.b	674 b	$\nu_{as}(VOV)$
480 w.sh	486 vw		499 m	$\nu_s(VOV)$
			457 vw.sp	
445 vw	443 w		433 w	$\delta(VO_2)$
			413 vw	
374 w	378 w	380 w	385 m	
			349 w	
333 m	325 m	326 m	311/300 s	
263 m	247 m	248 w	254 vw	$\nu_L(VO_3^-)_{chain}$
238 m	229 m	228 w		$\delta(VOV)$
217 vw	209 m	209 m		
194 b	192 m	192 m		
175 w	170 m		170 s	
	163 m	163 m-s	161 s	$\nu_T(K^+)$
147 m		143 m		$\nu_T(Na^+)$
135 m	138 s			
	119 s	119 m	122 m	$\nu_T(K^+)$
99 m	99 w	95 w		$\nu_T(VO_3^-)$
85 m				
70 w	74 w	68 m	65 sh	
65 w	57 m	58 m	60 m	
			45 w	

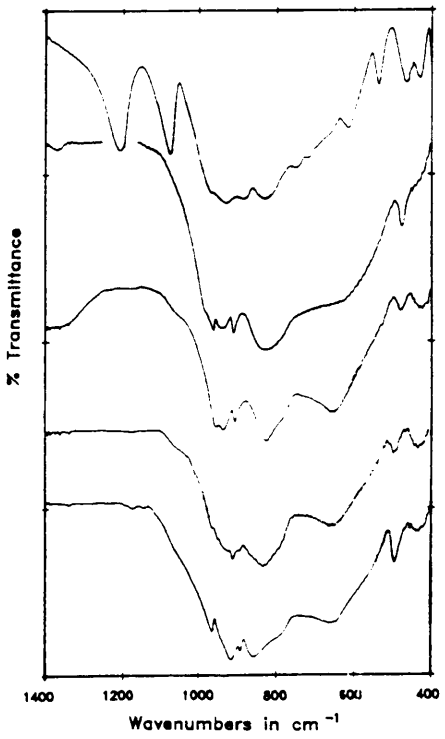

Figure IV.14 Mid-infrared spectra of $Na(V_{0.66}P_{0.34})O_3$, α-$NaVO_3$, $Na(V_{0.88}K_{0.12})VO_3$, $Na(V_{0.5}K_{0.5})VO_3$ and KVO_3 (from top to bottom)

Differences in the far-infrared spectra (Figures IV.15a and b) consist of shifts in vibrational, librational and translational modes of the VO_3^- chain. The frequency changes in the two terminal bending modes, $\delta(VO_2)$, at 374 and 339 cm^{-1} in α-$NaVO_3$ are respectively towards higher and lower wavenumbers with the latter forming a shoulder in $(Na_{0.5}K_{0.5})VO_3$ which develops into a band at 300 cm^{-1} in KVO_3. An additional band for this compound at 349 cm^{-1}

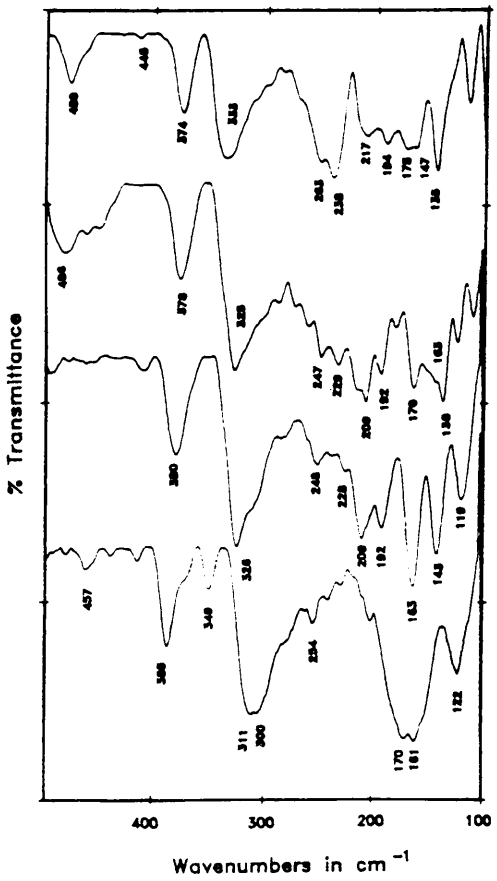

Fig.IV.15

Far-infrared spectra of α-$NaVO_3$, $(Na_{0.88}K_{0.12})VO_3$, $(Na_{0.5}K_{0.5})VO_3$ and KVO_3 (from top to bottom) beween:

(a) 100 and 500 cm^{-1}

(b) 35 and 120 cm^{-1}

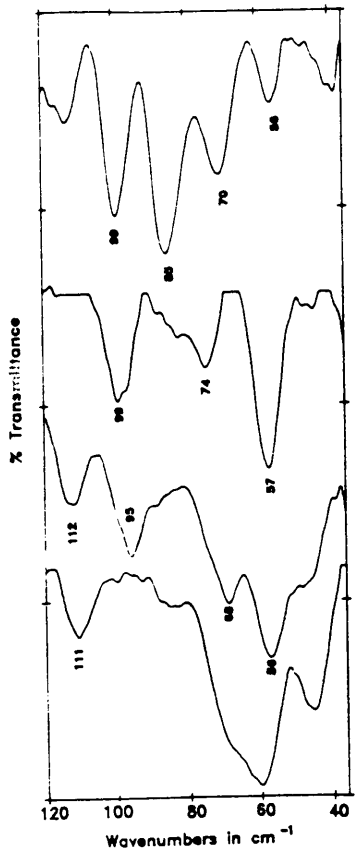

is also attributed to $\delta(VO_2)$. The translation modes for Na^+ appear at 147 and 135 cm^{-1} (Figure IV.15 (a)) with the K^+ translation modes at 119 and 163 cm^{-1}. However, not all three of the predicted translational modes have been observed and the observed Na^+ and K^+ translational modes do not necessarily correlate with one another. The intensity of the 163 cm^{-1} band reflects the amount of K^+ present in the various $(Na_xK_{1-x})VO_3$ compounds (Table IV.10).

The variation of infrared active modes with composition in the $(Na_xK_{1-x})VO_3$ system is shown in Figures IV.16-IV.18 and Raman active modes in Figure IV.19. The effect of the larger cation in the alkali metal metavanadate lattice can be compared to an increase in pressure on the structure. The pressure dependence of some Raman active V-O modes in NH_4VO_3 [10] and $RbVO_3$ [91] have been reported and can be compared to the variation in infrared active V-O modes in the $(Na_xK_{1-x})VO_3$ (x = 1.0; 0.88; 0.5; 0) series. Two each of the symmetrical and asymmetrical stretching V-O vibrations in the series are shown in Figure IV.16. One $\nu_s(VO_2)$ and one $\nu_{as}(VO_2)$ vibration move towards higher wavenumbers with the remaining bands shifting to lower

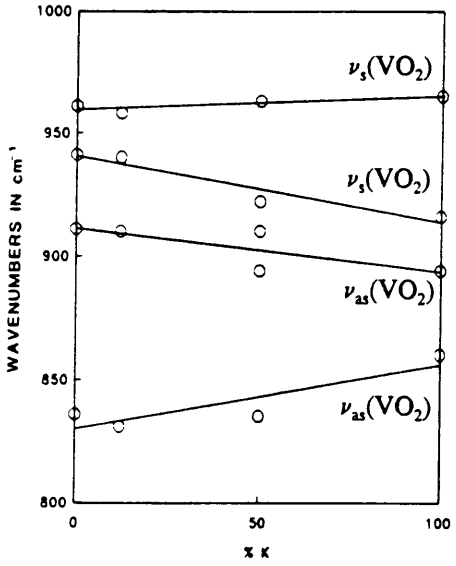

Figure IV.16 Variation of infrared active $\nu_s(VO_2)$ and $\nu_{as}(VO_2)$ modes (2 each) with composition in the $(Na_xK_{1-x})VO_3$ system

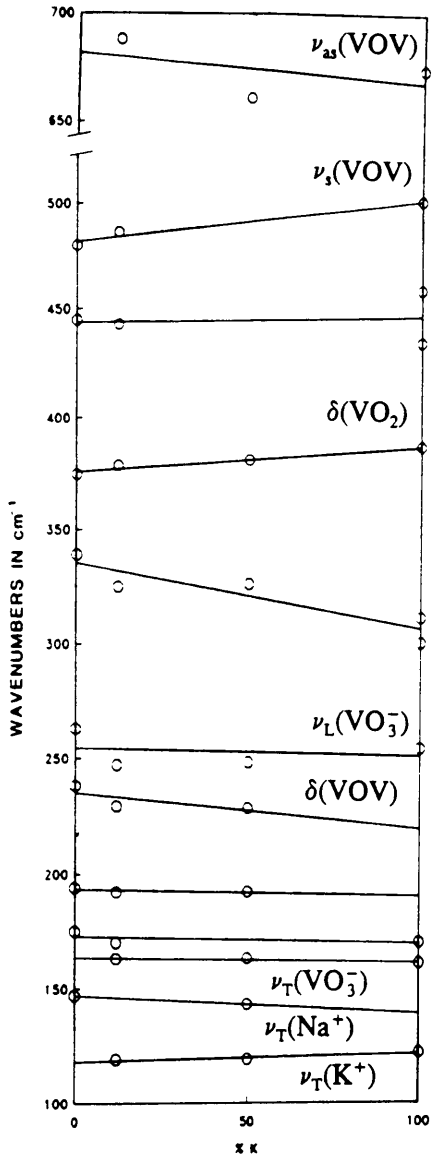

Figure VI.17 Variation of the following infrared active modes with composition (from top to bottom): ν_{as}(VOV), ν_s(VOV), $\delta(VO_2)$ (3 modes), $\nu_L(VO_3^-)$, δ(VOV) (3 modes), $\nu_T(VO_3^-)$, $\nu_T(K^+)$ and $\nu_T(Na^+)$

wavenumbers. Results indicate that the terminal stretching vibrations in both the ammonium [10] and rubidium [91] metavanadates exhibit behaviour similar to those of the former two stretching modes in the solid solutions, that is a blue shift upon an increase in pressure. Figure IV.17 shows the variation of some internal and external modes with potassium content. In ammonium metavanadate the V-O bridging stretching and bending modes were reported to be more pressure sensitive than the other modes, especially one

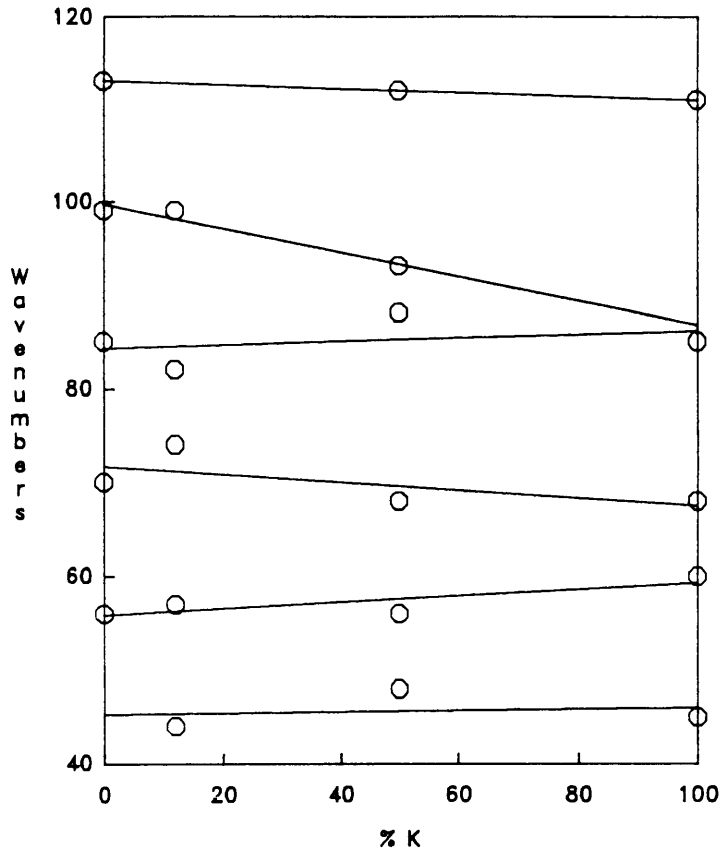

Figure VI.18 Behaviour of translation modes of the VO_3^- chain in the infrared upon cation substitution

particular asymmetric V-O-V stretching mode at 646 cm^{-1} [91]. The corresponding vibration of the solid solutions in Figure IV.17 shows a trend towards lower wavenumbers. Results for the symmetric V-O-V stretching vibration compare well to high pressure behaviour of similar modes in NH_4VO_3 [10] and $RbVO_3$ [91]. Two of the three infrared active terminal V-O bending vibrations of the series also show similar trends to the Raman active modes in $RbVO_3$. The discrepancies between the high pressure results and those of the solid solutions show that the introduction of the K^+-ion into the lattice of $NaVO_3$ does not only involve a pressure effect but that bonding and crystallographic factors such as the displacement of atoms also have a significant influence on the vibrational spectra of these compounds.

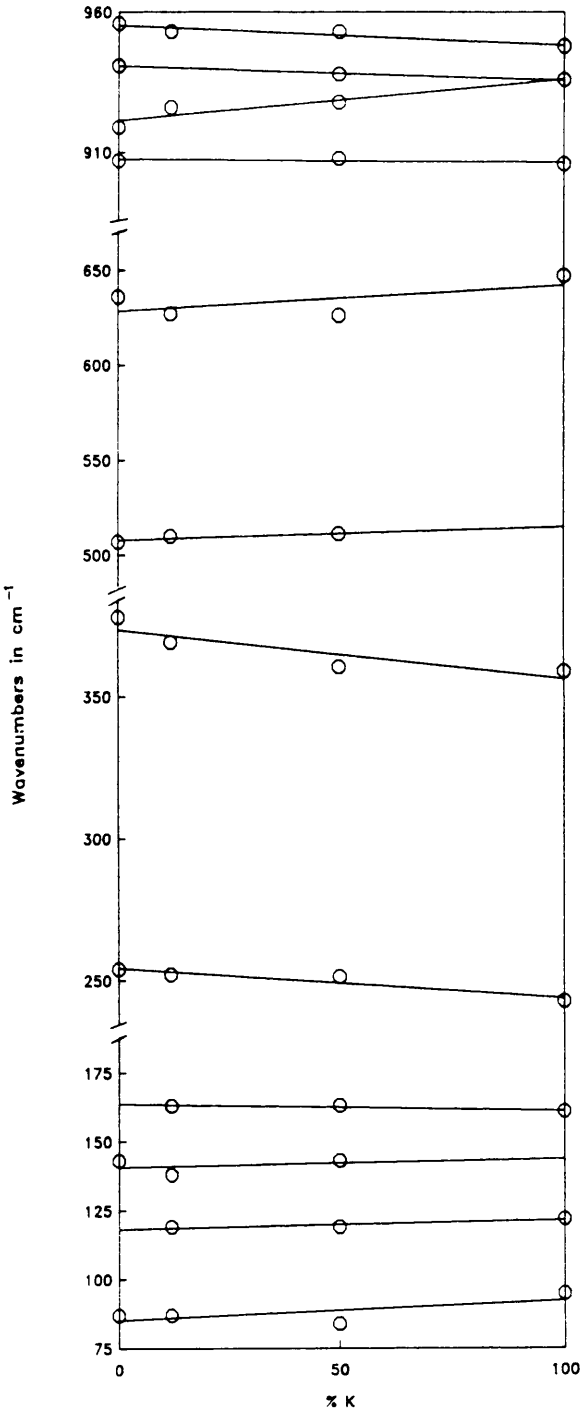

Figure IV.19 Variation of the following Raman active modes with composition (from top to bottom): $\nu_{as}(VO_2)$ (2 modes), $\nu_{as}(VO_2)$, $\nu_{as}(VOV)$, $\nu_{s}(VOV)$, $\delta(VO_2)$, $\nu_{L}(VO_3^-)$, $\nu_{T}(K^+)$, $\nu_{T}(Na^+)$, $\nu_{T}(K^+)$ and $\nu_{T}(\tilde{Na}^+)$

The VO_3^- librational modes which could be identified (Figure IV.15(b)) show a red shift with increasing K^+ content, reflecting the effect of a larger cation in the larger M2-site on rotation and displacement of the rigid $(VO_3)_\infty$ chains. An increase in the size of the M2 cation leads to an increase in <M2-O> with the structure responding to accommodate this change by decreasing the amount of tetrahedral chain displacement in the [001] direction, and thus a smaller β angle. This brings two additional bridging atoms from the chains into the primary coordination sphere of the M2 polyhedron [76].

Only slight changes are observed for the translation modes of the two cations (Figure IV.15(b)) and the (VO_3^-) chain (Figure IV.16) with cation substitution.

IV.6 CONCLUSIONS

1. Infrared spectra, particularly in the far-infrared region provide a clear distinction between the two phases, α- and β-$NaVO_3$. In addition to frequency shifts the broad absorption bands for β-$NaVO_3$ are in contrast with the well-defined bands observed for the α-phase.

2. The reported [82] phase transition in KVO_3 involving variations of the dielectric properties is not clearly reflected in the Raman spectra or X-ray powder diffraction patterns of the compound recorded at various temperatures around 593 K. The temperature dependence of many Raman active modes does, however, reveal anomalies around the phase transition temperature.

3. The substitution of $\frac{1}{3}$ of vanadium atoms with phosphorus in $NaVO_3$, obtaining $Na(V_{0.66}P_{0.34})O_3$, influences the vibrational spectra in such a way that the four terminal VO_2 stretching modes in the Raman spectrum of $NaVO_3$ are reduced to two for the solid solution. Two new modes representing terminal PO_2 stretches appear in both the infrared and Raman spectra.

4. Frequency shifts in the infrared and Raman spectra reflect the rotation and displacement in the metavanadate chains upon cation substitution in $(Na_xK_{1-x})VO_3$ where x = 1, 0.85, 0.50 and 0.

5. By comparing the spectra of $NaVO_3$ and KVO_3 with those of the $(Na_xK_{1-x})VO_3$ system, the translational modes of the cations could be clearly identified and the translational mode of K^+ at 163 cm^{-1} can be used to determine the concentration of this cation in the solid solution.

CHAPTER V

AN INVESTIGATION OF THE HIGH TEMPERATURE REACTION OF ALKALI METAL METAVANADATES WITH RARE EARTH OXIDES

V.1 INTRODUCTION

As was mentioned in [IV.4.3] it has been reported that the MVO_3 (M = Li, Na, K) compounds undergo phase transitions upon heating, showing variations in their dielectric properties [82, 83]. The Raman spectra of KVO_3 and $NaVO_3$, were shown in [IV.3] and [IV.4] including spectra of both the α- and β-phase of $NaVO_3$. An irreversible phase transition from α- to β-$NaVO_3$, occurs between 643 and 673 K [89]. Temperature dependence studies of Raman active modes and X-ray powder diffraction patterns of KVO_3 gave no clear indication of the occurrence of the reported phase transition which gives rise to variations of its dielectric properties around 593 K [IV.4.3].

The influence of Nd_2O_3 doping on the ferroelectric phase transitions in KVO_3 and $LiVO_3$ has been reported by Patil et.al. [82] in their study of the dielectric properties of these compounds. The dielectric constant was found to increase with dopant concentration up to 0.5 mol% Nd_2O_3 with a decrease at higher percentages, and a lowering in the Curie temperature with more Nd_2O_3 for all samples. As it is unlikely that the monovalent potassium ion will be replaced by the trivalent lanthanide ion in the metavanadate the

determination of the cause of the observed effects became of interest. In the present work low percentages of Ln_2O_3 [Ln = Er, Nd] were heated with MVO_3 [M = K, Na] after which the stoichiometric amounts of $NaVO_3$ with Er_2O_3 were reacted both in air and under vacuum. The influence of low percentages of the lanthanide oxides on the alkali metal metavanadates was investigated by Raman and infrared spectroscopy, X-ray powder diffraction and scanning electron microscopy with EDX-analysis.

V.2 EXPERIMENTAL

Samples were prepared according to the method described by Patil et.al. [82]. KVO_3 was obtained from stoichiometric amounts of the dried alkali metal carbonate and vanadium pentoxide: $K_2CO_3 + V_2O_5 \xrightarrow{\Delta} 2\ KVO_3 + CO_2\uparrow$. The mixture was heated at 1223 K in a platinum crucible for 5 hours. The $NaVO_3$, obtained from Fluka Chemie, was of analytical grade. For 'doped' samples the appropriate mol% of the lanthanide oxide (lanthanide = Er, Nd) was added to the alkali metal metavanadate and mixed twice, first dry and then with methanol using a pestle and mortar. The mixture was then heated to 1223 K for 5 hours. For the stoichiometric reaction the alkali metal metavanadate and the lanthanide oxide were heated together under two different conditions:

(1) At 1223 K for 106 hours in air, and
(2) At 923 K for 48 hours under vacuum.

Raman spectra were recorded using the 514.5 nm line for excitation of all samples. Additionally the 488 nm line was used for samples containing Er^{3+} to avoid the influence of emission lines in the recorded region.

V.3 RESULTS

V.3.1 X-Ray powder diffraction

The results of X-ray powder diffraction patterns of KVO_3 and the product of the high temperature reaction of KVO_3 and 5 mol% Er_2O_3 are shown in Table V.1 in comparison with that of $ErVO_4$. This indicates the formation of (1) pure KVO_3 from K_2CO_3 and V_2O_5, and (2) of the lanthanide orthovanadate in the alkali metal metavanadate after high temperature treatment with Er_2O_3. Relative intensities of the three most intense lines in the Guinier pattern of the orthovanadate agree with redundant ones in the two-phased product.

V.3.2 Raman spectra

The effect of the high temperature reaction between KVO_3 and 5 mol% Er_2O_3 on the Raman spectrum of the metavanadate is shown in Figure V.1. Three bands additional to those in KVO_3 appear between 800 and 900 cm^{-1} for the reaction product. The formation of $ErVO_4$ is confirmed by these bands at 817, 836 and 891 cm^{-1} which coincide with the one ν_1 and two ν_3 vibrations of the orthovanadate in $ErVO_4$. Similar results were found for the reaction of $NaVO_3$ with Nd_2O_3. The Raman spectra of $NaVO_3$ (the high temperature phase) and the products of the high temperature reaction of the metavanadate with

Table V.1 Results of X-ray powder diffraction patterns

KVO_3 (from K_2CO_3 + V_2O_5)				Product of KVO_3/Er_2O_3	$ErVO_4$		
hkl	I/I_1 (JCPDS)	d(JCPDS	d(obs)	d(obs)	d(JCPDS)	I/I_1	hkl
020	9	5.397	5.4155				
001	18	5.181	5.1874				
120	16	3.917	3.9236				
021	18	3.737	3.7417				
111	6	3.612	3.6142				
				3.5460[1]	3.549	100[1]	200
121	100	3.125	3.1278	3.1260			
200	45	2.847	2.8515	2.8449			
				2.6579[2]	2.660	70[2]	112
131	15	2.623	2.6237	2.6217			
002	18	2.590	2.5900	2.5899			
220	2	2.5185	2.5189				
				2.5078	2.510	22	220
140	18	2.4391	2.4405	2.4366			
041	7	2.3946	2.3951	2.3920			
112	10	2.3031	2.3053	2.3009			
				2.2128	2.2134	18	301
032	4	2.1018	2.1027				
231	3	2.0505	2.0507	2.0487			
051	3	1.9932	1.9945				
240	15	1.9594	1.9595	1.9581			
202	5	1.9164	1.9163	1.9149			
				1.8256[3]	1.8250	60[3]	312
142	6	1.7753	1.7761	1.7739			
				1.7739	1.7746	18	400
				1.5888	1.5868	12	420

JCPDS = Joint committee on powder diffraction standards (1975)

1,2,3 = First, second and third most intense lines in $ErVO_4$

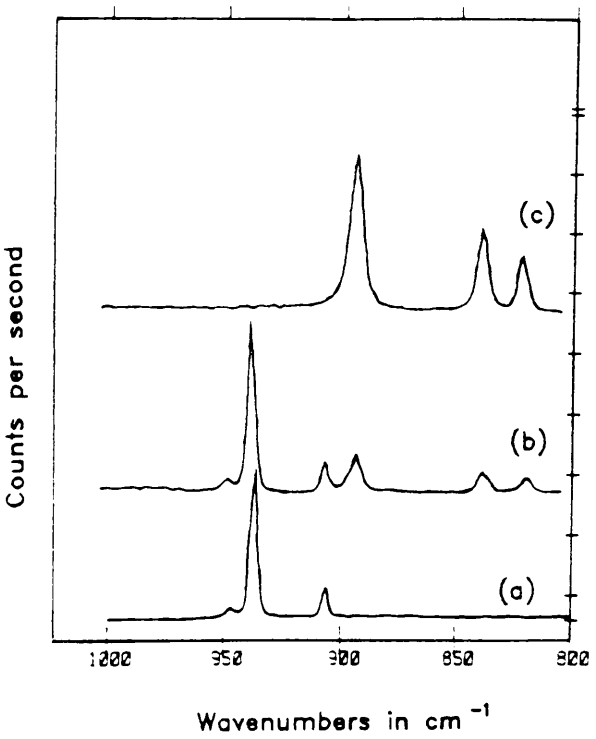

Figure V.1 Comparison of the Raman spectra between 800 and 1000 cm^{-1} of (a) KVO_3, (b) the reaction product of KVO_3, with 5 mol% Er_2O_3 after 5 hours at 1223 K, and (c) $ErVO_4$

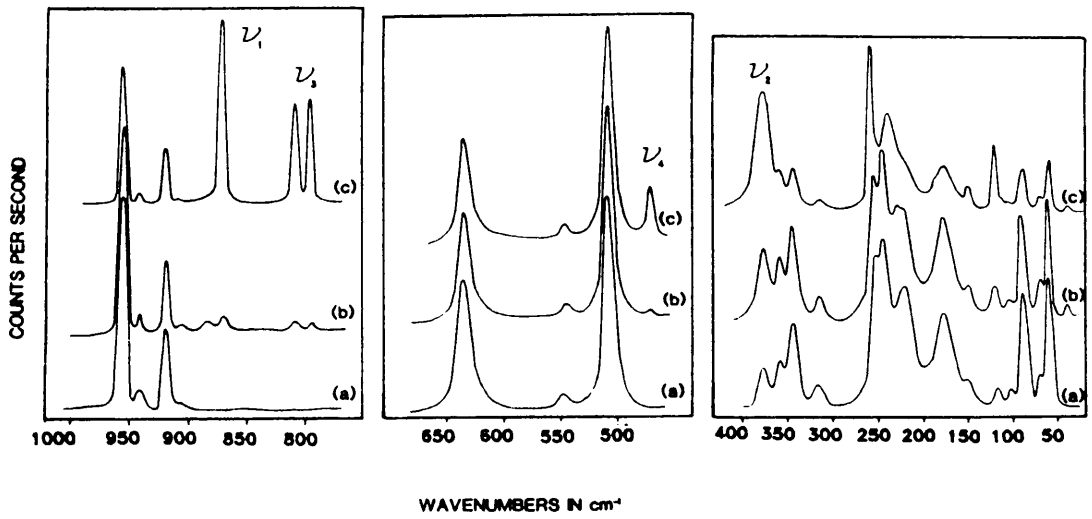

Figure V.2 Raman spectra of (a) α-$NaVO_3$ and the products of the high temperature reaction of $NaVO_3$ with (b) 0.5 mol% Nd_2O_3 and (c) 5 mol% Nd_2O_3. The vibrations of the tetrahedral orthovanadate ion are indicated with ν_1 to ν_4

0.5 and 5 mol% Nd_2O_3 respectively is shown in Figure V.2. Here the ν_1 (869 cm^{-1}), ν_3 (807, 793 cm^{-1}), ν_4 (469 cm^{-1}) and ν_2 (377 cm^{-1}) vibrations of the tetrahedral orthovanadate ion can be distinguished. The ν_2 mode almost coincides with the δ (VO_2) mode of $NaVO_3$ at 378 cm^{-1}, resulting in an apparent increase in the intensity of a metavanadate vibration with Nd^{3+} content. The relative intensities of the orthovanadate modes give an indication of the relative amounts of $NdVO_4$ formed.

The stoichiometric reaction of $NaVO_3$ with Er_2O_3 at 1223 K in air did not result in full conversion to the lanthanide orthovanadate, even after 106 hours. The Raman spectrum of the product (Figure V.3(b)) vibrations of both the meta- (934 and 937 cm^{-1}) and orthovanadate (891, 836 and 817 cm^{-1}) are present. Under vacuum, however, pure pink $ErVO_4$ is formed together with a thin grey surface layer.

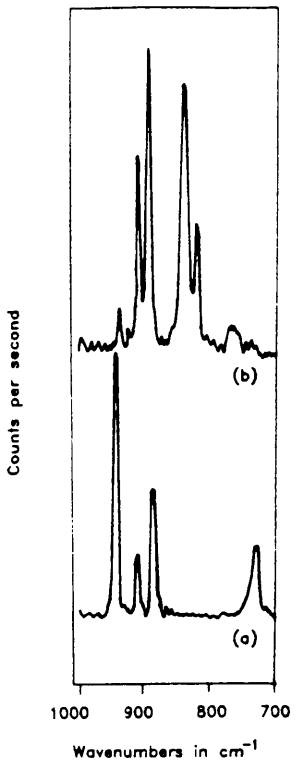

Figure V.3 Raman spectra of (a) $NaVO_3$ and (b) the reaction product of the stoichiometric reaction between $NaVO_3$ and Er_2O_3 in air after 106 hours at 1223 K

V.3.3 Infrared spectra

When $ErVO_4$ and $NdVO_4$ were formed in small quantities in the two alkali metal metavanadates it could not be detected in either the mid or the far-infrared.

In the stoichiometric reaction of $NaVO_3$ and Er_2O_3 under vacuum conditions two products are clearly distinguished. The mid-infrared spectrum of pink $ErVO_4$ which formed at the bottom of the crucible is shown in Figure V.4 in comparison with that of the grey surface layer which shows $ErVO_4$ with a new band at 880 cm^{-1} which could be ascribed to Na_2O formation.

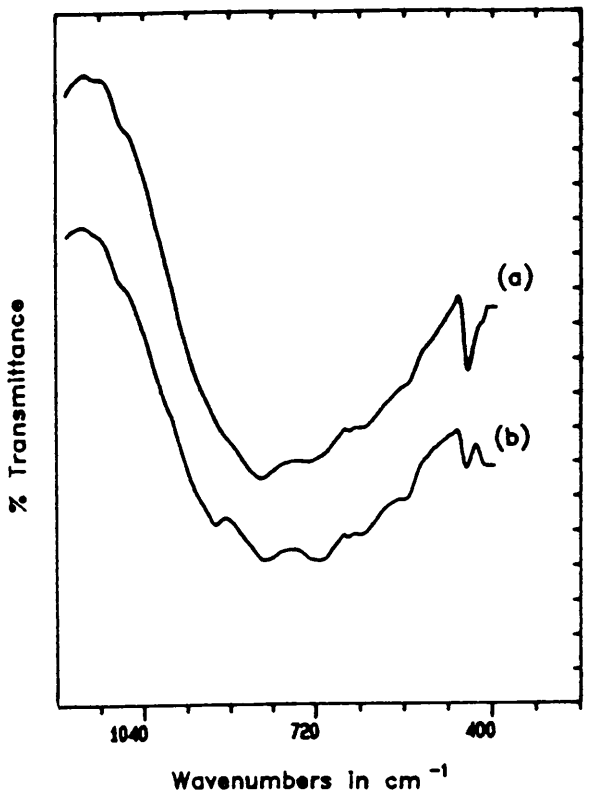

Figure V.4 Infrared spectra of (a) $ErVO_4$ (pink) and (b) $ErVO_4$ and the gray surface layer

V.3.4 Scanning electron microscope and energy dispersive X-ray analysis

The back scattering electron pictures of the KVO_3-sample treated with Er_2O_3 at high temperatures show small $ErVO_4$ crystals forming at the surface adjoining the platinum crucible during preparation. The surface is magnified 100x in Figure V.5 and 1000x in Figure V.6. In Figure V.7 the secondary electron picture of the same sample position as in Figure V.6 shows the topography of the surface in this region. A BSE-picture with magnification of 2000x is shown in Figure V.8 with the EDX-analysis performed in three marked spots. The resulting energy dispersive X-ray spectra obtained are shown in Figure V.9. The spot marked 'DDWER3' in the KVO_3 mass with the corresponding EDX-spectrum shows only potassium and vanadium present. The other two spots, marked 'DDWER1' and 'DDWER2', on the small crystals in the sample surface, clearly show the presence of vanadium and erbium. An infinitesimal amount of potassium is present at both of these spots, probably a result of the depth to which the electron beam penetrates the sample, reflecting a small amount of the potassium in the metavanadate mass.

The secondary and back scattering electron pictures of the opposite side of the KVO_3 surface show a melt which forms on the surface exposed to air during the high temperature reaction (Figure V.10 and V.11). The BSE-picture (Figure V.11) distinguishes the presence of two different materials. An EDX spot analysis of the same sample magnified 1000x (Figure V.12) results in the normal K/V ratio for KVO_3 in the spot marked 'DDWER4' (Figure V.13). The two spots marked 'DDWER5' and 'DDWER6', on the other hand, are part of a potassium rich melt on the KVO_3 surface. This high potassium content is probably due to K_2O formation during the high temperature reaction $2\ KVO_3 + Er_2O_3 \xrightarrow{\Delta} ErVO_4 + K_2O$.

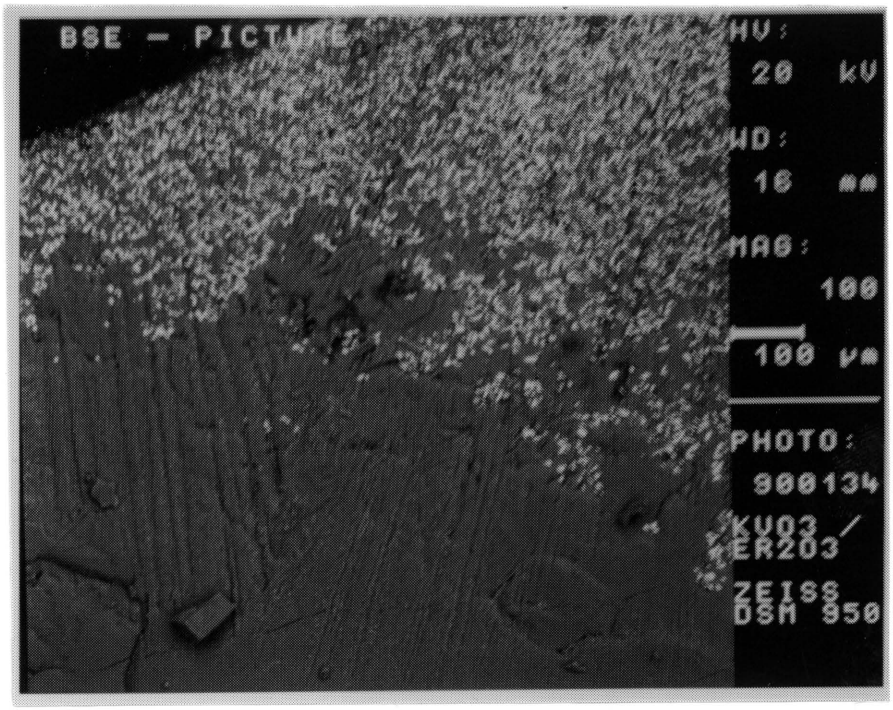

Figure V.5 Backscattering electron picture of $ErVO_4$ crystals on the surface of KVO_3 (Magnified 100x). The crystals are concentrated on the side closest to the platinum crucible during preparation

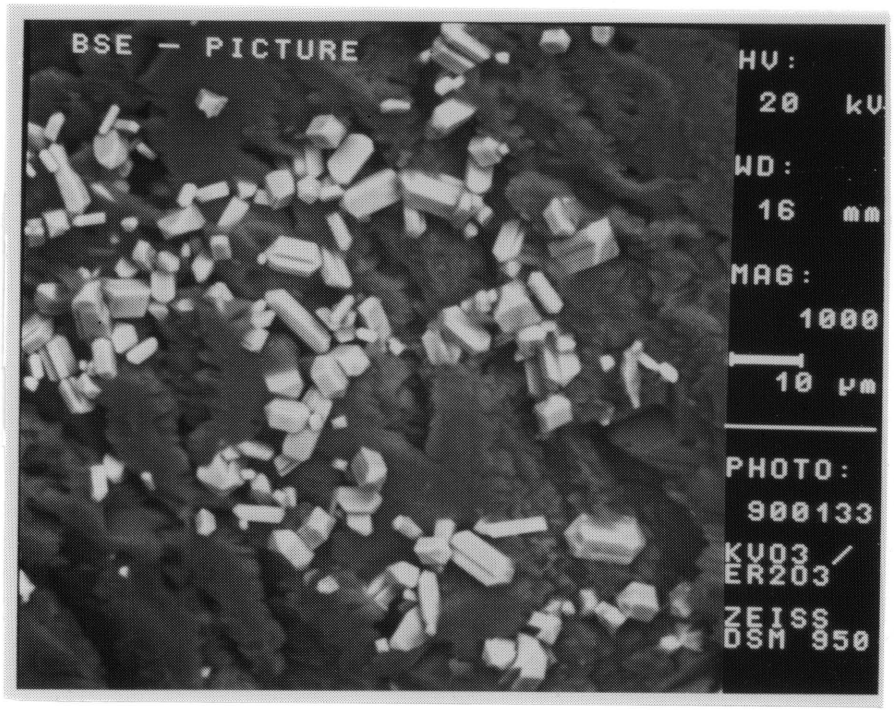

Figure V.6 Backscattering electron picture of the same surface as in V.5, magnified 1000x

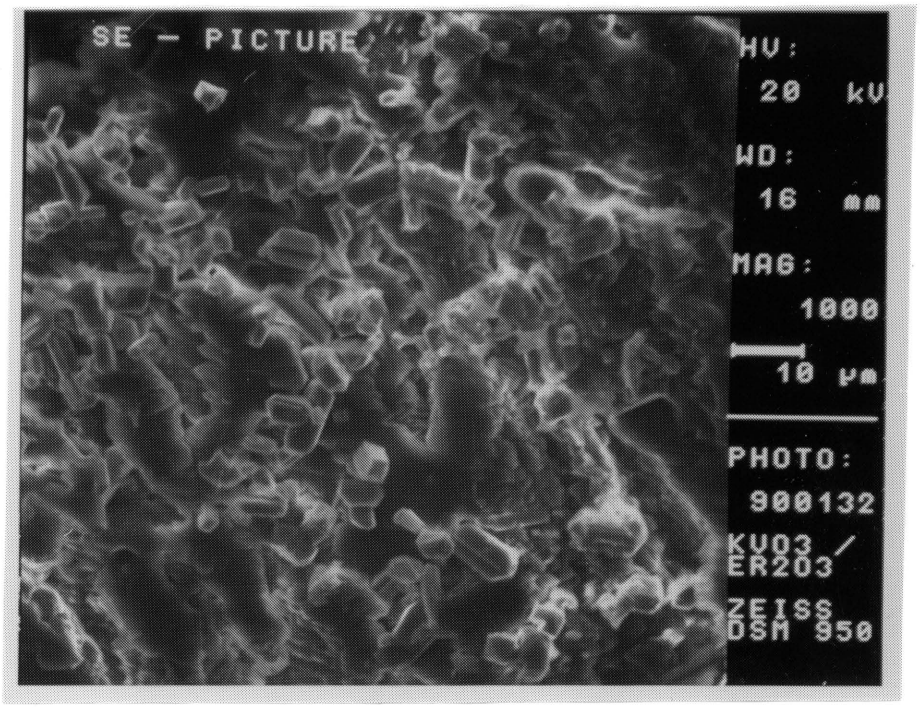

Figure V.7 Secondary electron picture of the same surface as in V.6, showing the topography of the sample (magnified 1000x)

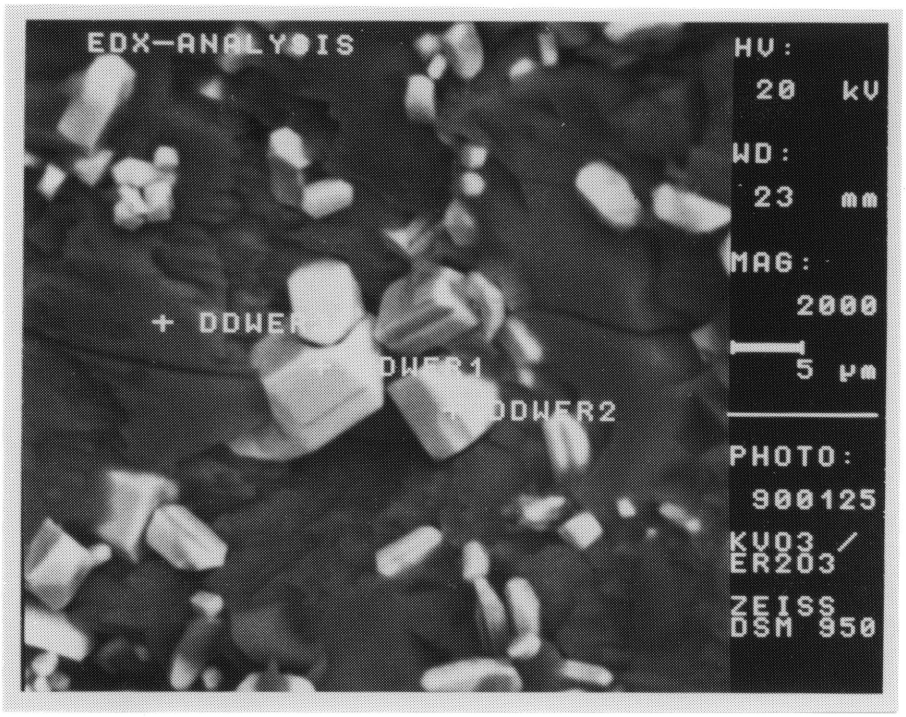

Figure V.8 BSE picture of $ErVO_4$ crystals in the KVO_3 mass (Magnified 2000x). EDX-analysis was performed in the three marked spots

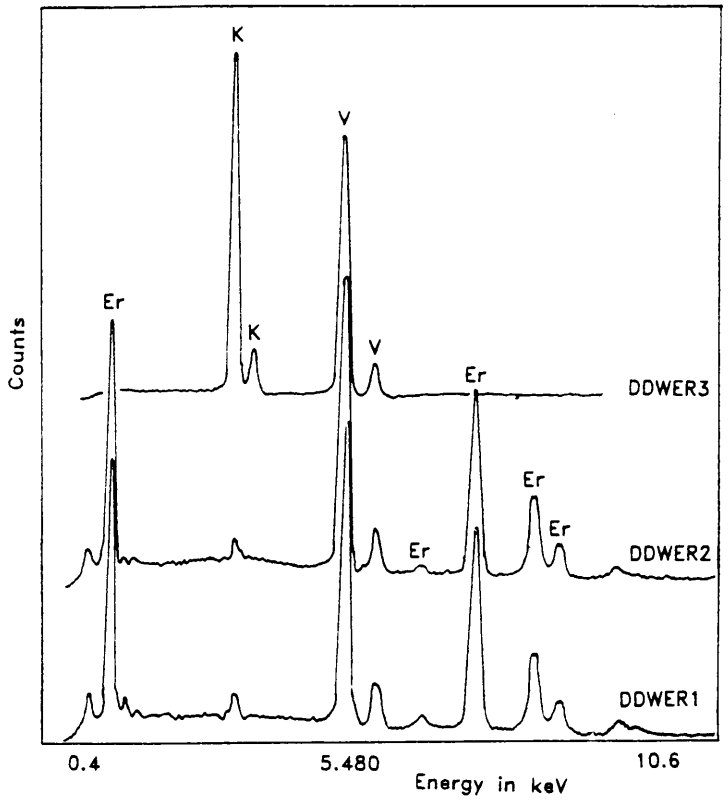

Figure V.9 Energy dispersive X-ray spectra of three different spots on the surface of the product obtained from KVO_3 and 5 mol% Er_2O_3 (Compare with Figure V.8)

The secondary electron picture (magnification 50x) of the surface adjoining the crucible during the heating process of $NaVO_3$ with 5 mol% Nd_2O_3 is shown in Figure V.I4, with the corresponding backscattered electron picture in Figure V.15. Needles of $NdVO_4$ are clearly distinguished on the surface with small crystals concentrated at the bottom left in the picture. A magnification of 1000x of this part (Figure V.16 and V.17) illustrates the formation of minute $NdVO_4$ crystals in the sodium metavanadate mass. Spot analysis on one of the needles on the surface confirms the presence of Nd

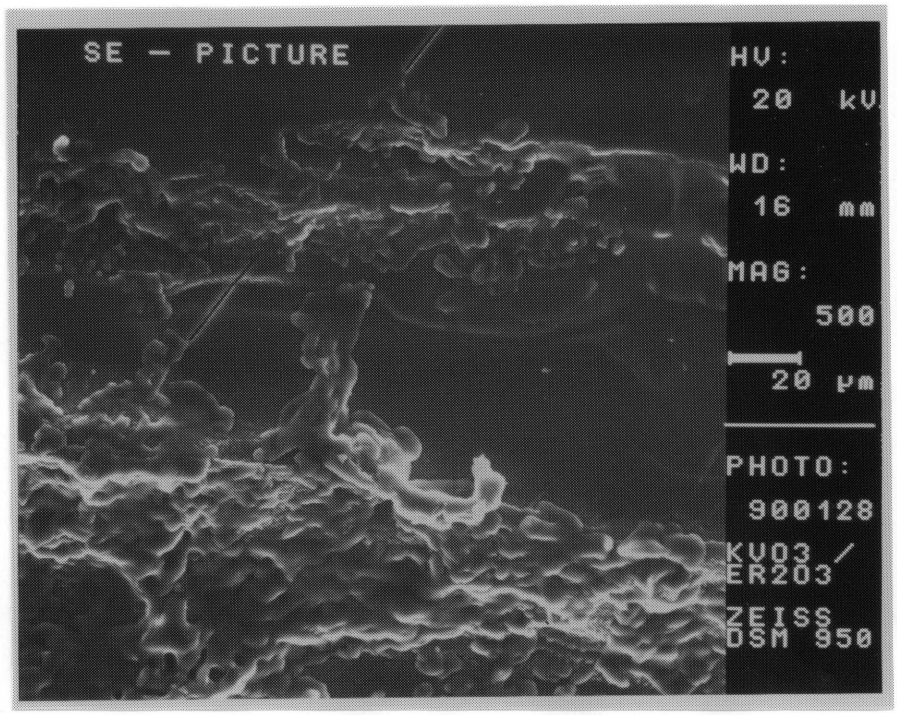

Figures V.10 Secondary electron picture of the surface of KVO_3 exposed to air during the high temperature reaction with 5 mol% Er_2O_3 (Magnified 500x)

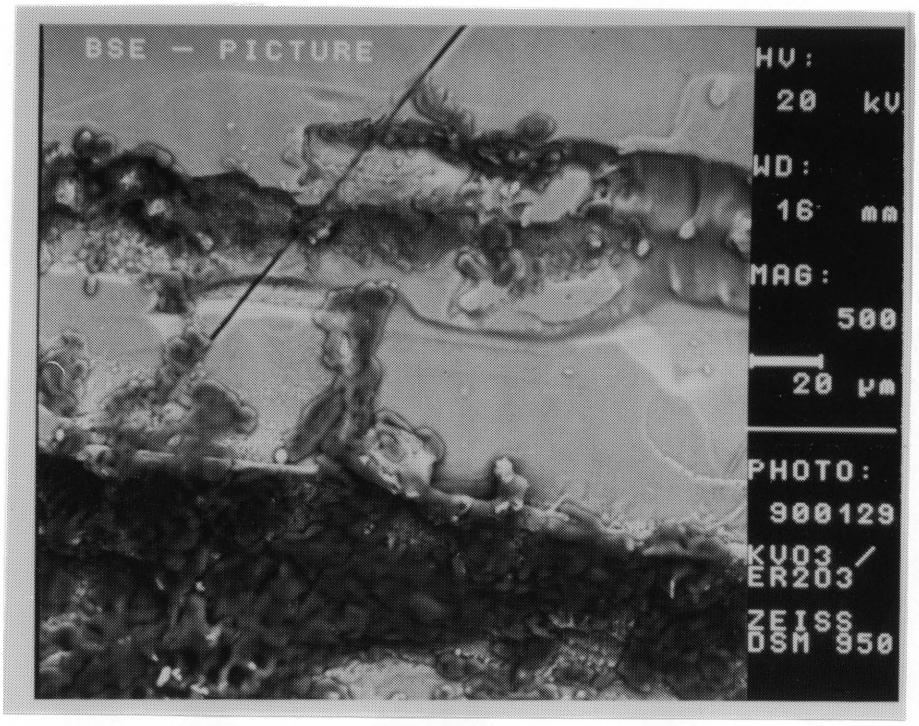

Figure V.11 Backscattering electron picture of the surface shown in Figure V.10 showing the potassium rich melt on the KVO_3 surface

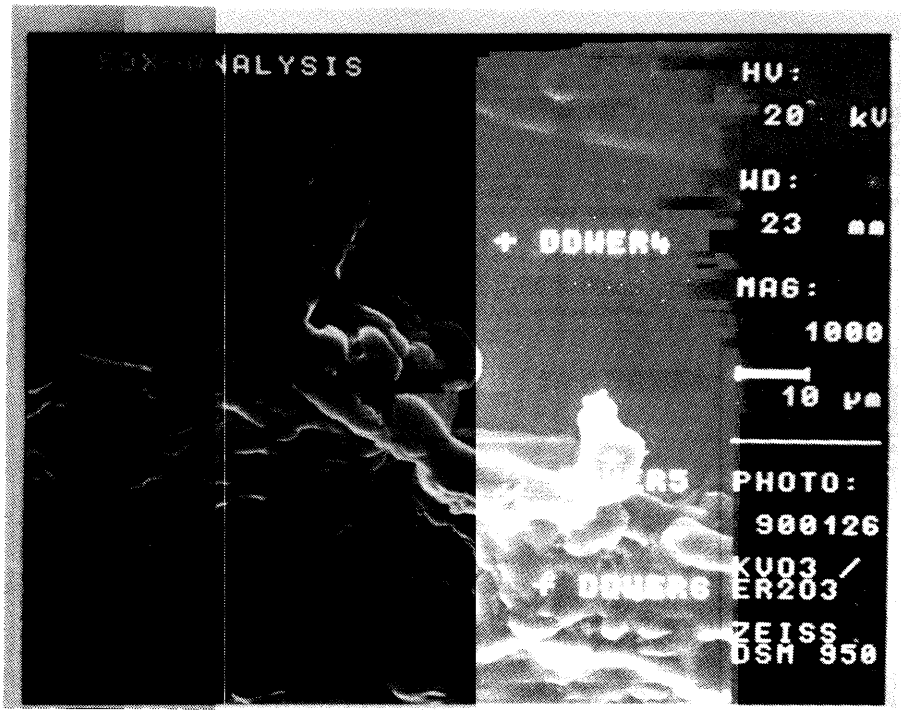

Figures V.12 EDX analysis of the same spot shown in Figures V.10 and 11, magnified 1000x

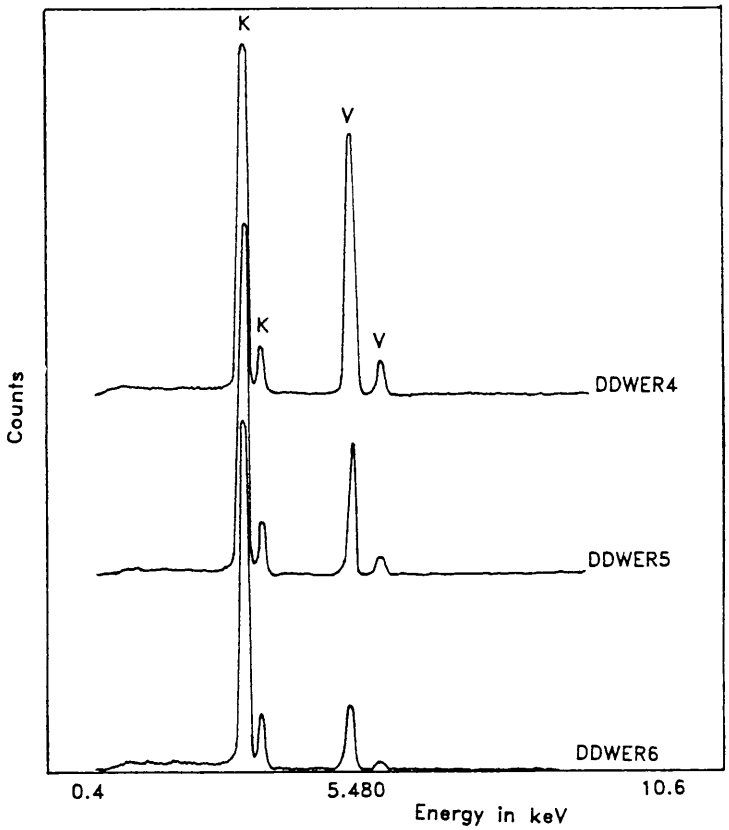

Figures V.13 Energy dispersive X-ray spectra of the surface exposed to air during the reaction of KVO_3 with 5 mol% Er_2O_3 (Compare Figure V.12)

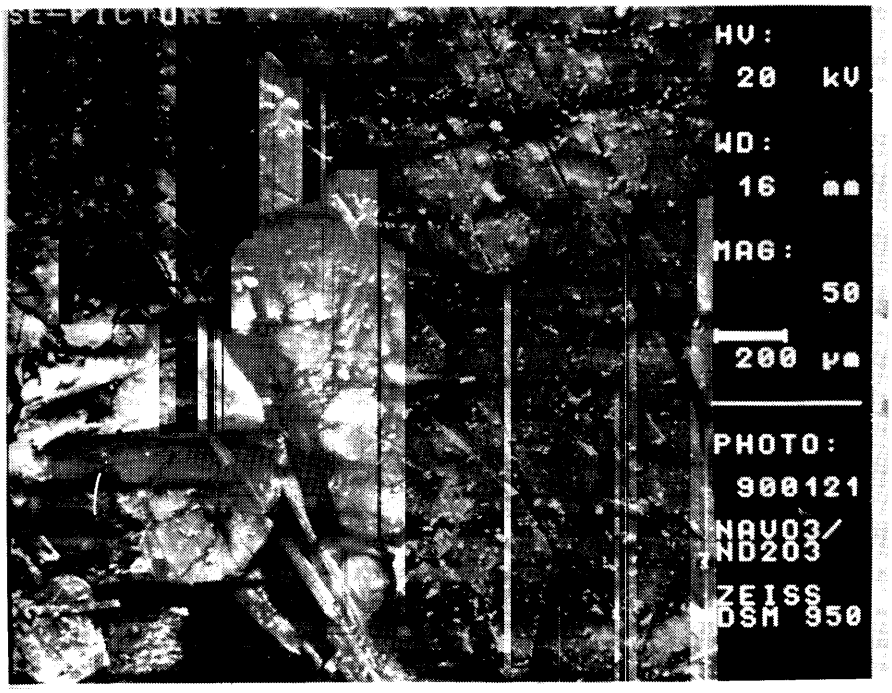

Figures V.14 Secondary electron picture of the surface closest to the platinum crucible during the reaction of $NaVO_3$ with 5 mol% Nd_2O_3

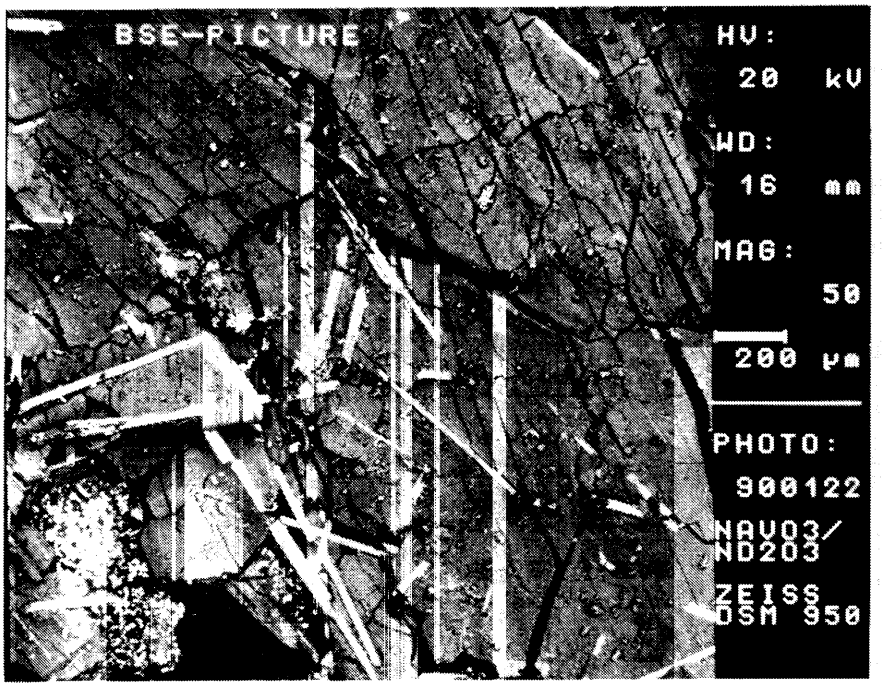

Figures V.15 Backscattering electron picture of the surface shown in Figure V.14 (Magnified 50x)

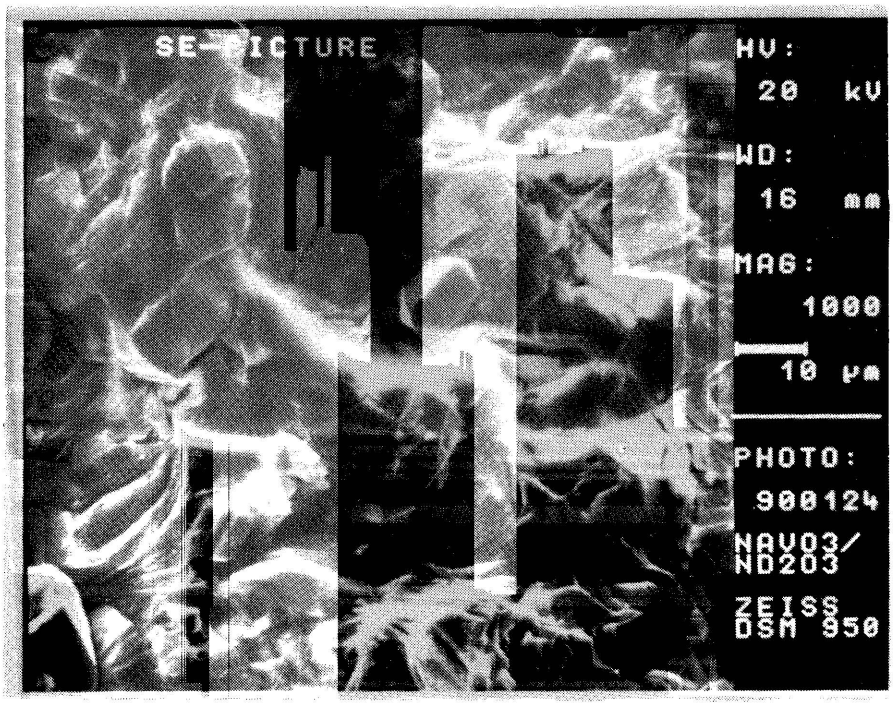

Figures V.16 Secondary electron picture of the same surface as in Figure V.14, magnified 1000x

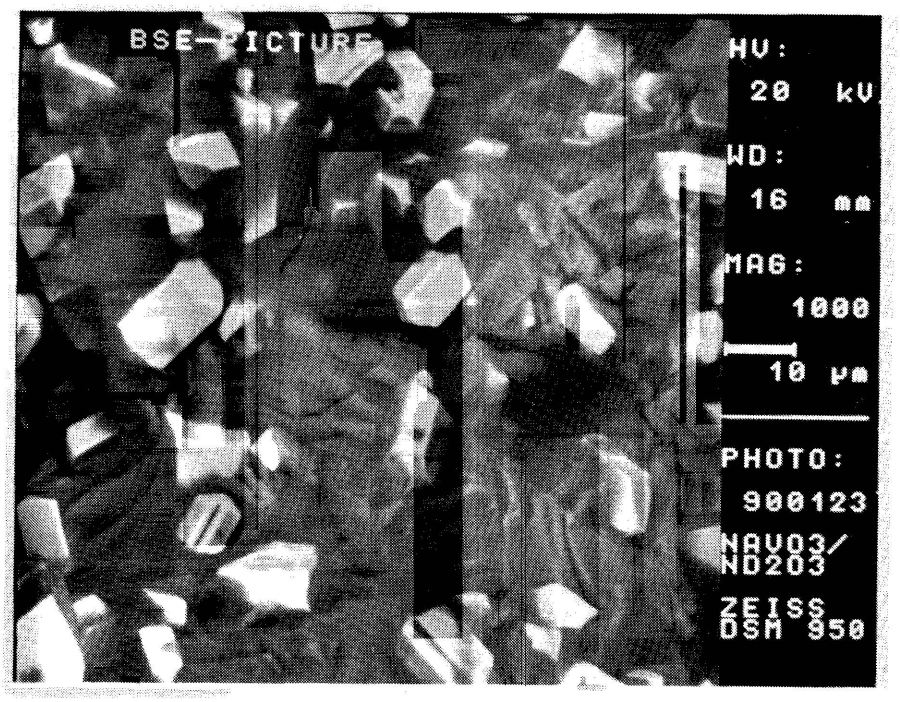

Figures V.17 BSE picture of the same surface as in Figure V.16 showing small $NdVO_4$ crystals in the $NaVO_3$ mass

and V as is evident from the energy dispersive spectrum in Figure V.18 marked 'DDWND1'. The EDX-spectrum of surrounding $NaVO_3$ is taken at the spot marked 'DDWND2' in Figure V.19. Inspection of the opposite side (Figure V.20) of the sample reveals a crack in the surface with a darker, sodium-rich melt appearing along the crack from within the sample. The EDX spectrum of a part of the melt, marked 'DDWND5', is shown in Figure V.20.

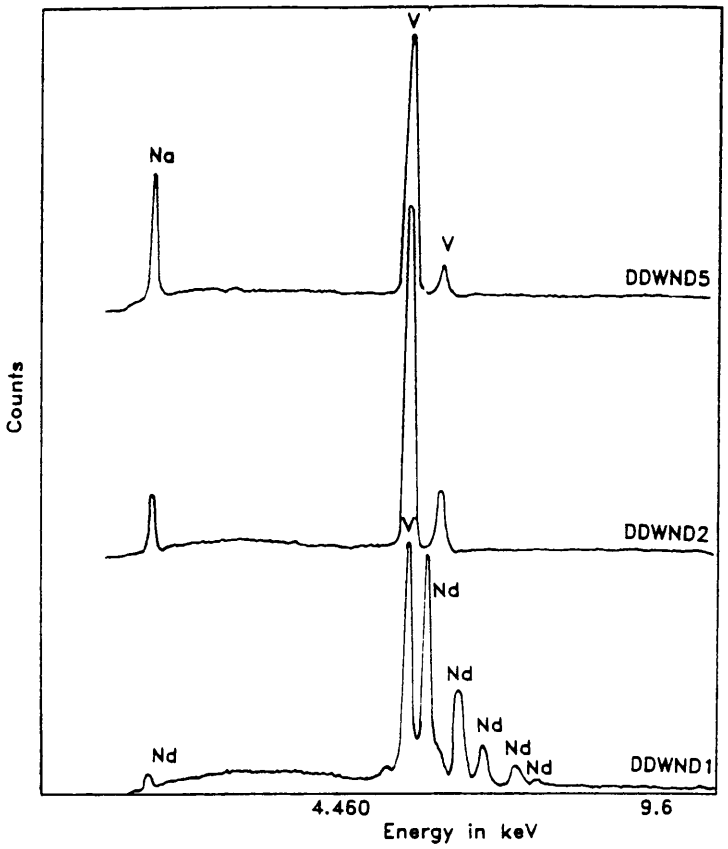

Figure V.18 EDX analysis on one of the $NdVO_4$ needles in Figure V.19, magnified 2000x, on a spot marked 'DDWND1', and the surrounding $NaVO_3$ mass marked 'DDWND2'

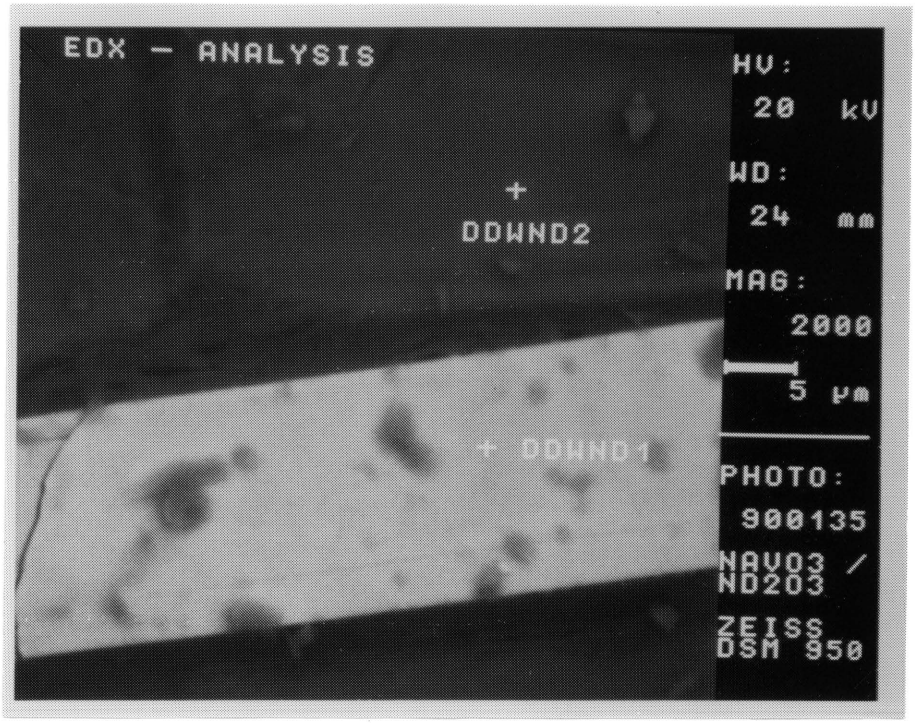

Figures V.19 EDX-analysis of (1) The $NdVO_4$ needle (DDWND1), and (2) The surrounding $NaVO_3$ mass (DDWND2) (Magnification 2000x)

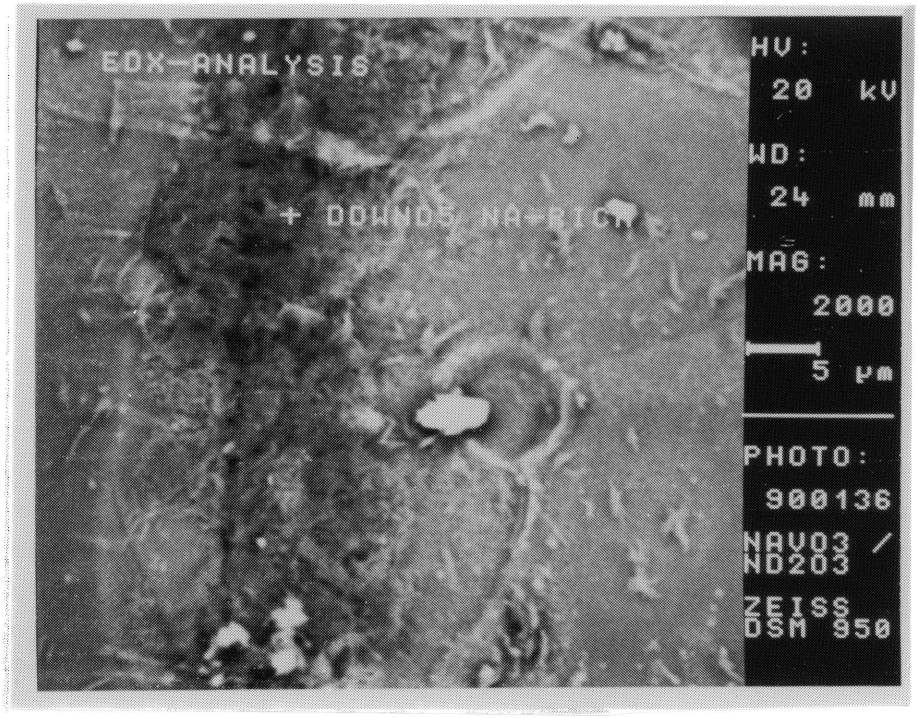

Figures V.20 The side of the $NaVO_3$ surface exposed to air during the reaction with 5 mol% Nd_2O_3. A sodium rich melt (Marked DDWND5- compare Figure V.18) is visible along the crack

From all of these results it is clear that a new compound is formed within the MVO_3 when it is mixed with a small percentage Ln_2O_3 and treated at high temperatures. The new compound, $LnVO_4$, is probably more stable than the alkali metal metavanadate at high temperatures as it did not melt in the crucible when heated up to 1223 K. When the reaction is performed with stoichiometric amounts of the reactants, total conversion does not occur, even after a few hours. When repeated under vacuum conditions for 48 hours, however, the rare earth orthovanadate was formed with the alkali metal oxide as a probable second product according to the reaction:

$MVO_3 + Ln_2O_3 \longrightarrow 2\ LnVO_4 + M_2O$.

V.4 CONCLUSION

It can be concluded that the 'doping' of alkali metal metavanadates with lanthanide oxides, leading to variations in the dielectric properties of the metavanadates, is in fact a high temperature reaction between MVO_3 [M = alkali metal] and Ln_2O_3 [Ln = lanthanide] resulting in the formation of the lanthanide orthovanadate, $LnVO_4$. By reacting the metavanadate with various percentages of the lanthanide oxide more or less of the lanthanide orthovanadate is formed, probably with the alkali metal oxide as second product. The reported [82] influence on the dielectric properties, therefore, is a direct result of the presence of two completely different materials, $LnVO_4$ and M_2O in the MVO_3, and not to the formation of a solid solution of the alkali metal metavanadate with the lanthanide ions.

CHAPTER VI

VIBRATIONAL AND ELECTRONIC SPECTRA OF SOME OF THE LANTHANIDE ORTHOVANADATES, $LnVO_4$ (Ln = Er, Nd, Eu)

VI.1 INTRODUCTION

All $LnVO_4$ compounds (Ln = La-Lu) are semiconducting materials with interesting structural and magnetic transformations [93, 94]. The lanthanide compounds have similar chemical properties, the reason for this mutual resemblance being that the series corresponds with the gradual filling of the f-orbitals and the f-electrons do not greatly influence the chemical properties. The trivalent state is the most common one among lanthanide ions with an electron configuration of $4f^n5s^25p^6$ [95].

The absorption and emission spectra of the rare earth ions in the solid state are characterized by the sharpness of many of the lines because of a weak interaction of the shielded 4f electrons with the crystalline environment. These spectra were recorded for some of the lanthanide orthovanadates and the energy levels so determined were compared to those of the free ions and the corresponding lanthanide oxides. The lanthanide sesquioxides have a variety of phases [96]. At ambient conditions, however, two stable phases exist mainly, viz. the trigonal (A-type) and the cubic (C-type) phases. The sesquioxides of the lanthanides have either the A-type structure or the C-structure. It must be added that a distorted arrangement of the A-modification occurs when a displacive first-order transition occurs in

these oxides at high temperatures (at 1900, 2050 and 2100°C for Sn_2O_3, Eu_2O_3 and Gd_2O_3 respectively) [96]. This monoclinic structure is closely related to the A-type modification. The trigonal A-type structure was first determined by Pauling [97] and belongs to the space group $P\bar{3}m1$ (D_{3d}^3) with Z = 1. The lanthanide ions are located on the 3 m (C_{3V})-sites and the oxygen atoms are distributed over the sites $\bar{3}$ m (D_{3d}) (O(I)) and 3 m (C_{3V}) (O(I)). The B-type belongs to the space group C2/m (C_{2h}^3) with Z = 6 [98]. The 18 oxygen atoms have five different crystallographic sites, four of m(C_s)-symmetry and one of 2/m (C_{2h})-symmetry. The lanthanide ions are situated on three different m(C_s)-sites. The C-type structure for the rare earth sesquioxides is cubic, with sixteen molecules in the unit cell [99]. The unit cell contains 24 rare earth ions on C_2-sites and eight on C_{3i}-sites.

Some aspects of the vibrational infrared and Raman spectra of some $LnVO_4$, compounds (Ln = Er, Eu, Nd) with the zircon structure are also analyzed and compared in the following section.

VI.2 EXPERIMENTAL

The zircon phase of $LnVO_4$ (Ln = Er,Eu,Nd) was obtained through the high temperature reaction of the lanthanide oxide with NH_4VO_3. A temperature of 1223 K was maintained on the stoichiometric mixture for 5 hours. Colours of the products are similar to that of the lanthanide oxide in the starting material. The $ErVO_4$ product has a pink-brown colour, $NdVO_4$ light blue and $EuVO_4$ white. Absorbance and emission measurements are described in detail in Appendix D(4).

VI.3 VIBRATIONAL SPECTRA

VI.3.1 Previous work

Infrared and Raman spectra of the lanthanide orthovanadates have been reported with predominant coverage of the internal vibrations of the VO_4^{3-} anion [100-104]. Raman spectra of rare earth orthovanadates, $LnVO_4$ (Ln = Pr-Lu), as well as $ScVO_4$ and YVO_4 have been recorded and interpreted between 300 and 1000 cm^{-1}. The ν_1 to ν_4 vibrations of the orthovanadate ion were identified for each compound in the series. The symmetric stretching vibration (ν_1) was plotted as a function of the atomic radius of the lanthanides, and the value for $ErVO_4$ was found to have an exceptionally low value [104]. The vibrational spectra of $NbBO_4$ and $TaBO_4$ which also crystallize in the zircon structure have also been reported [105]. Miller et.al. [106] analyzed and assigned the lattice vibrations of YVO_4 (zircon structure) group-theoretically. These modes were also reported for MXO_4 (M = Ca, Sr; X = Mo, W) with the scheelite structure.

The Raman spectra of the A-type rare earth sesquioxides have already been reported [107-110] and have also been compared with those of the B-type. Boldish and White [111] recorded single-crystal infrared and polarized Raman spectra of some lanthanide sexquioxides. Bloor and Dean [99] also recorded the far-infrared spectra of some rare earth sesquioxides.

VI.3.2 Vibrational analysis and spectra

$LnVO_4$ (Ln = Er, Eu, Nd) crystallize in the zircon structure when prepared at atmospheric pressure and can be converted to the scheelite phase under high pressure [112]. The space group of the zircon phase is $I4_1/amd$ (D_{4h}^{19}). The approximate tetrahedral VO_4^{3-} ion occupies a site with symmetry D_{2d} which

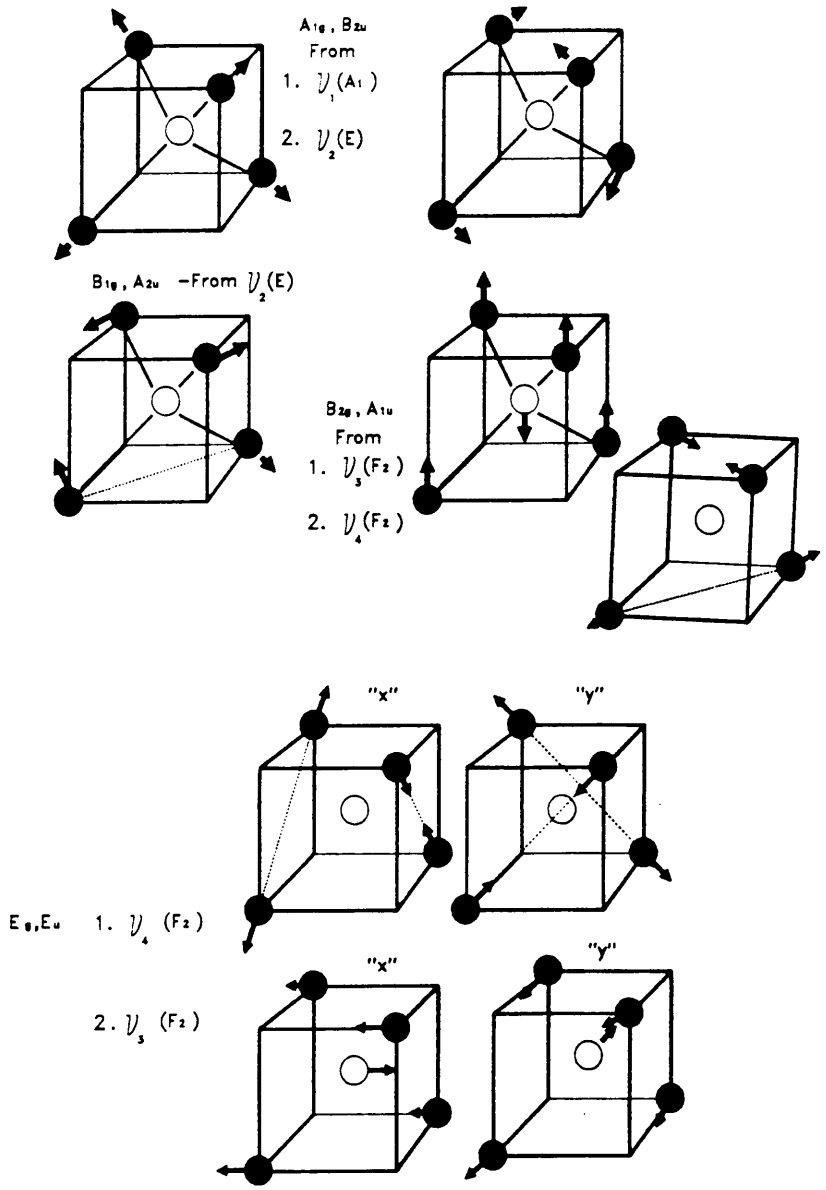

Figure VI.1 Internal modes of vibration of VO_4^{3-} in the zircon phase of $LnVO_4$ (Ln = Er, Eu, Nd)

Table VI.1 Site and factor group correlation for VO_4^{3-} in $LnVO_4$ (zircon phase) (Ln = Nd,Er,Eu). Assignment of observed vibrations are presented for $EuVO_4$ and $ErVO_4$.

'Free ion'	Site group	Factor group	$ErVO_4$	$EuVO_4$
Td	D_{2d}	D_{4h}		
$\nu_1(A_1)$	A_1	A_{1g} (R)	887	
		B_{2u} (-)		
$\nu_2(E)$	A_1	A_{1g} (R)	376	
		B_{2u} (-)		
	B_1	A_{1u} (-)		
		B_{2g} (R)	259	
$\nu_3(F_2)$	B_2	A_{2u} (IR)		
		B_{1g} (R)	812	
	E	E_g (IR, R)	831(R)	
		E_u (IR)	734	
$\nu_4(F_2)$	B_2	A_{2u} (IR)	448	445
		B_{1g} (R)	486	
	E	E_g (IR, R)	493(IR)	
		E_u (IR)	434	424
Translational and Rotational modes:			378 (IR)	396 (IR)
			260 (IR), 259 (R)	387 (IR)
			250 (IR)	335 (IR)
			164 (IR)	258 (IR), 261 (R)
			154 (R)	222 (IR)
			111 (IR), 114 (R)	172 (IR)
			100 (IR)	
			69 (IR), 59 (R)	
			45 (IR)	
			30 (IR), 36 (R)	

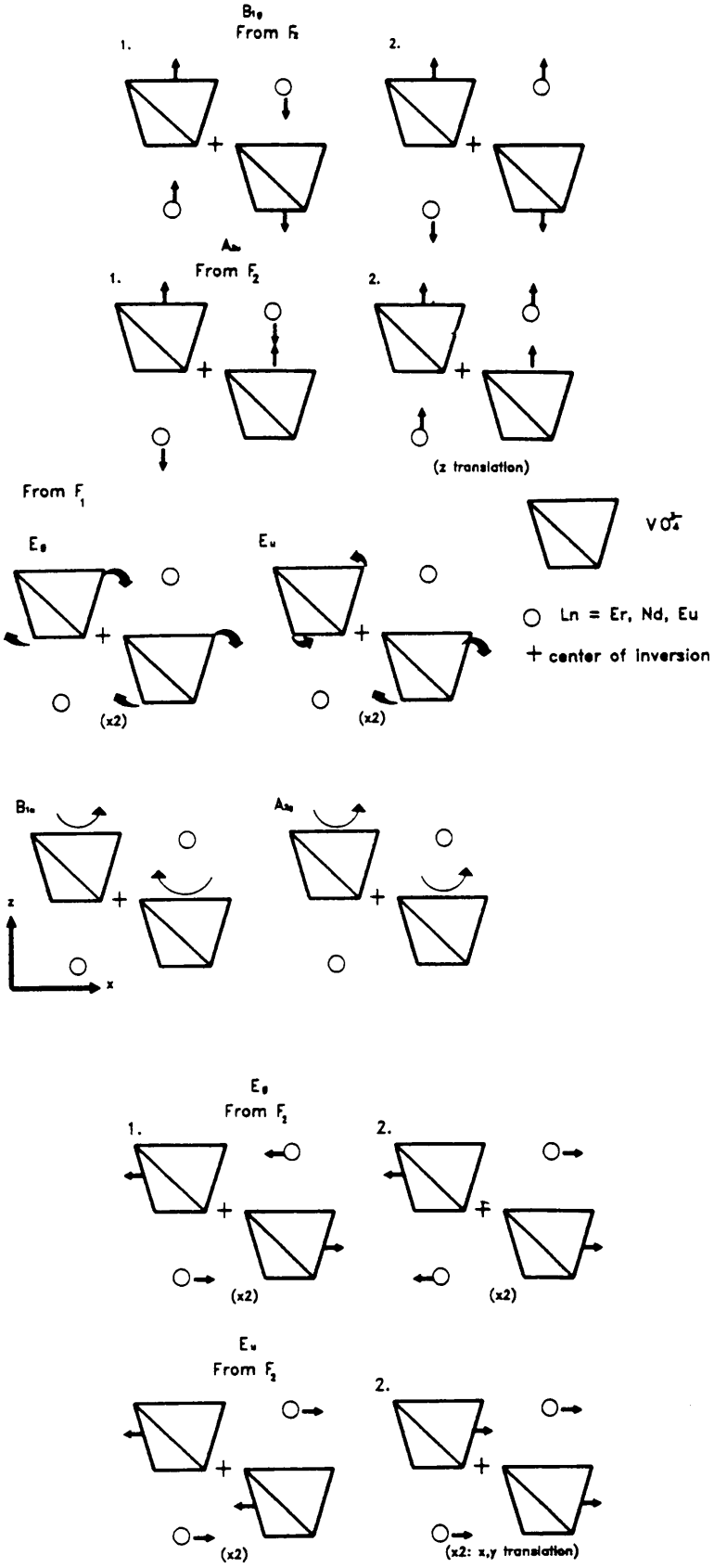

Figure VI.2 External modes in zircon phase $LnVO_4$ (Ln = Er, Eu, Nd)

results in an expected splitting of internal vibrations into 2 A_{1g} (R) + 2 B_{1g} (R) + B_{2g} (R) + 2E_g(IR, R) + A_{1u} (-) + 2A_{2u}(IR) + 2 B_{2u} (-) + 2 E_u (IR) under the factor group (Table VI.1). These are shown in Table VI.2 together with the different external modes which include rotational and translational modes of VO_4^{3-}. A representation of the symmetry coordinates of all these modes is shown in Figures VI.1 and VI.2. In total 12 Raman active (5 ext., 7 int.) and 15 infrared active (9 ext., 6 int.) modes are expected for $LnVO_4$. The infrared and Raman spectra of $ErVO_4$ and $EuVO_4$ are shown in Figures VI.3-VI.6, the assignment of the vibrations is shown in Table VI.1. These bands were observed without considerable shifting with at least two of the three exciting lines at 488, 514.5 and 632.8 nm.

VI.4 ELECTRONIC SPECTRA

VI.4.1 Introduction

The electron configurations of the three trivalent rare earth ions of which absorption and emission spectra will be presented are as follows:

Nd^{3+} : [Xe] $4f^3$

Eu^{3+} : [Xe] $4f^6$

Er^{3+} : [Xe] $4f^{11}$

$[Xe] \equiv 1s^2 2s^2 2p^6 3s^2 3p^6 3d^{10} 4s^2 4p^6 4d^{10} 5s^2 5p^6$

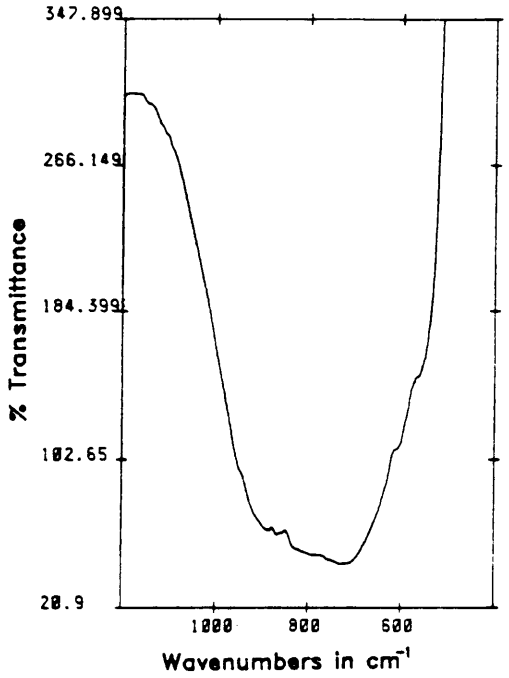

Figure VI.3 Mid-infrared spectrum of $ErVO_4$(z)

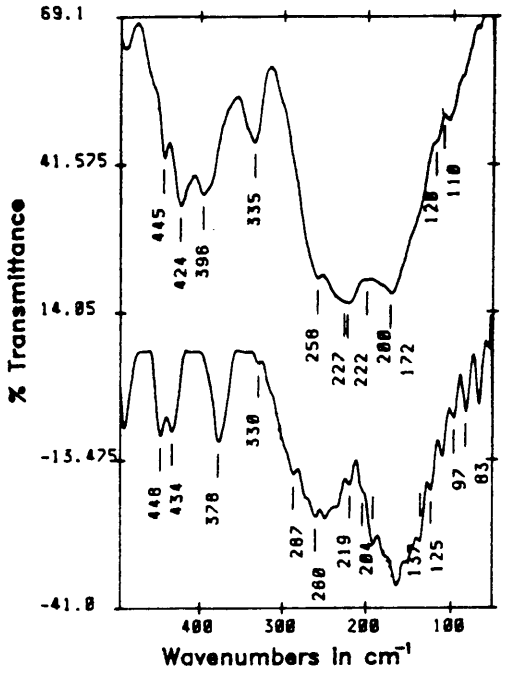

Figure VI.4 Far-infrared spectra of $EuVO_4$ (top) and $ErVO_4$(bottom) between 50 and 500 cm^{-1}

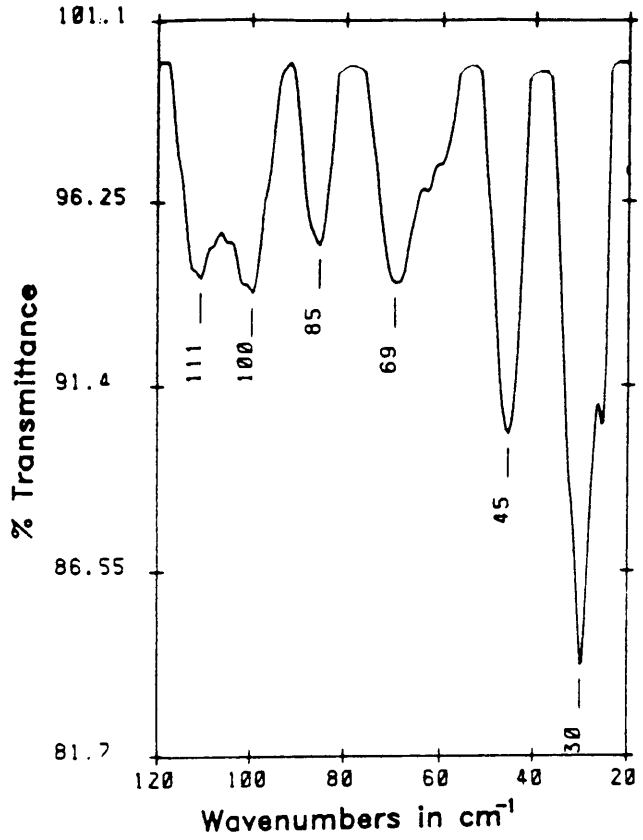

Figure VI.5 Far-infrared spectrum of $ErVO_4$ between 20 and 120 cm^{-1}

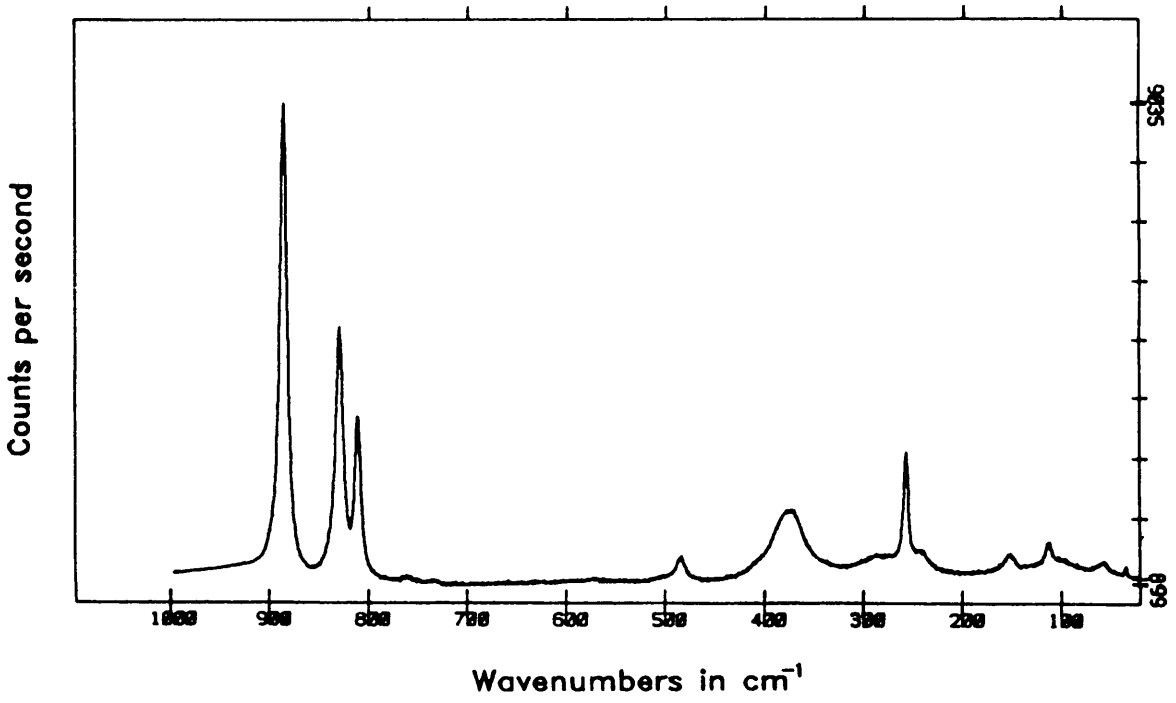

Figure VI.6 Raman spectrum of $ErVO_4$

The 4f electrons are not the outermost ones and are shielded from external fields by two electronic shells with larger radical extension ($5s^2 5p^6$). As a result 4f-electrons are only weakly perturbed by the charges of surrounding ligands. This leads to the rare earth ion being a useful probe in a solid as the crystal environment constitutes only a small perturbation on the atomic energy levels so that many of its solid state and hence spectroscopic properties can be understood from a consideration of the free ions. Positions of the energy level terms in the free ion and in an ionic solid are generally the same within a few hundred wavenumbers [95].

Table VI.2 Vibrational analysis of the Scheelite structure of $LnVO_4$(Ln = Er, Nd, Eu)

VO_4^{3-}	A_g	A_{2g}	B_{1g}	B_{2g}	E_g	A_{1u}	A_{2u}	B_{1u}	B_{2u}	E_u
Internal modes	2	0	2	1	2	1	2	0	2	2
Rotations	0	1	0	0	1	0	0	1	0	1
$T + T_A$	0	0	1	0	1	0	1	0	0	1
N(Total)	2	1	3	1	4	1	3	1	2	4
Cation (Er^{3+}, Nd^{3+} ,Eu^{3+})										
Translations	0	0	1	0	1	0	1	0	0	1

VI.4.2 **Previous work**

Various authors have reported the energy levels of trivalent ions in the rare earth oxides [113-117]. Photoacoustic spectra of Er_2O_3 and Nd_2O_3 with J-level assignments were presented by Schoonover et.al. [113]. Konstatinov et.al. [116] showed the absorption spectrum of Er_2O_3 without assignments and Stark levels for ground state manifolds in the same compound were reported for the two different sites C_2 and C_{3i} by Gruber et.al. [115]. Seven lines between 6610 and 6807 cm^{-1} in Er_2O_3 were attributed to the $^4I_{15/2}$ to $^4I_{13/2}$ transition of lanthanide ions in C_{3i} sites [118].

The optical absorption spectra of Er^{3+} in isostructural single crystals of YPO_4 and YVO_4 were reported by Kuse [119] between 14 000 and 29 000 cm^{-1} and crystal field splittings were interpreted in terms of crystal potentials of symmetry D_{2d}. A comparison of calculated and observed energy levels was shown and it was found that the crystal field parameters show significant differences in the two crystals. Resonance enhancement factors of 10 to 100 were observed for electronic transitions within the ground $^4I_{15/2}$ multiplet in $ErPO_4$ crystals [120]. Other interesting luminescence spectra of lanthanides include the study by Murray et. al. [121] where the Eu^{3+} ion is used as a probe in the structure of trisodiumtris(2,6-pyridine dicarboxylato)lanthanide(III) compounds and that of the Tb^{3+} ion adsorbed on a single resin head by Young et. al. [122].

VI.4.3 **Crystal symmetry and the structure of the spectrum**

A free ion energy level with total angular momentum J is 2 J + 1 fold degenerate, and part or all of this degeneracy is removed if the ion is placed in a crystal field as the symmetry of the crystal field is less than spherical. The number of components then depends on the symmetry of the crystal field. The relationship between crystal symmetry and level structure is best determined by group theoretical methods. The electric field at the position of the rare earth ion may or may not be the same as that of the total crystal [123].

VI.4.4 Diffuse reflectance spectra

The room temperature UV- and visible diffuse reflectance spectra of Nd_2O_3 and $NdVO_4(z)$ are shown in Figures VI.7 and VI.8. Energy levels of the trivalent neodymium ion are assigned to the various absorption bands in Table VI.3. The Stark levels in Nd^{3+} are at least twofold degenerate for an odd number of electrons. Degeneracy of each electronic J-level in the D_{2d} site in $NdVO_4(z)$ is only partially removed giving rise to $J + \frac{1}{2}$ crystalline Stark levels. Nd^{3+} occupies two different sites C_2 and C_{3i} in Nd_2O_3 (Space group Ia3 (T_h^7)). The spectrum of Nd_2O_3 and $NdVO_4$ are characterized by bands associated with transitions from the ground $^4I_{9/2}$ level to the $^4F_{5/2}$, $^2H_{9/2}$, $^4F_{7/2}$, $^4S_{3/2}$, $^4F_{7/2}$, $^2H_{11/2}$, $^4G_{5/2}$, $^4G_{7/2}$, $^4G_{7/2}$, $^2D_{3/2}$, $^4G_{11/2}$, $^2K_{15/2}$ and $^2P_{1/2}$ levels in the Nd^{3+} ion while the higher $^4D_{3/2}$ state is also observed for Nd_2O_3. In general less bands are observed in the room temperature spectrum than the amount of Stark components predicted for each level. An exception to this is the $^4F_{9/2}$ level with 5 Stark levels predicted and observed. The broad bands in the spectra of both compounds are an unusual feature for a lanthanide ion and are probably the result of the many closely spaced energy levels in Nd. The energy levels of the free Nd^{3+} ion are compared to observed energies for Nd_2O_3 and $NdVO_4$ in Figures VI.9 and VI.10 with a comparison of the term splitting in the two solids in Table VI.4.

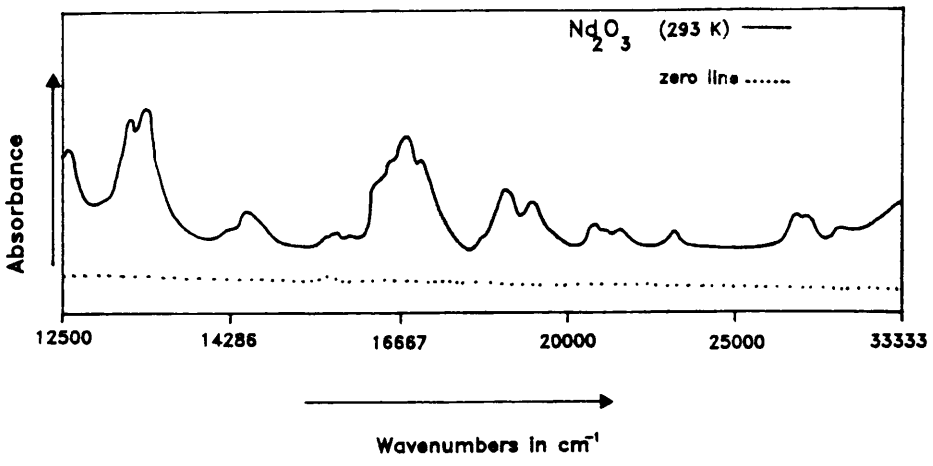

Figure VI.7 UV/VIS diffuse reflectance spectrum of Nd_2O_3

Table VI.3 Electronic energy levels of the Nd^{3+} ion in Nd_2O_3 and $NdVO_4$ at room temperature as determined by diffuse reflection UV- and visible spectroscopy. Values are given as wavenumbers (cm^{-1})

Nd_2O_3	$NdVO_4$	Assignment
12 579	12 516	$^4F_{5/2}$
12 804	12 706	$^4H_{9/2}$
12 937		
13 089	13 004	$^4F_{7/2}/^4S_{3/2}$
13 158	13 106	
13 298	13 280	
13 369	13 495	
14 245	14 368	$^4F_{9/2}$
14 430	14 535	
14 620	14 641	
15 456	14 771	
15 576		
15 723		
15 898	15 898	
16 234	16 026	$^2H_{11/2}$
16 340		
16 474	16 529	
16 694	16 835	
17 036		$^4G_{5/2}$
17 241	17 331	$^4G_{7/2}$
18 116		
18 657	18 622	
	18 832	
19 231		$^4G_{9/2}$
20 661		
20 877	20 877	$^2G_{7/2}$
21 368	21 186	$^2D_{3/2}/^4G_{11/12}/^2K_{15/2}$
	21 459	
22 472	21 739	
22 936	23 148	$^2P_{1/2}$
27 473		
28 090		$^4D_{3/2}$

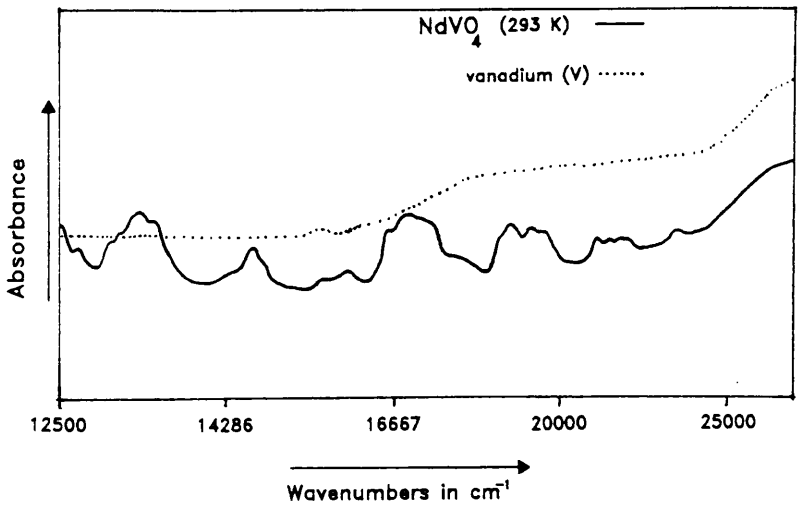

Figure VI.8 UV/VIS diffuse reflectance spectrum of $NdVO_4$

Table VI.4 Comparison of the term splitting (in cm^{-1}) in solid Nd_2O_3 and $NdVO_4$

Level	Nd_2O_3	$NdVO_4$
$^2H_{9/2}$	133	-
$^4F_{9/2}$	1653	1530
$^2H_{11/2}$	460	809
$^4G_{7/2}$	1416	1291
$^4G_{9/2}$	1430	-

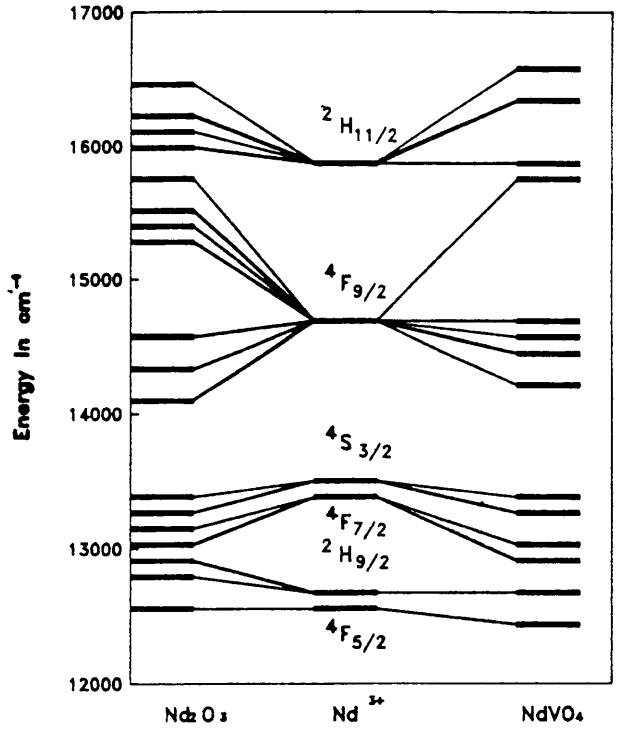

Figure VI.9 Observed energies for electronic levels of Nd^{3+} in Nd_2O_3 and $NdVO_4$ compared to the free ion (12 000-17 000 cm^{-1})

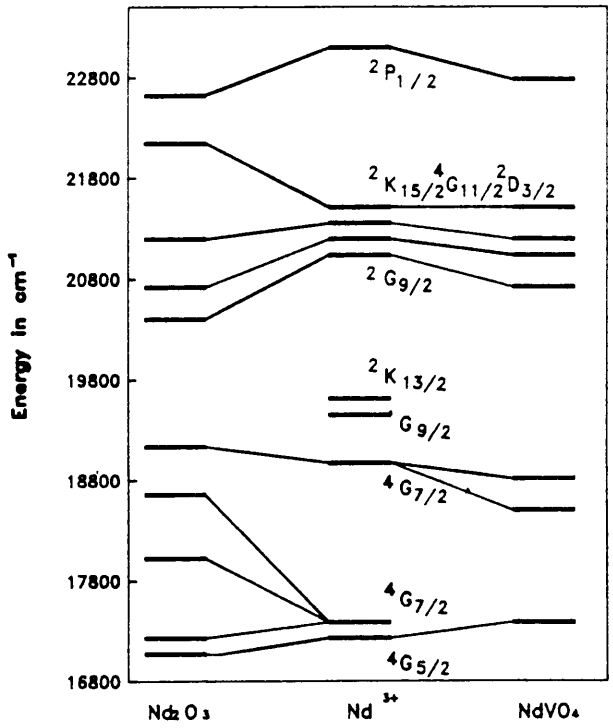

Figure VI.10 Observed energies for electronic levels of Nd^{3+} in Nd_2O_3 and $NdVO_4$ compared to the free ion (16 800-23 000 cm^{-1})

Table VI.5 Electronic energy levels (in cm^{-1}) of the Er^{3+} ion in Er_2O_3 and $ErVO_4$ at room temperature as determined by diffuse reflection UV- and visible spectroscopy

Er_2O_3	$ErVO_4$	Assignment
12 547	12 531	$^4I_{9/2}$
12 626	12 610	
14 706	14 993	$^4F_{9/2}$
14 859	15 106	
15 198	15 244	
15 385	15 337	
17 857		$^4S_{3/2}$
18 149	18 149	
18 349	18 416	
18 657	18 904	
19 231	19 120	$^2H_{11/2}$
19 608		
19 960	20 040	$^4F_{7/2}$
20 450	20 325	
20 877	20 534	
21 930	21 978	$^4F_{5/2}$
22 075	22 222	
22 573	22 523	$^4F_{3/2}$
24 673	24 691	$^2H_{9/2}$
25 840		$^4G_{11/2}$
26 525		
27 473		$^2G_{9/2}$
28 169		$^2K_{5/2}$
12 547	12 531	$^4I_{9/2}$

The UV- and visible diffuse reflectance spectra of Er_2O_3 and $ErVO_4(z)$ recorded at room temperature are shown in Figures VI.11 and VI.12. As for Nd^{3+} the Stark levels should be at least two fold degenerate in the Er^{3+} ion. $J + \frac{1}{2}$ crystalline Stark levels are expected for the erbium ion with D_{2d} site symmetry in $ErVO_4$. The two non-equivalent sites in cubic Er_2O_3, C_2 and C_{3i}, once again give rise to more absorption bands in the oxide than in the orthovanadate. This is indicated in Table VI.5 where observed energy levels are assigned and compared. Between 12 500 and 33 333 cm^{-1} the spectrum is dominated by absorption bands associated with transitions from the ground $^4I_{15/2}$ level of Er^{3+} to $^4F_{9/2}$, $^2H_{11/2}$ and $^4G_{11/2}$. Other bands correspond to transitions between the ground state level, $^4I_{15/2}$, in trivalent Er^{3+} and the following levels: $^4I_{9/2}$, $^4S_{3/2}$, $^4F_{7/2}$, $^4F_{5/2}$, $^2K_{15/2}$ are present in the oxide but cannot be distinguished for $ErVO_4$ because of the interference of a charge transfer band in vanadium(V) in this region of the spectrum. Energy levels of the free Er^{3+} ion are compared to observed energies for the lanthanide ion in Er_2O_3 and $ErVO_4$ in Figures VI.13-VI.16. The term splitting factors of the two compounds are presented in Table VI.6.

Table VI.6 Comparison of the term splitting (in cm^{-1}) in solid Er_2O_3 and $ErVO_4$

Level	Er_2O_3	$ErVO_3$
$^4F_{9/2}$	679	344
$^4S_{3/2}$	800	755
$^3H_{11/2}$	377	-
$^4F_{7/2}$	917	494
$^4F_{5/2}$	145	244
$^4G_{11/2}$	685	-

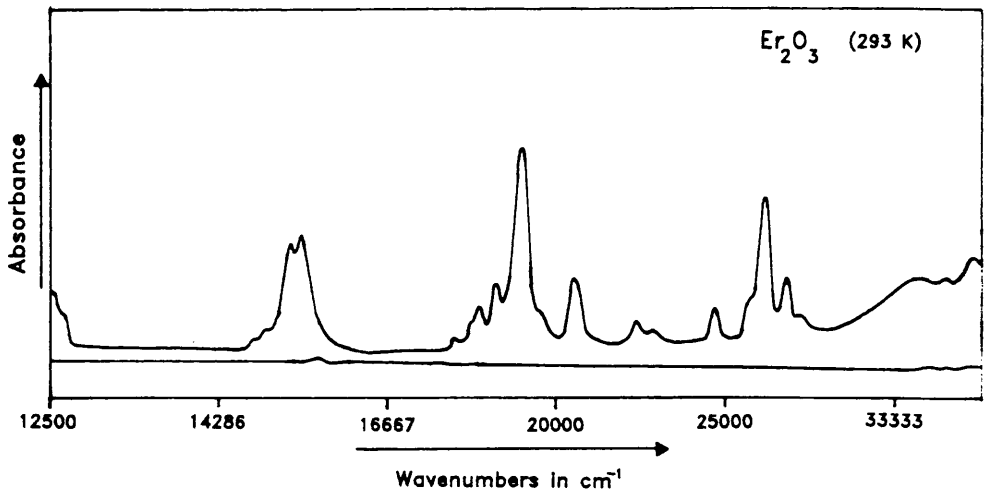

Figure VI.11 Diffuse reflectance UV/VIS spectrum of Er_2O_3

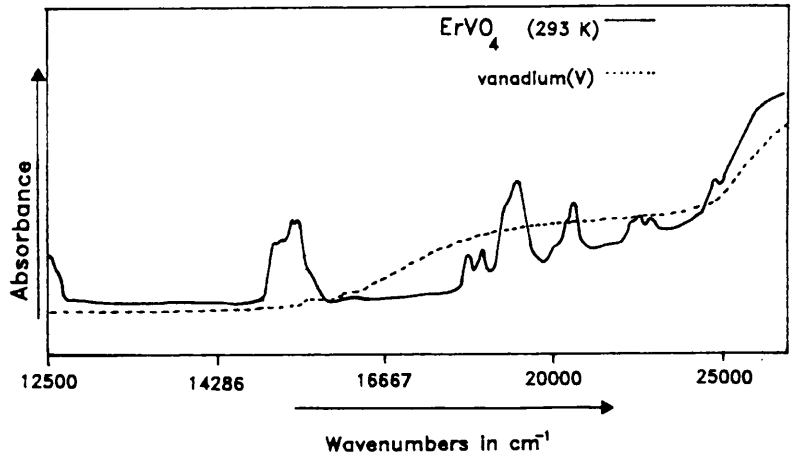

Figure VI.12 Diffuse reflectance UV/VIS spectrum of $ErVO_4$

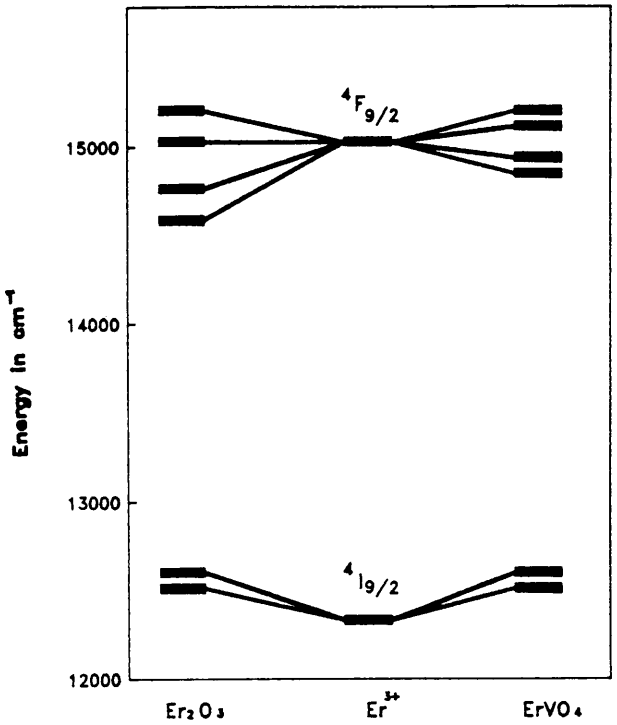

Figure VI.13 Observed electronic energy levels of Er^{3+} in the free ion, Er_2O_3 and $ErVO_4$ (12 000-16 000 cm^{-1})

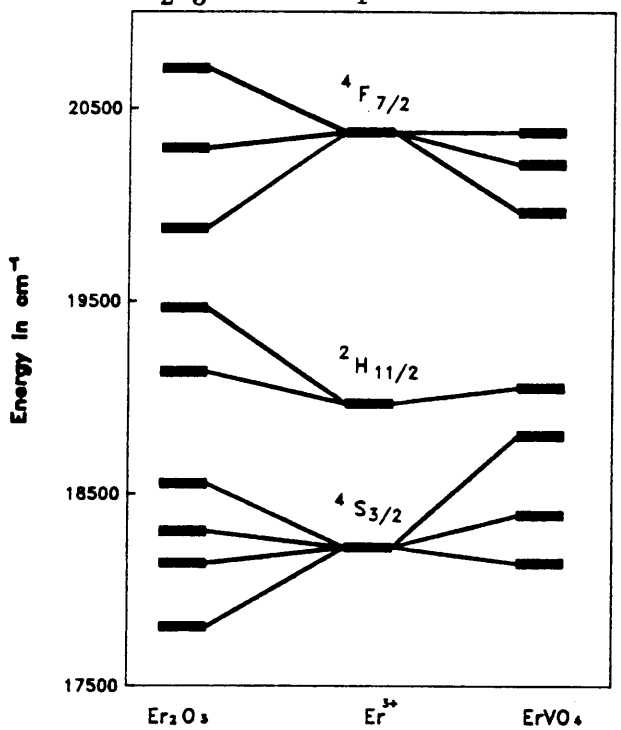

Figure VI.14 Observed electronic energy levels of Er^{3+} in the free ion, Er_2O_3 and $ErVO_4$ (17 500-21 000 cm^{-1})

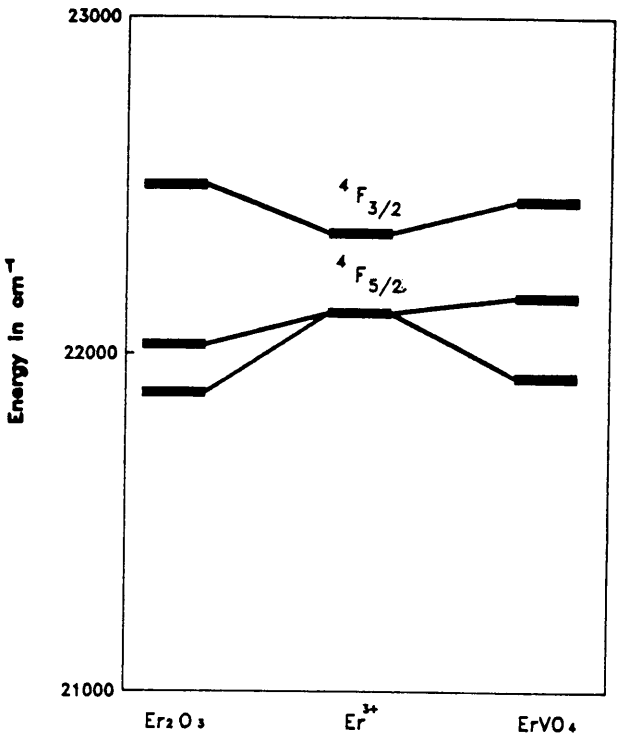

Figure VI.15 Observed electronic energy levels of Er^{3+} in the free ion, Er_2O_3 and $ErVO_4$ (21 000-23 000 cm^{-1})

VI.4.5 **Emission spectra**

(1) Er_2O_3

In Er_2O_3 the $^4I_{15/2} \longleftarrow {}^4F_{9/2}$ and $^4I_{15/2} \longleftarrow {}^4S_{3/2}$ fluorescence transitions were observed here in the vicinity of 15 000 and 18 000 cm^{-1}, respectively.

The observed transitions are shown in Figures VI.17-VI.19 and listed in Table VI.7. The room temperature $^4I_{15/2} \longleftarrow {}^4F_{9/2}$ emission band is very broad and weak (Figure VI.17) which make a distinction between Stark levels impossible. Theoretically fourty transitions should be possible between these levels for a single site. The $^4I_{15/2} \longleftarrow {}^4S_{3/2}$ transition was recorded both at 293 and 77 K (Figures VI.18 and VI.19). Fifteen of the sixteen transitions that are theoretically possible for one site only were observed between these two temperatures. The emission intensity of the latter transition is in the order of 10 times the intensity for the $^4I_{15/2} \longleftarrow {}^4F_{9/2}$ transition.

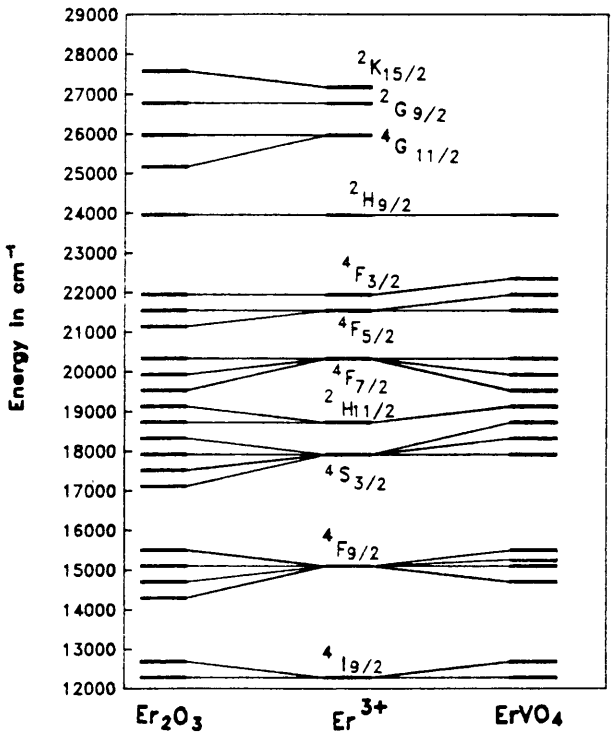

Figure VI.16 Total picture of electronic energy levels in Er_2O_3, the free ion and $ErVO_4$ between 12 000 and 29 000 cm^{-1}

Table VI.7 Observed fluorescence transitions and assignments in Er_2O_3.

Emission	Bandposition (cm^{-1})	
	293 K	77 K
$^4I_{15/2} \longleftarrow {}^4F_{9/2}$	14 619 vw	
	15 145 vw	
$^4I_{15/2} \longleftarrow {}^4S_{3/2}$	17 724 vs	17 701 vs
		17 765 sh
	17 811 m	17 804 m
	17 965 m	17 961 m
	18 048 m	18 044 m
		18 058 sh
		18 133 w
	18 143 w	18 147 sh
	18 190 w	18 184 w
	18 227 w	18 221 w
		18 234 sh
	18 274 w	18 268 w
	18 314 w	18 308 w
	18 535 vw	
	18 563 sh	

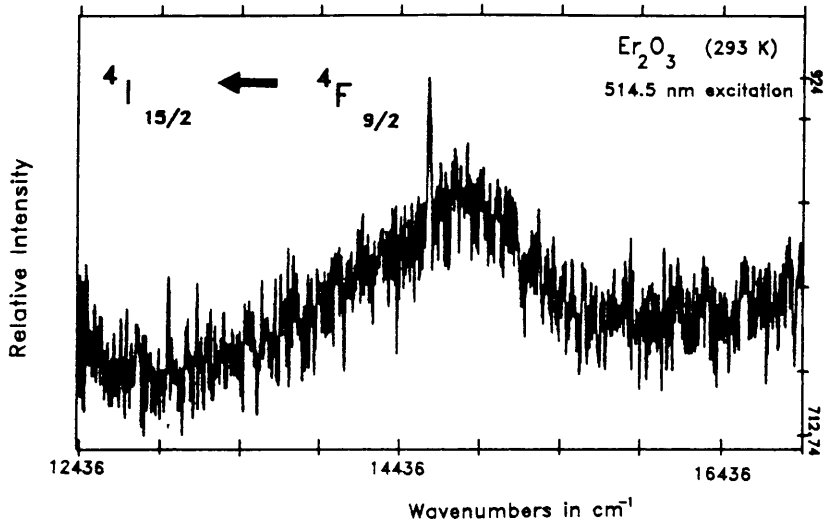

Figure VI.17 $^4I_{15/2} \longleftarrow {}^4F_{9/2}$ transition in Er_2O_3

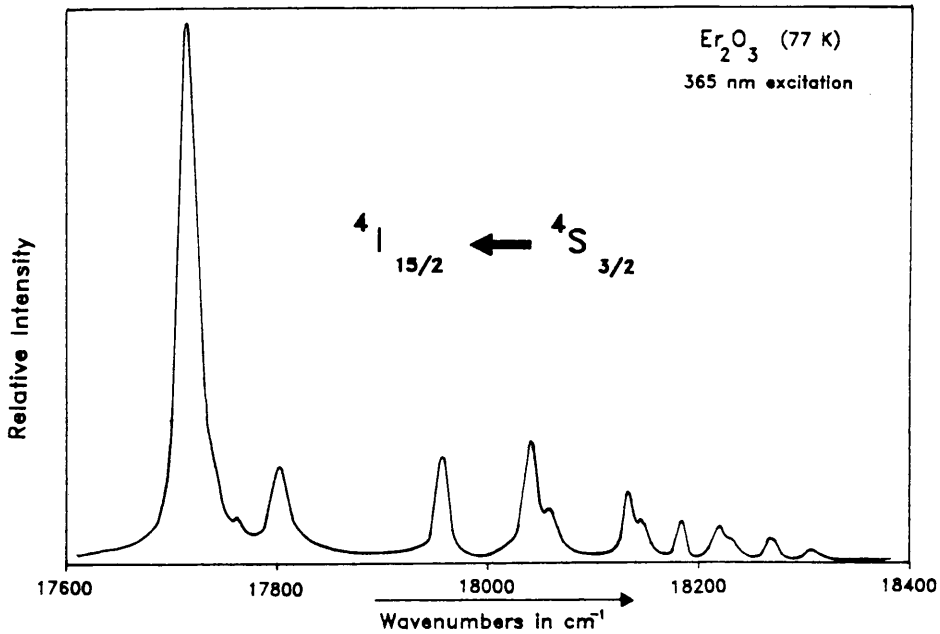

Figure VI.18 $^4I_{15/2} \longleftarrow {}^4S_{3/2}$ transition in Er_2O_3

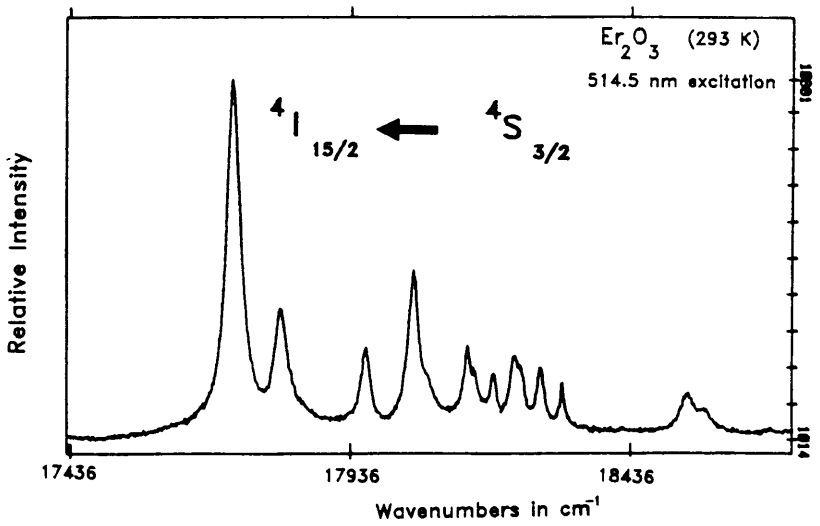

Figure VI.19 $^4I_{15/2} \longleftarrow {}^4S_{3/2}$ transition in Er_2O_3

(2) $ErVO_4$

The positions of the bands in the fluorescence spectra of $ErVO_4$ are shown in Table VI.8. The following three emission transitions were observed $^4I_{15/2} \longleftarrow {}^4F_{9/2}$; $^4I_{15/2} \longleftarrow {}^4S_{3/2}$ and $^4I_{15/2} \longleftarrow {}^2H_{11/2}$. The fluorescence originating from the $^4F_{9/2}$ level is very weak but sufficient for the observation of some crystal field splitting of the levels involved. This transition between $^4F_{9/2}$ and $^4S_{3/2}$ at room temperature is shown in Figure VI.20. The recorded intensity for the $^4I_{15/2} \longleftarrow {}^2H_{11/2}$ transition is considerably higher as is indicated in Figure VI.21 and about twelve Stark levels can be distinguished. Details of the 293, 77, 4.2 and 1.3 K spectra of the $^4I_{15/2} \longleftarrow {}^4S_{3/2}$ transition are shown in Figures VI.22 and VI.23. At low temperatures (Figure VI.23) the bands are well resolved compared to those recorded at room temperature (Figure VI.22). Over the temperature range between 1.3 and 293 K twelve components were observed. The maximum intensities in this transition at room temperature are more than twice that of the maximum emission intensity originating from the $^2H_{11/2}$ level (Figure VI.22).

(3) $EuVO_4$

In $EuVO_4$ emission was observed from the $^5D_1$ and $^5D_0$ levels after excitation to either 19 436 or 20 492 cm^{-1}. Transitions from $^5D_0$ to the $^7F_5$, $^7F_4$, $^7F_3$, $^7F_2$, $^7F_1$, $^7F_0$ levels occurred respectively in the 13 000, 14 500, 15 500, 16 000, 16 800 and 17 200 cm^{-1} regions. The $^5D_1$ to $^7F_1$ and $^7F_0$ transitions were observed around 18 500 and 19 000 cm^{-1} while the $^5D_1$ to $^7F_4$ and $^7F_3$ transitions respectively coincide with the $^5D_0$ to $^7F_2$ and $^7F_1$ bands around 16 000 and 16 800 cm^{-1} (Table VI.9). These transitions are illustrated in Figure VI.24.

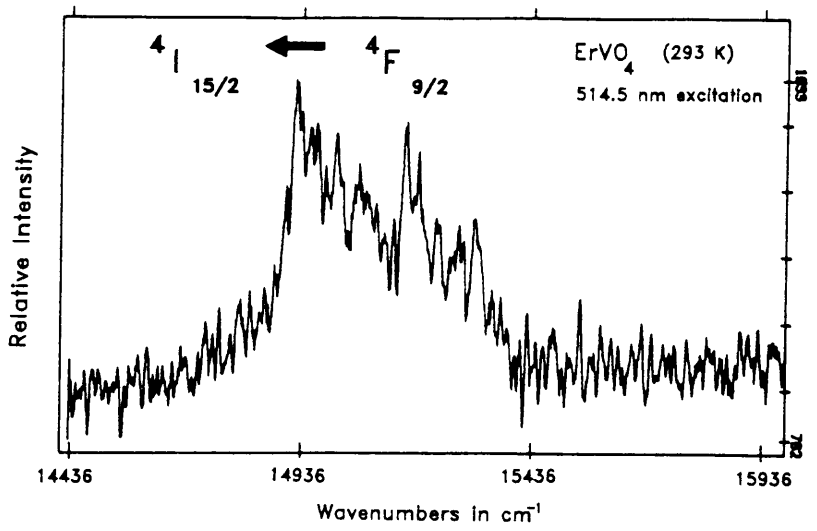

Figure VI.20 $^4I_{15/2} \longleftarrow {}^4F_{9/2}$ transition in $ErVO_4$

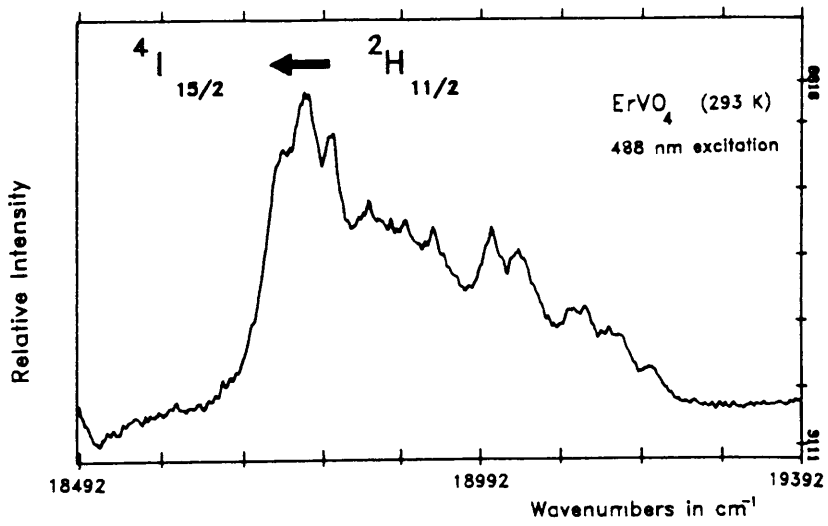

Figure VI.21 $^4I_{15/2} \longleftarrow {}^4H_{11/2}$ transition in $ErVO_4$

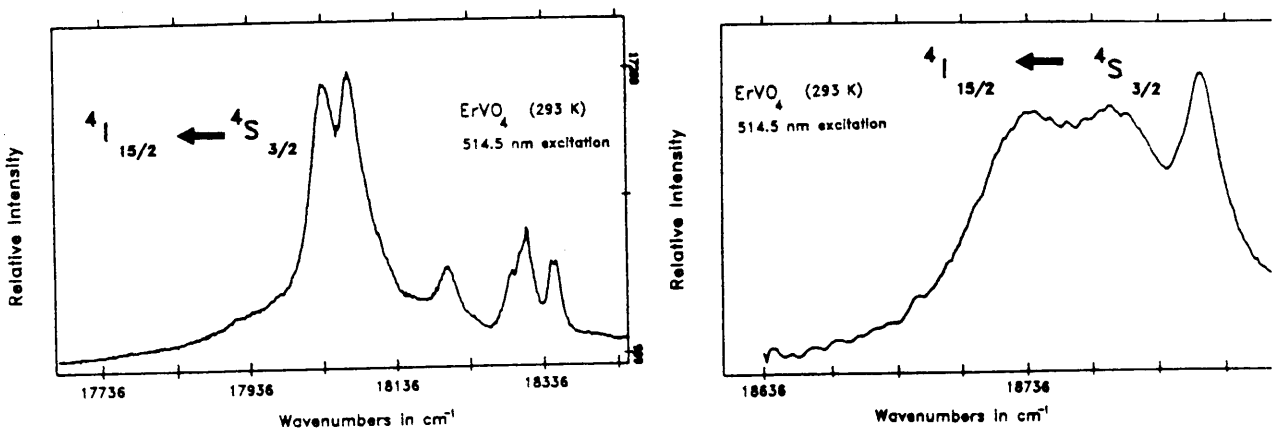

Figure VI.22 $^4I_{15/2} \longleftarrow {}^4S_{3/2}$ transition in $ErVO_4$

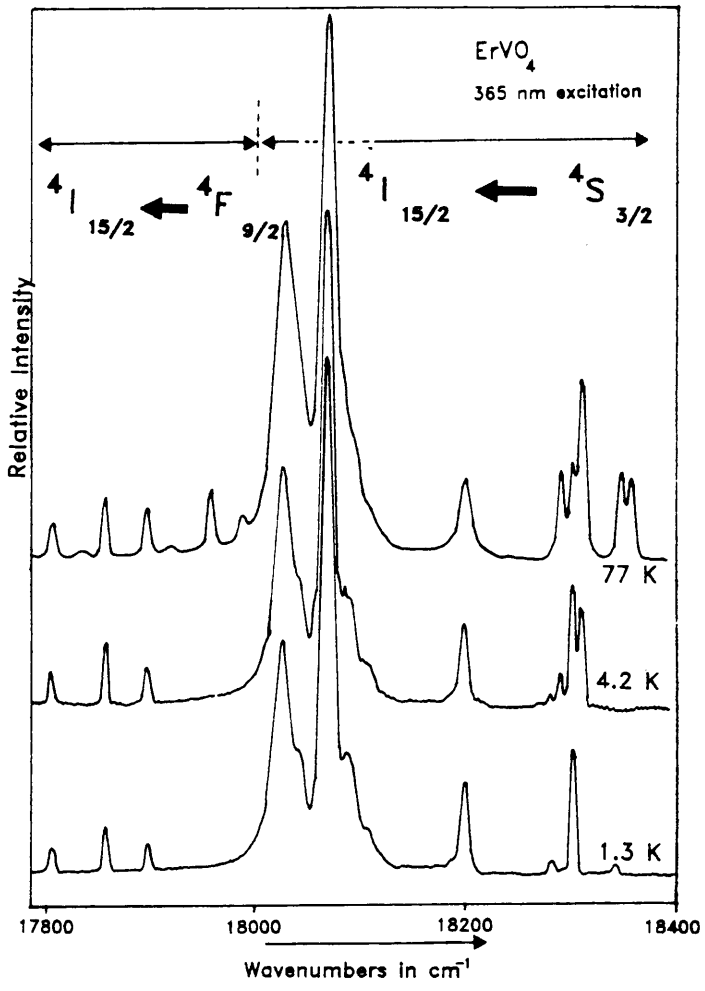

Figure VI.23 The $^4I_{15/2} \longleftarrow {}^4S_{3/2}$ and $^4I_{15/2} \longleftarrow {}^4F_{9/2}$ transitions in $ErVO_4$ at low temperatures

Table VI.8 Observed fluorescence transitions and assigments in $ErVO_4$

Emission	Bandposition (cm^{-1})			
	293 K	77 K	4.2 K	1.3 K
$^4I_{15/2} \longleftarrow {}^4F_{9/2}$	14 928 vw			
	15 020			
	15 067			
	15 160			
	15 186			
	15 277			
	15 927			
		17 806	17 805	17 805
	17 246	17 859	17 873	17 859
		17 897	17 897	17 900
	17 419	17 971		
		17 988		
	17 504			
$^4I_{15/2} \longleftarrow {}^4S_{3/2}$	18 041	18 029	18 028	18 029
	18 058 sh		18 040	18 044
	18 069 sh	18 070		
	18 074	18 092 sh	18 089 sh	18 109 sh
		18 106	18 110 sh	
	18 206	18 200	18 200	18 200
		18 281	18 291	18 281
	18 293	18 289		
	18 303 sh	18 300	18 303	18 300
	18 304	18 310	18 311	
	18 348	18 347		
	18 355	18 374		
	18 743			
	18 769			
	18 800			
	18 851			
$^4I_{15/2} \longleftarrow {}^2H_{11/2}$	18 898			
	18 933			
	19 005			
	19 037			
	19 104			
	19 120			
	19 152			
	19 198			

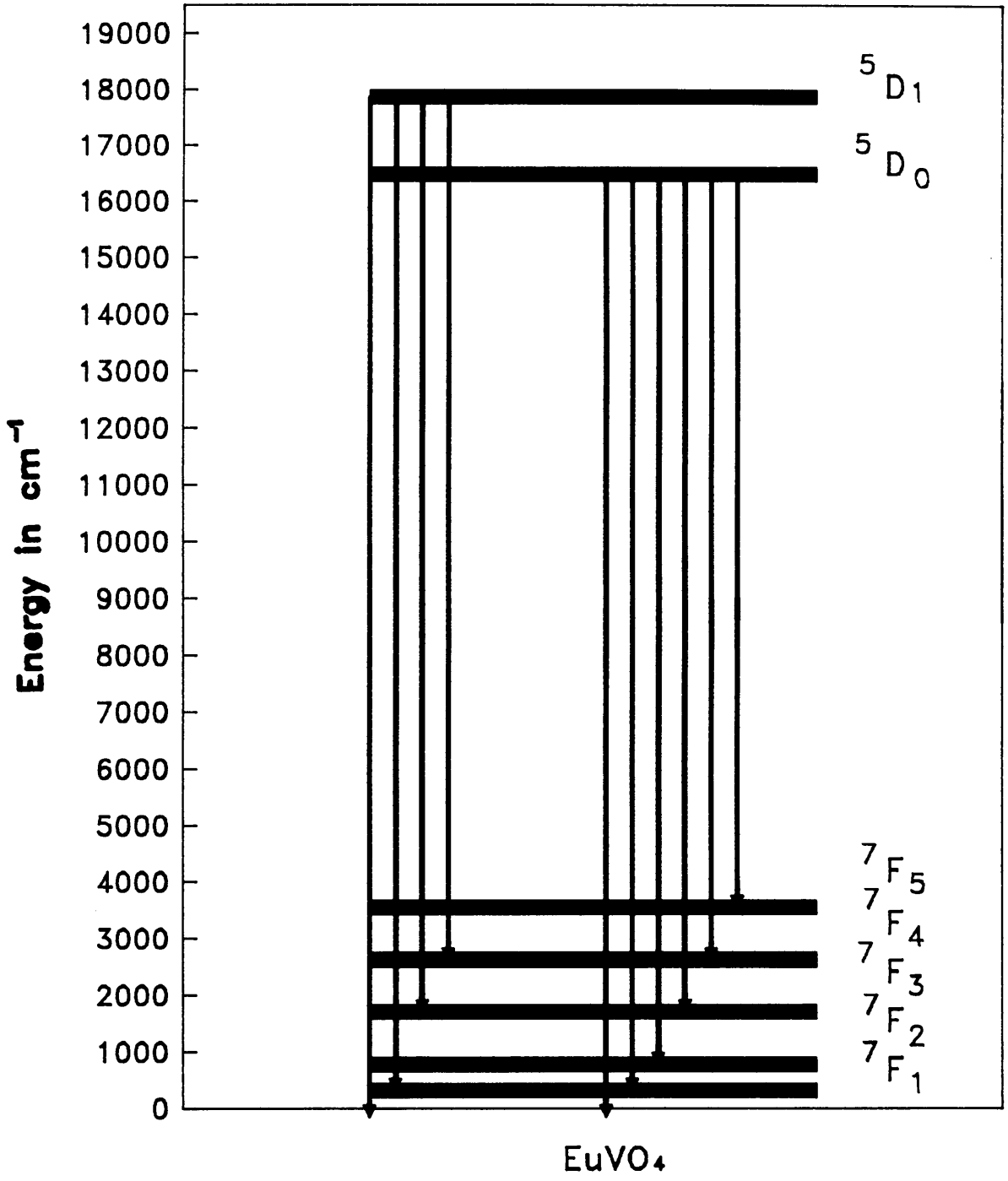

Figure VI.24 Diagram of observed transitions in $EuVO_4$

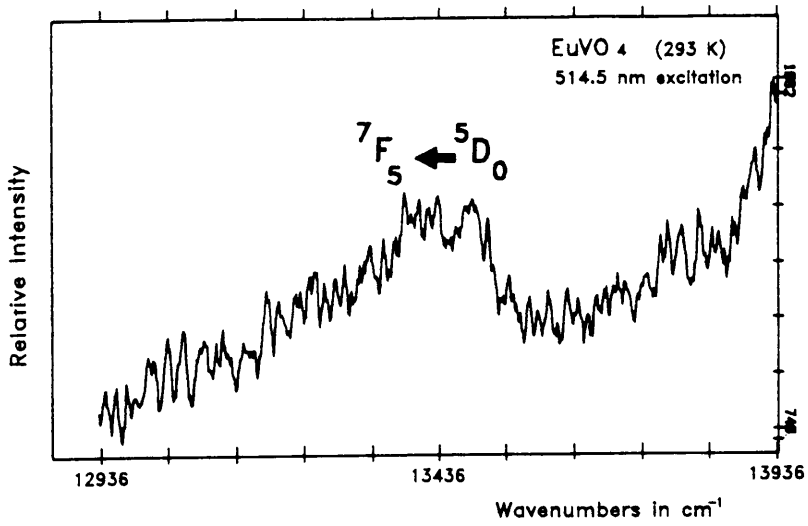

Figure VI.25 The weak $^7F_5 \longleftarrow {}^5D_0$ emission transition in $EuVO_4$

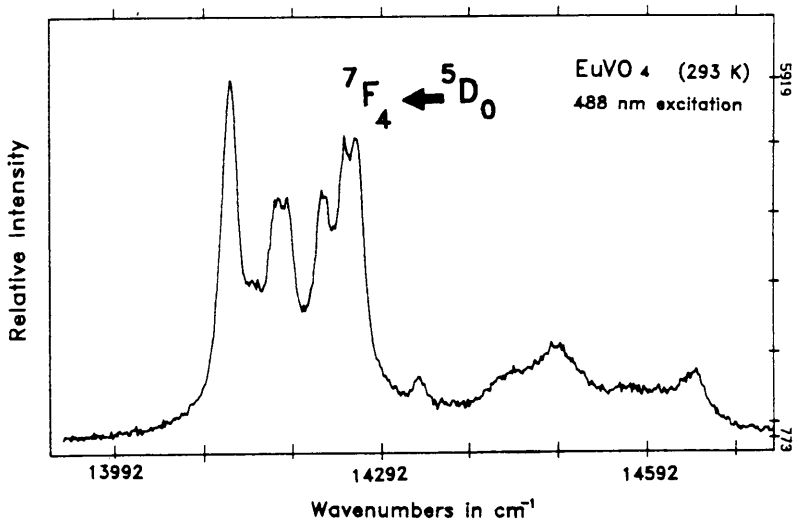

Figure VI.26 The $^7F_4 \longleftarrow {}^5D_0$ transition in $EuVO_4$. Some of the bands could also be attributed to $^7F_5 \longleftarrow {}^5D_1$

Table VI.9 Observed fluorescence transitions and assignments in $EuVO_4$ at 293 K

Emission	Bandposition (cm^{-1})		Emission	Bandposition (cm^{-1})	
	514.5 nm	488 nm		514.5 nm	488 nm
$^7F_5 \leftarrow {}^5D_0$	13 406 vw		$^7F_2 \leftarrow {}^5D_0$/	16 018	16 002
	13 486 vw		$^7F_4 \leftarrow {}^5D_1$	16 124	16 119
				16 213	16 229
$^7F_4 \leftarrow {}^5D_0$	14 124	14 122		16 263	16 266
	14 150			16 317	16 316
	14 175	14 175		16 349	
	14 189	14 197		16 367	16 366
				16 468	
	14 229	14 226		16 497	16 493
	14 252	14 251	$^7F_1 \leftarrow {}^5D_0$/	16 729	16 727
			$^7F_3 \leftarrow {}^5D_1$	16 844	
	14 265	14 262		16 907	16 906
				16 937	
	14 337	14 334		16 996	16 996
	14 437				
	14 487	14 485	$^7F_0 \leftarrow {}^5D_0$	17 240	17 242
		14 575		17 255	17 257
	14 641	14 642			
			$^7F_1 \leftarrow {}^5D_1$	18 475	
$^7F_3 \leftarrow {}^5D_0$	15 171			18 485	18 488
	15 183	15 183		18 686	18 695
				18 717	
	15 270	15 270		18 729	
	15 360	15 363			
		15 425	$^7F_0 \leftarrow {}^5D_1$	18 972	
	15 530	15 523		18 989	18 992
				19 009	

Brecher et.al. [124] have reported the polarized emission and absorption spectra of single crystals of yttrium vanadate doped with Eu^{3+} (zircon structure). The $^7F_5 \longleftarrow {}^5D_0$ transition, not observed by Brecher [124] as it was too weak for their experimental conditions, occurs as a broad and weak peak between 12 936 and 13 636 cm^{-1} with 514.5 nm excitation (Figure VI.25). No crystal field splitting of the levels can be distinguished here because of the low intensity of the broad band. The $^7F_4 \longleftarrow {}^5D_0$ emission in Figure VI.26 could possibly overlap with the $^7F_5 \longleftarrow {}^5D_1$ transition which is also expected in this region. The $^7F_3 \longleftarrow {}^5D_0$ transition is shown in Figure VI.27 and six components are observed. Only three of the seven possibly transitions should be optically active but Brecher et.al. [124] reported a fourth band which was ascribed to a possible higher level transition. Both the $^7F_4 \longleftarrow {}^5D_1$ and $^7F_2 \longleftarrow {}^5D_0$ transitions occur between 15 800 and 16 500 cm^{-1} (Figure VI.28) and both the $^7F_1 \longleftarrow {}^5D_0$ and $^7F_3 \longleftarrow {}^5D_1$ transitions between 16 729 and 16 996 cm^{-1} (Figure VI.29).

The optical activity for the $^7F_0 \longleftarrow {}^5D_0$ transition was reported to be forbidden for D_2d site symmetry [119] but appeared in the powder spectra of $YVO_4 : Eu^{3+}$. Two strong bands at 17 240 and 17 255 cm^{-1} are attributed to this transition in Figure VI.30. One or both of these bands can also be part of $^7F_3 \longleftarrow {}^5D_1$ emission. A higher level transition e.g. $^7F_3 \longleftarrow {}^5D_2$ is unlikely as the $^5D_2$ level lies at 21 400 cm^{-1}, much higher than the excitation lines respectively at 19 436 and 20 492 cm^{-1}. Both the $^4F_1 \longleftarrow {}^5D_1$ and $^7F_0 \longleftarrow {}^5D_1$ transitions are relatively weak and appear between vibrational Raman modes of the orthovanadate with 514.5 nm excitation (Figures VI.31 and VI.32).

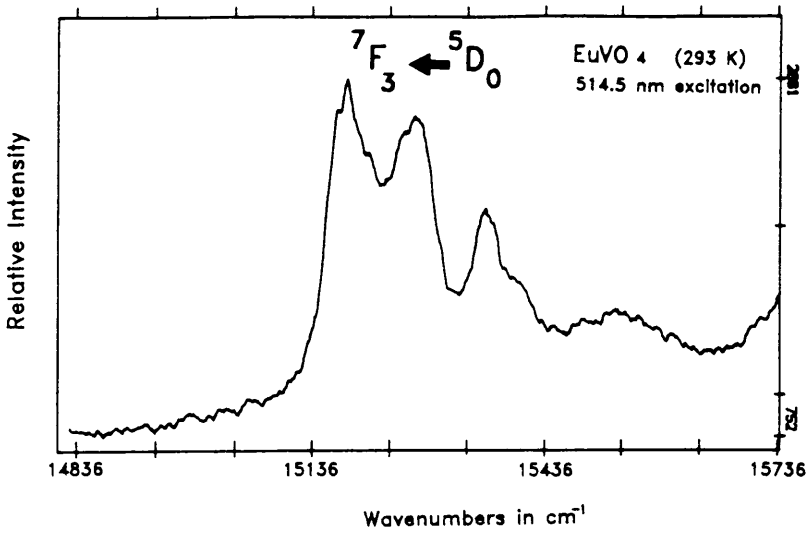

Figure VI.27 The $^7F_3 \longleftarrow {}^5D_0$ emission in $EuVO_4$

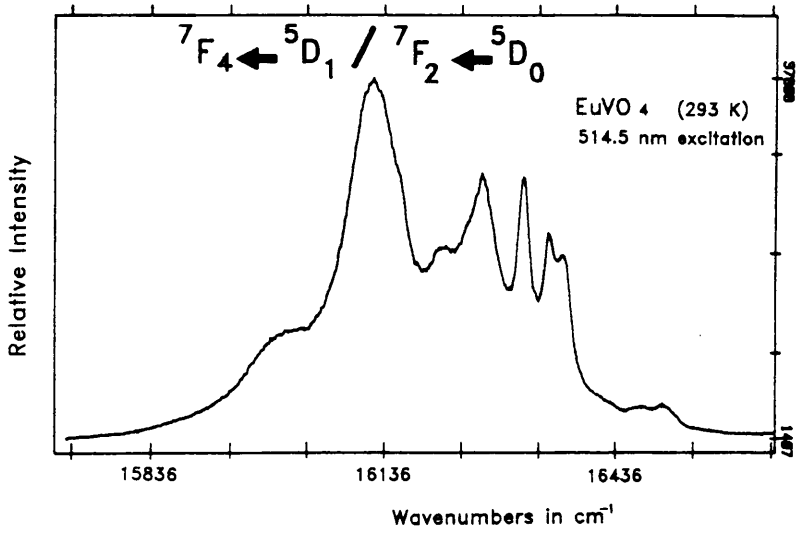

Figure VI.28 Two transitions of $EuVO_4$: $^7F_4 \longleftarrow {}^5D_1$ and $^7F_2 \longleftarrow {}^5D_0$

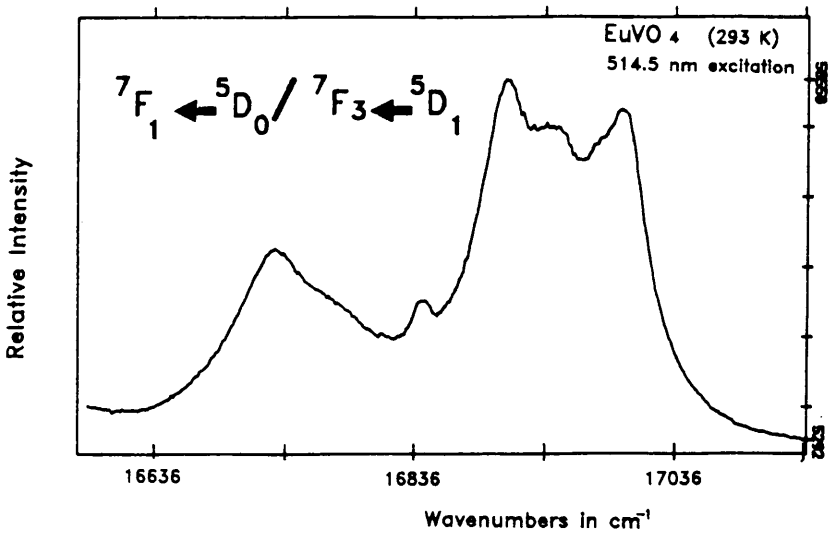

Figure VI.29 $^7F_3 \longleftarrow {}^5D_1$ and $^7F_1 \longleftarrow {}^5D_0$ transitions $EuVO_4$

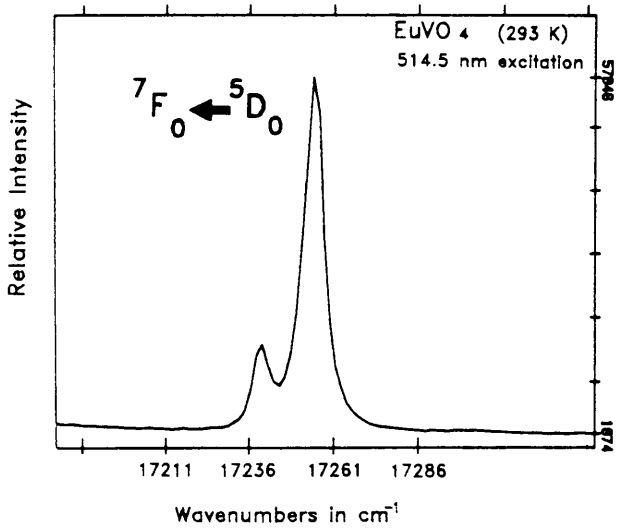

Figure VI.30 Bands in this region can be attributed to either the $^7F_0 \longleftarrow {}^5D_0$ or $^7F_3 \longleftarrow {}^5D_1$ transition

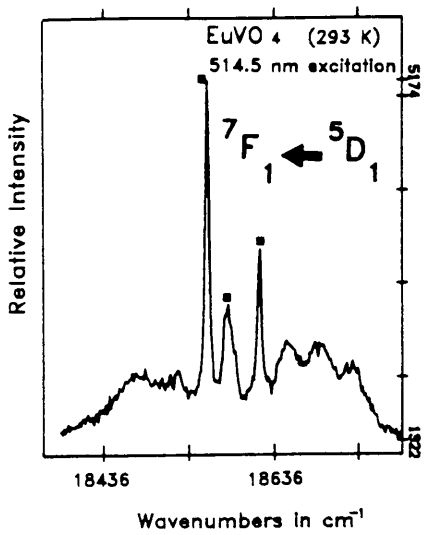

Figure VI.31 The $^7F_1 \longleftarrow {}^5D_1$ transition in $EuVO_4$. Bands marked ■ are Raman active vibrations of VO_4^{3-}

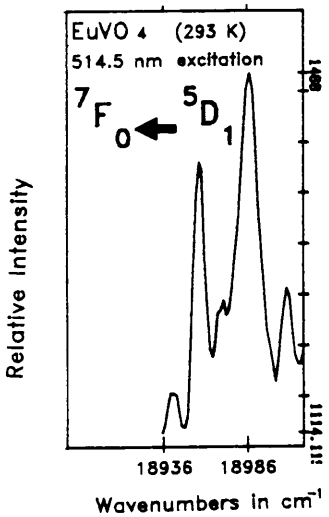

Figure VI.32 The $^7F_0 \longleftarrow {}^5D_1$ transition in $EuVO_4$

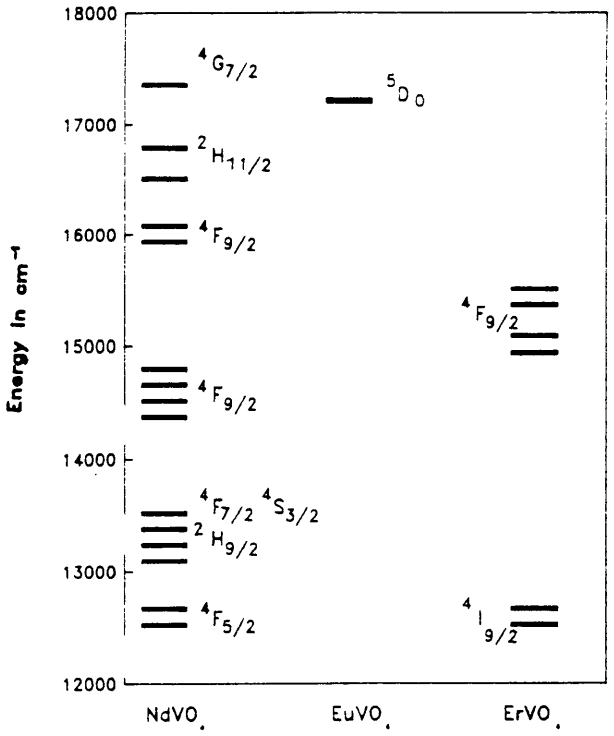

Figure VI.33 Comparison between observed electronic energy levels in $NdVO_4$, $EuVO_4$ and $ErVO_4$ (12 000-18 000 cm^{-1})

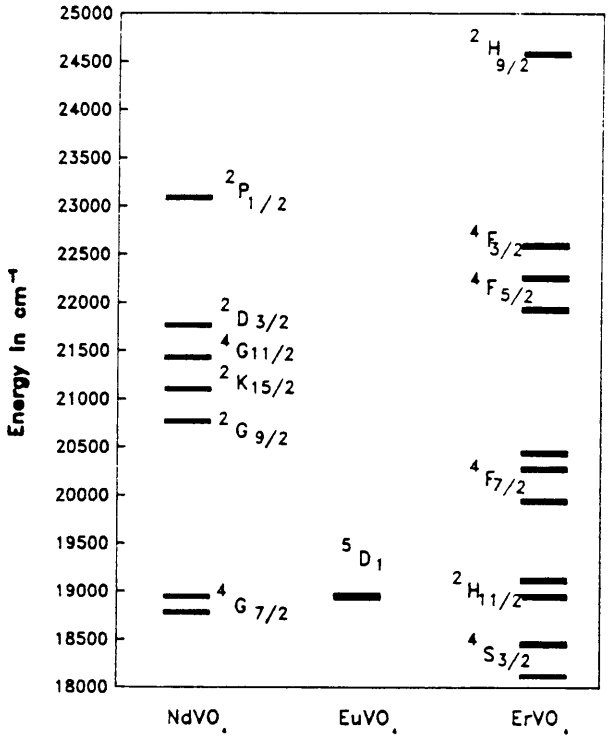

Figure VI.34 Comparison between observed electronic energy levels in $NdVO_4$, $EuVO_4$ and $ErVO_4$ (18 000-25 000 cm^{-1})

APPENDIX A - Kinetics Tables

Table A.1

Kinetic data for the decomposition of NH_4VO_3 to $(NH_4)_2V_6O_{16}$ at 423 K

$I_o = 687$

No	t[s]	ln t	I	$I/I_o = \chi_{VO_3^-}$
1	90	4.50	647	0.942
2	135	4.91	571	0.831
3	180	5.19	558	0.812
4	225	5.42	508	0.739
5	270	5.60	528	0.769
6	315	5.75	510	0.742
7	360	5.89	474	0.690
8	405	6.00	516	0.751
9	450	6.11	503	0.732
10	495	6.21	492	0.716
11	540	6.29	519	0.755

t = time in seconds

I_o = intensity at time 0

I = intensity at time t

$\chi_{VO_3^-}$ = fraction reactant present at time t

Table A.2

Kinetic data for the decomposition of NH_4VO_3 to $(NH_4)_2V_6O_{16}$ at 428 K

$I_o = 895$

No	t[s]	ln t	I	$I/I_o = \chi_{VO_3^-}$
1	90	4.50	788	0.880
2	135	4.91	705	0.788
3	180	5.19	608	0.679
4	225	5.42	610	0.682
5	270	5.60	567	0.634
6	315	5.75	565	0.631
7	360	5.89	556	0.621
8	405	6.00	578	0.646
9	450	6.11	557	0.622
10	495	6.21	595	0.665
11	540	6.29	607	0.678

Table A.3

Kinetic data for the decomposition of NH_4VO_3 to $(NH_4)_2V_6O_{16}$ at 433 K

$I_o = 462$

No	t[s]	ln t	I	$I/I_o = \chi_{VO_3^-}$
1	75	4.32	439	0.950
2	120	4.79	400	0.866
3	165	5.11	365	0.790
4	210	5.35	344	0.745
5	255	5.54	339	0.734
6	300	5.70	351	0.760
7	345	5.84	326	0.706
8	390	5.97	335	0.725
9	435	6.08	339	0.734
10	480	6.17	323	0.699
11	525	6.26	330	0.714
12	585	6.37	338	0.732

Table A.4

Kinetic data for the decomposition of NH_4VO_3 to $(NH_4)_2V_6O_{16}$ at 438 K

$I_o = 864$

No	t[s]	ln t	I	$I/I_o = \chi_{VO_3^-}$
1	90	4.50	658	0.762
2	135	4.91	567	0.656
3	180	5.19	499	0.578
4	225	5.42	469	0.543
5	270	5.60	403	0.466
6	315	5.75	390	0.451
7	360	5.89	391	0.453
8	405	6.00	384	0.444
9	450	6.11	402	0.465
10	495	6.21	407	0.471
11	540	6.29	416	0.481

Table A.5

Kinetic data for the decomposition of NH_4VO_3 to $(NH_4)_2V_6O_{16}$ at 443 K

$I_o = 698$

No	t[s]	ln t	I	$I/I_o = \chi_{VO_3^-}$
1	100	4.61	518	0.742
2	145	4.98	414	0.593
3	190	5.25	381	0.546
4	235	5.46	331	0.474
5	280	5.63	352	0.504
6	325	5.78	351	0.503
7	370	5.91	341	0.489
8	415	6.03	333	0.477
9	460	6.13	326	0.467
10	505	6.22	340	0.487
11	550	6.31	327	0.468
12	610	6.41	337	0.483

APPENDIX B - NH_4VO_3 Tables

Table B.1 Vibrational frequencies of NH_4^+ in the infrared spectra of NH_4VO_3 at 80 K and room temperature

Assignment	Wavenumbers in cm^{-1}	
	80 K	RT
ν_3	3207 s	3190 s
ν_3	3135 s	-
ν_3	3122 sh	-
$\nu_2 + \nu_4$	3088 m	-
$\nu_2 + \nu_4$	3060 m	-
$\nu_1 + \nu_5$	3019 m	3000 sh
ν_1	2926 s	2925 s
ν_1, $2\nu_4$	2899 sh	-
$2\nu_4$	2858 m	-
$2\nu_4$	2839 m	-
$2\nu_4$	2830 sh	-
$2\nu_4$	2810 m	-
$2\nu_4$	2790 s	2796 sb
$\nu_2 + \nu_6$	1944 b	-
$\nu_2 + \nu_6$	2004 b	2000 b.w
$\nu_4 + \nu_6$	1795 w	-
$\nu_4 + \nu_6$	1770 b	-
$\nu_4 + \nu_6$	1737 b	1737 b
ν_2	1663 sp	1559 w
ν_4	1422 vs	-
ν_4	1414 vs	1417 vs
ν_4	1406 sh	-

Table B.2 Vibrational frequencies of NH_4^+ in the infrared spectra of 1% NH_4VO_3 at 80 K and room temperature

Assignment	Wavenumbers in cm^{-1}	
	80 K	RT
$\nu_3(NH_4^+)$	3215 s	3185 s
$\nu_3(NH_4^+)$	3142 sh	-
$\nu_2 + \nu_4(NH_4^+)$	3088 s	-
$\nu_2 + \nu_4(NH_4^+)$	3060 m	-
$\nu_1 + \nu_5(NH_4^+)$	3025 m	-
$\nu_1(NH_4^+)$	2927 s	2953 s
$2\nu_4(NH_4^+)$	2857 m	-
$2\nu_4(NH_4^+)$	2793 s	2792 s
$\nu_1(NH_3D^+)$	2370 w	-
$\nu_1(NH_3D^+)$	2348 w	2351 w
$\nu_2 + \nu_4(ND_4^+)$	2273 w.b	2207 w
$\nu_1(NH_3D^+)$	2196 m	-
$\nu_2 + \nu_4(NH_4^+)$	2012 w.b	1981 w.b
$\nu_4 + \nu_6(NH_4^+)$	1766 m	1728 m.b
$\nu_2(NH_4^+)$	1664 m	1655 m
$\nu_2(NH_3D^+)$	1611 w	1605 m
$\nu_4(NH_4^+)$	1422 vs	-
$\nu_4(NH_4^+)$	1411 vs	1410 vs
$\nu_4(NH_3D^+)$	1276 m	-
$\nu_4(NH_3D^+)$	1267 m	-
$\nu_4(NH_3D^+)$	1257 m	1257 m
$\nu_4(NH_3D^+)$	1250 m	-
$\nu_2(ND_4^+)$	1144 w	1144 w
$\nu_4(ND_4^+)$	1127 vw	-
$\nu_4(ND_4^+)$	1050 vw	1047 vw

Table B.3 Ammonium vibrations in the infrared spectra of 5% D NH_4VO_3

Assignment	Wavenumbers in cm^{-1}		Assignment	Wavenumbers in cm^{-1}	
	80 K	RT		80 K	RT
$\nu_3(NH_4^+)$	3209 s	3195 m	$\nu_4(NH_3D^+)$	1267 m	-
$\nu_3(NH_4^+)$	3140 sh	-	$\nu_4(NH_3D^+)$	1257 m	1259 w
$\nu_2 + \nu_4(NH_4^+)$	3086 sh	-	$\nu_4(NH_3D^+)$	1250 m	-
$\nu_2 + \nu_4(NH_4^+)$	3061 sh	-	$\nu_2(ND_4^+)$	1194 vw	-
$\nu_1 + \nu_5(NH_4^+)$	3020 sh	-	$\nu_{4c}(NH_2D_2^+)$	1187 vw	-
$\nu_1(NH_4^+)$	2928 s	2954 bm	$\nu_2(ND_4^+)$	1182 vw	1183 vw
$2\nu_4(NH_4^+)$	2836 s	2829 sh	$\nu_4(ND_4^+)$	1124 w	1121 vw
$2\nu_4(NH_4^+)$	2810 s	-	$\nu_4(ND_4^+)$	1079 vw	-
$2\nu_4(NH_4^+)$	2795 s	2798 m			
$\nu_1(NH_3D^+)$	2371 w	2359 w			
$\nu_1(NH_3D^+)$	2354 vw	2348 w			
$2\nu_4(ND_4^+)$	2248 vw	2212 vw			
$\nu_1(NH_3D^+)$	2199 m	-			
$\nu_1(ND_4^+)$	2185 sh	-			
$2\nu_4(ND_4^+)$	2166 sh	-			
$\nu_2 + \nu_6(NH_4^+)$	2001 wb	-			
$\nu_4 + \nu_6(NH_4^+)$	1776 w	1782 vw			
$\nu_2(NH_4^+)$	1650 wb	1660 vw			
$\nu_2(NH_3D^+)$	1611 w	1603 w			
$\nu_4(NH_4^+)$	1433 sh	-			
$\nu_4(NH_4^+)$	1420 vs	1415 s			
$\nu_4(NH_4^+)$	1410 vs	-			
$\nu_4 + \nu_6(ND_4^+)$	1344 w	-			
$\nu_{4b}(NH_2D_2^+)$	1325 w	-			
$\nu_4(NH_3D^+)$	1276 m	1273 sh			

Table B.4 Ammonium vibrations in the infrared spectra of 30% D NH_4VO_3

Assignment	Wavenumbers in cm^{-1}		Assignment	Wavenumbers in cm^{-1}	
	80 K	RT		80 K	RT
$\nu_3(NH_4^+)$	3211 s	3194 m	$_{2a}(NH_2D_2^+)$	1564 vw	-
$\nu_3(NH_4^+)$	3134 sh	-	$\nu_2 + \nu_6(ND_4^+)$	1445 vw	-
$\nu_1 + \nu_5(NH_4^+)$	3027	-	$\nu_4(NH_4^+)$	1432 vw	-
$\nu_1(NH_4^+), \nu_3(NH_3D^+)$	2934 s	2953 b.m	$\nu_4(NH_4^+)$	1419 m	-
$2\nu_4(NH_4^+)$	2835 m	-	$\nu_4(NH_4^+)$	1141 vs	1413 vs
$2\nu_4(NH_4^+)$	2812 m	2822 b	$\nu_4 + \nu_6(ND_4^+)$	1344 w	1344 vw
$2\nu_4(NH_4^+)$	2798 s	2798 w	$\nu_{4b}(NH_2D_2^+)$	1325 w	1333 vw
$2\nu_4(NH_4^+)$	2729 vw	-	$\nu_4(NH_3D^+)$	1276 m	-
$\nu_2 + \nu_4(NHD_3^+)$	2478 vvw	-	$\nu_4(NH_3D^+)$	1268 m	-
$\nu_3(ND_4^+)$	2409 vw	-	$\nu_4(NH_3D^+)$	1258 m	1258 m.
$\nu_3(ND_4^+)$	2386 w	-	$\nu_4(NH_3D^+)$	1250 m	-
$\nu_1(NH_3D^+)$	2370 m	-	$\nu_2(ND_4^+)$	1192 w	-
$\nu_1(NH_3D^+)$	2352 sh	2358 m	$\nu_{4c}(NH_2D_2^+)$	1188 w	1186 vw
$2\nu_4(ND_4^+)$	2249 w	-	$\nu_2(ND_4^+)$	1182 w	1179 vw
$\nu_1(ND_4^+)$	2202 mb	2205 w	$\nu_4(ND_4^+)$	1124 w	2230 w
$\nu_1(ND_4^+)$	2184 m	-	$\nu_{4bc}(NHD_3^+)$,		
$\nu_1(NH_3D^+)$	2170 sh	-	$\nu_{4a}(NHD_3^+)$	1091 vvw	1084 vw
$2\nu_2(ND_4^+)$	2134 vw	-	$\nu_4(ND_4^+)$	1078 vvw	1071 vw
$\nu_4 + \nu_6(NH_4^+)$	1778 vw	-			
$\nu_2(NH_4^+)$	1655 vw	-			
$\nu_2(NH_3D^+)$	1608 w	1601 vw			

Table B.5 Ammonium vibrations in the infrared spectra of 50% D NH_4VO_3

Assignment	Wavenumbers in cm^{-1}		Assignment	Wavenumbers in cm^{-1}	
	80 K	RT		80 K	RT
$\nu_3(NH_4^+)$	3208 s	3188 s	$2\nu_4(ND_4^+)$	2115 w	-
$\nu_3(NH_4^+)$	3124 m	-	$\nu_4 + \nu_6(NH_4^+)$	1781 w	1771 w
$\nu_1(NH_2D_2^+)$	2946 m	2958 m	$\nu_2(NH_3D^+)$	1608 vw	-
$\nu_3(NH_2D_2^+)$	2919 m	2926 m	$\nu_{2a}(NH_2D_2^+)$	1563 w	1557 vw
$2\nu_4(NH_4^+)$	2834 m	-	$\nu_4(NH_4^+)$	1414 m	1416 m
$2\nu_4(NH_4^+)$	2798 w	2797 w	$\nu_4(NH_4^+)$	1403 sh	-
$2\nu_4(NH_4^+)$	2728 w	2734 vw	$\nu_2(NHD_3^+)$	1385 sh	-
$2\nu_{4b}(NH_2D_2^+)$	2669 vw	2669 vw	$\nu_4 + \nu_6(ND_4^+)$	1344 sh	1339 w
$\nu_3(ND_4^+)$	2409 sh	-	$\nu_{4b}(NH_2D_2^+)$	1325 w	1330 w
$\nu_3(ND_4^+)$	2389 m	-	$\nu_4(NH_3D^+)$	1278 w	-
$\nu_1(NH_3D^+)$	2377 m	2375 m	$\nu_4(NH_3D^+)$	1268 w	-
$\nu_3(NHD_3^+)$,			$\nu_4(NH_3D^+)$	1260 w	1261 w
$\nu_1(NH_3D^+)$	2354 sh	2359 sh	$\nu_4(NH_3D^+)$	1252 sh	1248 sh
$\nu_1(NH_2D_2^+)$	2337 w	2239 sh	$\nu_2(ND_4^+)$	1190 w	-
$2\nu_4(ND_4^+)$	2254 sh	-	$\nu_2(ND_4^+)$	1182 w	1186 w
$\nu_1(NH_3D^+)$	2190 m	2195 m	$\nu_4(ND_4^+)$	1123 mvw	1120 w
$\nu_1(ND_4^+)$	2167 sh	-	$\nu_{4bc}(NHD_3^+)$,		
$2\nu_2(ND_4^+)$	2134 m	2133 w	$\nu_{4a}(NHD_3^+)$	1080 w	1080 w
			$\nu_4(ND_4^+)$	1077 w	-

Table B.6 Ammonium vibrations in the infrared spectra of 75% D NH_4VO_3

Assignment	Wavenumbers in cm^{-1}		Assignment	Wavenumbers in cm^{-1}	
	80 K	RT		80 K	RT
$\nu_3(NH_4^+)$	3202 m	3184 m	$\nu_4 + \nu_6(ND_4^+)$	1788 w	1786 w
$\nu_3(NH_4^+)$	3123 v	-	$\nu_2(NH_3D^+)$	1610 w	1605 w
$\nu_3(NH_3D^+)$	2984 sh	2976 m.b	$\nu_{2a}(NH_2D_2^+)$	1559 m	1552 w
$\nu_1(NH_4^+)$	2935 m	-	$\nu_2 + \nu_6(ND_4^+)$	1455 w	-
$2\nu_4(NH_4^+)$	2833 m	2831 sh	$\nu_4(NH_4^+)$	1435 sh	-
$2\nu_4(NH_4^+)$	2725 m	2725 sh	$\nu_4(NH_4^+)$	1415 m	1413 m
$2\nu_{4b}(NH_2D_2^+)$	2669 w	2673 sh	$\nu_4(NH_4^+)$	1400 w	-
$2\nu_4(NH_3D^+)$	2528 vw	-	$\nu_2(NHD_3^+)$	1384 sh	-
$\nu_2 + \nu_4(NHD_3^+)$	2472 vw	-	$\nu_4 + \nu_6(ND_4^+)$	1344 m	1338 m
$\nu_3(ND_4^+)$	2404 sh	-	$\nu_{4b}(NH_2D_2^+)$	1325 m	1331 m
$\nu_3(ND_4^+)$	2385 m	-	$\nu_4(NH_3D^+)$	1277 m	-
$\nu_3(NHD_3^+)$	2369 s	2366 m	$\nu_4(NH_3D^+)$	1269 m	-
$2\nu_2(ND_4^+)$	2316 sh	-	$_4(NH_3D^+)$	1260 m	1260 m
$\nu_2 + \nu_4(ND_4^+)$	2272 sh	2280 sh	$\nu_4(NH_3D^+)$	1251 m	-
$2\nu_4(ND_4^+)$	2250 w	-	$\nu_2(ND_4^+)$	1190 m	-
$\nu_1(ND_4^+)$	2186 s	2194 s	$\nu_2(ND_4^+)$	1183 m	1184 m
$2\nu_2(ND_4^+)$	2127 s	2131 m	$\nu_4(ND_4^+)$	1123 m	1121 m
$2\nu_2(ND_4^+)$	2110 m	-	$\nu_{4bc}(NHD_3^+)$,		
			$\nu_{4a}(NHD_3^+)$	1089 m	-
			$\nu_4(ND_4^+)$	1078 m	1079 m

Table B.7 Ammonium vibrations in the infrared spectra of 90% D NH_4VO_3

Assignment	Wavenumbers in cm^{-1}		Assignment	Wavenumbers in cm^{-1}	
	80 K	RT		80 K	RT
$\nu_3(NH_4^+)$,			$\nu_3(NHD_3^+)$	2219 s	-
$\nu_3(NHD_3^+)$	3201 w	-	$\nu_1(ND_4^+)$	2192 s	2195 m
$\nu_3(NH_3D^+)$	3179 sh	3179 b.w	$2\nu_4(ND_4^+)$	2125 s	2127 m
$\nu_3(NH_4^+)$	3122 vw	-	$2\nu_4(ND_4^+)$	2110 s	2112 m
$\nu_1 + \nu_5(NH_4^+)$	3009 sh	-	$\nu_2(NH_4^+)$	1646 vvw	-
$\nu_3(NH_3D^+)$	2980 sh	2980 b.w	$\nu_{2a}(NH_2D_2^+)$	1558 m	1550 m
$\nu_1(NH_4^+)$	2934 w	-	$\nu_2 + \nu_6(NH_4^+)$	1456 m	1444 m
$2\nu_4(NH_4^+)$	2866 w	2866 w	$\nu_4(NH_4^+)$	1417 m	-
$2\nu_4(NH_4^+)$	2861 sh	-	$\nu_4(NHD_3^+)$	1396 m	1401 m
$2\nu_4(NH_4^+)$	2838 sh	-	$\nu_4 + \nu_6(ND_4^+)$	1344 m	1343 m
$2\nu_4(NH_4^+)$	2781 w	2776 w	$\nu_{4b}(NH_2D_2^+)$	1325 m	1331 m
$2\nu_4(NH_4^+)$	2728 vw	-	$\nu_4(NH_3D^+)$	1257 w	-
$2\nu_{4b}(NH_2D_2^+)$	2669 vw	-	$\nu_4(NH_3D^+)$	1268 w	1263 vw
$\nu_3(ND_4^+)$	2407 s	-	$\nu_4(NH_3D^+)$	1272 w	-
$\nu_3(ND_4^+)$	2384 s	2387 vs	$\nu_2(ND_4^+)$	1192 w	1187 w
$\nu_3(NHD_3^+)$	2354 sh	2349 s	$\nu_2(ND_4^+)$	1184 sh	-
$\nu_2 + \nu_4(ND_4^+)$,			$\nu_4(ND_4^+)$	1126 s	1124 m
$2\nu_2(ND_4^+)$	2309 m	2309 m	$\nu_4(ND_4^+)$	1078 vs	1074 vs
$\nu_2 + \nu_4(ND_4^+)$	2271 sh	-			

Table B.8 Wavenumbers of some infrared active bands in NH_4VO_3 at different temperatures

(1) 100% NH_4VO_3

Temperature in K	NH_4^+ modes							
	ν_3	ν_1	$2\nu_4$	$\nu_2 + \nu_6$	$\nu_4 + \nu_6$	$\nu_4 + \nu_6$	ν_2	ν_4
80	3211	2940	2797	2004/1944	1770	1737	1663	1422/1416
100	3212	2938	2797	2009/1945	1770	1740	1665	1422/1416
120	3212	2943	2797	2009/1944	1769	1735	1665	1422/1416
140	3213	2938	2798	2014/1953	1766	1738	1665	1417
160	3209	2935	2796	2011/1957	1766	1728	1665	1417
200	3204	2935	2796	2009	1764	1735	1663	1416
291	3198	2934	2790	-	1754	1737	1559	1415

(2) 1% D NH_4VO_3

Temperature in K	NH_4^+ modes				NH_3D^+ modes	
	ν_3	ν_1	$2\nu_4$	$\nu_2 + \nu_6$	ν_1	ν_1
80	3214	2937	2796	2014	2372	2200
100	3213	2945	2797	2008	2371	2201
120	3212	2939	2796	2009	2369	2202
140	3214	2936	2796	2013	2366	2204
160	3209	2938	2796	2013	2367	2204
180	3213	2936	2794	2024	2366	2206
200	3208	2937	2796	-	2366	2207
220	3205	2937	2795	-	2364	2207
240	3206	2938	2795	2023	2362	2209
260	3201	2944	-	-	2362	2210
291	3211	-	-	2020	2360	2210

(3) 30% D NH_4VO_3

Temperature in K	NH_4^+ modes			ND_4^+	NH_3D^+	
	ν_3	ν_1	$2\nu_4$	ν_1	ν_1	ν_1
100	3213	2940	2799	2185	2372	2204
120	3209	2939	2800	2186	2370	2205
140	3209	2940	2799	2187	2368	2206
160	3209	2940	2799	2189	2368	2206
200	3199	2940	2799	-	2362	-
291	3201	2940	2797	2202	-	2211

(4) 90% D NH_4VO_3

Temperature in K	NH_4^+ modes			ND_4^+ modes							
	ν_3	ν_1	$2\nu_4$	ν_3	ν_3	ν_1	$2\nu_4$	$2\nu_4$	ν_2	ν_4	ν_4
80	3203	2940	2784	2408	2373	2187	2125	2110	1194	1123	1077
100	3203	2941	2786	2407	2373	2190	2126	2111	1194	1123	1077
120	3200	2941	2783	2405	2373	2188	2126	2111	1190	1123	1076
140	3198	2941	2781	2405	2366	2193	2126	2111	1190	1123	1076
160	3199	2941	2784	-	2372	2194	2126	2111	1190	1123	1076
200	3193	2942	2781	-	2377	2194	2127	2112	1189	1123	1075
291	-	-	-	-	2377	2196	-	2111	-	1122	1075

APPENDIX C - $(NH_4)_2V_6O_{16}$ Tables

Table C.1 Vibrational frequencies of NH_4^+ in the infrared spectra of $(NH_4)_2V_6O_{16}$ at 90 K and room temperature

Assignment	Wavenumbers in cm^{-1}	
	90 K	RT
ν_3	3250 m	3216 m
ν_3	3194 m	-
ν_3	3177 sh	-
ν_1	3115 m	-
$\nu_2 + \nu_4$	3041 m	-
$2\nu_4$	2846 vw	-
$2\nu_4$	2814 w	-
$2\nu_4$	2766 w	-
$\nu_2 + \nu_6$	1974 vw	-
$\nu_2 + \nu_6$	1930 vw	1930 vw
ν_2	1638 b.w.	1660 w
$2\nu_4$	1420 s	-
ν_4	1398 s	1405 s
ν_4	1385 s	-

Table C.2 Ammonium vibrations in the infrared spectra of 5% D $(NH_4)_2V_6O_{16}$

Assignment	Wavenumbers in cm^{-1}		Assignment	Wavenumbers in cm^{-1}	
	90 K	RT		90 K	RT
$\nu_3(NH_4^+)$	3247 m	3218 m	$\nu_2(NH_4^+)$	1653 vw	1630 vw
$\nu_3(NH_4^+)$	3197 s	-	$\nu_{2a}(NH_2D_2^+)$	1559 vw	-
$\nu_3(NH_4^+)$	3177 sh	-	$\nu_4(NH_4^+)$	1421 vs	-
$\nu_1(NH_4^+)$	3103 m	-	$\nu_4(NH_4^+)$	1399 vw	-
$\nu_2 + \nu_4(NH_4^+)$	3050 m	-	$\nu_4(NH_4^+)$	1375 vw	-
$\nu_3(NH_2D_2^+)$	2917 w	-	$\nu_2(NHD_3^+)$	1363 vw	-
$2\nu_4(NH_4^+)$	2846 w	-	$\nu_4 + \nu_6(ND_4^+)$	1339 w	-
$2\nu_4(NH_4^+)$	2818 w	-	$\nu_{4b}(NH_2D_2^+)$	1319 w	-
$2\nu_4(NH_4^+)$	2770 vw	-	$\nu_4(NH_3D^+)$	1261 w	-
$2\nu_2(NHD_3^+)$	2739 vw	-	$\nu_4(NH_3D^+)$	1245 w	1252 w
$\nu_1(ND_4^+)$	2388 sh	-	$\nu_4(NHD_3^+)$	1176 w	-
$\nu_1(NH_3D^+)$	2356 w.sp.	-	$\nu_4(NHD_3^+)$	~1160 vvw	-
$\nu_1(NH_3D^+)$	2345 w.sp.		$\nu_2(ND_4^+)$	~1104 vvw	-
$\nu_1(NH_3D^+)$	2287 w	-			

Table C.3 Ammonium vibrations in the infrared spectra of 30% D $(NH_4)_2V_6O_{16}$

Assignment	Wavenumbers in cm^{-1}		Assignment	Wavenumbers in cm^{-1}	
	90 K	RT		90 K	RT
$\nu_3(NH_4^+)$	3250 s	-	$2\nu_2(ND_4^+)$	2241 vw	-
$\nu_3(NH_4^+)$	3198 s	3222 s	$\nu_2 + \nu_6(NH_4^+)$	1967 b.vw	1958 vw
$\nu_3(NH_4^+)$,			$\nu_{2a}(NH_2D_2^+)$	1588 w	~1580 vw
$\nu_3(NHD_3^+)$	3184 sh	-	$\nu_4(NH_4^+)$	1423 s	-
$\nu_1(NH_4^+)$	3103 m	3129 sh	$\nu_4(NH_4^+)$	1398 s	1406 m
$\nu_2 + \nu_4(NH_4^+)$	3090 sh	-	$\nu_4 + \nu_6(ND_4^+)$	1345 w	-
$\nu_2 + \nu_4(NH_4^+)$	3079 sh	-	$\nu_{4b}(NH_2D_2^+)$	1322 s	-
$\nu_3(NH_2D_2^+)$	2918 vw	-	$\nu_4(NH_3D^+)$	1260 s	-
$2\nu_4(NH_4^+)$	2848 w	2853 vw	$\nu_4(NH_3D^+)$	1245 w	1252 w
$\nu_3(NH_3D^+)$	2836 w	-	$\nu_4(NHD_3^+)$	1183 w	-
$2\nu_4(NH_4^+)$	2820 w	-	$\nu_4(NHD_3^+)$	1173 vvw	1173 vw
$2\nu_4(NH_4^+)$	2734 vw	-	$\nu_{4bc}(NHD_3^+)$,		-
$2\nu_4(NH_3D^+)$	2479 vw	-	$\nu_{4a}(NHD_2^+)$	1116 vw	1117 vw
$\nu_3(ND_4^+)$	2386 w	2380 w	$\nu_2(ND_4^+)$	1111 w	1107 vw
$\nu_1(NH_3D^+)$	2359 w		$\nu_4(ND_4^+)$	1084 vw	-
$\nu_1(NH_3D^+)$	2351 w	2349 w	$\nu_4(ND_4^+)$	1068 vw	-
$\nu_1(NH_3D^+)$	2287 w	-			

Table C.4 Ammonium vibrations in the infrared spectra of 50% D $(NH_4)_2V_6O_{16}$

Assignment	Wavenumbers in cm^{-1}		Assignment	Wavenumbers in cm^{-1}	
	90 K	RT		90 K	RT
$\nu_3(NH_4^+)$,			$\nu_4(NH_4^+)$	1426 m.sp	-
$\nu_3(NHD_3^+)$	3247 m	3221 m	$\nu_2 + \nu_6(ND_4^+)$	1412 sh	1415 sh
$\nu_3(NHD_3^+)$	3188 s	-	$\nu_4(NH_4^+)$	1397 m.sp	1402 m
$\nu_1(NHD_3^+)$	3120 m.sh	3128 sh	$\nu_4(NH_4^+)$	1386 sh	1362 sh
$\nu_2 + \nu_4(NH_4^+)$	3060 m.sh	-	$\nu_2(NHD_3^+)$	1370 vw.sh	-
$\nu_3(NH_2D_2^+)$	2915 w	2924 vw	$\nu_4 + \nu_6(ND_4^+)$	1346 w	1338 vw
$2\nu_2(NH_4^+)$	2846 w	2852 vw	$\nu_{4b}(NH_2D_2^+)$	1324 w	-
$2\nu_4(NH_4^+)$	2819 vw	-	$\nu_2(NH_2D_2^+)$	1316 w	-
$2\nu_4(NH_3D^+)$	2474 vw	-	$\nu_4(NH_3D^+)$	1260 s	-
$\nu_3(NH_3D^+)$	2420 sh.vw	-	$\nu_4(NH_3D^+)$	1245 w	1251 w
$\nu_3(ND_4^+)$	2404 sh	-	$\nu_4(NHD_3^+)$	1185 m	-
$\nu_3(ND_4^+)$	2390 sh	2389 v	$\nu_4(NHD_3^+)$	1174 m	1169 vw
$\nu_1(ND_4^+)$	2379 vw		$\nu_{4bc}(NHD_3^+)$	1131 sh	-
$\nu_1(NH_3D^+)$	2355 w	2353 sh	$\nu_4(NH_2D_2^+)$	1116 vw	-
$2\nu_{4bc}(NH_3D^+)$	2306 sh	2304 sh	$\nu_2(ND_4^+)$	1111 w	1106 vw
$\nu_1(NH_3D^+)$	2284 w	-	$\nu_{4bc}(NHD_3^+)$	1094 sh	-
$2\nu_2(ND_4^+)$	2237 vvw		$\nu_4(ND_4^+)$	1085 vw	-
$\nu_2 + \nu_4(NH_4^+)$	~1950 w.b	~1950 w.b.	$\nu_4(ND_4^+)$	1069 vw	
$\nu_{2a}(NH_2D_2^+)$	1583 v	1588 w.b			

Table C.5 Ammonium vibrations in the infrared spectra of 70% D $(NH_4)_2V_6O_{16}$

Assignment	Wavenumbers in cm^{-1}		Assignment	Wavenumbers in cm^{-1}	
	90 K	RT		90 K	RT
$\nu_3(NHD_3^+)$	3243 m	-	$\nu_2 + \nu_6(NH_4^+)$	~1923 w.b	~1920 vw
$\nu_3(NHD_3^+)$	3185 s	3187 m.b	$\nu_{2a}(NH_2D_2^+)$	~1558 w.b	~1550 vw
$\nu_3(NHD_3^+)$	~ 3140 sh	-	$\nu_4(NH_4^+)$	1420 sh	-
$\nu_1(NHD_2^+)$	3117 m	-	$\nu_4 + \nu_6(ND_4^+)$	1409 m	-
$\nu_2 + \nu_4(NH_4^+)$	~3070 sh	-	$\nu_4(NH_4^+)$	1402 m	1400 s
$\nu_3(NH_2D_2^+)$	2916 w	2923 w	$\nu_4(NH_4^+)$	1385 w	-
$2\nu_2(NH_4^+)$	2847 w	2852 w	$\nu_2(NHD_3^+)$	1379 w	-
$2\nu_4(NH_4^+)$	2786 w	-	$\nu_4 + \nu_6(ND_4^+)$	1345 w	1338 w
$2\nu_4(NHD_3^+)$	2727 vw	-	$\nu_{4b}(NH_2D_2^+)$	1323 w	1321 w
$2\nu_4(NH_3D^+)$	2482 vw	-	$\nu_2(NH_2D_2^+)$	1316 w.sh	-
$\nu_3(ND_4^+)$	2436 s	-	$\nu_4(NH_3D^+)$	1260 w	-
$\nu_3(ND_4^+)$	2427 s	-	$\nu_4(NH_3D^+)$	1243 w	-
$\nu_3(ND_4^+)$	2404 vs	2412 vs	$\nu_4(NHD_3^+)$	1184 w	-
$\nu_1(ND_4^+)$	2385 vs.sh	2346 m	$\nu_4(NHD_3^+)$	1173 w	1169 w
$2\nu_{4b}(NHD_3^+)$	2306 vw	-	$\nu_{4bc}(NHD_3^+)$	1136 m	-
$\nu_1(NH_3D^+)$	2283 w	-	$\nu_2(ND_4^+)$	1124 s	-
$2\nu_2(ND_4^+)$	2165 vw	2183 vw	$\nu_2(ND_4^+)$	1109 sw	1110 sh
$2\nu_4(ND_4^+)$	2139 w	-	$\nu_4(NHD_3^+)$	1083 vs	1081 s
			$\nu_4(ND_4^+)$	1067 sh	-
			$\nu_4(ND_4^+)$	1059 s	-

Table C.6 Wavenumbers of some infrared active bands in $(NH_4)_2V_6O_{16}$ at different temperatures

(1) 100% $(NH_4)_2V_6O_{16}$

Temperature in K	NH_4^+ modes								
	ν_3	ν_3	ν_1	$\nu_2 + \nu_4$	$2\nu_4$	$2\nu_4$	ν_2	ν_4	ν_4
80	3255	3199	3096	3046	2830	2816	1632	1420	1400
100	3252	3201	3097	3046	2823	2816	1632	1420	1401
120	3248	3200	3097	3046	2830	2818	1632	1420	1401
140	3216	3216	3102	3049	2824	2818	-	1417	1402
160	3237	3221	3103	3046	2825	2817	-	1415	1402
200	3236	3230	3092	3045	2829	2819	-	-	1404
291	3242	3232	-	-	-	-	-	-	1408

(2) 5% D $(NH_4)_2V_6O_{16}$

Temperature in K	NH_3D^+ modes		
	ν_1	ν_1	ν_1
80	3254	3249	2287
100	2354	2349	2294
160	2350	2348	2305
180	2355	2344	2298
200	2350	2349	2304
220	2350	2349	2305
240	2348	2347	2302
260	2350	2348	2308
291	2349	2349	-

Table C.6 Wavenumbers of some infrared active bands in $(NH_4)_2V_6O_{16}$ at different temperatures (cont.)

(3) 30% D $(NH_4)_2V_6O_{16}$

Temperature in K	NH_4^+ modes			
	ν_3	ν_3	ν_4	ν_4
80	3252	3199	1426	1398
120	3248	3204	1422	1400
140	3231	3217	1416	1401
160	3236	-	-	1402
200	3231	3225	-	1402
291	3252	3244	-	1405

(4) 90% D $(NH_4)_2V_6O_{16}$

Temperature in K	ND_4^+ modes			
	ν_3	ν_1	ν_2	ν_4
80	2400	2379	1109	1082
120	2403	2361	1111	1080
160	2409	2341	1114	1078
200	2415	2360	1113	1079
291	2418	2350	-	1077

APPENDIX D - Instrumental details

1. Vibrational spectra

Mid-infrared spectra were recorded on either the Bruker IFS 113v or the Bomem Michelson-100 FT-IR spectrometer. Samples were in the form of KBR pellets. Far-infrared spectra were recorded on the Bruker instrument with samples in the form of polyethylene pellets.

All Raman measurements were made on the Z-24 Dilor Raman spectrometer using one of three lines to excite the spectra:

(1) 632.8 nm - A He-Ne laser (Spectra Physics Stabelite Model 124B)
(2) 514.5 nm - from an Ar^+ ion laser (Coherent Innova 90)
(3) 488 nm - The Ar^+ ion laser (Coherent Innova 90)

2. High temperature Raman measurements

A high temperature cell obtained from Dilor, Lille, France was used to heat the samples in a glass tube, 3 mm in diameter. The utilization range is from room temperature to 673 K [125].

3. Low temperature infrared recordings: The continuous flow cryostat

The CF1104 Oxford instruments continuous flow cryostat with optical shield and vacuum case operate on the principle of a continuous and controlled transfer of coolant from a storage vessel to the cryostat. The storage vessel containing liquid nitrogen is maintained at a pressure close to atmospheric pressure and a flow pump is used to create a pressure difference between the storage vessel and the return line shown in Figure D.1. Flow is controlled by valves on the transfer tube leg in the storage vessel and in the flow controller unit while a vacuum gauge and flow meter provide details of coolant flow. Liquid nitrogen flows through the heat exchange of the cryostat where the temperature is measured and a heater is used to maintain the temperature anywhere above 77 K. Samples are mounted in vacuum on a copper finger (Figure D.2) and are cooled or heated by conduction as the transfer tube is loaded through the entry port and the cryogen is delivered directly into the copper heat exchanger. Gas flows out back around the outside of the tube tip and passes out through the transfer tube [126].

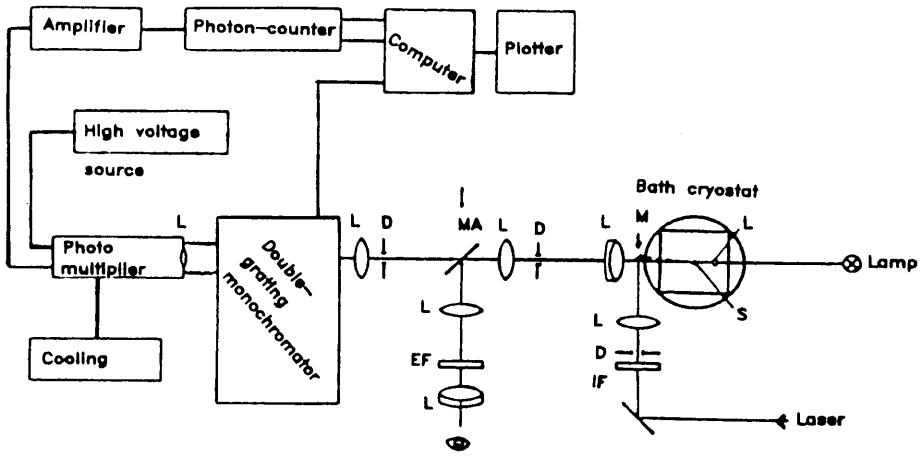

Figure D.1 Block diagram of the continuous flow system used in low temperature studies [126].

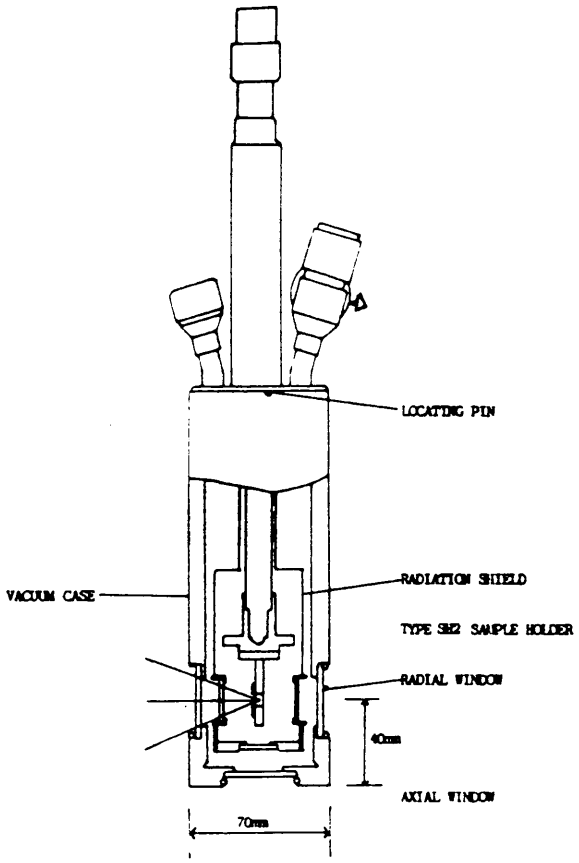

Figure D.2 The CF1104 cooling/heating unit with radiation shield and vacuum case with optical access to the sample position [126].

4. Absorbance and emission spectra

Absorbance spectra of Er_2O_3, $ErVO_4$, Nd_2O_3 and $NdVO_4$ were recorded on a Carey 2390 (UV-VIS-NIR) spectrometer from Varian.

(Diffuse reflectance measurements were made between 300 and 800 nm (333 333 to 12 500 cm^{-1}).

Room temperature emission spectra were recorded on the Z-24 Dilor Raman spectrometer. The 514.5 and 488 nm lines of an Argon ion laser were used for excitation of the samples. The spectrometer for recording low temperature emission spectra of Er_2O_3 (77 K) and $ErVO_4$ (77, 4.2 and 1.3 K) is shown in Figure D.3. Samples were filled into a sample holder of copper with two quartz windows (diameter: 5 mm), which are separated by a teflon ring. The emission was measured in a liquid helium bath cryostat (Leybold Heraeus, type 09907301.1), which enables measurements at T = 77 K and in the temperature interval 1.3 K < T < 4.2 K. The 365 nm-line of an argon ion laser (Coherent, Innova 90) was used as excitation source. The emitted light was analyzed by a double-grating monochromator (Spex 1401) and was detected by a cooled photomultiplier (RCA, type C7164R).

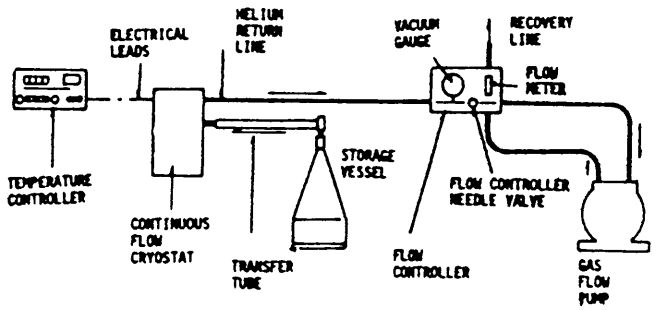

Figure D.3 Spectrometer for the measurement of emission spectra at low temperatures. D, diaphragm; L, quartz glass lens; S, sample; EF, interference filter; M, mirror (to make the adjustment of the sample possible; putted aside during the measurement)

The optical system is described in detail in Messtechnik 4/72.

5. The scanning electron microscope and EDX-analysis

The scanning electron microscope (SEM) can provide different information on a sample e.g. topography of the sample with deeper layers producing additional secondary electron emission from the surface. Backscattered electrons help to discriminate between different materials in a specimen through the increase of the probability of backscattering with the atomic number of an element. Energy dispersive X-ray analyses in conjunction with SEM provides information on different points in the sample, producing an energy dispersive X-ray spectrum with characteristic X-rays of all elements in the area hit by the primary electron beam.

Secondary and backscattering electron pictures were obtained from a scanning electron microscope, Zeiss DSM 950, with the X-ray analysis system, Link QX 200, providing point analysis on the samples. NaCl, KCl, metallic Er and Nd as well as V_2O_5 were used as external standards.

6. X-ray powder diffraction

X-ray powder diffraction patterns were recorded using a Guinier camera, Huber Guinier-system 621 (Fa. Huber, Rimsting).

REFERENCES

REFERENCES

1. B. Rohrmann, J.S. Afr. Inst. Min. Metall. **85**, 141 (1985).

2. M. Taniguchi and T.R. Ingraham, Can. J. Chem. **42**, 2467 (1964).

3. T. Palanisamy, J. Gopalakrishnan and M.V.C. Sastri, J. Solid State Chem. **9(3)**, 273 (1974).

4. J. Trau, J. Therm. Anal. **16(1)**, 201 (1979).

5. J. Lamure and G. Colin, C.R. Acad. Sci. (Paris) **258** (26), 6433 (1964).

6. S.A. Selim, Ch. A. Philip and R. Sh. Mikhail, Thermochim. Acta **36**, 287 (1980).

7. A. Deschanvres, G. Nouet and B. Raveneau, C.R. Acad. Sci. (Paris) **261** (16), 3144 (1965).

8. K.-J. Range and R. Zintl, Mat. Res. Bull. **18**, 41 (1983).

9. A.M. Heyns and J.B. Clark, J. Raman Spectroscopy **14**, 362 (1983).

10. A.M. Heyns, M.W. Venter and K.-J. Range, Z. Naturforsch **426**, 843 (1987).

11. K.-J. Range, R. Zintl and A.M. Heyns, Z. Naturforsch **436**, 309 (1988).

12. M.E. Brown and B.V. Stewart, J. Thermal Anal. 2, 287 (1970).

13. M.E. Brown, L. Glasser and B.V. Stewart, J. Thermal Anal. 6, 529 (1974).

14. M.E. Brown, L. Glasser and B.V. Stewart, J. Thermal Anal. 7, 125 (1975).

15. M.H. Askar, R.S. Girgis and M.A. Khilla, J. Therm. Anal. 35(5), 1315 (1989).

16. U. von Sacken and J.R. Dahn, J. Power Sources 26(3-4), 461 (1989).

17. A. Legrouri,T. Baird and J.R. Fryer, React. Solids 5(1), 53 (1988).

18. K.-J. Range, C. Eglmeier, A.M. Heyns and D. de Waal, Z. Naturforsch 456, 31 (1990).

19. D. de Waal, A.M. Heyns and K.-J. Range, J. Solid State Chem. 80, 170 (1989).

20. J. Davies, Raman Spectroscopy 9, 381 (1980).

21. F. Ephraim and G. Beck, Helv. Chim. Acta 9, 38 (1926).

22. A.D. Kelmers, J. Inorg. Nucl. Chem. 21, 45 (1961).

23. U.M. Levanto, Acta Polytech. Scand. 82, 8 (1969).

24. F.R. Théobald, J.-G. Théobald, J.C. Vedrine, R. Clad and J. Reward, J. Phys. Chem. Solids **45**, 581 (1984).

25. L.V. Kristallov, O.V. Koryakova, L.A. Perelyaeva and M.P. Tsvetkova, Russ. J. of Inorg. Chem. **3** (8), 1073 (1987).

26. H.T. Evans and S. Block, Inorg. Chem. **5**, 1808 (1966).

27. W.G. Fateley, F.R. Dollish, N.T. McDevitt and F.F. Bentley, Infrared and Raman Selection Rules for Molecular and Lattice Vibrations: The Correlation Method, Wiley-Interscience, New York (1972).

28. L.V. Kristallov, Summary of Candidate's Thesis, Institute of Chemistry, Urals Research Centre, Academy of Sciences of the USSR, Sverdlovsk, 1985, p. 18.

29. V. Baran, J. Mol. Struct. **13** (1), 1 (1972).

30. V. Satava, Coll.Czech. Chem. Comm. **24**, 2172 (1959).

31. J. Trau, Roczwiki Chem. **36**, 1365 (1962).

32. M. Taniguchi and T.R. Ingraham, Can. J. Chem. **42**, 2467 (1964).

33. J. Trau, Zeszyty Nauk. Politechn. Krakow **21**, 113 (1966).

34. H.O. Becker, Ph.D. Thesis, University of Heidelberg (1971).

35. M. Avrami, J. Chem. Phys. **7**, 1103 (1939).

36. M. Avrami, J. Chem. Phys. **8**, 1103 (1940).

37. M. Avrami, J. Chem. Phys. **9**, 117 (1941).

38. B.V. Erofe'ev, Dokl. Akad. Nauk SSSR **52**, 511 (1964).

39. J.H. Sharp, G.W. Bridley and B.N.N. Achar, J. Amer. Ceram. Soc. **49**, 379 (1966).

40. C.J. Keattch and D. Dollimore, "An Introduction to Thermogravimetry", 2nd Ed., Heyden, New York (1975).

41. C.N.R. Rao and K.J. Rao, "Phase Transitions in Solids", McGraw-Hill, London (1978).

42. J.W. Christian, "The Theory of Transformations in Metals and Alloys", Pergamon, Press, Oxford (1965), (2d Ed., Part I. 1975).

43. J. Burke, "The Kinetics of Phase Transformations in Metals", Pergamon Press, Oxford (1965).

44. F.W. Loomis, Astrophys. J. **52**, 248 (1920); A. Kratzer, Z. Physik **3**, 460 (1920); A. Kratzer, Z. Physik **4**, 476 (1921).

45. H.C. Urey, F.C. Brickwedde and G.M. Murphy, Phys. Rev. **39**, 144 (1932).

46. A.J. Barnes and W.J. Orville-Thomas (Eds.) Vibrational Spectroscopy-Modern Trends, Elsevier (1977), p. 139.

47. I.A. Oxton, O. Knop and M. Falk, J. Phys. Chem. **80** (11), 1212 (1976).

48. I.A. Oxton, O. Knop and M. Falk, J. Phys. Chem. **53**, 2675 (1975).

49. S.D. Hammon, Aust. J. Chem. **31**, 11 (1978).

50. G.J. Kearly and I.A. Oxton, Adv. Infrared and Raman Spectrosc. **10**, 111 (1983).

51. I.A. Oxton, O. Knop and M. Falk, J. Phys. Chem. **53** (22), 3394 (1975).

52. I.A. Oxton, O. Knop and M. Falk, Can. J. Chem. **54** (6), 892 (1976).

53. I.A. Oxton, O. Knop and M. Falk, Can. J. Chem. **37**, 9 (1977).

54. I.A. Oxton and O. Knop, J. Molc. Struct. **49**, 309 (1978).

55. I.A. Oxton, O. Knop and M. Falk, Can. J. Chem. **57**, 404 (1979).

56. O. Knop, W.J. Westerhaus and M. Falk, Can. J. Chem. **58** (3), 270 (1980).

57. O. Knop, W.J. Westerhaus and M. Falk, Can. J. Chem. **58** (9), 867 (1980).

58. O. Knop, T.S. Cameron, M.A. James and M. Falk, Can. J. Chem. **59** (16), 2250 (1981).

59. W.J. Westerhaus, O. Knop and M. Falk, Can. J. Chem. **58**, 1355 (1980).

60. O. Knop, I.A. Oxton, W.J. Westerhaus and M. Falk, J. Chem. Soc. Faraday Trans. 2, **77** 309 (1981).

61. O. Knop, I.A. Oxton, W.J. Westerhaus and M. Falk, J. Chem. Soc. Faraday Trans. 2, **77**, 811 (1981).

62. O. Knop, W.J. Westerhaus, M. Falk and W. Massa, Can. J. Chem. **63**, 3328 (1985).

63. F.C. Hawthorne and C. Calvo, J. Solid State Chem. **22**, 157 (1977).

64. R. Zintl, PhD thesis, Regensburg (1984).

65. S. Onodera and Y. Ikegami, Inorg. Chem. **18**, 466 (1979).

66. S. Block, Nature **186** (4724), 541 (1960).

67. H.T. Evans and S. Block, Inorg. Chem. **5**(10), 1808 (1966).

68. H.R. Wyss and S. Block, Inorg. Chem. **48**, 608 (1970).

69. D. de Waal, A.M. Heyns, K.-J. Range and C. Eglmeier, Spectrochim. Acta **45A**, 1639 (1990).

70. D. de Waal, A.M. Heyns, K.-J. Range and C. Eglmeier, Spectrochim. Acta **46A**, 1649 (1990).

71. M. Lacharte, Bull. Chim. Soc. France, **35**, 321 (1924).

72. C. Eglmeier, PhD thesis, University of Regensburg, Regensburg (1989).

73. A.R. West, Solid State chemistry and its applications, John Wiley and Sons Ltd. (1984).

74. R.D. Shannon and C. Calvo, Can. J. Chem. **51**, 265 (1973).

75. F. Marumo, M. Isobe and S. Iawa, Acta Cryst. **B30**, 1628 (1974).

76. K.L. Idler, C. Calvo and H.N. Ng, J. Solid State Chem. **25**, 285 (1978).

77. F.C. Hawthorne and C. Calvo, J. Solid State Chem. **22**, 157 (1977).

78. A.G. Bergman and Z.I. Sanzharova, Russ. J. Inorg. Chem. **15**, 877 (1970).

79. S. Ohashi, "Topics in phosphorus chemistry" (M. Grayson and E.J. Griffith, Eds.) Vol. 1, Wiley, New York (1964).

80. J. Perraud, Rev. Chim. Miner **11**, 3202 (1974).

81. M.P. Glazarin, Dokl. Akad. Nauk SSSR **221**, 91 (1975).

82. R.T. Patil, N.B. Patil, A.P. Kashid and S.H. Chavan, Mat. Res. Bull. **25**, 57 (1990).

83. M. Matsuda, J. Phys. Soc. Jpn **36**, 759 (1974).

84. I. Lukas and C. Strusievici, Z. Anorg. Allg. Chem. **315**, 323 (1962).

85. R.S. Fiegelson, G.W. Martin and B.C. Johnson, J. Cryst. Growth **13/14**, 686 (1972).

86. S. Sawada and S. Nomura, J. Phys. Soc. Jpn **6**, 192 (1950).

87. K. Ramani, A.M. Shaikh, B.S. Reddy and M.A. Viswamitra, Ferroelectrics **9**, 49 (1975).

88. A.M. Shaikh, PhD thesis, Indian Institute of Science (1979).

89. S. Seetharaman, H.L. Bhat and P.S. Narayanan, J. Raman Spectroscopy **14(6)**, 401 (1983).

90. D.M. Adams and D.C. Newton, Tables for Factor group and Point group analysis, Beckman-RIIIC Ltd, Croydon, England (1970).

91. D.M. Adams and P.A. Fletcher, Spectrochim. Acta **44A**(2), 233 (1988).

92. Y.S. Park and H.F. Shurvell, J. Raman Spec. **18(4)**, 247 (1987).

93. G.A. Gehringand and K.A. Gehring, Rep. Prog. Phys. **35**, 1 (1975).

94. K. Gaur and H.B. Lal, J. Mat. Sci. **21**, 2289 (1986).

95. S. Hüfner in Systematics and properties of the lanthanides, Shyana P. Sinha (ed.), D. Reidel publishing co., Lancaster (1982).

96. H.L. Yakel, Acta Cryst. Sect. B **35**, 564 (1979).

97. L. Pauling, Z. Kristallogr. **A69**, 415 (1928).

98. J. Gouteron, D. Michel, A.M. Lejus and Z. Zarembowitch, J. Solid State Chem. **38**, 288 (1981).

99. D. Bloor and J.R. Dean, J. Phys. **C5**, 1237 (1972).

100. W.P. Griffith, J. Chem. Soc. A, 286 (1976).

101. W.P. Griffith and P.J.B. Lesniak, J. Chem. Soc. A, 1066 (1969).

102. A. Müller, E.J. Baran and P.J. Hendra, Spetrochim Acta **25A**, 1654 (1969).

103. A. Hezel and S.D. Ross, Spectrochim. Acta **22**, 1949 (1966).

104. E.J. Baran, M.E. Escobar, L.L. Fournier and R.L. Filguera, Z. Anorg. Allg. Chem. **472**, 193 (1981).

105. A.M. Heyns, K.J. Range and M. Wildenauer, Spectrochim. Acta **46A**, 1621 (1990).

106. S.A. Miller, H.H. Caspers and H.E. Rast, Phys. Rev. **168**, 964 (1968).

107. C.R. Gopinath and I.D. Brown, J. Raman Spectroscopy **12** 278 (1982).

108 J.H. Deming and S.D. Ross, J. Phys. C**5**, 1123 (1972).

109. J. Zarembowitch, J. Gouteron and A.M. Lejus, Phys. Status Solidi **B94**, 249 (1979).

110. J. Zarembowitch, J. Gouteron and A.M. Lejus, J. Raman Spectroscopy **9**, 263 (1980).

111. S.I. Bolidish and W.B. White, Spectrochim. Acta **A35**, 1235 (1979).

112. H. Meister, PhD thesis, Regensburg university (1985).

113. J.R. Schoonover, YNG-LongLee, S.N. Su, S.H. Lin and L. Eyring, Applied Spectroscopy **38**, 154 (1984).

114. V.L. Konstatinov, V.I. Rogovitch, V.A. Sapozhnikov and G.P. Skornyakov, Spectroscopy Letters **10**, 7 (1977).

115. J.B. Gruber, R.D. Chririco and E.F. Westrum, Jr., J. Chem. Phys. **76**, 4600 (1982).

116. E.F. Westrum Jr. and B.H. Justice, J. Chem. Phys. **67**, 659 (1963).

117. J.R. Dean and D. Bloor, J. Phys. C.: Solid State Physics **5**, 2921 (1972).

118. G. Schaak and J.A. Koningstein, J. Opt. Soc. Amer. **60**, 110 (1970).

119. D. Kuse, Zeitschrift für Physik **203**, 49 (1967).

120. P.C. Becker, G.M. Williams, R.E. Russo, N. Edelstein, J.A. Koningstein, L.A. Boatner and M.M. Abraham, Optics Letters **11** (5), 282 (1986).

121. G.M. Murray, R.v. Sarrio and J.R. Peterson, Applied Spectroscopy **44** (10), 1647 (1990).

122. J.P. Young, G.M. Murray, D.D. Ensor and D.O. Vick, Applied Spectroscopy **45** (1), 134 (1991).

123. G.H. Dieke, Spectra and energy levels of Rare Earth ions in Crystals, Interscience publishers, New York (1968).

124. C. Brechner, H. Samelson, A. Lempicki, R. Riley and J. Peters, Phys. Rev. **155**, 178 (1967).

125. Multichannel Spectroscopy Attachments Manual, Dilor, Lille, France.

126. Instructions manual: Continuous flow cryostat CF1100, CF1104, CF1108, Oxford instruments limited, Osney Mead, Oxford, England (1984).